Hydrothermal Spallation Drilling and Advanced Energy Conversion Technologies for Engineered Geothermal Systems

By

Chad R. Augustine

B.S., Chemical Engineering
Iowa State University, 2000

M.S., Chemical Engineering Practice
Massachusetts Institute of Technology, 2003

Submitted to the Department of Chemical Engineering in partial fulfillment of the requirements
for the degree of

DOCTOR OF PHILOSOPHY IN CHEMICAL ENGINEERING

at the

MASSACHUSETTS INSTITUTE OF TECHNOLOGY

June 2009

Signature of Author: _____

Department of Chemical Engineering
May 21, 2009

Certified By: _____

Professor Jefferson W. Tester
Thesis Supervisor

Accepted By: _____

William M. Deen
Professor of Chemical Engineering
Chairman, Committee for Graduate Students

Hydrothermal Spallation Drilling and Advanced Energy Conversion Technologies for Engineered Geothermal Systems

By

Chad R. Augustine

Submitted to the Department of Chemical Engineering on May 21, 2009 in partial fulfillment of the requirements for the degree of Doctor of Philosophy in Chemical Engineering

ABSTRACT

The purpose of this research was to study the various factors affecting the economic and technical feasibility of Engineered Geothermal Systems, with a special emphasis on advanced drilling technologies. The first part of the thesis was devoted to modeling and analysis of the technologies used to develop EGS projects. Since the cost of completing wells is a major factor in determining the economic feasibility of EGS projects, it is vital to be able to accurately predict their costs. Historic well cost data was analyzed to identify trends, and a drilling cost index for updating historic geothermal well costs to present day costs was developed. The effects of different advanced drilling technologies on drilling costs were estimated and incorporated into a techno-economic model to estimate their impact, as well as the impact of advanced reservoir stimulation technologies, on EGS levelized electricity costs. A technical analysis of geothermal binary Rankine cycle surface power plants was also performed to determine the effect of novel working fluids on plant efficiency for both sub- and supercritical binary cycles.

The objective of the second part of the thesis was the application of thermal spallation drilling to deep boreholes. Thermal spallation is the fragmentation of a brittle solid into small, disc-like flakes by rapidly heating a confined fraction of the rock. It was proposed that the necessary temperatures and heat fluxes needed to induce thermal spallation in the high pressure, high density deep borehole environment could be achieved using hydrothermal flame technologies. An autoclave reaction system was designed and constructed to create flame jets in water at a pressure of 250 bar. The temperatures of these flames were measured, and attempts were made to use the flames to spall small rock samples. The experimental system was modified to study the centerline temperature decay of supercritical water jets injected at temperatures up to 525 $^{\circ}$C into ambient temperature water. A device for measuring the heat flux from these jets was designed, constructed, and used to determine the heat transfer coefficients of the jets impinging against a flat surface. Together, these studies indicate that the necessary temperatures and heat fluxes required to induce thermal spallation in rocks can be achieved in a deep borehole.

Thesis Supervisor: Jefferson W. Tester
                      Herman P. Meissner Professor of Chemical Engineering

"It's not a church."

- Col. Russell P. Lachance

Acknowledgements:

I would like to express my deepest thanks to the people who helped me in my journey through MIT, without whom this thesis would have never happened.

First, to my advisor Jeff, whose lessons and instruction extended well beyond the areas of my research topic,

To Gwen Wilcox, my "classmate" in the Tester group, who kept the wheels on the train and helped me out of more jams than I'll probably remember,

To my thesis committee members Bill Deen, Bill Green, Mark Wilkinson, and especially Ahmed Ghoniem, who was especially helpful and patient with me in my foray into modeling jet behavior,

To Tester Group members who were always there to listen and discuss research problems, or whatever – Andy Peterson, Scott Paap, Rocco Ciccolini, Kury Frey, Hidda Thorsteinsson, Jason Ploeger, and Russ Lachance. Russ gave me the great advice on the previous page that helped me move on when I was stuck in the equipment construction phase of the thesis. It's a phrase his dad would tell him to justify some of the shortcuts he took during home renovation projects. I have paraphrased the quote to mean "if good is enough, better is not necessary." As I continue to learn and do more, I believe that being able to determine when good is enough is the defining characteristic of a good engineer, and possibly the key to success in life,

To MIT friends, especially Ramin and Anna, Mike and Wanda, Jason and Sarah, Greg and Melissa, Dan, Sandeep, Curt, Jie, et al. for the good times and keepin' it rollin',

To P. Rudolph van Rohr and his group at ETH, including Beat Wellig, Karol Príkopský, and Karl Goosens, for donating us equipment, time, and expertise,

A special big thanks to Robert and Jared Potter, Tom Wideman and all the other people at Potter Drilling, without whose help this project would definitely not had made it as far as it did. I wish them continued success in the spallation drilling business.

To the Augustine and Boettger families for their support,

Most of all, to my wife, best friend, and occasional SROP, Adi, who sacrificed more than I did to make this thesis a reality and whose patience, support and belief in me never wavered.

Thank you all.

TABLE OF CONTENTS

Chapter 1: Introduction and Background

1.1. Motivation

Interest in EGS has increased recently due in large part to the publication of a report by an 18-member panel of experts led by MIT called "The Future of Geothermal Energy" (Tester et al., 2006), which explored the potential of using EGS to make up a significant portion of US electricity generating capacity. The report estimated the size and distribution of the EGS resource in the US, reviewed critical findings from previous demonstration studies, and assessed the technical and economic factors involved in developing and deploying EGS resources, including the cost and feasibility of drilling wells, stimulating and managing the reservoir, and producing electricity. The study concluded that with a total investment of about one billion dollars in research and development spread over 10-15 years, EGS has the potential to supply the US with 100,000 MW of geothermal electrical generating capacity by 2050 at prices competitive with conventional electricity generating technologies.

High drilling and well completion costs are a major factor in determining the economic feasibility of developing geothermal resources for energy production. Economic studies show that drilling costs alone could account for 50-70% of the total capital investment in an EGS geothermal electric plant. These costs increase as the temperature gradient of the resource decreases and deeper wells are needed to access temperatures high enough to produce electricity efficiently (Armstead and Tester, 1987; Thorsteinsson et al., 2008). A typical EGS well will be 3-8 km deep and will usually occur in hard, granitic basement rock. Hence, any technology that could substantially reduce the costs associated with drilling in hard rock would increase the number of feasible EGS sites and greatly benefit its development as an energy source.

Thermal spallation drilling presents a possible solution to both drilling in hard rock and reducing drilling costs. Thermal spallation drilling consists of rapidly heating a confined area of a rock surface to induce compressive thermal stresses that cause the rock to fracture and eject small, disk-like chips referred to as "spalls." Flame-jet thermal spallation drilling systems were first used commercially to drill blast holes for mining taconite ore in 1947 (Calaman and Rolseth,

1961). These systems have been used to drill holes to depths of about 330 meters (1000 feet) (Browning, 1981) and have been found to have penetration rates 2-5 times faster than those of conventional rotary drilling systems (Dey and Kranz, 1985). In addition to higher penetration rates in hard rocks, since flame-jet thermal spallation drilling tools do not actually come into contact with the rock surface, they are not subject to the wear and failure mechanisms of conventional drill bits. This reduces the need to remove and reinsert the drill string in the hole, or "tripping," to replace worn parts, further reducing drilling costs.

For tests conducted to date, thermal spallation drilling has only been performed in air-filled holes in a low density (~1 kg/m^3), gaseous environment at near ambient pressures. This limits the depth to which an open, uncased hole can be drilled, due to a number of factors including borehole wall stability, lost circulation, and concerns about effective rock chip removal. In deep drilling applications, boreholes are filled with drilling muds – liquids with densities ranging from 1000 to 2000 kg/m^3 that provide a hydrostatic force to stabilize the borehole in the presence of in-situ stresses that increase with increasing lithostatic pressure. The drilling mud also entrains and removes drill cuttings from the hole, controls or eliminates pore fluid inflow from the borehole walls, and provides buoyancy for any drill string system, lessening its load carrying requirements. A deep borehole thermal spallation drill system would likely also require the use of a drilling mud to perform some of these functions. Therefore, the success of applying thermal spallation to drilling deep boreholes requires the ability to rapidly heat a rock surface at heat fluxes high enough to induce thermal spallation in a high pressure, aqueous environment at liquid densities.

Producing electricity from EGS has the potential to have large impact on the US and world energy picture, but it is not yet commercially viable. The motivation for this thesis was the application of thermal spallation to drilling deep boreholes as a means of potentially reducing the high cost of drilling wells and making EGS economically feasible over a wider range of geothermal resources grades. To assess the impact that using thermal spallation for drilling deep boreholes could have on EGS, it is first necessary to understand the various factors affecting the economic and technical feasibility of EGS. The application of thermal spallation to deep

boreholes would require thermal spallation to be performed in an environment radically different than that encountered during its conventional use in drilling shallow, open-air blast holes. An overview of EGS, its potential impact, and economic models used to estimate the cost of producing electricity from EGS is given below. This is followed by a review of past and current theories and experimental studies of thermal spallation, and a discussion of the challenges associated with extending thermal spallation drilling to use in deep boreholes.

1.2. Engineered Geothermal Systems

Conventional geothermal systems, referred to here as hydrothermal systems, require three natural phenomena to occur simultaneously to be developed commercially. First, a rock formation at high temperatures must be located near the earth's surface, usually within 1 to 4 km, so that it can be easily reached by drilling. Second, the rock formation must be naturally fractured and have sufficient permeability for fluid to circulate and flow to the drilled production well. Finally, the formation must contain naturally occurring fluids in sufficient quantities to economically produce electricity for a long period of time.

Engineered Geothermal Systems (EGS) are artificially created geothermal systems made to mimic naturally occurring hydrothermal resources by hydraulically stimulating a formation of high temperature rock to create a network of interconnected wells and then circulating fluid through the reservoir. For EGS resources, at least one of the criteria needed for a successful hydrothermal resource is lacking and must be created, or engineered, to transform the EGS resource into a functional geothermal reservoir. A conceptual, two-well Engineered Geothermal System is shown schematically in Figure 1.1. The steps in creating such an EGS reservoir are as follows. First, a well is drilled into a reservoir of hot rock. The reservoir will most likely be composed of a low permeability, hard crystalline basement rock, such as granite. If the reservoir does not have sufficient permeability to easily circulate fluid through the reservoir, as is normally the case for non-conventional geothermal resources, then it is hydraulically stimulated with high pressure fluid to open existing fractures. The reservoir is monitored for microseismic events so that the growth of the reservoir, along with its size, position, and orientation, can be monitored. Once the reservoir has grown to a sufficient size, a second well is drilled into the

reservoir that intersects the growing fractures so that connectivity between the wells is established. Fluid is then circulated between the wells through the reservoir for a period of time to determine the degree of connectivity between the wells. At this point, additional hydraulic stimulation or fracturing may be performed to decrease flow impedance between the wells. Once adequate flow rates have been established, fluid can be circulated through the reservoir, and the stored heat extracted from the rock by the produced fluid can in turn be used to run a power plant and produce electricity. The cooled fluid is then re-injected into the reservoir to complete a closed loop and extract more heat. In most designs, thermal energy contained in the produced fluid would be transferred to a secondary fluid in a binary organic Rankine cycle, although for fluid temperatures greater than 200 ^{o}C it may be desirable to use the fluid directly in a flash cycle as in many conventional hydrothermal power plants. The extracted thermal energy could also be used for direct heating, as in a district heating system.
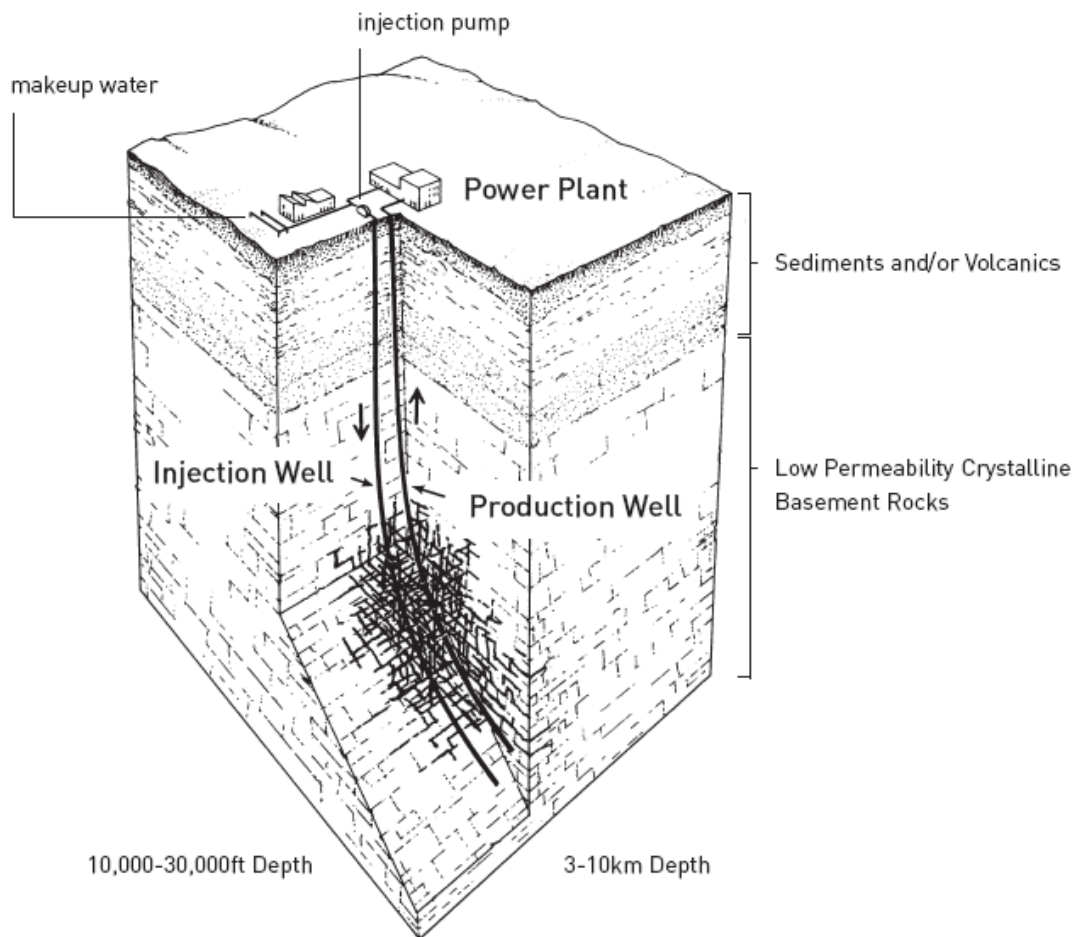
Figure 1.1 Schematic of conceptual two-well Engineered Geothermal System (EGS) (Tester et al., 2006).

The idea and initial vision of creating Engineered Geothermal Systems and using them to produce heat and electricity was conceived at the Los Alamos National Laboratory in the early 1970's. The program was called the Hot Dry Rock (HDR) project, and for quite some time all such projects were referred to as HDR projects. Only in the last decade was the phrase Engineered or Enhanced Geothermal Systems[1] adopted to more accurately describe the nature of the projects. Fenton Hill, New Mexico was chosen as the site of the first EGS demonstration project, due to its high temperature gradient, accessibility to public roads, and proximity to Los Alamos. The project consisted of 2 phases, starting in 1974 and continuing at varying levels of activity until 2000. In Phase I, a 3-km deep reservoir with a temperature of about 200 $^{\circ}$C was developed and studied until about 1980, when in Phase II, a deeper reservoir (4.4 km, ~300 $^{\circ}$C) was developed. During both phases, two wells, an injector and a producer, were drilled and hydraulically stimulated separately, with the hope that the reservoirs would grow in such a way that a hydraulic connection could be established between them. In both instances, the reservoirs did not grow as anticipated, and one of the wells had to be directionally re-drilled in an attempt to establish a connection. In both cases, a successful connection was eventually established and successful flow tests of differing lengths were performed. Despite these successes, funding for the Fenton Hill project diminished over time, and operations were continually scaled back until the point where all field experiments were terminated by 2000, and the site decommissioned.

Although the sizes of the reservoirs at Fenton Hill were never large enough to produce heat or electricity on a commercially viable scale, the project was a success in showing that EGS was technically feasible. The project demonstrated that wellbores could be drilled in hard rock, that low-permeability crystalline rock can be pressurized and stimulated to create hydraulically conductive fractures, that these fractures could form a connected network between injector and producer boreholes, and that fluids could be circulated through the engineered geothermal

---

[1] In this thesis, the phrase "Engineered Geothermal Systems" was adopted over "Enhanced Geothermal Systems," since the EGS resource must artificially altered or engineered to allow heat to be mined on a practical scale. "Enhanced" implies that heat could already be mined from a geothermal resource, and steps were taken to merely increase its productivity. Although this may be true for some marginal conventional hydrothermal systems, it will rarely be the case for EGS resources in low permeability conduction-dominated regions.

system and brought to the surface at elevated, commercial temperatures for extended periods of time.

The lessons learned at Fenton Hill served as a knowledge base and launching pad for other demonstration plants around the world. EGS demonstration projects at Rosemanowes, UK and at Hijiori and Ogachi, Japan were undertaken as part of an International Energy Agency collaboration agreement between the US, UK, France, Germany, and Japan. A project at Soultz, France supported by the European Union (EU) was also born out of that agreement, and work on demonstrating the technical feasibility of EGS continues at that site today. Recently, commercial enterprises have entered into developing EGS demonstration sites, with plans to continue with commercial scale development of EGS reservoirs for producing electricity. Notable among these is the Cooper Basin site being developed by Geodynamics, Ltd. in Australia, which was conducting long-term circulation tests at the time of this writing. In the U.S., the Department of Energy has begun a joint project with Ormat Technologies, Inc., and GeothermEx, Inc. to develop a commercial EGS site at Desert Peak near Reno, NV, and AltaRock Energy has announced plans to also undertake an EGS demonstration project and is currently assessing potential sites in the Western US.

Overall, EGS is still in the early stages of development and deployment. However, all the steps necessary to create EGS reservoirs have been proven to be technically feasible. Directionally controlled wells similar to those needed to develop commercial EGS resources have been drilled repeatedly for the oil and gas industry, for conventional hydrothermal projects, and in numerous EGS demonstration projects. The EGS projects have also demonstrated that pre-existing sealed fractures at depth can be stimulated to make connections between wells, circulate fluids, and extract thermal energy from the reservoir. The produced hot fluids could be used directly for heating or to produce electricity using existing binary Rankine cycle or flash plant technology. Collectively, all the technical and resource elements are in place to make EGS work (Tester et al., 2006). The question remains whether EGS reservoirs of sufficient size, connectivity, and production flow rates can be made to produce electricity competitive at existing market prices.

1.2.1. EGS Resource Base

Currently, conventional geothermal (hydrothermal) energy is a rapidly-growing industry both in the US and worldwide. While hydrothermal electric capacity in the US stands at only 2958 MW_e, there are almost 4000 MW_e of conventional geothermal projects currently under development (Geothermal Energy Association, 2008). Worldwide, hydrothermal electric capacity was close to 10,000 GW_e in 2007, with 200-250 MW_e of additional capacity being added annually since 2005 (Bertani, 2007). Despite this growth, conventional geothermal energy is limited in its ability to scale due to its dependence on the presence of a natural hydrothermal resource to exploit, and is confined primarily to regions in the western United States. EGS, on the other hand, has the potential to be a large scale, base load, renewable energy. Since EGS can theoretically be developed wherever there is accessible high temperature rock, the resource base is huge and spread across the entire United States. This is illustrated by Figure 1.2, which shows rock formation temperatures in the continental US at a depth of 6 km.
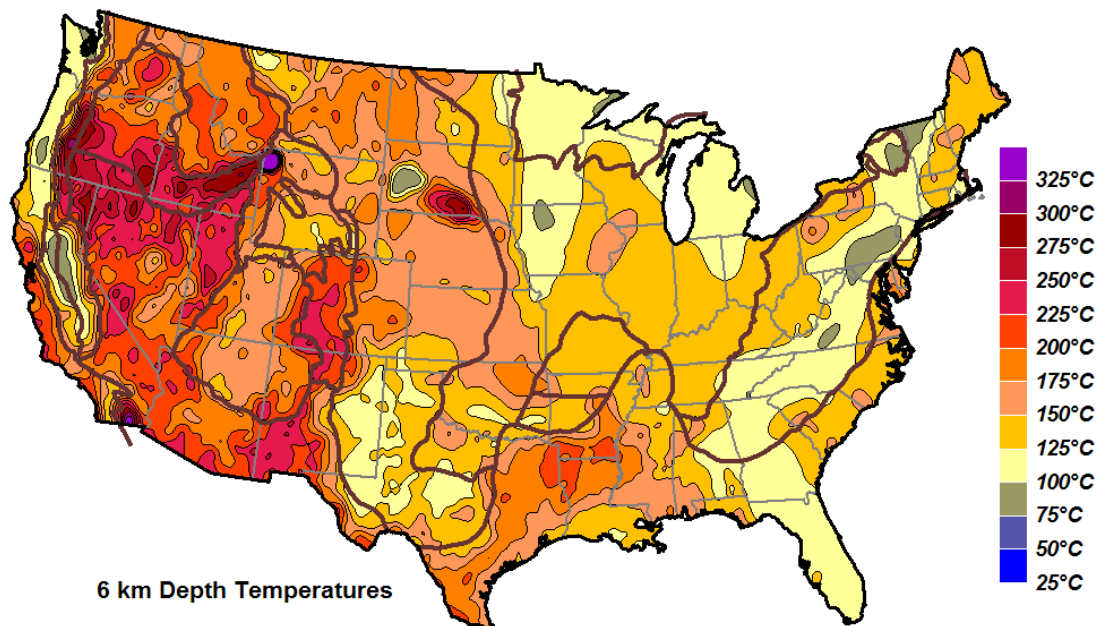
Figure 1.2 Rock formation temperatures in the continental US at a depth of 6 km (Blackwell and Richards, 2007).

As is often the case for mineral resources, the quantity of a particular grade of EGS resource varies inversely with its quality. Figure 1.3 shows the estimated resource base for the

sedimentary and basement sections of EGS resources, computed by subdividing the subsurface into 1-km thick horizontal slices and using depth vs. temperature data to calculate the amount of stored thermal energy in each interval for the entire US (Tester et al., 2006). The grade of resource varies by temperature and accessibility, with the greatest amount of energy available at low temperatures over a range of depths. As the temperature, and hence quality, of the resource increases, the average depth of the resource also increases, while the total heat content at that temperature decreases. This can be seen more easily in Figure 1.4, which compares the estimated EGS resource base to the estimated hydrothermal resource base. The EGS resource base has been divided into two grades, low-mid and mid-high, based on the temperature and depth of the resource (Thorsteinsson et al., 2008). Both low-mid and mid-high grade EGS resources are estimated to be many orders of magnitude greater than the conventional hydrothermal resource.
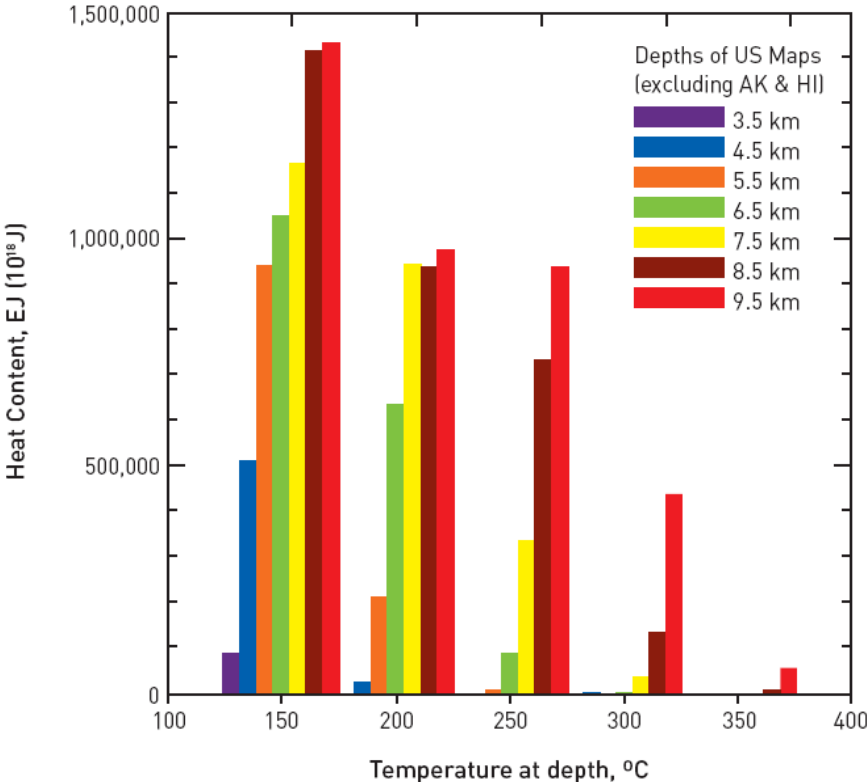
Figure 1.3 Histogram of total heat content as thermal energy contained in 1 km-thick slices over the entire US area (from Tester et al., 2006).
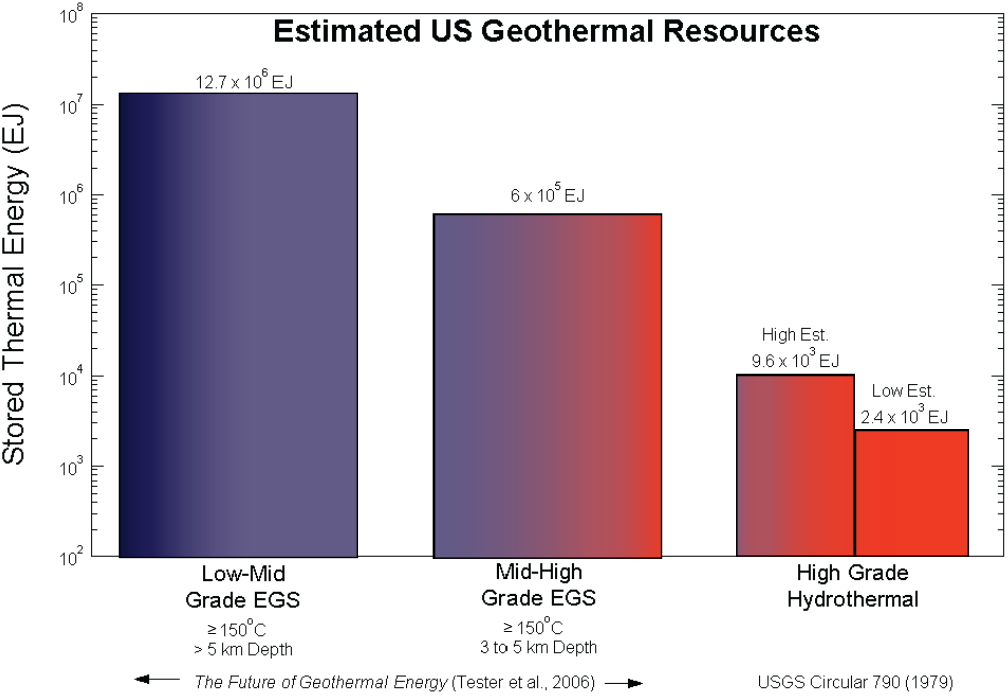
Figure 1.4 Stored thermal energy resource base for different types of geothermal resources. Data from (Tester et al., 2006) and (Muffler and Guffanti, 1979). Figure adapted from (Thorsteinsson et al., 2008).

Although the resource base for EGS is large, the ability to tap this resource depends on being able to develop EGS reservoirs for electricity generation at costs that are competitive with current and future electricity prices. The first EGS projects will likely be developed on the edges of conventional hydrothermal fields and will utilize many of the same technologies as conventional hydrothermal plants. Low- and mid-grade EGS resources, which are more evenly distributed nationally, make up the vast majority of the overall geothermal resource base. A means of developing EGS economically for these lower resource grades will eventually be needed to harness the full potential of the U.S. geothermal resource. For EGS to achieve significant scale nationally, there must be advancement in technologies such as drilling and reservoir stimulation, in addition to demonstration projects and consistent policy support.

1.2.2. Potential Impact of EGS on CO_2 Emissions

As part of a study on EGS technologies (Thorsteinsson et al., 2008), it was found that a significant displacement of fossil fuel use and subsequent CO_2 mitigation could be realized with large scale deployment of EGS technology. The amount of CO_2 reduction possible by EGS electric power generation was calculated using 2006 data from the Energy Information

Administration (EIA). According to EIA data, 2006 U.S. electricity generation was 4092 TW_h and U.S. electric generating capacity was 1.0 TW_e. In 2030, EIA projects that generation will have reached 5,800 TW_h and U.S. generation capacity will grow to 1.2 TW_e (Energy Information Administration, 2007a). For the study, EIA's electricity production prediction up to 2030 was assumed and, as a "worst case" scenario, extrapolated to 2100 using the same energy mix predicted for 2030 and growth rate predicted between 2029 and 2030. Under these conditions, U.S. generation and electric capacity in 2100 would be 10,200 TWh and 2.3 TWe, respectively. Further, it was assumed that EGS would only replace coal and natural gas for electric power generation and that the replacement of coal and natural gas was non-preferential. Also, for simplification, EGS power plants were specified as non-CO_2-emitting binary plants with a capacity factor of 95%.

Figure 1.5 shows the effects of displacing coal and gas fired plants with EGS electricity generation. The chart shows that CO_2 emissions would be 30% lower than current energy sector emissions if 100 GW_e of EGS capacity were online today. In 2030, 100 GW_e of EGS capacity online would decrease CO_2 emissions by 21%, and the same capacity of EGS in 2100 would reduce CO_2 emissions by 11%. 300 GW_e of EGS capacity today would lower CO_2 emissions by 77% and the same EGS capacity in 2030 and 2100 would lower CO_2 emissions by 35% and 13% respectively. The reason such a large reduction in emissions is achieved with only 300 GW_e of EGS capacity is due to the large capacity factor of EGS plants compared to coal and natural gas plants, which have an average capacity rating of 72.6% and 38.3% respectively (Energy Information Administration, 2007b). For comparison, *The Future of Geothermal Energy* report (Tester et al., 2006) estimates that EGS has the potential to supply the US with 100 GW_e of geothermal electrical generating capacity by 2050 at prices competitive with conventional electricity generating technologies
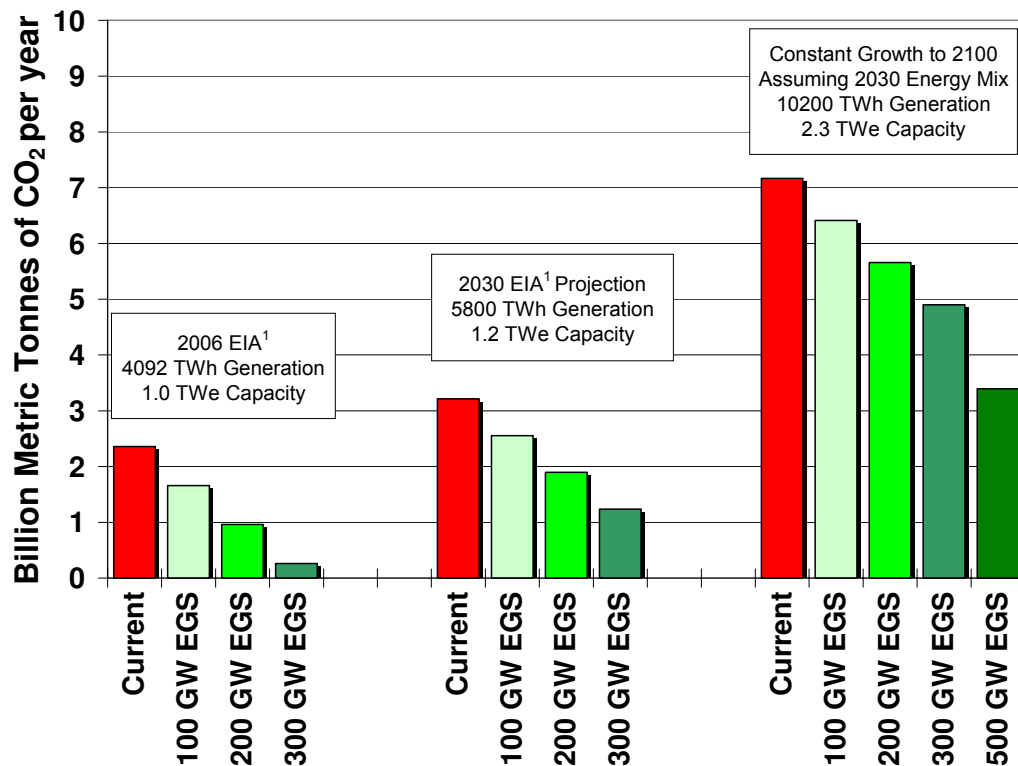
1. EIA Annual Energy Outlook 2007

Figure 1.5 Effect of EGS deployment on CO2 emissions from US electricity generation (from Thorsteinsson et al., 2008).

1.2.3. EGS Economic Models

Despite its large resource base and CO_2 mitigating potential, in order for EGS to be deployed on a large scale, the projects must be able to produce electricity at costs competitive with existing technologies. Without commercially mature EGS power plants in existence, economic models were created to explore their economic feasibility. The basic design of any economic model for an EGS project takes into account both cost and performance factors associated with EGS projects to estimate the capital and levelized cost of producing electricity. The levelized cost refers to the levelized busbar cost or levelized electricity cost (LEC) (see Armstead and Tester, 1987).

The cost factors consist of the capital costs to develop the EGS reservoir and build the electricity generating plant, operating and maintenance costs during the life of the project, and the financial

costs of borrowing money for the project. In keeping with the steps necessary to develop an EGS project, capital costs can be divided into three main expenditures (Tester et al., 2006):

1. Drilling costs for the wells,
2. Reservoir stimulation, re-drilling, and maintenance, and
3. Surface plant costs.

As in hydrothermal projects, the fuel costs for an EGS project are embedded in the capital costs for the subsurface system (wells and reservoir). Coal and natural gas electricity plants purchase their fuel as they operate, so their capital costs are smaller in comparison, but they have larger operating and maintenance costs. They are also vulnerable to fluctuations in fuel supply and prices. In EGS projects, capital costs dominate in determining the overall economic feasibility of the project while operating and maintenance costs are smaller and predictable. Financial factors, such as the equity rate of return and debt interest rate, reflect the level of assumed risk associated with an EGS project. Since EGS is an unproven technology, these rates will be proportionally higher than for conventional power plants, especially for early EGS projects, and will be an important factor in determining overall economic feasibility.

The performance factors reflect the economic quality of an EGS resource and control the level of cost factors, especially the capital costs (Armstead and Tester, 1987). The three main performance factors for an EGS reservoir are:

1. Temperature gradient/temperature as a function of depth,
2. Reservoir temperature, and
3. Reservoir productivity/production well flow rate.

The temperature gradient controls the depth of the wells. Reservoirs with a low temperature gradient will require deeper wells, which will increase drilling costs. The reservoir temperature controls the surface plant costs.   A higher reservoir temperature will produce fluid with a higher enthalpy, so that a smaller and less expensive plant is needed to produce a given amount of electricity. The reservoir productivity controls drilling and stimulating costs by determining the number of wells needed to produce a given amount of electricity. The reservoir productivity also controls the thermal drawdown of the reservoir, determining how quickly the reservoir will be cooled off and how often restimulation will be needed. There is a great deal of interaction

among these performance factors in determining the optimum strategy for developing an EGS resource. For example, the temperature gradient will affect the optimum reservoir temperature by pitting increasing drilling costs against decreasing surface plant costs. The reservoir productivity interacts with the reservoir temperature to determine the number of wells needed, which in turn affects the total drilling costs and either increases or decreases the effect of the temperature gradient on overall project costs. The models take these performance factors, their interactions, and their affect on cost factors into account when determining the optimum reservoir conditions for a given EGS resource.

Economic models that studied the feasibility of EGS projects first appeared in the 1970's, in conjunction with the original Hot Dry Rock demonstration project at Fenton Hills, New Mexico. Due to the lack of data and experience with EGS projects at the time, the models were not intended to give accurate projections of EGS electricity costs (Armstead and Tester, 1987), but could give order of magnitude estimates. More importantly, the models allowed researchers to determine the relative effects of EGS parameters on electricity costs and see how performance factors affected EGS feasibility.

One of the earliest EGS economic model studies was performed by Milora and Tester (1976). Although the approach they used was simplified, it was able to predict optimum reservoir depths as a function of fixed temperature gradient using assumed drilling and plant equipment costs based on depth and reservoir temperature, respectively. Later, more rigorous studies (Cummings and Morris, 1979; Tester and Herzog, 1990) confirmed that the predicted trends were qualitatively correct. These effects were generalized by Armstead and Tester (1987) and are shown graphically in Figure 1.6. The generating costs of EGS reservoirs with a high temperature gradient are controlled by surface plant costs, due to relatively low drilling costs to reach high reservoir temperatures. Conversely, reservoirs with low temperature gradients are dominated by drilling costs due to the deep wells needed to reach economically viable reservoir temperatures. Within this context, higher well productivity (assuming a constant thermal drawdown rate) results in lower levelized electricity costs due to the need for fewer wells. For a given reservoir at fixed temperature gradient and well productivity, the lower figure shows that an optimum well

depth does exist for each reservoir. The minimum occurs at the point where the increase in drilling costs due to deeper wells is no longer offset by the decrease in per unit plant costs (or increase in power plant production) due to higher reservoir temperatures. However, even for reservoirs with high temperature gradients, drilling costs were still found to be significant, accounting for almost half of the levelized electricity cost (Murphy et al., 1982).
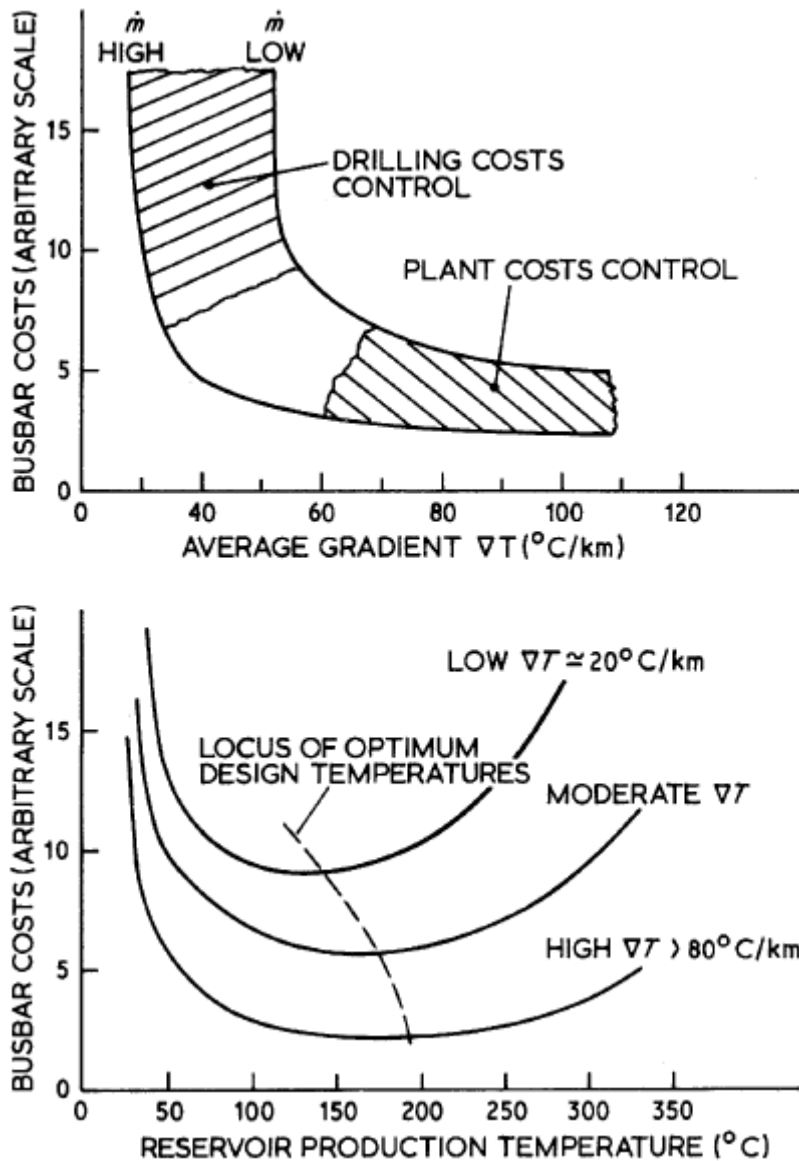
Figure 1.6 Generalized effects of reservoir performance factors on levelized electricity costs (busbar costs) for EGS projects (from Armstead and Tester, 1987).

More studies were done for a range of conditions as the number of EGS demonstration sites increased and data on drilling and stimulation costs and EGS technology became more refined.

A review of six of these studies was done by Tester and Herzog (1990), along with a reformulation of an economic model for EGS using revised cost components. The model from this study was developed further and eventually became "EGS Modeling for Windows," a Windows based software tool for economic analysis of EGS systems. The model was further modified for use in the "Future of Geothermal Energy" assessment and updated using the results of that study to come up with a set of base-case parameters for different stages of EGS technology ranging from today's technology to commercially mature. These parameters were then used to estimate levelized electricity costs for six potential EGS sites in the US. A sensitivity analysis of the model results to variations in the parameters was also performed (Tester et al., 2006). The model is now referred to as the MIT EGS model.

The results of the MIT EGS model for this assessment were compared to results from another advanced geothermal economic model called the Geothermal Electric Technology Evaluation Model (GETEM). GETEM is an Excel spreadsheet-based model developed by the US Department of Energy (DOE) (Entingh and Mines, 2006; Mines, 2008) to assist the DOE in identifying and prioritizing geothermal research areas by predicting the levelized cost of geothermal electric power and determining how specific technology improvements affect these costs. The model uses a matrix of about 80 user-defined input variables, dependent on whether a binary or flash-steam power plant is used in the model, to assign values to technical and economic parameters and estimate the costs of exploration, well field development, power plant construction, and operating and maintenance costs. The input variables are also used to predict the impact of a technology improvement by varying those parameters affected by the technology improvement. The GETEM model was not originally designed specifically to predict levelized electricity costs from EGS, but has been updated to do this by, among other changes, using the inputs for well stimulation to account for stimulation costs and accounting for the expected decrease in reservoir productivity with time. Such a version of GETEM was used to predict electricity costs from EGS in a recent US geothermal supply characterization (Petty and Porro, 2007). The adequacy of the well cost correlations is also questionable, since many EGS reservoirs will likely require deeper wells than anticipated by the GETEM model (Mines, 2008).

The HDRec (Hot Dry Rock economic) model (Heidinger et al., 2006) is another program used to perform cost-benefit analysis for geothermal projects. Like the MIT EGS model, it combines economic aspects with technical characteristics of the reservoir and surface plant to estimate levelized energy costs based on discounted cash flows, and has many of the same input parameters. However, the HDRec model incorporates sub-models to determine many of aspects of reservoir capital costs and performance. For example, the HDRec model uses a fracture-extension model to estimate hydraulic stimulation duration and power requirements to aid in estimating stimulation costs. Several different flow models are used to determine pressure losses in the casing, near the wellbore at the inlet and outlet of the reservoir, and within the EGS reservoir itself when determining parasitic pumping requirements. Also, a heat extraction model is used to determine the reservoir temperature characteristics during the life of the project. The MIT EGS model requires credible input parameters to specify stimulation costs and reservoir characteristics. While the HDRec model may enhance reservoir performance predictions by using technical reservoir models, it also requires site specific input parameters for them and a greater level of detail for the overall EGS project, and is probably best suited for estimating costs and performing sensitivity analysis for a specific potential EGS site. Along these lines, the HDRec was used to estimate the levelized electricity costs for a hypothetical EGS site in the Upper Rhine Valley of France and Germany and to optimize well production flow rates at a site similar to the EGS project at Soultz-sous-Forêts in France.

Another model currently in use for the prediction of levelized electricity costs from EGS was developed by Sanyal et al. (2007) of GeothermEx, Inc. independent of the MIT EGS and GETEM models. As in previous models, the GeothermEx model takes into account capital costs, operating and maintenance costs, and financial costs to estimate levelized electricity costs. Unlike previous models, which determine total plant generating capacity based on reservoir temperature, well productivity, and number of wells drilled – regardless of the total number of wells or level of production flow rate – the net power capacity is determined as a function of the total stimulated volume of the reservoir. The correlation assumes a linear relationship between produced power and stimulated reservoir volume, but sets a limit of 7 MW_e for a well pair based on current pump limitations. The cost and performance parameters are based on conditions at

the Desert Peak EGS project in Nevada, but can be changed to match any project. The net effect of these assumptions is to place an upper limit on the productivity of an EGS injector-producer well pair. The model assumes a 30-year life span for the reservoir with no indication of using re-drilling to recharge the reservoir, which differs from assumptions in the MIT EGS model. Also, a range of drilling, stimulation, and power plant costs is assumed rather than using correlations based on depth and reservoir temperature, and the uncertain variables were subjected to Monte Carlo sampling and used in a probabilistic assessment of the levelized electricity cost. Due to these assumptions, the GeothermEx model finds that the stimulated reservoir volume should be made as large as possible in contiguous units to decrease capital costs, but finds the minimum capital costs per EGS unit to still be higher than those for conventional geothermal projects. The model can also be used to perform a sensitivity analysis of electricity costs to model parameters. EGS costs in the year 2050 were also projected based on assumed technology improvements and financial costs.

The purpose of this section was to provide an overview of the distinguishing features of available economic models and not to give an in-depth description of each one or to compare their results. One common characteristic of all models was the inclusion of capital costs (including drilling, stimulation, and power plant costs), operating and maintenance costs, and financial costs in estimating EGS electricity costs. Not surprisingly, these models all indicate that capital costs dominate the overall cost of an EGS project, and that drilling costs make up a significant portion of these capital costs, often accounting for half of total capital costs or more. Moreover, sensitivity analyses of the effect of drilling costs on EGS projects also show that EGS electricity costs are heavily influenced by drilling costs. The models indicate that any technology that could significantly decrease well drilling costs would substantially lower electricity costs for EGS projects and expand the number and type of EGS resources that could be economically developed.

1.3. Thermal Spallation Drilling

Today, all deep wells are drilled using conventional rotary drilling methods. A conventional rotary drilling rig consists of a tall, steel derrick that supports a long string of pipe which turns a

drill bit in order to crush and grind its way through rock. This system works well in the soft, sedimentary rocks usually encountered when drilling oil and gas wells. In these softer rocks, penetration rates of 30 m/hr are typical. However, problems arise in harder, crystalline rocks such as granite and taconite, where instantaneous conventional drilling penetration rates slow to 1-7 m/hr (update and cite), with overall drilling speeds even lower due to the need for frequent bit replacement (Armstead and Tester, 1987).

Another major drawback of conventional rotary drilling is that the costs increase significantly and in a non-linear fashion with depth. Historic data shows that onshore, US oil and gas well costs increase exponentially with depth, and that US geothermal well costs follow the same trend, but at costs 2-3 times higher than oil and gas wells at similar depths. This exponential drilling cost dependence on well depth has been attributed to decreased rates of penetration with depth and increased time spent tripping to replace worn drill bits (Tester et al., 1994).

A possible solution to both drilling in hard rock and reducing drilling costs that increase exponentially with depth may be to use flame-jet induced thermal spallation drilling. Thermal spallation drilling is characterized by the rapid heating of the confined rock surface. This rapid heating induces compressive thermal stresses due to the tendency of the rock to expand as temperature is increased. The compressive stress causes pre-existing fractures in the rock surface to propagate, fracturing the surface into small, disk-like chips called spalls. These spalls are ejected violently from the rock surface due to the stresses built up in the surface before fracture. In conventional, open-hole flame-jet drilling, spalls are swept away from the advancing rock surface by the high velocity gas stream.

Penetration rates in crystalline, granitic rock using flame-jet thermal spallation have been seen to be 5-10 times faster than those of conventional rotary drilling (Tester et al., 1994). Tests done by the Los Alamos National Laboratory achieved rates of 6-7.5 m/hr in granite rock using the thermal spallation method, compared to rates of 1.2-3 m/hr in granite at the HDR Geothermal Site in Fenton Hill, New Mexico using conventional drilling (Dey and Kranz, 1985). Browning drilled a hole about 330 meters deep using flame-jet thermal spallation in well-characterized

surface-exposed granite formations in Conway, New Hampshire at an average drilling rate of 15.8 m/hr, with penetration rates exceeding 30 m/hr near the end of the operation (Browning, 1981). These tests show the potential for significant improvements in drilling in hard rock using flame-jet thermal spallation over conventional rotary drilling methods.

Additionally, since flame-jet thermal spallation drilling tools do not actually come into contact with the rock surface, they are not subject to the wear and failure mechanisms of conventional drill bits. This reduces the need to remove and reinsert the drill string in the hole, called "tripping," to replace worn drill bits. Since tripping time increases with well depth, eliminating this step from the drilling process should decrease costs overall and lessen the impact of depth on drilling costs. It was speculated without field-validated proof that a drilling system that results in higher penetration rates with significantly less wear on parts such as thermal spallation drilling could lead to a more linear dependence of cost with depth (Tester et al., 1994).

1.3.1. Commercial Applications of Thermal Spallation Drilling

Two major companies are known to have developed thermal spallation drilling systems for industrial use: the Linde Air Division of Union Carbide and Browning Engineering. In 1947, the Linde Company introduced a jet-piercing tool that used thermal spallation to drill blast holes for mining taconite ore. The tool used a mixture of fuel oil and pure oxygen to drill blast holes to a depth of up to 16 meters. Up to January, 1961, the jet-piercing tool was used in the production of 140 million tons of crude taconite ore. The tool was also used in the production of 25 million tons of granite, quartzite, syenite, and sandstone (Calaman and Rolseth, 1961). During its use, a significant amount of work was done to optimize the jet-piercing tool, and 40 systems from 3 different models of the tool were developed. Linde's spallation activity decreased in the 1970's and ended in 1983 due to increasing fuel and oxygen prices, improvements in conventional roller-cone and percussion bits, and a return by Union Carbide to their principal job of selling industrial gases (Pierce et al., 1996).

Browning Engineering made a hand-held spallation tool for cutting rock in the 1960's, and sold hundreds of the units. They also developed a truck mounted flame jet system in the 1970's for

drilling holes or creating chambers in hard rock. Their system used #2 fuel oil and compressed air, and could drill to depths of over 300 meters (Pierce et al., 1996).

1.3.2. Mechanics of Thermal Spallation

Thermal spallation can be broadly defined as the fragmentation of a brittle solid into small, disk-like flakes by rapidly heating a relatively small fraction of the solid. Thermal stresses caused by expansion of the solid with increasing temperatures lead to failure of the solid. Typical spalls are 0.1 to 2 mm thick and have diameters 10-20 times their thickness (Dey and Kranz, 1985). Not all types of rock spall, or at least do not spall readily. Rocks that have been shown to spall easily include granites, taconites, quartzites, and hard sandstones. Rocks that are generally thought to be "non-spallable" include "soft" rocks such as limestones, shales, basalts, and soft sandstones. These rocks are typically encountered in oil and gas drilling (Wilkinson and Tester, 1993). There is no single property of a rock that determines whether or not a rock is spallable.

Over the years, numerous qualitative and quantitative mechanisms have been proposed to describe thermal spallation. The first of these, proposed by (Norton, 1925), attributed thermal spallation to shearing between isotherms parallel to the surface. Norton determined this by studying spheres and bricks of clay that were heated and then quickly cooled. However, Norton failed to realize that in true spallation, shear between layers is not possible due to confinement of the rock, so shearing cannot be the mechanism that causes spallation. What he observed was the normal tensile failure of the solid core of his sample due to the stress exerted by the expanding outer heated layer.

Preston (1934) was the first to develop a correct qualitative description of spallation. He realized that confinement of the rock face was key, and developed two criteria for spallation for an unconfined sample: 1.) the heated area must be small compared to the sample size, so that no far-field displacements at the surface exist and the heated area is confined, and 2.) the heating rate of the surface must be fast enough to force the surface temperatures to attain a high value before an appreciable fraction of the sample volume is affected by heating; otherwise thermal expansion will cause stress relief in the direction of least resistance.

With the Preston criteria met, a qualitative mechanism for spallation, illustrated in Figure 1.7, was proposed. Heating of the confined surface leads to a buildup of compressive stresses. These compressive stresses act on a pre-existing flaw near the surface, causing it to propagate in the direction of the applied stress, parallel to the surface. The high ratio of the diameter to thickness of the resulting plate under stress leads to buckling and a rapid release of the elastic energy of the compressed spall, explaining why the spalls are often ejected violently from the surface.

HEATED FACE	HEATED FACE
a. HEAT PENETRATES TO DOTTED LINE	b. CRITICAL FLAW LOCATED AT THIS POINT
c. SURFACE LAYER ARCHES AND BUCKLES AS FLAW LENGTHENS	d. SPALL FORMATION COMPLETES AS SIDES SEPARATE
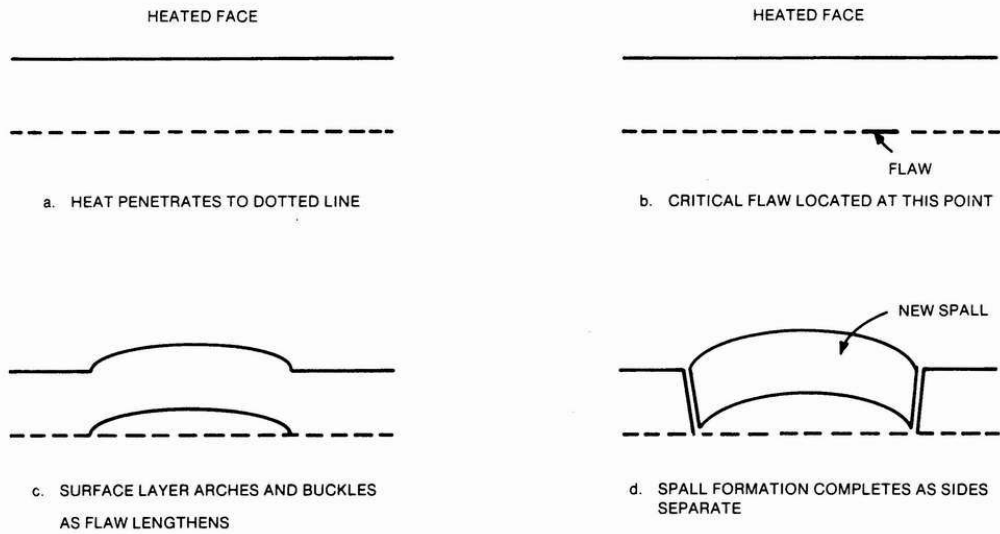
Figure 1.7 Qualitative mechanism of spall formation upon sudden heating of rock surface (Preston and White, 1934; figure adapted from Rauenzahn and Tester, 1989).

Using Preston's qualitative model as a jumping off point, Rauenzahn and Tester (1989) outlined the methodology shown below to arrive at a plausible thermal spallation theory. The theory states that if the heated rock is considered to be a semi-infinite solid with a 1-D temperature profile, then the compressive stresses (σ_{xx} and σ_{yy}) parallel to the surface are proportional to the temperature rise at that depth (Carslaw and Jaeger, 1959). This results in the following relationship:

$$\sigma_{xx} = \sigma_{yy} = \frac{\beta_r E \Delta T}{1 - \upsilon}$$

Eq. (1-1)

where: β_r = rock linear expansion coefficient
E = Young's modulus of the rock
ΔT = temperature rise from the point of zero stress in the rock
ν = Poisson's ratio

Determination of the rock stresses does not indicate at what point rock failure will occur; a suitable theory is still need to describe rock fracturing. Griffith (1920) was one of the first to recognize that the existence of pre-existing rock flaws was extremely important in formulating and evaluating failure criteria. He showed that a single crack aligned at an arbitrary angle to the stress field will extend due to tension at the tip of the crack and align itself with the existing stress field (Figure 1.8). Griffith went on to develop a simple global failure model, in which rock failure occurred at a single critical stress, σ_c.
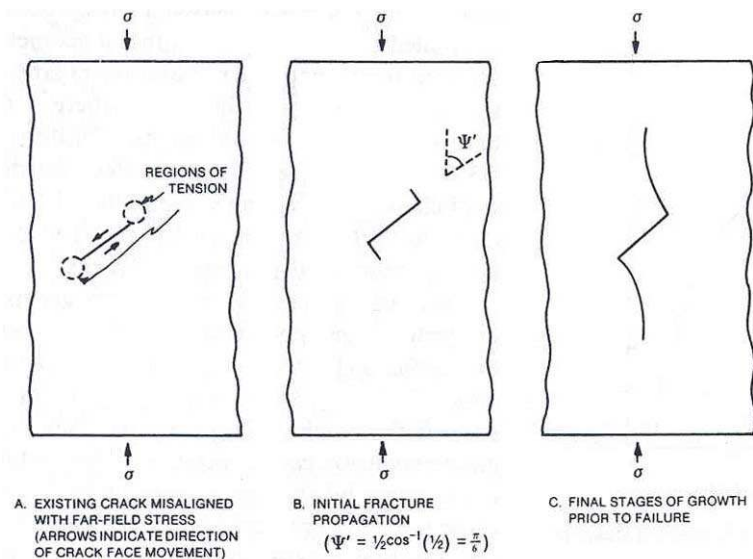
Figure 1.8 Non-planar crack extension induced by far-field applied compressive stress (from Rauenzahn and Tester, 1989).

Rauenzahn and Tester (1989) point out that this simple global failure model fails to take into account that a distribution of flaws exist in the rock, and that if a single or a few flaws are responsible for failure, then it is not reasonable to assign a unique value of the compressive strength to the rock for all loadings. They point out that experimental tests yield a distribution of failure strengths rather than a single value. This suggests that the use of Weibull statistical failure theory would be appropriate.

Weibull statistical theory attempts to account for the dependence of failure strength on sample size. Because of pre-existing flaws, a material can never achieve its true potential strength. The probability of failure depends on the distribution of flaws, the stress applied to the region, and the size of the region being stressed. A larger flaw can only handle a certain level of stress

before failure, but the chances of encountering such a flaw are less in a smaller region than in a larger region. Hence, Weibull's theory reduces to a distribution of material strengths dependent on the stressed volume (Rauenzahn and Tester, 1989). The Weibull distribution of size-dependent strengths is given by the following cumulative failure probability distribution (Weibull, 1939):

$$G(\sigma) = 1.0 - \exp\left[\int_0^V \left(\frac{\sigma}{\sigma_o}\right)^m dV\right]$$
Eq. (1-2)

where:
σ = compressive stress on the rock
σ_o = compressive strength of the rock
V = sample volume under stress
m = homogeneity factor

The parameters σ_o and m depend on the rock sample and must be determined experimentally.

Dey and Kranz (1985), in collaboration with Rauenzahn and Tester (Rauenzahn, 1986; Rauenzahn and Tester, 1989), extended the Weibull theory and the work of several other authors to develop a quantitative description of the temperature distribution and heat flux obtained in thermal spallation. They based their development on four key assumptions:

1.) Spalls are formed by compressive stresses via the same mechanism that causes uniaxial splitting in conventional compressive test samples.

2.) Heat diffuses into the rock only a short distance, so the thermal stress state is not influenced by hole shape.

3.) Conventional beam and plate buckling theory can be used to describe the conditions at which the spall separates from the rock.

4.) Weibull distributions describe heterogeneous variation of rock strength at small scales (~ 1 mm thickness) typical of spalls.

Evaluating the integral in Eq. (1-2) requires knowledge of the stress distribution and the volume over which the integral is performed. To determine the stress distribution from Eq. (1-1), the temperature profile in the rock face must be specified. The temperature field is determined by

treating the rock as a subliming solid, assuming that the rock surface disappears at the drilling velocity during the spallation process. The resulting heat balance is:

$$k_r \frac{\partial^2 T}{\partial x^2} = -u_r \frac{\partial T}{\partial x}(\rho C_p)_r \qquad \text{Eq. (1-3)}$$

where:
$$k_r = \text{rock thermal conductivity}$$
$$u_r = \text{drilling velocity}$$
$$(\rho C_p)_r = \text{rock volumetric heat capacity}$$

Assuming a surface temperature of T_s during spallation, the solution to Eq. (1-3) is:

$$T = (T_S - T_{r0})\exp\left(\frac{-u_r x}{\alpha_r}\right) + T_{r0} \qquad \text{Eq. (1-4)}$$

where:
$$T_{r0} = \text{temperature of rock at } x = \infty$$
$$\alpha_r = k_r/(\rho C_p)_r = \text{the rock thermal diffusivity}$$

Since the volume of the rock surface that will be removed takes the form of a cylinder, the region over which the integral must be performed can be thought of as a cone, with its apex at the rock surface and a radius of $C_L x/2$, where C_L is the aspect ratio (diameter/thickness) of the spall and x is the normal distance into the rock surface. Hence the differential volume is transformed into a differential depth, where:

$$dV = 3\pi \left(C_L \frac{x}{2}\right)^2 dx \qquad \text{Eq. (1-5)}$$

The stress distribution is given by Eq. (1-1), with $\Delta T = (T - T_{r0})$ described by Eq. (1-4). At median spalling conditions, G, the cumulative failure probability, is assumed to be 0.5. Eq. (1-2) then becomes:

$$0.693 = \left(\frac{\sigma_s}{\sigma_o}\right)^m \frac{\pi C_L^2}{4} \int_0^\infty x^2 \exp\left(-\frac{m u_r}{\alpha_r}\right) dx \qquad \text{Eq. (1-6)}$$

with σ_s given by Eq. (1-1), where $\Delta T = \Delta T_S$.

The heat flux to the rock surface, Q_r, can be determined from Eq. (1-4):

$$Q_r = -k_r \left(\frac{dT}{dx}\right)_{x=0} = (\rho C_p)_r u_r (T_S - T_{r0}) \qquad \text{Eq. (1-7)}$$

When combined with Eq. (1-6), this produces the following expression for the applied heat flux:

$$Q_r = \left(\rho C_p\right)_r \left(\frac{1-\upsilon}{\beta_r E}\right)\sigma_0 \left(\frac{2(0.693)}{\pi C_L^2}\right)^{1/m} \left(\frac{mu_r}{\alpha_r}\right)^{3/m} u_r \qquad \text{Eq. (1-8)}$$

Likewise,   Eq. (1-7) and   Eq. (1-8) can be combined to give the rock surface temperature during spallation:

$$T_S = T_{r0} + \left[\left(\frac{Q}{\rho C_p}\right)_r^3 \left(\frac{(1-\upsilon)\sigma_0}{\beta_r E}\right)^m \left(\frac{2(0.693)}{\pi C_L^2}\right)\left(\frac{m}{\alpha_r}\right)^3\right]^{1/m+3} \qquad \text{Eq. (1-9)}$$

The heat flux to the rock surface, drilling velocity, and spallation surface temperature can be determined from   Eq. (1-7) –   Eq. (1-9) once the rock properties are known and one of these three variables is specified. An aspect ratio (C_L) must be assumed to do the analysis. For most spalls, C_L has been observed to have a value of between 8 and 15. Buckling theory can also be used to determine a likely value of C_L, and results in a value of about 10. Using (Eq. 1-8), Rauenzahn and Tester (1989) estimated a spallation temperature range of between 400 to 550 $^\text{o}$C for average rock properties.

1.3.3. Experimental Studies

In addition to field studies by Browning (1981) and the Los Alamos National Laboratory (Dey and Kranz, 1985), a number of laboratory scale experiments have been performed to characterize thermal spallation. For example, an early study done by Thirumalai (1969) studied the relationship between temperature gradient in the rock surface and spallability. Thirumalai chose three rock types for his study: a continuously spallable quartzite, a non-continuously spallable charcoal granite, and a non-spallable Dresser basalt. He drilled holes in the backs of the rocks, inserted temperature probes, and measured the thickness of the heated layer and the maximum temperature of the rock before breakthrough of the flame. Thirumalai found that for easily spalled quartzite, the thickness of the heated layer was only about 1 mm, with temperature gradients of over 200 $^\text{o}$C/mm during spallation. Charcoal granite had difficulty spalling, and a buildup of partially melted rock on the surface had to be mechanically cleaned in order to continue spallation. Temperature gradients of approximately 100 $^\text{o}$C/mm were found. The basalt would not spall, but simply melted. Thirumalai's experiments confirm Dey and Kranz's assumptions that in spallable rocks, the heat diffuses into the rock surface only a short distance.

Experiments at MIT in our by Rauenzahn (1986), Rauenzahn and Tester (1989), Wilkinson (1989), and Wilkinson and Tester (1993) have focused on verifying the spallation theory developed by Dey and Kranz (1985) by measuring spallation surface temperatures and fitting Weibull parameters. Rauenzahn and Tester (1989) attempted to determine the rock surface temperatures during spallation using both a 500 W CO_2 laser and a propane welding torch as heating sources. The surface temperature was calculated indirectly using the solution of the transient heat flux equation by assuming a constant heat flux and measuring the time required for the first spall to form using high speed videotape (2000 frames/sec):

$$\Delta T_S = \frac{2Q_r}{k\sqrt{\alpha_r t / \pi}}$$
Eq. (1-10)

The heat flux from the laser was easily calculated since previous work had shown that almost all the infrared energy from the CO_2 source is absorbed by the rock. A separate calibration experiment was done on a copper block to determine heat flux delivered by the propane torch. The tests were performed on Westerly and Barre granite. Results of the propane torch tests are shown in Figure 1.9. Rauenzahn points out that if Weibull parameters of *m* in the range of 15-25 are used, then the Weibull theory does a good job of predicting the correct range of spallation temperatures. Results from the 500 W CO_2 laser tests were not considered reliable because it was determined that the lasers heated too small of a rock face area was heated by the incident laser for the 1-D temperature profile assumption used to develop the spallation theory to apply. The radius of the constant heat flux region was only 2 mm, while the depth of the heated region was on the order of 1 mm. Also, the small volumes that were heated may not have included enough flaws for the Weibull-based theory to apply.

Wilkinson and Tester (1993) performed similar experiments but with more success using larger diameter laser and flame heating sources. They point out that determining surface spallation temperatures from the transient heat flux solution using the time for the first spall to appear is flawed, since according to Weibull theory, the first rock piece to spall will come from the "weakest" flaw at the tail end of the flaw distribution curve. A better method would be to determine the time for random points on the surface to spall and average them for a more
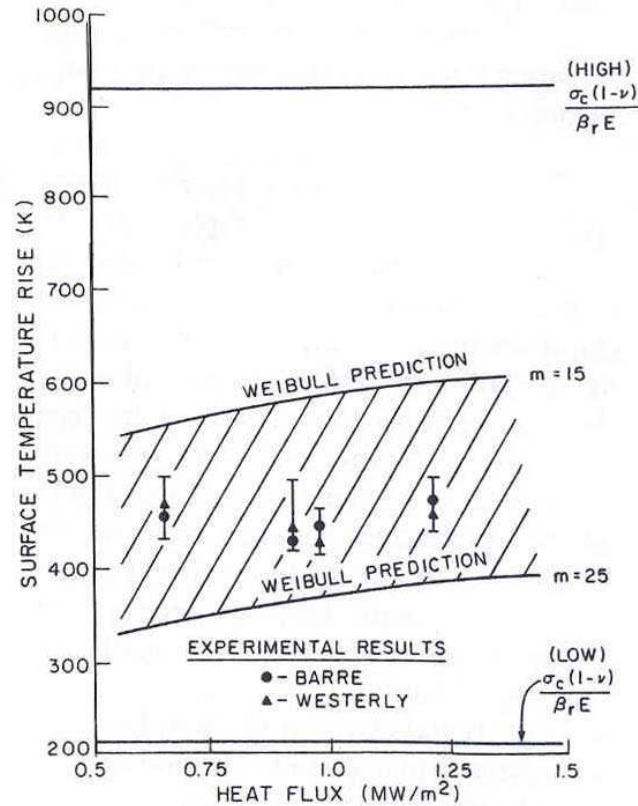
Figure 1.9 Experimental rock surface spallation temperature rise vs. applied heat flux, compared to predictions from Weibull theory using reasonable parameters (from Rauenzahn and Tester, 1989).

representative determination of the median spalling temperature. Wilkinson used an infrared scanner, calibrated for granite (with an emissivity of 0.90), to determine spallation temperatures in his experiments. Wilkinson (1989) performed his experiments using a 25 kW CO_2 laser and a modified propane-oxygen torch. Large beam diameters of 5 and 15.8 cm incipient on the rock surface were produced using the laser, assuring that the 1-D heating assumption used in the theory was satisfied. Heat fluxes for both the laser and torch experiments were calculated using the transient temperature analysis from   Eq. (1-10), with the temperatures measured using the IR scanner. Heat fluxes were also calculated for the propane torch tests using an empirical correlation from experiments done by Rauenzahn and Tester (1991) that related drilling rate to stand-off distance (the distance from the torch to the rock surface). The results from the experiments are shown in Figure 1.10 where spallation surface temperature is plotted as a function of heat flux, and also the values predicted from theory using Weibull parameters of $m = 20$ and $\sigma_0 = 70$ MPa-m$^{3/20}$, calculated from mechanical tests at ambient temperature and pressure

performed by Dey and Kranz (1985). Wilkinson was able to fit Weibull parameters of **m** = 8 and σ_o = 42 MPa-m$^{3/8}$ to the laser data. The predicted 90% probability envelopes contain most of the data. Wilkinson attributed some of the data scatter to uncertainties in time and temperature determination and the limited resolution of the IR scanner.
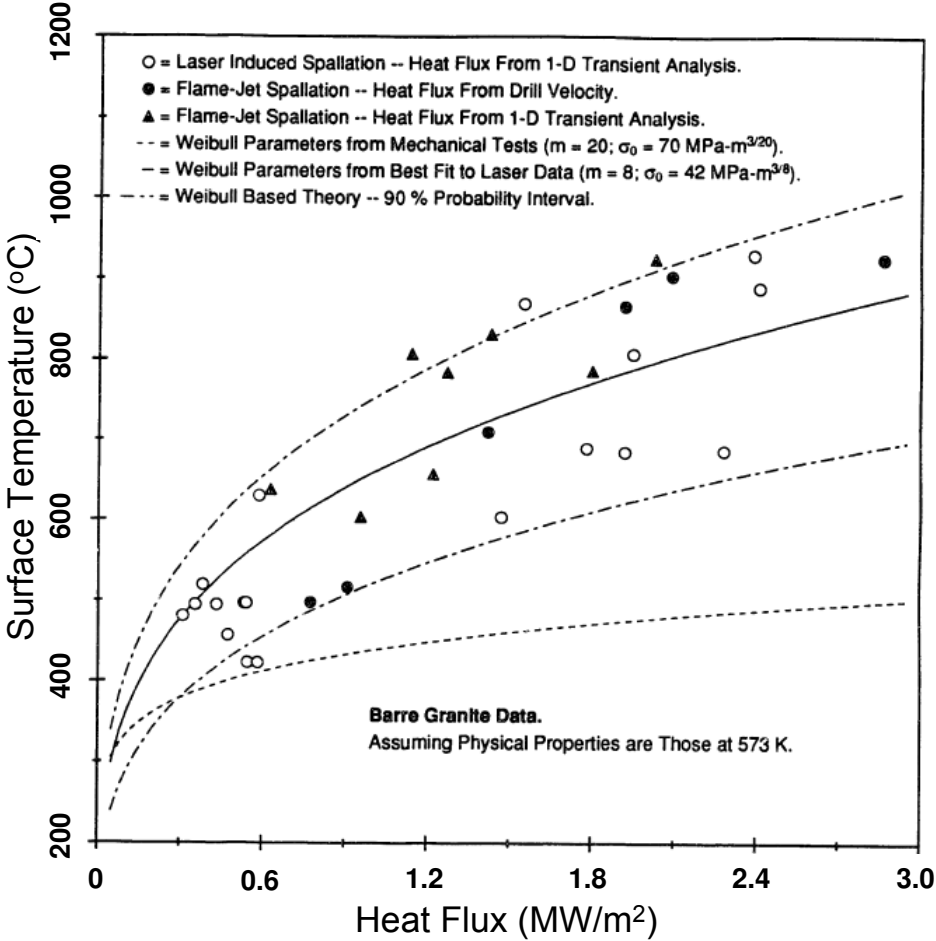
Figure 1.10 Surface temperature vs. heat flux for Barre granite from both laser and flame-jet induced thermal spallation (from Wilkinson, 1989)

Theory suggests that Weibull parameters should be functions of temperature. Stresses caused by grain-grain interactions with mismatched coefficients of thermal expansion result in an increase in the number of flaws in the rock as the temperature increases. Therefore, a rigorous analysis should include *m* and σ_o as functions of temperature, but obtaining such data is not feasible, so a temperature averaged value is usually used (Rauenzahn and Tester, 1989; Wilkinson and Tester, 1993). Therefore, it is not surprising that experimentally fitted Weibull parameters obtained

from laser heating at the onset of spallation by Wilkinson and Tester differed from those obtained by mechanical tests by Dey and Kranz at ambient temperature.

In addition to attempting to confirm spallation theories, experiments have been performed that attempted to spall traditionally "non-spallable" rocks. As early as 1965, Browning studied the effect of flame temperature and heat flux emanating from a flame jet on drilling efficiency. His experiments focused mainly on granites, but he also performed experiments on softer rocks as well. His results are hard to interpret because he chose as variables the volume of rock removed per volume oxygen combusted and the heat flux from the jet, rather than heat flux into the rock, and controlled these values by changing burner nozzles and the oxygen to fuel ratio, which in turn affected flame-jet temperatures and velocities. However, his results do show that for softer rocks, such as slate, the optimum flame temperature is considerably lower than it is for granite, but requires much higher jet velocities to maintain an adequate heat flux. If the surface temperature climbs too high, he observed that the surface would melt and spallation would cease (Browning et al., 1965). This suggests that spallation of softer, non-spallable rocks may be achieved by more closely controlling the surface temperature of the rock.

Williams, Potter, and Miska (1996) attempted to spall softer, sedimentary rocks by both using flames at lower temperatures and by alternately heating and cooling the rock surface. A small burner, or "Lance" that burned diesel fuel and air to create a flame-jet was used to spall rocks. Lower temperatures were achieved by injecting cooling water into the exhaust stream after the combustion zone. Using this method, the flame-jet temperature could be reduced from 2100 $^{\circ}$C to below 1800 $^{\circ}$C. Samples were also alternately heated and cooled by rotating them under a flame (placed 7 cm from the center of rotation) on a turntable. The optimal rotational speed was found to be 2 rpm. It was found that harder rocks like granite and rhyolite spalled best at the maximum flame temperature. Attempting to spall at lower temperatures did not produce any conclusive results in any of the rocks tested. Dense limestone rocks that would not spall under normal conditions were seen to spall using the heat and quench method. However, less compact limestone from the same quarry could not be spalled using this method. Many of the rock samples spalled on their surface briefly before spallation stopped altogether. The authors noted

that most of the rocks were weathered, and this may have affected their spallability. This claim is supported by the observations of Calaman and Rolseth (1961), who also noted that for taconite, drilling speed increased with depth as the rock became less weathered and oxidized.

1.3.4. Challenges in the Deep Borehole Environment

Extending the study and application of thermal spallation drilling to developing geothermal resources will require developing a drilling system capable of drilling deep boreholes (2-10 km deep). Despite the impressive results from field drilling tests using flame-jet thermal spallation, there are some limitations to its use. The most obvious of these limitations is that to date, thermal spallation has been limited to use in hard crystalline rocks such as granites, taconites, quartzites, and hard sandstones. However, many hydrothermal resources occur in these types of rock, and it is envisioned that many EGS locations will be developed in deep crystalline basement rocks, so except for initial drilling through a sedimentary overburden, thermal spallation drilling appears uniquely suited for geothermal applications. Moreover, novel spallation techniques may one day permit the use of thermal spallation in some sedimentary rocks. For example, Williams et al. (1996) reported by the successful drilling of travertine limestone by alternately heating and chilling the rock surface

Perhaps of greater concern is the application of thermal spallation drilling in deep boreholes (>3 km depth). To date, flame-jet drilling commercial operations and studies have been performed exclusively in shallow, open-air holes using low-density jets at ambient pressures. To develop EGS resources, wells varying in depth from 2-10 km will be required. At these depths, conventional rotary drilling must be done in a high-density, fluid filled hole in order to produce hydrostatic pressures needed to stabilize the walls of the hole and to prevent the influx of reservoir fluids. The simplest drilling fluid to consider is water, so early deep borehole thermal spallation experiments and demonstrations will be done in an aqueous environment. At the depths encountered in deep-well drilling, the hydrostatic head from a water-filled hole will result in extremely high pressures, approaching and exceeding the critical pressure of water (221 bar) at the bottom of the hole. This is illustrated in Figure 1.11 for the case of a water-filled borehole

that is in temperature equilibrium with its formation. Average temperature gradients of 0 to100 ^{o}C/km are assumed.
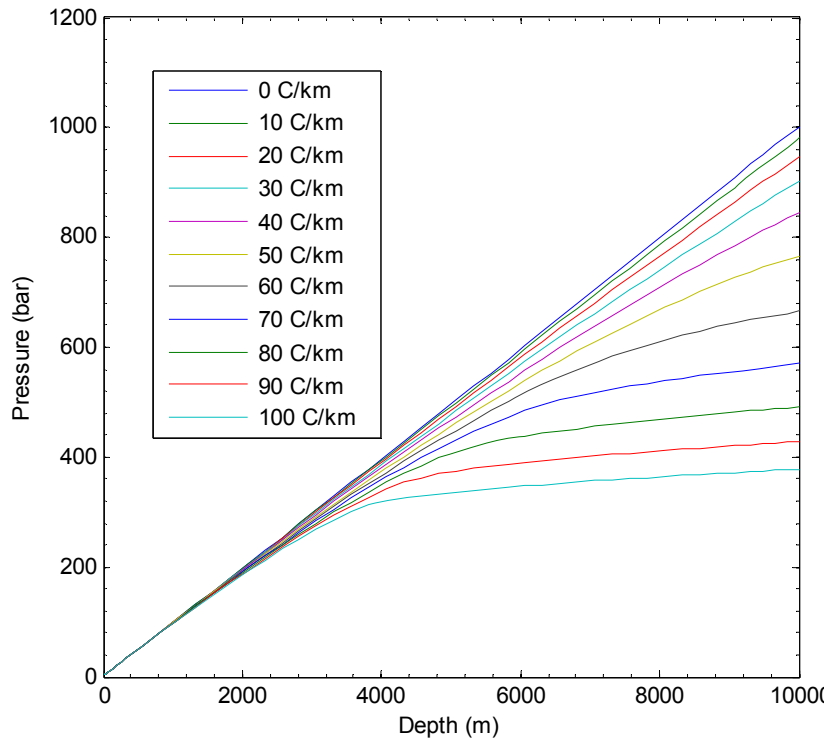
Figure 1.11 Hydrostatic pressure in borehole as a function of depth for different temperature gradients. Pressure calculations assume hole is water filled and in temperature equilibrium with the formation temperatuer profile.

One means of possibly achieving thermal spallation under these conditions is by using hydrothermal flames, which are flames produced in a supercritical water environment. The application of hydrothermal flame jets to thermal spallation drilling was first proposed by Potter and Tester (1998) in a patent which describes a continuous vertical borehole drilling system. Since the borehole will be water-filled, the flame jet will have to exist in an aqueous environment at pressures that increase as the hole is drilled to greater depths. As Figure 1.11 shows, at depths >~2 km, the bottom-hole pressure will likely exceed the critical pressure of water, and the flame will exist in a supercritical water (or supercritical fluid mixture) environment. Flames in supercritical water were first produced in the 1980's, and hydrothermal flame studies for the purpose of waste remediation have been performed by several researchers since then. A lengthy review of hydrothermal flame studies is presented in Chapter 6. The use of hydrothermal jets, which are jets consisting mainly of water at temperatures and pressures

above the critical point of water, were also considered in the patent. The hydrothermal jets would be created using electrical resistance heaters. In conventional, open-air jet-flame thermal spallation studies, supersonic flame-jets were created by forcing the combustion products through a converging-diverging nozzle. The high velocity resulted in higher heat fluxes from the flame-jet to the rock. The criteria for creating a supersonic jet includes a characteristic pressure ratio across the nozzle. Due to the high ambient pressures at the bottom of the hole under deep borehole conditions, it would be impractical and perhaps impossible to create a large enough pressure ratio across the nozzle to create a supersonic jet. Therefore, the hydrothermal jet used in the deep borehole environment will exit the nozzle at subsonic velocities.

A key question remains whether or not hydrothermal flame jets of sufficiently high temperatures and heat fluxes can be initiated and sustained in the high-density, high pressure environment encountered in deep boreholes to induce thermal spallation in rocks. This thesis represents the first experimental study of hydrothermal flames in a high density aqueous environment similar to deep borehole conditions performed by our research group at MIT, and the first attempt to apply hydrothermal flames to induce thermal spallation drilling at these conditions. This research was carried out in collaboration with Potter Drilling, LLC, who are attempting to develop the deep borehole thermal spallation drilling system for commercial purposes (Potter Drilling LLC, 2009; Augustine et al., 2007).

References

Armstead, H. C. H. and J. W. Tester (1987). <u>Heat Mining</u>. London, New York, E. & F. N. Spon.

Augustine, C., J. Potter, R. Potter and J. W. Tester (2007). "Feasibility of Spallation Drilling in a High Pressure, High Density, Aqueous Environment: Characterization of Heat Transfer from an H_2-O_2 Flame Jet." <u>Geothermal Resources Council Transactions</u> **31**: 241-245.

Bertani, R. (2007). "World Geothermal Generation in 2007." Proceedings European Geothermal Conference 2007, Unterhaching, Germany, May 30 - June 1.

Blackwell, D. D. and M. Richards (2007). "Rock Formation Temperatures at 6 km Depth". Personal Communication, Southern Methodist University Geothermal Laboratory.

Browning, J. A. (1981). Flame-Jet Drilling in Conway, N.H. Granite, University of California, Work Order Number 4-L10-2889R-1.

Browning, J. A., W. B. Horton and H. L. Hartman (1965). "Recent Advances in Flame Jet Working of Minerals." 7th Symposium on Rock Mechanics, Pennsylvania State University.

Calaman, J. J. and H. C. Rolseth (1961). "Technical Advances Expand Use of Jet-Piercing Process in Taconite Industry." International Symposium on Mining Research, University of Missouri, Feb. 22-25, U.S. Bureau of Mines.

Carslaw, H. S. and J. C. Jaeger (1959). <u>Conduction of Heat in Solids</u>. Oxford, Clarendon Press.

Cummings, R. G. and G. E. Morris (1979). "Economic Modeling of Electricity Production from Hot Dry Rock Geothermal Reservoirs: Methodology and Analyses." Electric Power Research Institute, Palo Alto, CA, EA-630.

Dey, T. N. and R. L. Kranz (1985). "Methods for Increasing Drilling Performance of the Thermal Spallation Drilling System." 1985 International Symposium on Geothermal Energy, Kailua Kona, Hawaii, The Council, 103-106.

Energy Information Administration (2007a). <u>Annual Energy Outlook 2007</u>. Energy Information Administration, U.S. Department of Energy, DOE/EIA-0383(2007).

Energy Information Administration (2007b). <u>Electric Power Annual 2006</u>. Energy Information Administration, U.S. Department of Energy, DOE/EIA-0248(2006).

Entingh, D. J. and G. L. Mines (2006). "A Framework for Evaluating Research to Improve U.S. Geothermal Power Systems." <u>Geothermal Resources Council Transactions</u> **30**: 741-746.

Geothermal Energy Association (2008). "U.S. Geothermal Power Production and Development Update: August 2008." Geothermal Energy Association, Washington, D.C., (August 7, 2008). published online at http://www.geo-energy.org/.

Griffith, A. A. (1920). "The Phenomena of Rupture and Flow in Solids." <u>Philosophical Transactions of the Royal Society of London</u> **221**: 163.

Heidinger, P., J. Domstadter and A. Fabritius (2006). "HDR Economic Modelling: HDRec Software." <u>Geothermics</u> **35**(5-6): 683-710.

Milora, S. L. and J. W. Tester (1976). <u>Geothermal Energy as a Source of Electric Power: Thermodynamic and Economic Design Criteria</u>. Cambridge, MA, MIT Press.

Mines, G. L. (2008). "Geothermal Electricity Technology Evaluation Model DOE Tool for Assessing Impact of Research on Cost of Power." Proceedings, Thirty-Third Workshop on Geothermal Reservoir Engineering, Stanford University, Stanford, CA, Janurary 28-30.

Muffler, L. J. and M. Guffanti, Eds. (1979). <u>Assessment of Geothermal Resources of the United States - 1978</u>. Washington, D.C., U.S. Dept. of Interior, Geological Survey, Circular 790.

Murphy, H., R. Drake, J. Tester and G. Zyvoloski (1982). "Economics of a 75-MW(e) Hot Dry Rock Geothermal Power Station Based upon the Design of the Phase II Reservoir at Fenton Hill." Los Alamos National Laboratory, Los Alamos, N.M., LA-9241-MS.

Norton, F. H. (1925). "A General Theory of Spalling." <u>Journal of the American Ceramic Society</u> **8**: 29-39.

Petty, S. and G. Porro (2007). "Updated U.S. Geothermal Supply Characterization." Proceedings, Thirty-Second Workshop on Geothermal Reservoir Engineering, Stanford University, Stanford, CA, January 22-24, 2007.

Pierce, K., J. T. Finger and B. Livesay (1996). "Advanced Drilling Systems Study." Sandia National Laboratories, (May). SAND95-0331.

Potter Drilling LLC. (2009). "Potter Drilling."   Retrieved March 12, 2009, from www.potterdrilling.com.

Potter, R. M. and J. W. Tester (1998). <u>Continuous Drilling of Vertical Boreholes by Thermal Processes: Including Rock Spallation and Fusion</u>. US Patent No. 5,771,984.

Preston, F. W. and H. E. White (1934). "Observations on Spalling." <u>Journal of the American Ceramic Society</u> **17**: 137-144.

Rauenzahn, R. M. (1986). <u>Analysis of Rock Mechanics and Gas Dynamics of Flame-Jet Thermal Spallation Drilling</u>. Doctoral Thesis, Massachusetts Institute of Technology.

Rauenzahn, R. M. and J. W. Tester (1989). "Rock Failure Mechanisms of Flame-Jet Thermal Spallation Drilling - Theory and Experimental Testing." <u>International Journal of Rock Mechanics and Mining Sciences & Geomechanics Abstracts</u> **26**(5): 381-399.

Rauenzahn, R. M. and J. W. Tester (1991). "Numerical-Simulation and Field Testing of Flame-Jet Thermal Spallation Drilling .1. Model Development." <u>International Journal of Heat and Mass Transfer</u> **34**(3): 795-808.

Sanyal, S. K., J. W. Morrow, J. S. Butler and A. Robertson-Tait (2007). "Cost of Electricity from Enhanced Geothermal Systems." Proceedings, Thirty-Third Workshop on Geothermal Reservoir Engineering, Stanford University, Stanford, CA, January 22-24.

Tester, J. W., B. J. Anderson, A. S. Batchelor, D. D. Blackwell, R. DiPippo, E. M. Drake, J. Garnish, B. Livesay, M. C. Moore, K. Nichols, S. Petty, M. N. Toksoz and R. W. Veatch (2006). "The Future of Geothermal Energy." MIT, Cambridge, MA, INL/EXT-06-11746.

Tester, J. W. and H. J. Herzog (1990). "Economic Predictions for Heat Mining: A Review and Analysis of Hot Dry Rock (HDR) Geothermal Energy Technology." Energy Laboratory, Massachusetts Institute of Technology, Cambridge, MA, MIT-EL 90-001.

Tester, J. W., H. J. Herzog, Z. Chen, R. M. Potter and M. G. Frank (1994). "Prospects for Universal Geothermal Energy from Heat Mining." <u>Science & Global Security</u> **5**: 99-121.

Thirumalai, K. (1969). "Process of Thermal Spalling Behavior in Rocks - an Exploratory Study." 11th Symposium of Rock Mechanics, University of California.

Thorsteinsson, H., C. Augustine, B. J. Anderson, M. C. Moore and J. W. Tester (2008). "The Impacts of Drilling and Reservoir Technology Advances on EGS Exploitation." Proceedings, Thirty-Third Workshop on Geothermal Reservoir Engineering, Stanford University, Stanford, CA, Janurary 28-30.

Weibull, W. (1939). "A Statistical Theory on the Strength of Materials." <u>Ingeniors Vetenskaps Akademien, Handlingar</u> **151**(3): 45-55.

Wilkinson, M. A. (1989). <u>Computational Modeling of the Gas-Phase Transport Phenomena and Experimental Investigation of Surface Temperatures During Flame-Jet Thermal Spallation Drilling</u>. Doctoral Thesis, Massachusetts Institute of Technology.

Wilkinson, M. A. and J. W. Tester (1993). "Experimental-Measurement of Surface Temperatures during Flame-Jet Induced Thermal Spallation." <u>Rock Mechanics and Rock Engineering</u> **26**(1): 29-62.

Williams, R. E., R. M. Potter and S. Miska (1996). "Experiments in Thermal Spallation of Various Rocks." <u>Journal of Energy Resources Technology - Transactions of the ASME</u> **118**(1): 2-8.

Chapter 2: Objectives and Approach

The factors controlling the overall costs and commercial feasibility of Engineered Geothermal Systems (EGS) interact in more complex ways than for other energy generating technologies. For example, a change in drilling costs can eventually change the type of surface plant used to produce electricity. To study one aspect or one technology in isolation risks failing to understand how it affects the system as a whole. The main focus of this research was to study thermal spallation as a means of drilling deep borehole for use in EGS systems. Just as important though was to understand how this new drilling technology would impact the importance and utilization of other EGS technologies such as reservoir stimulation techniques and surface plants. With this in mind, **the overall research objectives of this thesis were**:

1. **To assess the feasibility of technical and economic aspects of EGS through modeling and analysis.**

2. **To gain quantitative understanding of the behavior and use of combustion jet flames in high pressure, high density, hydrothermal media for rock drilling.**

The approach used to achieve these objectives was carried out in two parts.

Part I – Modeling and Analysis of Drilling & Advanced Energy Capture and Conversion for Engineered Geothermal Systems

The costs associated with drilling and completing wells are a major factor in determining the economic feasibility of producing energy from geothermal sources since they make up a significant portion of the initial capital costs. When modeling the economics of an EGS system, it is vital to be able to accurately predict drilling costs. Historic cost data is useful to this end, but before it can be used, it must be updated to current costs. Too little data on geothermal well costs exists for normalizing costs. Therefore, general trends in oil and gas well costs were analyzed and used to create an index for updating geothermal well costs. The methodology for creating the index and results from the study are presented in Chapter 3.

Using a lessons-learned approach based on conventional drilling technology, a study of the effect of technology advances on EGS electricity costs was carried out. Drilling costs for conventional

and advanced drilling technologies were estimated. The effects of advances in reservoir stimulation were also considered. The MIT EGS economic model was used to explore the effects of drilling costs, reservoir production flow rates, reservoir depth and temperature gradients to predict levelized electricity costs for EGS projects. These results are presented in Chapter 4.

In addition to an economic analysis of the impacts of advanced drilling and stimulation technologies, a technical analysis of surface power plants was carried out. Models of subcritical and supercritical binary Rankine cycle power plants were developed using Aspen Plus 2006 software. A range of working fluids were tested in simulations of power plants using geofluid temperatures ranging from 100-200 $^{\circ}$C to find the optimum working fluid and operating condition combinations to maximize net power generation. The results of the analysis are presented in Chapter 5.

Part 2 – Hydrothermal spallation in a deep borehole environment

Laboratory experiments and analyses were carried out to determine the feasibility of deep borehole thermal spallation drilling and to characterize the processes that control heat transfer to the rock surface under deep borehole conditions. Based on earlier work, it was believed that the necessary temperatures and heat fluxes needed to induce thermal spallation in rock in deep borehole environments, where pressures and fluid densities are high, could be achieved using hydrothermal flame technology. An in-depth review of previous research on hydrothermal flames was conducted and is presented in Chapter 6. The lessons learned from this review were applied to the design and construction of a hydrothermal flame reaction system, described in Chapter 7.

Preliminary experiments were carried using the hydrothermal flame reaction system to first demonstrate the ability to reliably produce hydrothermal flames, and then to characterize the capabilities and limitations of the reactor system. Hydrothermal flames were produced using both methanol and hydrogen as a fuel, and the properties of the hydrothermal flame were

studied. Several attempts were made to spall rock samples using hydrothermal flames. The results of these hydrothermal flame studies are presented in Chapter 8.

Results from the hydrothermal flame experiments showed that the flame jet was rapidly quenched after leaving the nozzle exit. Igniting flames using the WCHB reaction system also proved to be more difficult than anticipated. A means of studying high temperature jet behavior under deep borehole conditions was devised by reconfiguring the WCHB sytem to produce hot water jets rather than flame jets. This set up was used to study the behavior of supercritical temperature water jets injected into ambient temperature liquids. The results are presented in Chapter 9. A heat flux meter capable of measuring the rate of heat transfer from impinging high temperature water jets and flame jets in a high pressure aqueous environment was designed and constructed, and was used in the WCHB system to measure the heat flux from impinging supercritical water jets. The measured heat fluxes and derived heat transfer coefficients are described in Chapter 10. Toghether, the supercritical jet temperature and heat flux measurements combined to describe the temperature and heat transfer characteristics of high temperature jets in a high pressure, high density environment similar to conditions expected during deep borehole spallation drilling.

Chapter 3: Comparison of Geothermal Drilling Costs with Oil and Gas Drilling Costs

The costs associated with drilling and completing wells are a major factor in determining the economic feasibility of producing energy from geothermal resources. Drilling and completing injector and producer wells make up a significant portion of the initial capital costs for an EGS power plant. For example, a recent detailed techno-economical model of a hypothetical EGS site similar to the one in Soultz, France estimated that the cost of the boreholes alone would make up more than 50% of total plant capital costs (Heidinger et al., 2006). Since developing the reservoir essentially accounts for the "fuel" costs of operating a geothermal power plant, and these costs are incurred entirely before any electricity can be produced, the initial capital costs required to drill wells and develop the reservoir greatly affect the economic feasibility of the plant. This is especially true for EGS resources with low temperature gradients that require deeper, more expensive wells. An early study of electricity costs from EGS power plants placed drilling costs as accounting for 42% of the estimated levelized electricity cost for high-grade EGS resources with an average temperature gradient of 80 ^{o}C/km. For a low-grade EGS resource with a 20 ^{o}C/km average temperature gradient, that figure rose to 95% (Tester et al., 1994).

Because of the important role drilling costs play in determining the economic feasibility of developing EGS resources, it is vital to be able to accurately predict their costs when assessing a potential EGS project (Cummings and Morris, 1979). Unfortunately, due to the relatively small number of geothermal wells drilled each year, there are little data for developing geothermal well costs models. Moreover, the existing data are spread over more than three decades, so that a means of normalizing costs to a common basis is needed before they can be compared. However, a large amount of drilling data for oil and gas wells is available. Noting that the technologies for drilling oil and gas wells and geothermal wells are similar, a drilling cost index based on oil and gas well data from the *Joint Association Survey (JAS) on Drilling Costs* (American Petroleum Institute, 1976-2005) was developed by Tester and Herzog (1990) as a means of scaling geothermal well costs. The index was used to normalize both hydrothermal and

EGS well costs and compare them to the costs of oil and gas wells drilled to similar depths. This chapter updates and extends their earlier work. Oil and gas well costs were analyzed based on data from the 2005 JAS for onshore, completed US oil and gas wells. A new, more accurate drilling cost index, the MIT Depth Dependent (MITDD) index, was created using the JAS database (1976-2005) taking into consideration both the depth of a completed well and the year it was drilled. The MITDD index was used to normalize predicted and actual completed well costs for both EGS and hydrothermal systems from various sources to year 2005 US dollars, and then compare and contrast these costs with oil and gas well costs at similar depths.

The work presented in this chapter was done collaboratively with Susan Petty and Bill Livesay, along with Brian Anderson in our group at MIT, and was presented at the Thirty-First Workshop on Geothermal Reservoir Engineering at Stanford University (Augustine et al., 2006).

3.1. General Trends in Oil and Gas Well Completion Costs

Tabulated data of average costs for drilling oil and gas wells in the US from the *Joint Association Survey (JAS) on Drilling Costs* published by the American Petroleum Institute (1976-2005) illustrate how drilling costs increase non-linearly with depth. Completed well data in the JAS report are broken down by well type, well location, and the depth interval to which the well was drilled. The wells considered were limited to onshore oil and gas wells drilled in the United States. The JAS does not publish individual well costs due to the proprietary nature of the data. Instead, well cost data are presented in aggregate with average values used to show trends. Ideally, a correlation to determine how well costs vary with depth would use individual well cost data, but since these data were not available, mean values for each depth interval were used. Each depth interval was comprised of data from between hundreds to thousands of completed wells. Assuming the well costs are normally distributed, the resulting mean averages should reflect an accurate value of the typical well depth and cost for wells from a given interval to be used in the correlation. Using median well costs for each depth interval was considered, but these data were only available from the JAS beginning in 1996.

In plotting the JAS data, the average cost per well of oil and gas wells for a given year was calculated by dividing the total cost of all onshore oil and gas wells in the US by the total number of oil and gas wells drilled for each depth interval listed in the JAS report. These average costs are tabulated in Table 3.1. Onshore US oil and gas wells were considered because only onshore geothermal wells have been drilled to date. Wells in the 0 - 1249 ft (0 - 380 m) and 20,000+ ft (6100+ m) depth intervals were not included because wells under 1250 ft (380 m) are too shallow to be of importance in this study, and not enough wells over 20,000 ft (6100 m) are drilled in a year to give a representative average cost per well.

Table 3.1 Average costs of oil and gas onshore wells drilled in the US during the year 2005 from JAS data for listed depth intervals.

Drilling Interval (feet)	Average Depth (meters)	Average Depth (feet)	Average Cost (Year 2005 US M$)
1250-2499	553	1814	0.296
2500-3749	955	3132	0.368
3750-4999	1326	4349	0.439
5000-7499	1899	6231	0.801
7500-9999	2652	8701	1.726
10000-12499	3363	11035	3.020
12500-14999	4130	13550	5.979
15000-17499	4860	15945	7.965
17500-19999	5615	18421	15.155

A cursory analysis quickly shows that well costs are not a linear function of depth. A high order polynomial, such as:

$$\Phi_{well} = c_0 + c_1 z + c_2 z^2 + c_3 z^3 + ...$$

Eq. (3-1)

where:
$$\Phi_{well} = \text{completed well cost}$$
$$z = \text{well depth}$$
$$c_i = \text{fitted parameters}$$

could be used to accurately correlate well costs as a function of depth. However, it is not obvious what order polynomial would best fit the data. Reasonably accurate fits would require at

least three parameters, if not more. By noting that an exponential function can be expanded as an infinite series of polynomial terms:

$$e^x = 1 + x + \frac{x^2}{2!} + \frac{x^3}{3!} + \dots$$

Eq. (3-2)

one might be able to describe the well cost data as a function of depth using only a few parameters:

$$\Phi_{well} = a \cdot \exp(b_1 \cdot \text{depth}) = a \cdot \exp(b_1 z)$$

Eq. (3-3)

where a and b_1 are fitted parameters. If this were the case, a plot of $\log_{10}(\Phi_{well})$ vs. depth, or conversely plotting Eq. (3-3) on a semi-log graph, would result in a straight line:

$$\log_{10}(\Phi_{well}) = \log_{10}(a) + b_2 z$$

Eq. (3-4)

As Figure 3.1 shows, the average costs of completed oil and gas wells for the depth intervals from 1250 ft (380 m) to 19999 ft (6100 m) can be described adequately as an exponential function of depth.

The "Oil and Gas Average" trend line in Figure 3.1 shows that an exponential function adequately describes year 2005 JAS average completed well costs as a function of depth for the depth intervals considered while requiring only two parameters. The correlation coefficient (R^2) value for the year 2005 JAS data, when fit to Eq. (3-4), was 0.993. This indicates a high degree of correlation between the log of the completed well costs and depth. Similar plots for each year of JAS report data from the years 1976-2005 show high levels of correlation between the $\log_{10}$ of well costs and depth, with all years having an R^2 value of 0.968 or higher. Figure 3.2 shows how the regressed slope (b_2) and intercept ($\log_{10}(a)$) vary from year to year assuming an exponential model for well costs as a function of depth.

An insufficient number of ultra deep wells, with depths of >20,000 ft (6,100 m), were drilled in 2005 to give an accurate average. Instead, a number of ultra deep well costs from 1994-2002 were corrected to year 2005 US$ using the MITDD index values (see below) for the 17,500 – 19,999 foot depth interval and plotted in Figure 3.1. For depths >20,000 ft (6,100 m), some of the data points correspond to individual wells drilled in that depth interval, while others are an average of several (2 or 3) ultra-deep wells drilled during a given year. Extrapolation of the average JAS line in Figure 3.1 beyond 20,000 ft (6,100 m), indicated by the dashed line, is

generally above the scatter of costs for these individual ultra deep wells. The ultra deep well data demonstrate how much well costs can vary depending on factors other than well depth. Similar scatter in completed well costs exists for wells at all depth intervals s.
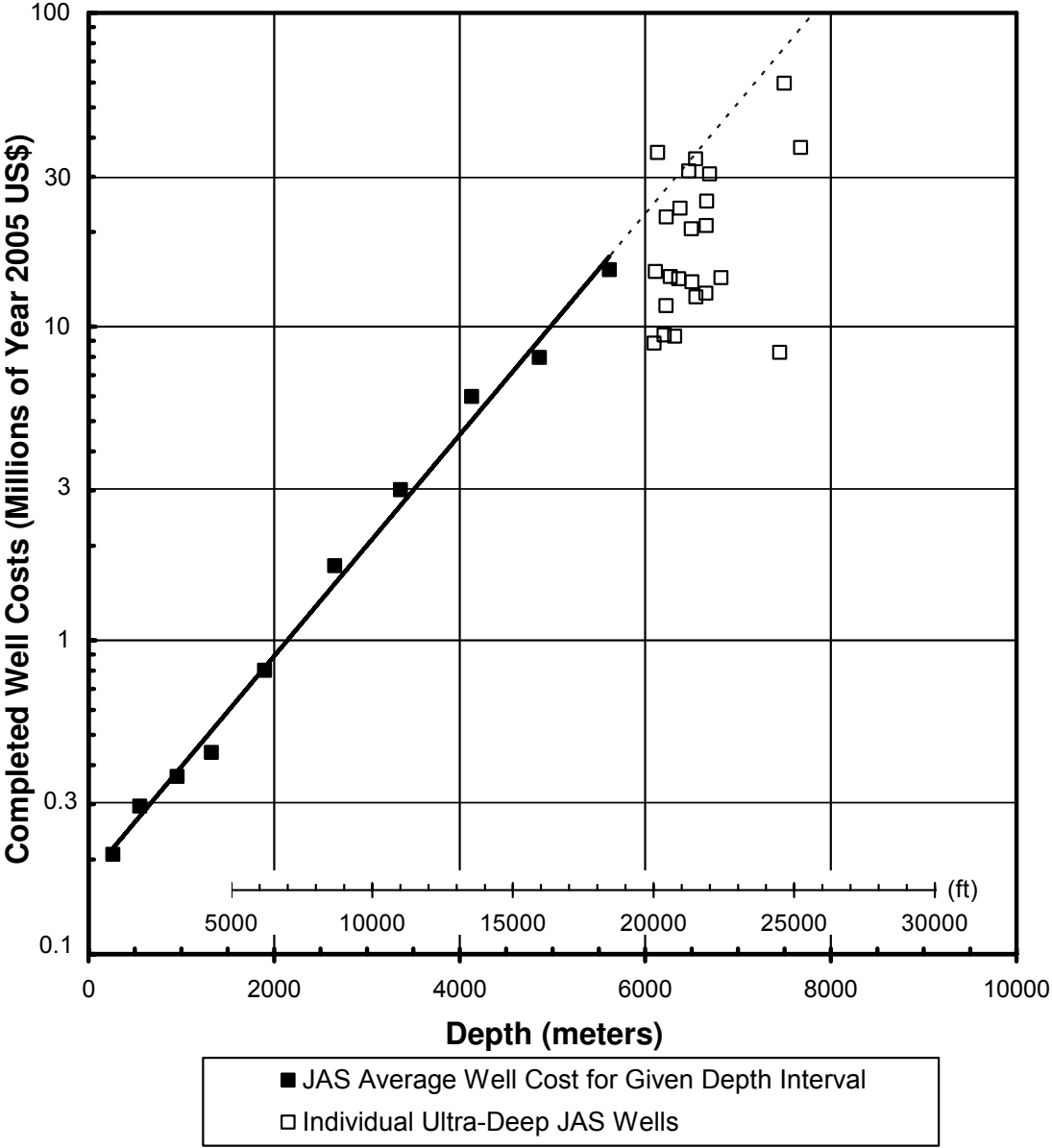
1. JAS = *Joint Association Survey on Drilling Costs* .
2. Ultra deep well data points for depth greater than 6 km are either individual wells
   or averages from a small number of wells listed in JAS (1994-2002).

Figure 3.1 Completed onshore oil and gas well costs in year 2005 US$ as a function of depth.
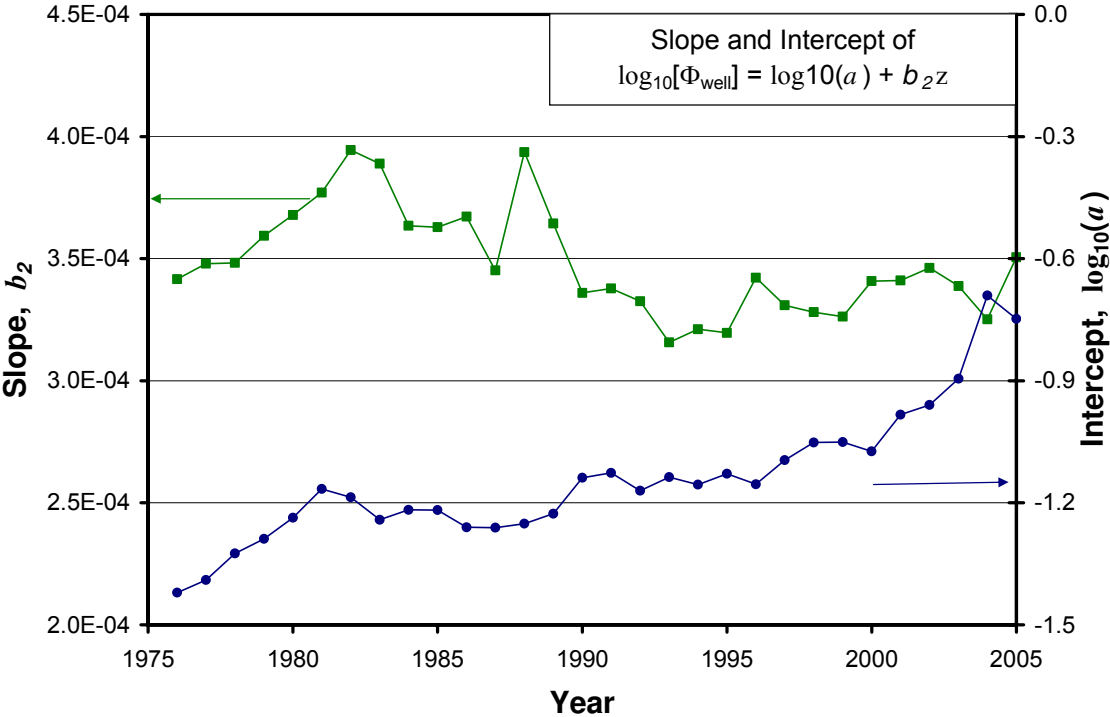
Figure 3.2 **Slope and intercept of exponential fit of JAS wells cost data vs. depth for years 1976 – 2005.**
The JAS completed well cost data show that an exponential fit adequately describes completed oil and gas well costs as a function of depth over the intervals considered using only two parameters. The correlation in Figure 3.1 provides a good basis for estimating drilling costs based on the depth of a completed well alone. However, as the scatter in the ultra-deep well cost data shows, there are many factors affecting well costs that must be taken into consideration to accurately estimate the cost of a particular well. The correlation in Figure 3.1 provides a good initial guess, but once more details about a particular well are known, a more accurate estimate can be made using other well cost modeling methods, e.g. Wellcost Lite (Mansure et al., 2005).

3.2. MIT Depth Dependent (MITDD) Drilling Cost Index

3.2.1. Formulation of Drilling Cost Index

In order to make comparisons between geothermal well costs and oil and gas well costs, a drilling cost index is needed to update the costs of drilling hydrothermal and EGS wells from their original completion dates to current values. Insufficient geothermal well cost data exist to create an index based on geothermal wells alone. In contrast, the oil and gas well drilling

industry drilled thousands of wells each year whose costs are reported by the JAS. Therefore, because of the similarity of the drilling process for oil, gas and geothermal wells, the JAS database provides means for correlation and extrapolation of limited geothermal well cost data. Therefore, data from the JAS (American Petroleum Institute, 1976-2005) were used to create a drilling index, and this index was used to normalize geothermal well costs to year 2005 US$.

There are many factors that affect the cost of a completed well, including the final depth of the well, the type of rock formation that is being drilled, hole diameter, the casing program, and the remoteness of the drilling site to name a few. Some of these factors are more important than others. For example, the hole depth largely determines the drilling and casing program that must be used to give a desired bottom hole diameter. The type (oil, gas, or geothermal) generally determines the type of rock formation, and to some extent, the lithology, that will be encountered. The well location dictates rig rental rates and material delivery costs, especially if the wells being compared are as onshore vs. offshore wells. A drilling cost index should take as many of these factors into account as possible, yet most do not. For example, the drilling index published yearly in the JAS, shown in Figure 3.3, was considered for updating geothermal well costs, but it was decided the index was inadequate for several reasons. First, it only extends back to 1984, whereas some of the geothermal wells date back to 1972. Second, the JAS published index is normally based on the current year's drilling activity and hence changes from year to year. It does not provide a consistent basis for comparison and is also influenced by the drilling trends (an unusually large number of shallow holes, for example) of the current year. Last, and most importantly, it fails to account for the effect of well depth on drilling costs. Instead, it uses the average cost per well for all onshore US wells. This approach biases the index towards the cost of the more numerous shallow holes. As will be shown, costs for drilling to different depth intervals have varied greatly over the last 30 years, and lumping without accounting for depth leads to significant estimation errors.
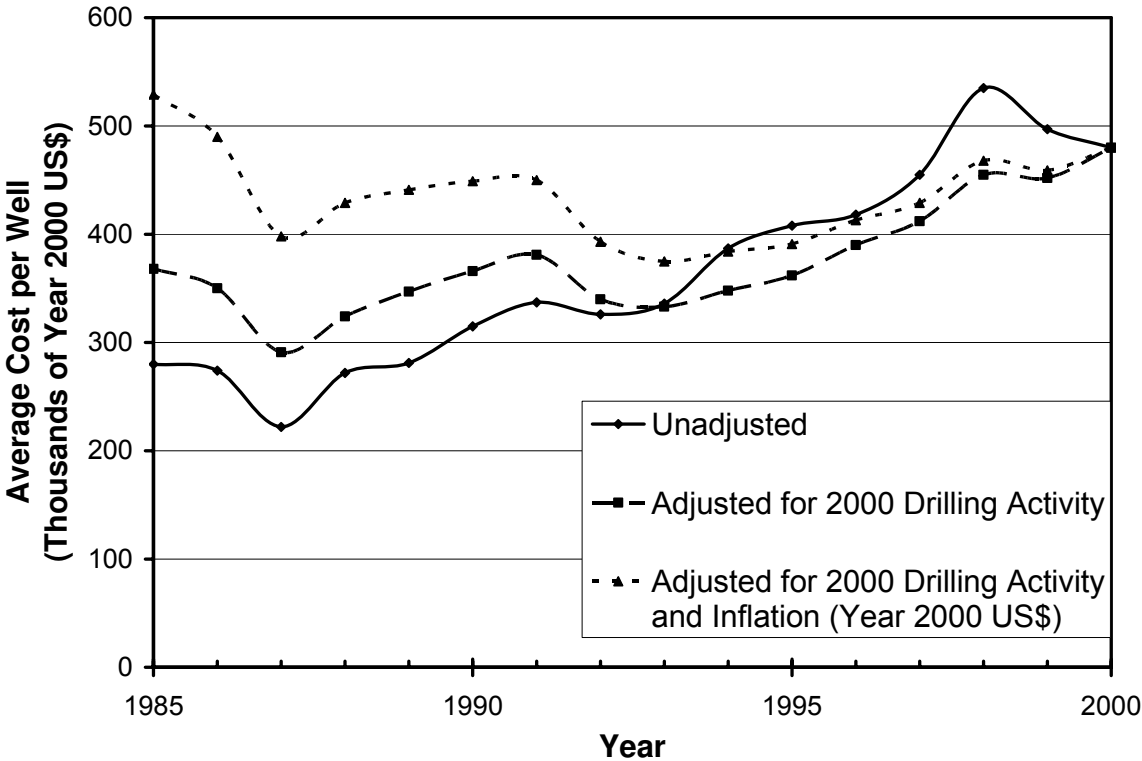
Figure 3.3 Drilling cost index from *2000 Joint Association Survey on Drilling Costs.* Average cost per well for onshore US wells vs. year drilled (adapted from American Petroleum Institute, 2000).

Figure 3.4 gives the MIT Composite Weighted Average drilling cost index previously developed by Tester and Herzog (1990) which accounts for well type by considering only completed onshore oil and gas wells in the United States. Like the JAS index, it used the average cost per foot of wells drilled each year as its index. This resulted in condensing all information from the various depth intervals into a single index number for each year, thus biasing the index towards the cost of shallower wells, since a larger number of these wells are normally drilled each year. This index is also prone to error in years where a disproportionate number of either deep or shallow wells are drilled. Because of these limitations, a modified method of creating a drilling cost index that accounted for well depth was explored.

An index based on calculating the average cost per foot at each depth interval and then giving equal weight to each of these intervals was considered. This index avoids the problem of overweighting from the more numerous shallow wells experienced by the MIT Composite index. However, since costs rise non-linearly with depth, the deeper wells would contribute more
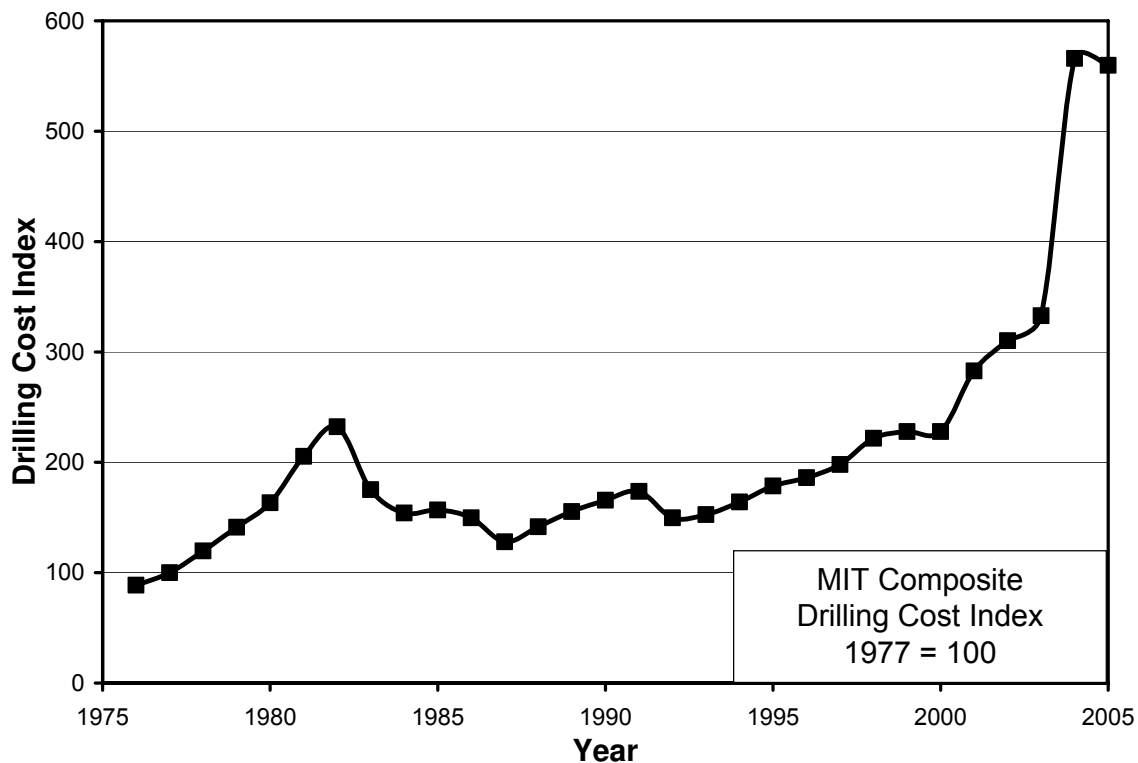
Figure 3.4 MIT composite drilling cost index (1977 = 100) made using average cost per foot drilled each year for onshore US oil and gas wells (adapted from Tester and Herzog, 1990 and updated).

heavily to the index, resulting in an index that favors changes in drilling costs in deep wells. A

drilling index that gives equal weight to each interval would be unfairly biased towards the costs

of deep wells. A method for correctly weighting the intervals is not immediately obvious. As

Figure 3.2 shows, any non-linear weighting correlation would have to change on a yearly basis.

It was concluded that any index based on weighted depth intervals risks either over- or

underestimating updated well costs depending on the method used.

To avoid these weighting limitations, an individual index was developed for each depth interval.

The average cost per well at each depth interval in the JAS reports (1976-2005) was used. A

17% inflation rate was assumed for pre-1976 index points. Only onshore, completed oil and gas

wells in the US were considered, since all hydrothermal and EGS wells to date have been drilled

onshore. A three-year moving average was used to smooth out short-term fluctuations in price.

Since most wells are drilled over a period of weeks to months, and the drilling industry is an

industry in which technological change occurs slowly, this smoothing should more accurately

reflect actual changes in drilling costs. Nonetheless, there will be situations where rapid changes in rig availability, driven by fuel supply shortages, for example, would cause well price fluctuations on a short time scale of months or less. The index was referenced to 1977, which is the first year for which a moving average could be calculated using data reported by JAS from the previous and following years. Although this method requires slightly more information and more work, it results in superior estimates of normalized drilling costs. This new index, dubbed the MIT Depth Dependent (MITDD) drilling cost index, is tabulated in Table 3.2

3.3. MITDD Index Results and Discussion

As Figure 3.5 shows, the MITDD Index clearly illustrates how widely the drilling indices vary among the different depth intervals. Before 1986, the drilling cost index rose more quickly for deeper wells than shallower wells. By 1982, the index for the deepest wells is almost double the index for shallow wells. After 1986, the index for shallow wells began to rise more quickly than the index for deeper wells. By 2005 the index for wells in the 1250-2499 ft (380-760 m) range is ~50% greater than all other intervals. Although it has the same general trend as the MITDD index, the MIT Composite index does not capture these subtleties. Instead, it incorrectly over- or under predicts well cost updates, depending on the year and depth interval. For example, using the previous method, the index would incorrectly over predict the cost of a deep well drilled in 1982 by about 55% when normalized to year 2005 US$. The MIT Composite index is heavily skewed upwards starting in 1995. The MITDD indices are up to 38% lower for wells over 2,499 ft (760 m) deep in 2005 than the previous index. The often drastic difference between index values of the MIT Composite index and the new MITDD index shown in Figure 3.5 from two given years demonstrates the superiority of the new MITDD index for more accurately updating well costs.

Although the drilling cost index correlates how drilling costs vary with depth and time, it does not provide any insights into the root causes for these variations. An effort was made to determine what factors influence the drilling cost index and to explain the sometimes erratic changes that occurred in the index. The spikes in the drilling index appearing in 1982 and again in 2005 are correlated with escalations in prices of crude oil and wellhead natural gas, as shown

Table 3.2 Values of MIT Depth Dependent (MITDD) drilling cost index made using average cost per well for each depth interval from Joint Association Survey on Drilling Costs (American Petroleum Institute, 1976-2005), with data smoothed using a three-year moving average. MIT Composite drilling cost index included for comparison.

Year	MIT Composite Drilling Cost Index	MITDD Drilling Cost Index								
		Depth Interval (Feet)								
		1250-2499	2500-3749	3750-4999	5000-7499	7500-9999	10000-12499	12500-14999	15000-17499	17500-19999
		Depth Interval (Meters)								
		381-761	762-1142	1143-1523	1524-2285	2286-3047	3048-3809	3810-4571	4572-5333	5334-6096
1972	47.3	49.4	50.3	49.8	50.0	48.5	47.5	49.1	49.5	48.9
1973	55.4	57.8	58.8	58.2	58.5	56.8	55.6	57.4	58.0	57.2
1974	64.8	67.6	68.8	68.1	68.4	66.4	65.0	67.2	67.8	67.0
1975	75.8	79.1	80.5	79.7	80.1	77.7	76.1	78.6	79.3	78.4
1976	88.7	92.5	94.2	93.3	93.7	91.0	89.0	92.0	92.8	91.7
1977	100.0	100.0	100.0	100.0	100.0	100.0	100.0	100.0	100.0	100.0
1978	119.7	114.3	109.1	110.2	112.9	117.4	117.0	116.9	117.1	119.9
1979	141.2	132.8	126.4	127.0	132.6	139.9	136.0	138.0	140.4	154.4
1980	163.3	152.1	149.3	152.4	161.3	169.7	162.3	171.7	180.6	214.8
1981	205.4	161.7	163.1	167.1	180.1	188.3	183.7	206.3	221.4	269.0
1982	232.2	165.5	165.6	169.0	181.6	190.5	185.5	216.5	236.4	279.1
1983	175.3	158.9	160.7	160.0	168.5	173.6	168.6	203.6	225.5	270.2
1984	154.1	155.1	155.3	150.4	154.9	153.7	144.8	165.1	193.6	216.6
1985	156.8	151.7	155.1	144.8	150.6	148.3	139.0	149.0	176.7	181.3
1986	149.7	150.8	149.1	136.3	140.5	142.3	133.1	138.8	171.4	162.6
1987	128.1	152.3	127.4	125.1	127.4	134.4	131.9	132.4	150.4	146.5
1988	141.5	162.4	129.3	127.8	124.5	136.5	133.5	129.2	146.2	153.4
1989	155.3	177.3	148.0	140.3	132.1	147.6	142.6	135.8	157.2	162.9
1990	165.6	183.7	190.0	152.2	138.6	153.7	145.3	139.3	164.9	174.3
1991	173.6	190.1	199.3	157.0	138.5	145.4	140.5	127.1	153.3	162.5
1992	149.6	198.3	196.6	154.0	133.9	134.9	134.9	118.2	136.3	161.5
1993	152.6	201.7	173.7	147.4	129.8	128.9	132.4	114.5	111.3	150.8
1994	164.1	202.7	169.4	149.9	135.4	131.4	134.7	123.7	110.3	142.7
1995	178.6	198.6	165.8	151.2	144.2	141.0	137.4	136.2	125.2	153.9
1996	186.1	210.0	178.2	160.5	159.3	151.8	133.7	143.7	142.7	167.1
1997	198.1	226.6	191.0	170.0	170.4	163.6	136.3	157.3	165.4	180.9
1998	221.7	238.8	202.7	179.2	177.9	169.8	142.8	161.3	170.8	182.3
1999	227.9	237.1	205.7	186.5	185.0	179.2	157.3	169.1	181.8	190.8
2000	227.9	231.5	200.0	186.0	185.7	182.5	165.6	167.8	189.4	189.9
2001	282.8	287.8	231.4	212.8	224.8	226.6	198.4	203.9	233.7	253.2
2002	310.3	364.6	265.0	228.3	220.3	248.4	229.0	222.4	247.8	307.9
2003	332.8	489.4	328.6	268.8	314.6	346.2	328.7	312.2	300.1	334.5
2004	566.0	564.9	377.9	312.1	359.1	403.4	366.8	395.8	345.0	419.9
2005	559.7	605.3	411.0	342.2	400.0	466.6	403.5	456.1	377.1	433.6

1. Depth interval indicates vertical well depth.
2. Index for years prior to 1976 made assuming 17% annual inflation factor.
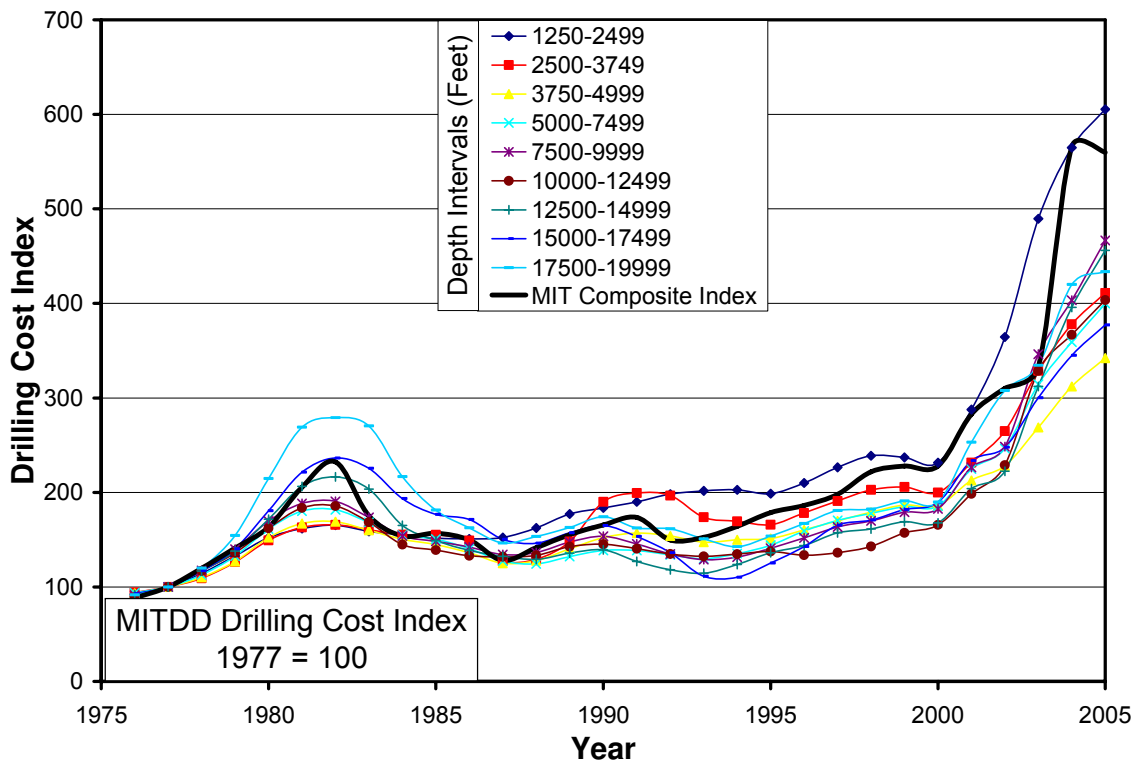
Figure 3.5 MITDD drilling cost index made using average cost per well for each depth interval from Joint Association Survey on Drilling Costs (1976-2005), with data smoothed using a three-year moving average (1977 = 100 for all depth intervals, 1 ft = 0.328 m).

in Figure 3.6, where only the MIT Composite drilling index was shown for simplicity. This correlation is likely due to the effect of crude oil prices on the demand for rotary drilling rigs. The average number of rotary drilling rigs in operation in the US and worldwide each year is shown in Figure 3.7. The drilling cost index maximum in 1982 was in response to the drastic increase in the price of crude oil, which resulted in increased oil and gas exploration and drilling activity and a decrease in drilling rig availability. By simple supply and demand arguments, this led to an increase in the costs of rig rental and drilling equipment, and a subsequent boom in the construction and number of operating rotary drilling rigs. The increase in drilling costs in recent years, especially for shallow wells, is also due to decreases in rig availability. This effect is not apparent in Figure 3.7, however, because very few new drilling rigs have been built since the mid 1980's. Instead, rig availability is dependent in part on the ability to salvage parts from older rigs to keep working rigs operational. As the supply of salvageable parts has decreased with time, drilling rig rental rates have increased. Since most new rigs are constructed for intermediate or deep wells, shallow well costs have increased the most. This line of reasoning is
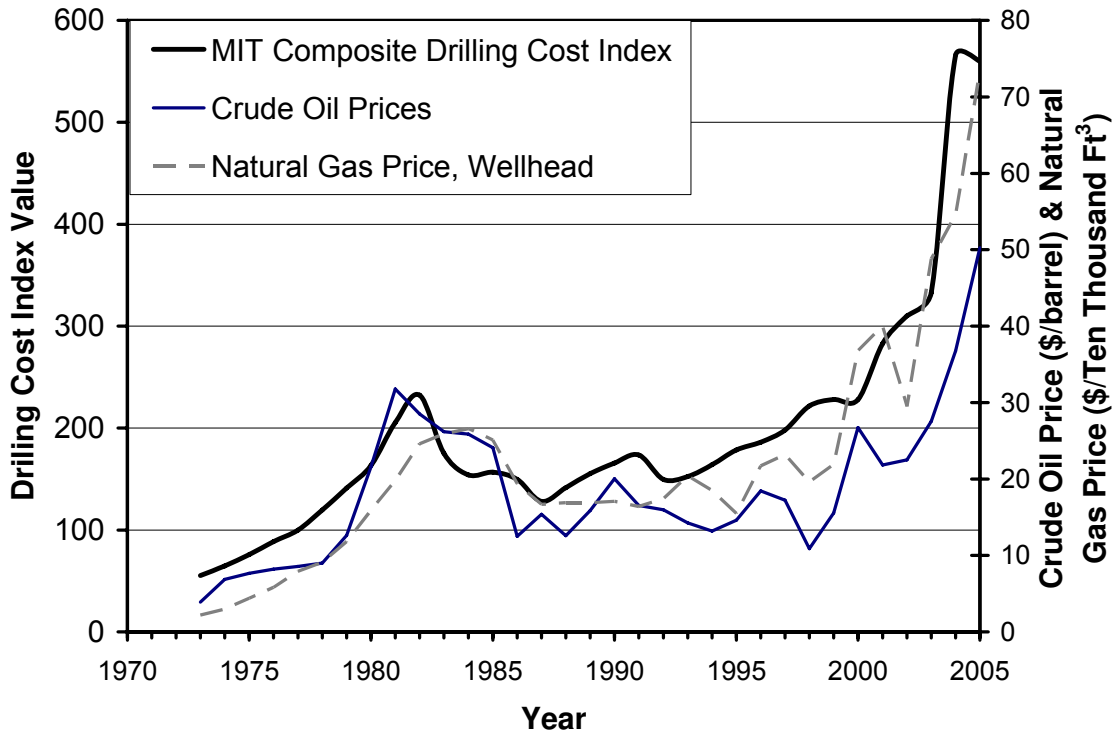
Figure 3.6 Crude oil and natural gas prices, unadjusted for inflation (Energy Information Administration, 2008) compared to MIT Composite Drilling Index (see also Figure 3.4).
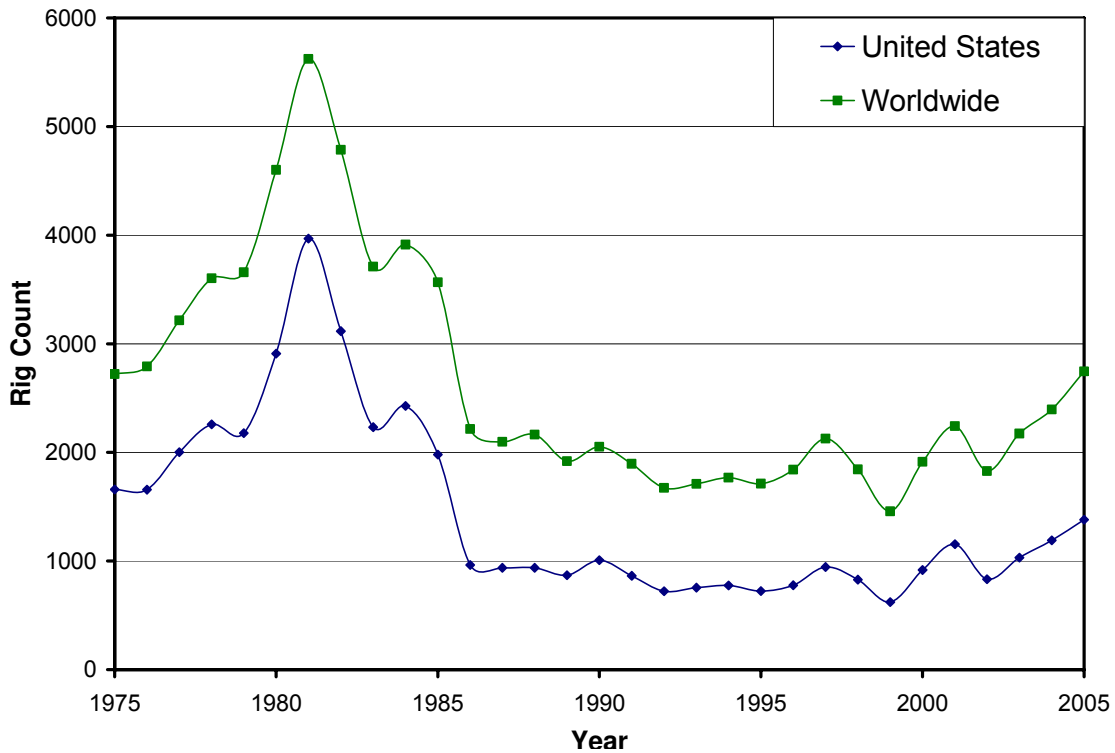
Figure 3.7 Average operating rotary drilling rig count by year, 1975-2005 (Baker Hughes, 2008).

supported by Bloomfield and Laney (2005), who used similar arguments to relate rig availability to drilling costs. Rig availability, along with the non-linearity of well costs with depth, can account for most of the differences between the previous MIT index and the new depth dependent indices.

The effect of inflation on drilling costs was also considered. Figure 3.8 shows the gross domestic product (GDP) deflator index (U. S. Office of Management and Budget, 2008), which is often used to adjust costs from year to year due to inflation, compared to the MITDD drilling cost index. Figure 3.8 shows that inflation has been steadily increasing, eroding the purchasing power of the dollar. For the majority of depth intervals, the drilling cost index has only recently increased above their highs in 1982, despite the significant decrease in average purchasing power. Since the MITDD index does not account for inflation, this means the actual cost of drilling in terms of present US$ had actually decreased in the past two decades until recently. This point is illustrated in Figure 3.9, which shows the drilling index adjusted for inflation, so that all drilling costs are in year 2005 US$. For most depth intervals shown in Figure 3.9, the actual cost of drilling in year 2005 US$ had dropped significantly since 1981 before the recent increases in crude oil prices. Only shallower wells (1,250-2,499 ft) do not follow this trend, possibly due to the rig availability issues discussed above. This argument is further supported by the drilling cost index for onshore wells from the 2000 JAS report, shown in Figure 3.3. The JAS index shows unadjusted drilling costs, costs adjusted so that all years reflect year 2000 drilling activity, and costs adjusted for both year 2000 drilling activity and inflation. The adjustment for inflation further verifies that when inflation is taken into account, the cost of drilling wells had decreased in current US$. This decrease is likely due to both technological advances in drilling, such as better drill bits, more robust bearings, and expandable tubulars, as well as overall increased experience in drilling wells.
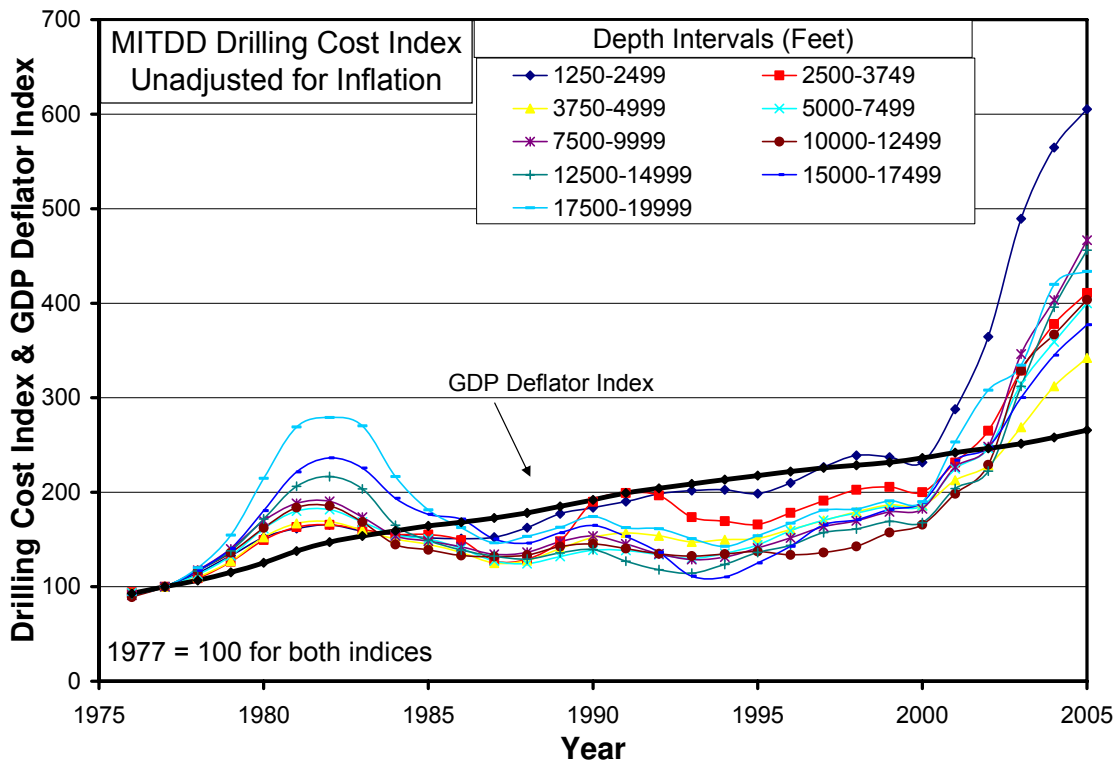
Figure 3.8 MITDD drilling cost index compared to GDP deflator index for 1977-2005 (U. S. Office of Management and Budget, 2008).
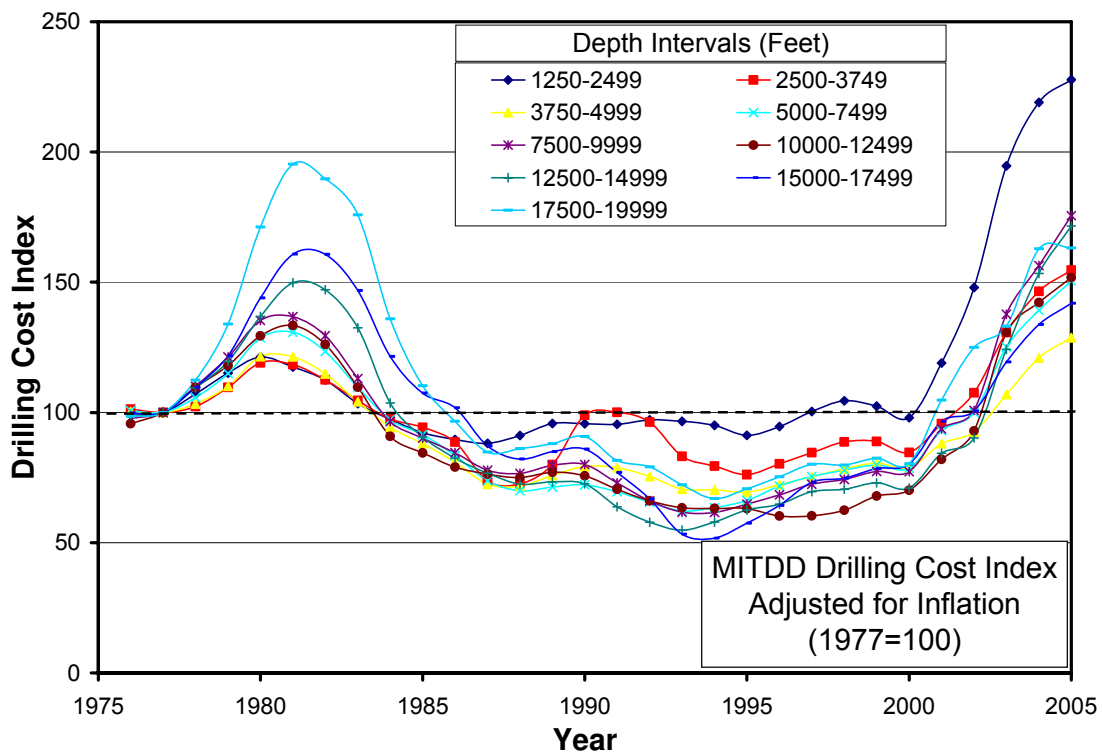
Figure 3.9 MITDD drilling cost index made using new method, adjusted for inflation to year 2005 US$. Adjustment for inflation made using GDP Deflator index (1977 = 100).

3.4. Updated Geothermal Well Costs

Table 3.3 lists and updates the costs of geothermal wells originally listed by Tester and Herzog (1990) as well as geothermal wells completed more recently. The MITDD drilling cost index was used to update completed well costs to year 2005 US$ for actual and predicted EGS/HDR and hydrothermal wells. Actual and predicted costs for completed EGS and hydrothermal wells were plotted and compared to completed JAS oil and gas wells for the year 2005 in Figure 3.10. Figure 3.10 contains the "Oil and Gas Average" trend line and ultra-deep JAS wells included in Figure 3.1 and described above. Although actual and predicted geothermal well costs vs. depth are clearly non-linear, no attempt has been made to add a trend line to this data, due to the inadequate number of data points.

Like oil and gas wells, Figure 3.10 shows that geothermal well costs appear to increase non-linearly with depth, although there is considerable scatter. However, EGS and hydrothermal well costs are considerably higher than oil and gas well costs – often 2 to 5 times greater than oil and gas wells of comparable depth. It was also observed that costs for the deeper geothermal wells (>3 km) approach the JAS Oil and Gas Average. The geothermal well costs show a lot of scatter in the data, much like the individual ultra-deep JAS wells, but appear to be generally in good agreement, despite being drilled at various times over the last 30 years. This suggests that the MITDD index is properly normalizing well costs.

Table 3.3 Actual and predicted geothermal well drilling and completion costs update to year 2005 US$ using the MITDD index (adapted from Tester and Herzog, 1990 and updated).

Well ID	Depth (meters)	Depth (feet)	Cost When Drilled (M$)	Year Drilled	Cost Year 2005 (M$)	Comments
GT-1	732	2402	0.060	1972	0.74	Fenton Hill Site, New Mexico, USA. Actual Costs (Tester and Herzog, 1990)
GT-2	2932	9619	1.900	1974	13.34	
EE-1	3064	10052	2.300	1975	12.19	
EE-2	4660	15289	7.300	1980	15.24	
EE-3	4250	13944	11.500	1981	25.42	
EE-3a	4572	15000	5.160	1988	13.30	
RH-11 (low)	2175	7136	1.240	1981	2.75	Rosemanowes Site, Cornwall, UK. Actual Costs. (Tester and Herzog, 1990) Low: $1 = 1£ GBP High: $1.6 = 1£ GBP
RH-11 (high)	2175	7136	1.984	1981	4.40	
RH-12 (low)	2143	7031	1.240	1981	2.75	
RH-12 (high)	2143	7031	1.984	1981	4.40	
RH-15 (low)	2652	8701	2.250	1985	7.08	
RH-15 (high)	2652	8701	3.600	1985	11.33	
UK (Shock, 1986)	6000	19685	8.424	1985	20.15	Camborne School of Mines ($1=1£ GBP)
(Bechtel, 1988)	3657	11998	3.359	1987	10.27	Predictions for Roosevelt Hot Springs, UT
(Hori, 1986)	3000	9843	6.000	1985	18.88	Predicted Costs
(Entingh, 1987) I	3000	9843	6.900	1984	20.94	Predicted Costs based on Heat Mining
(Entingh, 1987) II	3000	9843	3.800	1984	11.53	
(Entingh, 1987) III	3000	9843	3.000	1984	9.11	
Heat Mining (1987)	3000	9843	3.000	1984	9.11	Predicted Costs
The Geysers	1800	5906	0.486	1976	2.07	Actual costs (Milora and Tester, 1976)
The Geysers	3048	10000	2.275	1989	6.44	Actual costs (Batchelor, 1989)
Other Hydrothermal	1600	5249	0.165	1976	0.70	Actual costs (Milora and Tester, 1976)
IM-GEO IV-FL	1829	6001	1.123	1986	3.20	Meridian predictions of hydrothermal wells from their IM-GEO data base (Entingh, 1989). Only base well costs are shown.
IM-GEO IV-BI	2743	8999	0.956	1986	3.14	
IM-GEO BR-FL	2438	7999	1.217	1986	3.99	
IM-GEO BR-BI	914	2999	0.556	1986	1.53	
IM-GEO CS-FL	3048	10000	2.032	1986	6.16	
IM-GEO CS-BI	914	2999	0.576	1986	1.59	
IM-GEO YV-FL	1524	5000	0.906	1986	4.38	
IM-GEO YV-BI	152	499	0.406	1986	4.64	
IM-GEO GY-DS	3048	10000	1.155	1986	3.50	
SNL – Non-US	2317	7603	1.539	1996	4.73	Actual geothermal well costs from Sandia National Laboratories (SNL) (Mansure, 2004)
SNL – Non-US	2374	7789	1.729	1997	4.93	
SNL – Non-US	2377	7800	1.377	1996	4.23	
SNL – Non-US	2739	8986	1.867	1997	5.33	
SNL – Non-US	2760	9055	1.320	1997	3.77	
SNL – Non-US	2807	9210	2.979	1996	9.16	
SNL – Non-US	2819	9249	0.915	1997	2.61	
SNL – Non-US	2869	9414	1.030	1996	3.17	
SNL – Non-US	3021	9912	1.060	1996	3.26	
SNL – Non-US	3077	10096	1.514	1996	4.57	
SNL – US	2277	7471	1.186	1985	3.15	
SNL – US	2334	7658	0.822	1986	2.70	
SNL – US	1703	5588	0.804	1986	2.29	
SNL – US	2590	8496	2.220	1991	7.12	
SNL – US	2627	8618	1.760	1997	5.02	
GPK-3	5101	16731	6.571	2003	8.26	Soultz, France. Trouble costs excluded. (1 USD = 1.13 EUD) (Baria, 2005)
GPK-4	5100	16728	5.14	2004	5.62	
Cooper Basin, Australia-Habenero 2	4725	15498	6.3	2004	6.89	Trouble costs excluded. (1 USD = 0.724 AUD) (Wyborn, 2005)

1. M$ = millions of US$.
2. A discussion of the origins of many of the actual and predicted well costs is given in Tester and Herzog (1990).

Figure 3.10 Completed well costs in year 2005 US$ as a function of depth. Well costs are tabulated in Table 3.1 and Table 3.3.

3.5. Conclusions

Historic oil and gas well cost data were analyzed and found to have a strong dependence on depth. The dependence can be well described using an exponential function to relate well costs to drilling depth. A new drilling index, called the MIT Depth Dependent (MITDD) drilling cost index, was developed based on an extensive databases of oil and gas well costs available from the JAS. The index captures the strong dependence of drilling costs on depth and more accurately updates drilling costs to current US$. Analysis of historic data showed that well costs are strongly linked to the price of crude oil due to fluctuations in demand for rotary drilling rigs for exploration and production of oil. The MITDD index was used to normalize predicted and actual completed well costs for both EGS and hydrothermal systems from various sources to year 2005 US$, and then compare and contrast these costs with oil and gas well costs. From the analysis, it was concluded that both oil and gas well and geothermal well costs increase non-linearly with depth, but geothermal wells cost 2 to 5 times more than oil and gas wells drilled to comparable depths.

3.6. References

American Petroleum Institute (1976-2005). Joint Association Survey on Drilling Costs. Washington, D.C., American Petroleum Institute, Statistics Dept.

Armstead, H. C. H. and J. W. Tester (1987). Heat Mining. London, New York, E. & F. N. Spon.

Augustine, C., J. W. Tester, B. J. Anderson, S. Petty and B. Livesay (2006). A Comparison of Geothermal with Oil and Gas Well Drilling Costs. Proceedings, Thirty-First Workshop on Geothermal Reservoir Engineering, Stanford University, Stanford, CA, January 30-February 1.

Baker Hughes. (2008, December 4, 2008). "Worldwide Rig Counts (incl. North America) - Current & Historical Data."   Retrieved December 31, 2008, from http://investor.shareholder.com/bhi/rig_counts/rc_index.cfm.

Baria, R. (2005). Personal Communication to S. Petty, November 11, Mil-Tech UK Limited.

Batchelor, A. S. (1989). Personal Communication to J. W. Tester and H. J. Herzog, December 12. Falmouth, UK, Geosciences, Ltd.

Bechtel National, I. (1988). "Hot Dry Rock Venture Risk Investigation." US DOE, San Fransisco, CA, DE-AC03-86SF16385.

Bloomfield, K. K. and P. T. Laney (2005). "Estimating Well Costs for Enhanced Geothermal System Applications." Idaho National Laboratory, Idaho Falls, ID, (August 2005). INL/EXT-05-00660.

Cummings, R. G. and G. E. Morris (1979). "Economic Modeling of Electricity Production from Hot Dry Rock Geothermal Reservoirs: Methodology and Analyses." Electric Power Research Institute, Palo Alto, CA, EA-630.

Energy Information Administration. (2008). "Monthly Energy Review December 2008: Tables 9.1 and 9.11."   Retrieved December, 2008, from www.eia.doe.gov/mer.

Entingh, D. J. (1987). "Historical and Future Cost of Electricity from Hydrothermal Binary and Hot Dry Rock Reservoirs, 1975-2000." Meridian Corp., Alexandria, VA, (October). 240-GG.

Entingh, D. J. (1989). Personal Communication to J. W. Tester and H. J. Herzog, November, 1989. Alexandria, VA, Meridian Corporation.

Heidinger, P., J. Domstadter and A. Fabritius (2006). "HDR Economic Modelling: HDRec Software." Geothermics **35**(5-6): 683-710.

Hori, Y. e. a. (1986). "On Economics of Hot Dry Rock Geothermal Power Station." Corporate Foundation Central Research Institute for Electric Power, Japan, (March). Hot Dry Rock Geothermal Power Station Cost Study Committee Report 385001.

Mansure, A. J. (2004). Personal Communication to C. Augustine, April 12. Albequerque, NM, Sandia National Laboratories.

Mansure, A. J., S. J. Bauer and B. J. Livesay (2005). "Geothermal Well Cost Analyses 2005." Geothermal Resources Council Transactions **29**: 515-519.

Milora, S. L. and J. W. Tester (1976). Geothermal Energy as a Source of Electric Power: Thermodynamic and Economic Design Criteria. Cambridge, MA, MIT Press.

Shock, R. A. W. (1986). "An Economic Assessment of Hot Dry Rocks as an Energy Source for the U.K." Energy Technoloy Support Unit, UKDOE, Oxforshire, UK, ETSU-R-34.

Tester, J. W. and H. J. Herzog (1990). "Economic Predictions for Heat Mining: A Review and Analysis of Hot Dry Rock (HDR) Geothermal Energy Technology." Energy Laboratory, Massachusetts Institute of Technology, Cambridge, MA, MIT-EL 90-001.

Tester, J. W., H. J. Herzog, Z. Chen, R. M. Potter and M. G. Frank (1994). "Prospects for Universal Geothermal Energy from Heat Mining." Science & Global Security **5**: 99-121.

U. S. Office of Management and Budget. (2008). "Budget of the United States Government: Historical Tables Fiscal Year 2008, Table 10.1." Retrieved December 31, 2008, from http://www.gpoaccess.gov/usbudget/fy08/hist.html.

Wyborn, D. (2005). Personal Communication to S. Petty, November 11. Queensland, Australia, Geodynamics, Ltd.

Chapter 4: Effect of Technology Advances on EGS Electricity Cost Projections

In 2005-2006, a panel assembled by the Massachusetts Institute of Technology (MIT) conducted a 15-month assessment of the potential of geothermal energy in the U.S. The study report (Tester et al., 2006) documented their analysis of the EGS resource, established requirements for extracting and utilizing energy from EGS resources and estimated the costs for EGS supplied electricity. The report concluded that EGS has the potential to provide the United States with 100,000 MW of geothermal electricity by 2050 at competitive prices with an investment of about one billion dollars in research and development, field demonstration projects and deployment assistance spread over the next ten to fifteen years (Tester et al., 2006). To achieve the goals outlined in the MIT report, there is a critical need for EGS resource assessment, reservoir testing and development, and deployment assistance, and for sustained research, development, and funding support that would reduce technical and economic risks and thus increase the impact of geothermal energy as a major energy supply in the U.S.

To focus research and development to develop EGS resources quickly and efficiently, the factors that most affect the economic and technical feasibility of EGS were identified. Models that take into account performance factors that determine EGS resource, such as reservoir depth, temperature gradient, well productivity, and cost factors such as drilling, stimulation, and power plant costs, were used to estimate the economic feasibility of developing an EGS resource, as well as identify which factors have the greatest influence on project costs. In Chapter 1, several such models were identified. This chapter explores the effects of resource quality, reservoir performance, and drilling costs on EGS economics using a cash flow model that was developed by the MIT team to predict levelized electricity costs and sensitivity to performance and financial parameters to identify areas that could benefit from intensified R&D. Both reservoir performance factors and costs factors were explored to determine their interplay and impact on electricity costs using the MIT EGS model. Specifically, the impact of advances in drilling technology that lead to lower drilling costs, and advances in EGS reservoir development that increase production well flow rates were investigated.

The work presented in this chapter was done in collaboration with Hildigunnur Thorsteinsson, Brian Anderson, Michal Moore, and Jeff Tester, and was presented at the Thirty-Third Workshop on Geothermal Reservoir Engineering at Stanford University (Thorsteinsson et al., 2008).

4.1. MIT EGS Economic Model

An updated version of the MIT EGS model was used to predict Levelized Electricity Costs (LEC), surface plant capital costs and well costs. The model uses a levelized life cycle cost analysis that takes into account the full financial cash-flow of the EGS project, including income from the sale of electricity and expenses such as investment principal repayment, interest, operating and maintenance costs, taxes, and any other expenses related to the project, to determine the levelized electricity price (LEC) at which the income over the lifetime of the project is equivalent to all the expenses associated with the project. The costs are normalized to fixed year dollars to remove the impact of inflation, so that the costs of different projects and/or different technologies (with potentially different cost structures) can be compared on a common basis. The MIT EGS model was originally developed by Tester and Herzog (1990), and is based on the methodology put forth by the Electric Power Research Institute (EPRI) which uses an intertemporal optimization approach to account for re-drilling and re-stimulation decisions that must be made during the lifetime of an EGS reservoir when determining LEC (Cummings and Morris, 1979). The methodology was incorporated into an existing levelized life cycle cost computer code (Hardie, 1981). Subsequent work on the model at the MIT Energy Laboratory by Tester, Herzog and co-workers (1997) eventually resulted in the "EGS Modeling for Windows," which was updated for "The Future of Geothermal Energy" assessment by Anderson (Tester et al., 2006) and slightly modified to facilitate the analysis given in this chapter.

The MIT EGS model takes into account both the performance parameters for the resource and the reservoir, such as the average temperature gradient, reservoir temperature, well depth and productivity, and cost factors, such as capital costs, operating and maintenance costs, and financial factors including debt and interest and equity rates. The capital costs for drilling, reservoir stimulation, and the surface plant are discussed first, with an emphasis on the economic

effects of drilling technologies. Finally, a summary of the model, including additional base case parameter values, is given.

4.2. Drilling Costs

Two scenarios were used to represent drilling costs for EGS plants: one based on current technology and the other on projected advanced technology improvements. The current technology scenario uses drilling costs generated by the Wellcost Lite model originated by Livesay and collaborators (Mansure et al., 2005) and updated by the MIT study (Tester et al., 2006). The advanced technology scenarios do not assume or endorse any technology in particular, but instead estimates costs for advanced wells with certain characteristics that lead to lower increases in costs as a function of well depth. Both the current and advanced drilling cost scenarios assume 2004 drilling cost numbers.

4.2.1. Wellcost Lite

The Wellcost Lite model (Mansure et al., 2005; Augustine et al., 2006) estimates the cost of drilling a well by sequentially accounting for the events and materials that occur during the course of drilling. The model calculates the time needed to drill each interval, including drilling time, tripping time, logging and maintenance time, etc., as well as the costs of mobilization and demobilization, daily rig rental, and/or purchasing items for each of these events. These costs are then combined and reported on a per-casing interval basis, and the interval costs are summed to obtain a total well cost for a specified total drilling depth.

The drilling costs used in this study assume the same wells and assumptions presented in Chapter 6 in (Tester et al., 2006). Well costs were estimated for depths from 1,500 m (4,900 ft) to 10,000 m (32,800 ft). The drilling costs estimated by the Wellcost Lite model are given in Table 4.1. A second-order polynomial was fit to correlate drilling costs as a function of depth, and subsequently used to calculate drilling costs for the economic model. Drilling costs of ±25% were also assumed and used in the economic model to determine how variations in these estimated costs, such as those that might be expected when drilling in different lithologies, affect overall EGS costs.

Table 4.1 Wellcost Lite base case costs (from Table A.6.3b in Tester et al., 2006).

Well Depth (m)	Well Depth (ft)	Estimated Cost (2004 M$)
1500	4921	2.303
2500	8202	3.372
3000	9842	4.022
4000	13123	5.223
5000	16404	6.740
6000	19685	9.172
7500	24606	14.645
10000	32808	19.731

4.2.2. Advanced Drilling Technologies

Well costs for advanced drilling technologies were also estimated. These estimates were used to determine how substantially lower drilling costs could affect EGS development costs in the future. Previous studies have identified the use for an increasing number of casing intervals with depth as a reason that drilling costs increase significantly and non-linearly with depth (Augustine et al., 2006). Conventional wells are drilled in intervals that are cased and cemented in segments that telescope down to the final well diameter. These cased intervals are needed to control and stabilize the well and prevent collapse of the well as the depth increases. Adding extra casing strings adds significantly to cost if a specified bottom hole diameter is maintained. The upper casing intervals must have a large enough diameter to allow subsequent casing intervals to fit inside them, so larger drill bits, larger-diameter, thicker-walled casing, and a larger drilling rig are required. As the number of intervals increases, the amount of casing and cementing needed, as well as the size and expense of drilling equipment needed to complete the hole increases along with costs. Additionally, extra time is required to complete the intervals.

Another major factor affecting drilling costs is the rate of penetration of the drill bit itself. Lower rates of penetration mean longer drilling time and increased rig rental costs. This could be a significant problem for EGS if wells are drilled in hard, crystalline rock. As well depth increases, tripping time, the time needed to remove and replace the drill string to change worn drill bits, also becomes a significant issue in influencing costs by reducing the actual drilling time to a smaller percentage of the total time.

Advanced drilling technologies that mitigate or eliminate some of the factors that lead well costs to increase non-linearly with depth were explored. Three cases of progressively advanced technologies to eliminate these factors were assumed. The particular technologies used to achieve these advances were not specified. Instead, it was assumed that the technology existed and was technically mature when it was deployed, and then the attributes of the advanced drilling technology were incorporated into the Wellcost Lite model to estimate drilling costs. The advanced drilling technologies and their attributes are explained in greater detail in the following three cases:

Case 1: Single-Diameter Wells

Technologies that eliminate the need for intermediate casing intervals that telescope down to the final well diameter could lower the cost of drilling substantially. Such technologies would create a "monobore" or "single-diameter" well that eliminates the need for much of the tangible costs and time associated with creating casing intervals. These wells could be envisioned by using an advanced expandable tubular system, a polymer or composite resin that coats the well wall and creates a temporary "casing" that adequately stabilizes the well for several weeks or months while the well is completed, or by simply assuming that deep EGS wells will typically be in competent, crystalline hard rock that can be drilled as an open hole over very long intervals, as for example in deep EGS holes (>3 to 4 km) at Fenton Hill. As stated above, the specific particular drilling technology used is not important, only the well attributes that result from employing that technology.

In this case, the following assumptions were made:

1. The well was drilled in three segments:
    a. A 36" (91 cm) conductor pipe to a depth of ~100 ft (30.5 m) at the surface (pre-spud).
    b. A 14-¾" (37.5 cm) diameter hole with 11-¾" (30 cm) casing from the surface to the top of the production zone.
    c. A 10-5/8" (27 cm) diameter hole drilled the final 4,000 ft (1,200 m) into the production zone and finished with 8-5/8" (22 cm) perforated production liner.
2. All other intermediate intervals were excluded.
3. Trouble costs were kept to a minimum.

Case 2: Continuous Drilling

In addition to the assumptions made in Case #1, a technology that allows continuous drilling in rock was envisioned for Case #2. Such a technology would assume a different, revolutionary mechanism of rock penetration, such as thermal spallation or fusion (Potter and Tester, 1998), chemical dissolution (Polizzotti et al., 2003), particle impact (Geddes and Curlett, 2006), or some other form of drilling where the "drill bit" does not wear out and need to be replaced. This type of drilling would eliminate the need for tripping and reduce rig rental times, especially for deep wells. Such a technology would also complement a "single-diameter" well system nicely.

In this case, the following assumptions were made:

1. Assumptions from Case #1 still apply.
2. Drilling system does not require bit replacement, so tripping time can be eliminated.
3. Rate of penetration does not change with depth, and was assumed to be 25 ft (7.62 m) per hour, which is slightly higher than rates assumed for conventional drilling in Wellcost Lite model.

Case 3: Reduced Casing Costs

In addition to the assumptions made in Case #1 and Case #2, a technology that reduces the tangible material costs for the casing used in the "single-diameter" 14-3/4" (37.5 cm) interval was envisioned for Case #3. Substantially reduced casing costs could result from conventional casing designs constructed with some newly developed, significantly cheaper material: for example, an advanced polymer or resin that coats the well wall while drilling and is strong and stable enough to act as permanent casing, or some sort of reinforced cement with advanced strength and stability properties.

In this case, the following assumptions were made:

1. Assumptions from Case #1 and Case #2 still apply.
2. The material costs for casing for the 11-3/4" (30 cm) casing interval is half what it would be for conventional steel casing.
3. Cementing costs are still assumed to apply, whether or not actual cement would be used to affix whatever form the casing may take.
4. Smaller rigs are needed to implement these new drilling and casing technologies due to their smaller size, weight, or the manner in which they are installed. Pre-spud costs and rig rental rates needed for a 10,000 ft (~3 km) conventional hole are assumed for all well depths.

Advanced Drilling Cost Estimates

For each of the advanced drilling cases, costs for wells ranging in depth from 10,000 ft (3,050 m) to 30,000 ft (9,150 m) were estimated using a method similar to that employed by the Wellcost Lite model for conventional drilling technology. Costs for the pre-spud, conductor pipe interval, intermediate interval, and production interval were calculated and summed. It was assumed that most of the equipment and tools, or similar versions of them, would be used in the advanced technologies wells, so that costs for these individual items and services would be similar in both cases. Therefore, costs in the intervals were based on the costs associated with conventional drilling technology, with appropriate adjustments made depending on the case considered. For example, the costs estimated for Case 1 are very similar to those used in Wellcost Lite for conventional wells, except only one intermediate interval is used and it is extended over the entire length between the surface and the production interval. As the depth increased, adjustments were made for increased rig sizes, different rates of penetration and bit life, and more expensive casing.

The resulting well cost estimates for the three different technology cases presented above are given in Table 4.2 - Table 4.4. Estimated well costs varied linearly with depth. The results of this fit are also included in the table. These correlations were subsequently used in the EGS economic model to estimate drilling costs for the three cases.

Completed well costs as a function of drilling depth are shown in Figure 4.1, including the estimated well costs from Wellcost Lite, with the ±25% cases shown as dashed red lines above and below the base case, and the estimated linear well costs from the advanced technology cases shown as dashed black lines. For comparison, the figure also includes average oil and gas well completion costs as a function of depth, and historic data of actual and estimated well costs for hydrothermal and EGS wells updated to year 2004 US $ (Augustine et al., 2006). The figure illustrates the range of costs that result for the different drilling scenarios that were used to explore the sensitivity of LEC to variable drilling costs for EGS plants.

Table 4.2 Estimated well costs and linear fit of well cost estimates versus depth for Advanced Drilling Technology Case 1 (Year 2004 US $).

	Well Depth (ft)						Linear Well Cost Fit (with 95% Confidence Interval)	
	10000	12000	16000	20000	25000	30000		
PreSpud	$188,000	$313,000	$346,000	$346,000	$346,000	$346,000	Slope ($/ft)	304 ± 23
Interval 1	$1,460,000	$1,985,000	$2,872,000	$4,282,000	$5,600,000	$6,876,000	Intercept ($)	-191955 ± 457710
Interval 2	$995,000	$1,177,000	$1,483,000	$1,463,000	$1,520,000	$1,576,000	R^2 Value	0.997
Total	**$2,715,000**	**$3,474,000**	**$4,701,000**	**$6,091,000**	**$7,466,000**	**$8,798,000**		

Table 4.3 Estimated well costs and linear fit of well cost estimates versus depth for Advanced Drilling Technology Case 2 (Year 2004 US $).

	Well Depth (ft)						Linear Well Cost Fit (with 95% Confidence Interval)	
	10000	12000	16000	20000	25000	30000		
PreSpud	$188,000	$313,000	$346,000	$346,000	$346,000	$346,000	Slope ($/ft)	204 ± 37
Interval 1	$1,230,000	$1,595,000	$2,253,000	$3,498,000	$4,138,000	$5,008,000	Intercept ($)	332366 ± 746979
Interval 2	$774,000	$822,000	$955,000	$985,000	$939,000	$945,000	R^2 Value	0.983
Total	**$2,264,000**	**$2,730,000**	**$3,554,000**	**$4,829,000**	**$5,424,000**	**$6,298,000**		

Table 4.4 Estimated well costs and linear fit of well cost estimates versus depth for Advanced Drilling Technology Case 3 (Year 2004 US $).

	Well Depth (ft)						Linear Well Cost Fit (with 95% Confidence Interval)	
	10000	12000	16000	20000	25000	30000		
PreSpud	$188,000	$260,000	$260,000	$260,000	$260,000	$260,000	Slope ($/ft)	132 ± 6
Interval 1	$1,086,000	$1,323,000	$1,745,000	$2,373,000	$3,005,000	$3,612,000	Intercept ($)	788897 ± 112607
Interval 2	$774,000	$771,000	$862,000	$840,000	$844,000	$848,000	R^2 Value	0.999
Total	**$2,120,000**	**$2,353,000**	**$2,867,000**	**$3,473,000**	**$4,108,000**	**$4,720,000**		

4.3. Stimulation costs

Following the methodology used earlier in the MIT EGS assessment (Tester et al., 2006), reservoir stimulation costs were assumed to be $500,000 for each well regardless of depth, temperature gradient or production well flow rate.

4.4. Surface Plant Costs

Surface plant costs were predicted using the same assumptions as were used in the MIT EGS assessment (Tester et al., 2006). As a conservative estimate, it was assumed that binary type power plants would be used to convert the thermal energy extracted from EGS resources to electricity regardless of the reservoir field temperature. Surface plant costs were calculated using the following empirical correlation:

$$C = 2642.025 - 3.5 * T \qquad \text{Eq. (4-1)}$$

Where:

C = surface plant costs ($/kW in 2004 US $)
T = geothermal fluid temperature (^{o}C)

Figure 4.1 Predicted and actual drilling costs as a function of depth (adapted from Augustine et al., 2006).

4.5. Reservoir Characteristics

The thermodynamic quality of an EGS resource is determined by its temperature and productivity (the sustainable rate at which heat can be mined). A range of depths, average temperature gradients and flow rates were explored to analyze the effect of reservoir performance factors on levelized costs of electricity. In order to explore the space, drilling depths ranging from 3 km to 10 km were analyzed along with average temperature gradients ranging from 10°C per km to 100°C per km. This range of reservoir temperatures as a function of depth will allow the effects of drilling technology improvements to be studied. Production well flow rates of 20, 40, 60, 80 and 100 kg/s were examined to study the effects of reservoir stimulation technology improvements. Implicit in the variation of production well flow rates is the assumption that the reservoir can be stimulated to give sufficient volume and surface area to support production flow rates at the specified level of thermal drawdown. Feasible fluid temperatures for electricity production were limited to between 100°C and 400°C, so that not all possible reservoir depth and temperature gradients combinations were considered.

4.6. Model Summary

A summary of the parameter values used in the model is given in Table 4.5. The parameters varied during the study, and the values considered for them, are shown in bold. The cost correlations for drilling, stimulation, and power plants discussed above were used in the model. Technical and financial parameters similar to those used in the MIT study (Tester et al., 2006, Chapter 9) for a commercially mature EGS system were assumed with several notable changes. First, the production to injection well ratio was changed from being a quartet with three production wells and one injection well to being five production wells for every four injection wells. Second, the debt to equity ratio was changed from 60/40 to 70/30 to reflect industry practice. Third, no drilling contingency factor was assumed for drilling costs. Finally, the thermal drawdown rate, or the percentage of thermal energy mined from the reservoir each year, was increased from 3%/yr to 3.33%/yr, so that re-drilling and re-stimulation is required roughly every six years. All financial and cost figures cited are in 2004 US $ unless otherwise noted.

Table 4.5 Parameter values used in MIT EGS model. Values in bold are varied as part of parametric study.

Parameter Description	Value(s)
Reservoir Characteristics	
Depth (km)	**3-10 (1 km intervals)**
Temperature Gradient (^{o}C/km)	**10-100 (10 ^{o}C/km intervals)**
Production well Flow Rate (kg/s)	**20, 40, 60, 80, 100**
Thermal Drawdown Rate (%/yr)	3.33
Thermal Drawdown before Rework	20%
Ratio Producer/Injector Wells	5/4
Surface Temperature (^{o}C)	15
Impedance per Well (MPa-s/L)	0.15
Power Plant Characteristics	
Plant Type	Binary Organic Rankine Cycle
Plant Life Time (years)	30
Max/Min Geofluid Temps (^{o}C)	400/100
Capacity Factor	95%
Geofluid Pump Efficiency	80%
Well Completion Characteristics	
Drilling Scenarios Considered	**WCL[1] Base, WCL +25%, WCL -25%, Advanced Drilling Case 1, 2, 3**
Financial Terms	
Debt/Equity Ratio	70%/30%
Debt Rate of Return	7.5%
Equity Rate of Return	17%
Inflation Rate	3%
Property Tax Rate	2%
Sales Tax Rate	6.5%

[1]**WCL – Wellcost Lite model**

4.7. Electricity Price Forecast

To analyze the feasibility of drilling scenarios, a market electricity price forecast for baseload energy was made. The price of baseload energy is a reflection of the lowest price energy available for dispatch in the system. The system operator will dispatch from the bottom of the bid stack in order to satisfy load at the lowest price. Today, baseload operators will typically bid zero, and the system operator will pay for electrical energy based on the estimated marginal cost for generating electricity from the last units accepted for dispatch. This will vary depending on the area served, but presuming that both coal and nuclear were available, nuclear would be dispatched first and coal second given their operating price schedule. Higher priced coal would

be dispatched for load following. Firming would typically be done first with hydroelectric supplies followed by the next most expensive bid.

Baseload energy demands are not specifically forecast by most energy agencies such as the EIA (Energy Information Administration) or the NEB (National Energy Board). In these cases the forecast will typically address the composite energy price that includes fuel prices by source such as coal, natural gas, or oil, (but not renewable sources). In addition, contracts for power delivery from these sources will reflect long term and

relatively stable (i.e. less volatile) pricing. Available forecasts are limited in their time horizon. For instance, the EIA forecast goes to 2030 (and is projected to increase linearly at the same rate of 1.4% per year and the NYMEX only projects prices until 2016.

In the base case electricity cost forecast used in this study, the energy price is assumed to increase at 2% per year in excess of the rate of inflation. Primarily, it reflects the influence of growth in U.S. population and associated demand increases plus some small margin for energy intensity changes. An average of the estimated price of coal and nuclear energy is used as a base price estimate. Projected natural gas prices were not included in the base case forecast.

Additionally, a high price case prediction was made use the following assumptions:

1. 10% of the existing coal fleet is replaced in 2015 and 40% in 2020.
2. 60% of the existing nuclear fleet is re-licensed in 2010 for an additional 20 years and 100% of the fleet is retired in 2030.
3. Limited new nuclear plant construction begins in 2015 and prices increase by 25% over the previous year and then inflate at 3% per year, while coal inflates at 2% per year.
4. Nuclear price increases occur again in 2020 (25%) and 2030 (50%) and then inflate at 3% per year to 2050.
5. New coal construction in 2015 causes 25% rise in delivered price from previous year.
6. Coal price increases occur again in 2020 (25%) and 2030 (50%) and then inflate at 2% per year to 2050.

Figure 4.2 shows the base case and high case baseload electricity price projections. In 2050 the base case price forecast projects the price of electricity to be 7 cents/kWh, while the high price case forecast projects the 2050 price to be just below 29 cents/kWh.
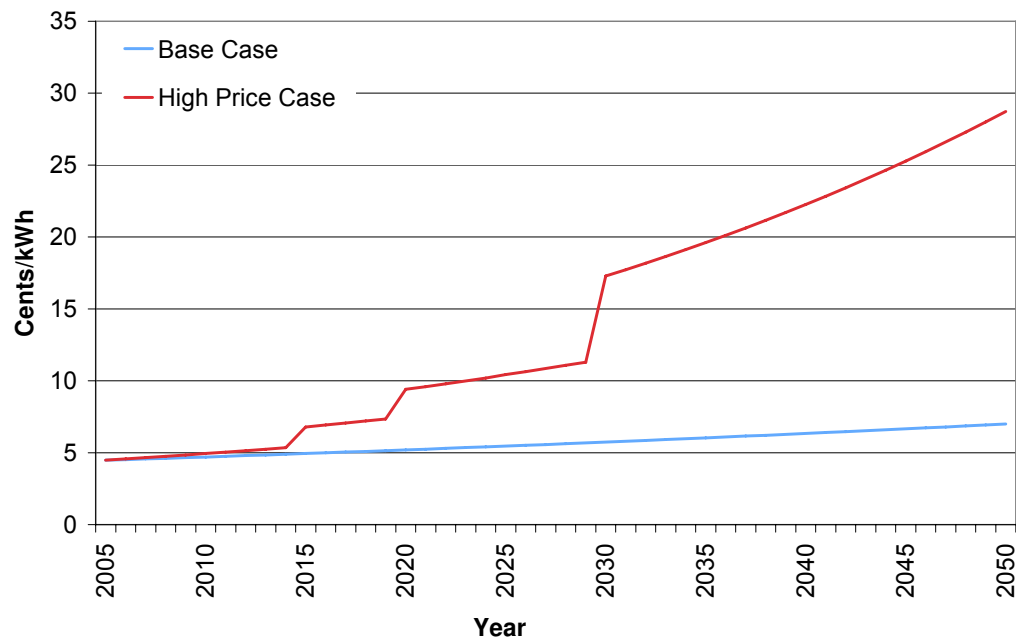
Figure 4.2 U.S. electricity price forecast in 2007 $.

4.8. Results

Estimates[2] of the levelized cost of electricity (LEC) along with total well costs and surface plant capital costs well produced for each set of parameters considered. In all, the LEC for 1,200 different cases were estimated. To assess this large amount of data in a concise and manageable manner, a color-coded diagram that condenses the multi-dimensioned parameter space explored into a two-dimensional space was conceived. The model run results were analyzed to determine economically feasible scenarios with respect to both base case and high electricity price forecasts. Base case price feasibility was defined as those scenarios with an LEC less than 7 cents/kWh. Feasibility for the high market electricity price case was defined as those scenarios where the LEC is less than 29 cents/kWh. The diagram consists of a grid of the reservoir temperature gradients and depths considered. Each box on the grid is divided into an upper and lower triangle. The color in each triangle represents the lowest production well flow rate interval

---

[2] Due to an error in one of the model parameter inputs, the LEC estimates in this study differ from those in (Thorsteinsson et al., 2008) for cases with reservoir temperatures of 215 $^{\circ}$C and higher. A thermal drawdown rate of 6%/year was used instead of the intended 3.33% for those cases. The incorrect parameter led to slightly higher LEC estimates, so they can be viewed as conservative. The model has been corrected for the results presented in this chapter.

at which electricity production is feasible, with the upper triangle corresponding to the base case electricity costs, and the lower triangle high case costs. A key for the diagram is given in Figure 4.3, and a diagram for each drilling cost scenario is shown in Figure 4.4 – Figure 4.9. LEC data for all the cases considered is tabulated in the appendix.

Figure 4.3 Key for figures 4.4-4.7.
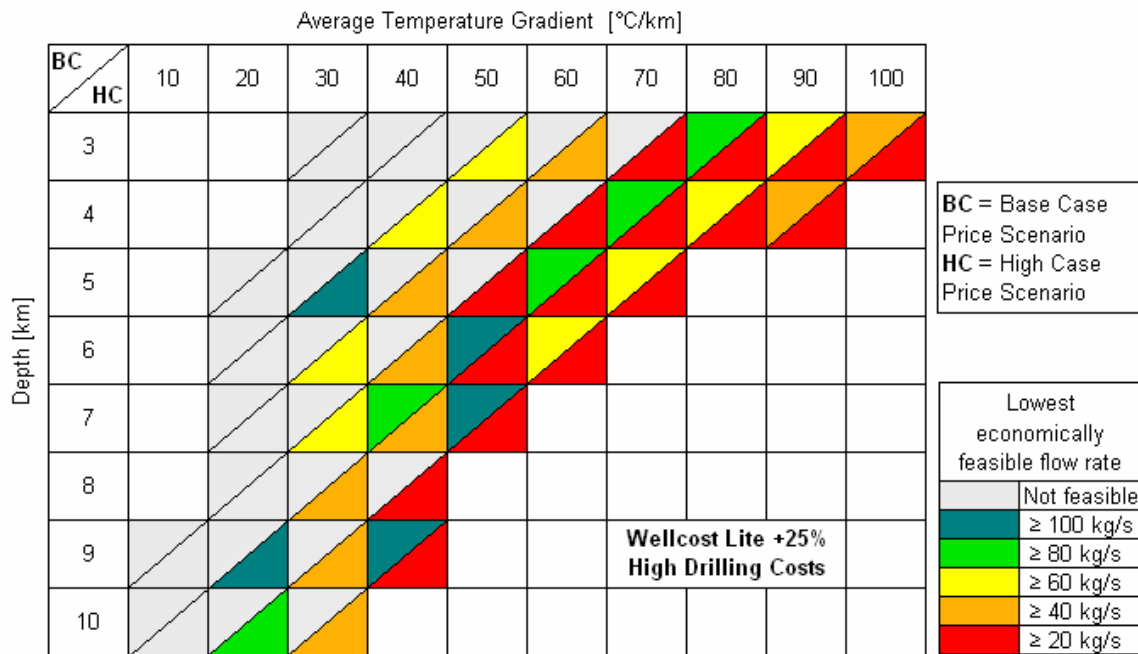
Figure 4.4 Base case and high case price scenario economic feasibility for drilling cost case Wellcost Lite +25%.
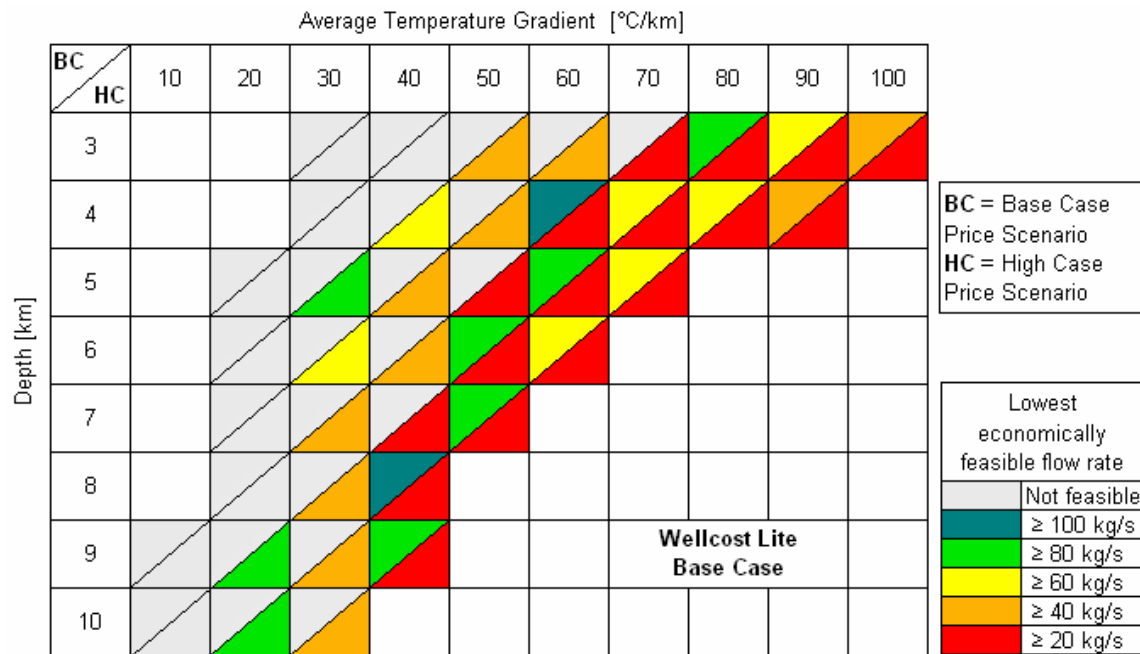
Figure 4.5 Base case and high case price scenario economic feasibility for drilling cost case Wellcost Base Case.
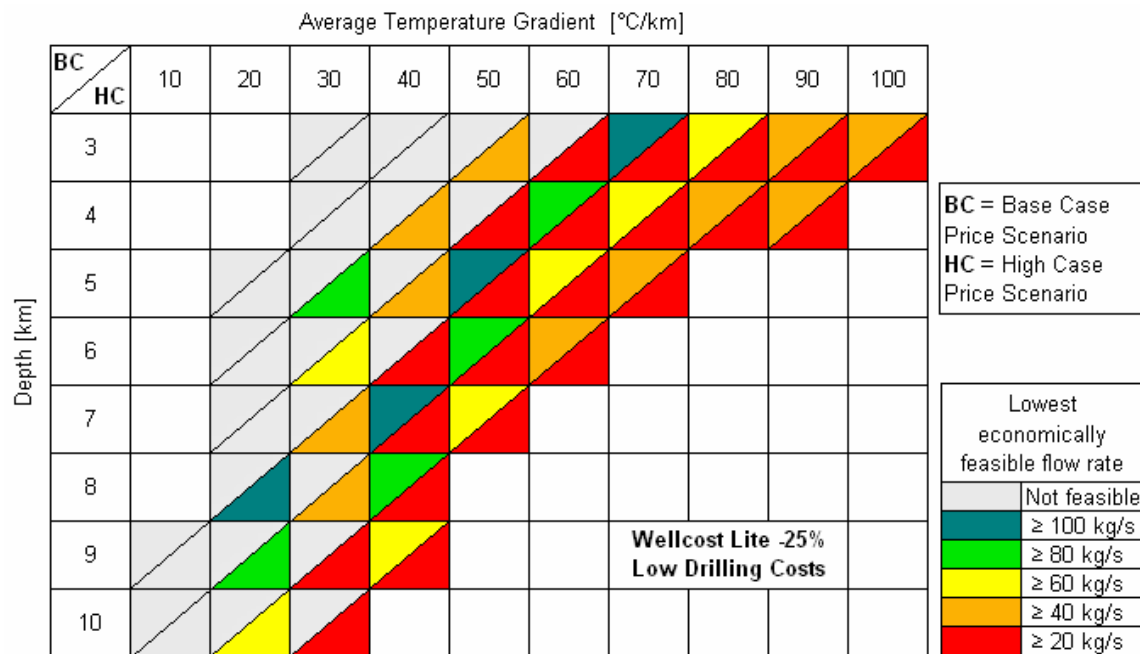
Figure 4.6 Base case and high case price scenario economic feasibility for drilling cost case Wellcost Lite - 25%.
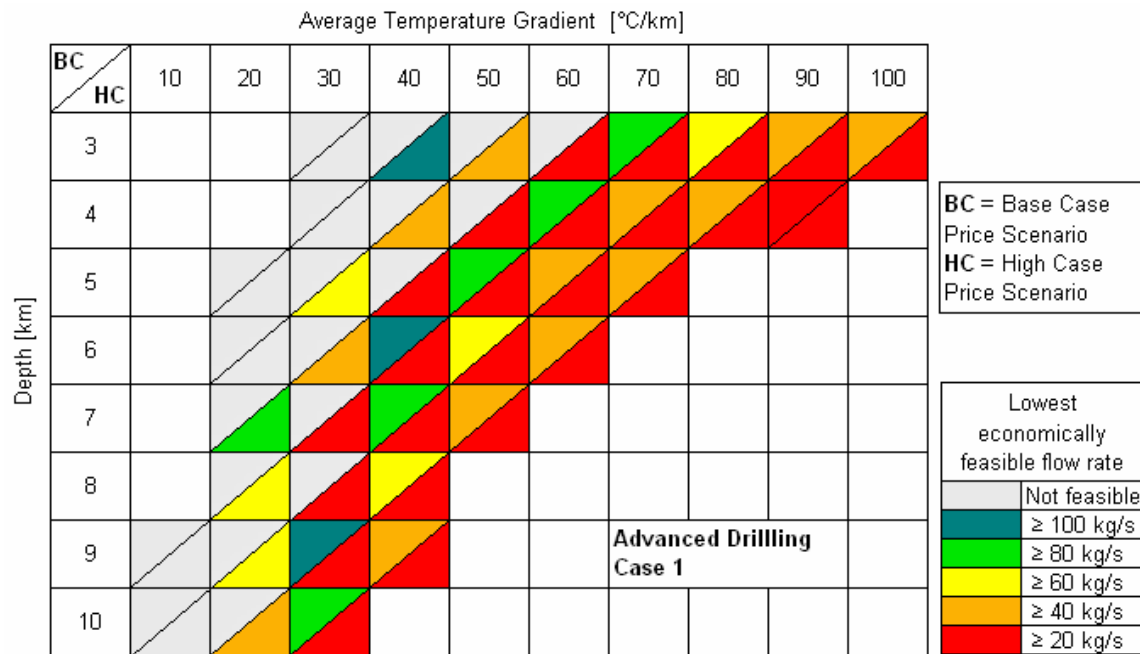
Figure 4.7 Base case and high case price scenario economic feasibility for drilling cost Case 1.
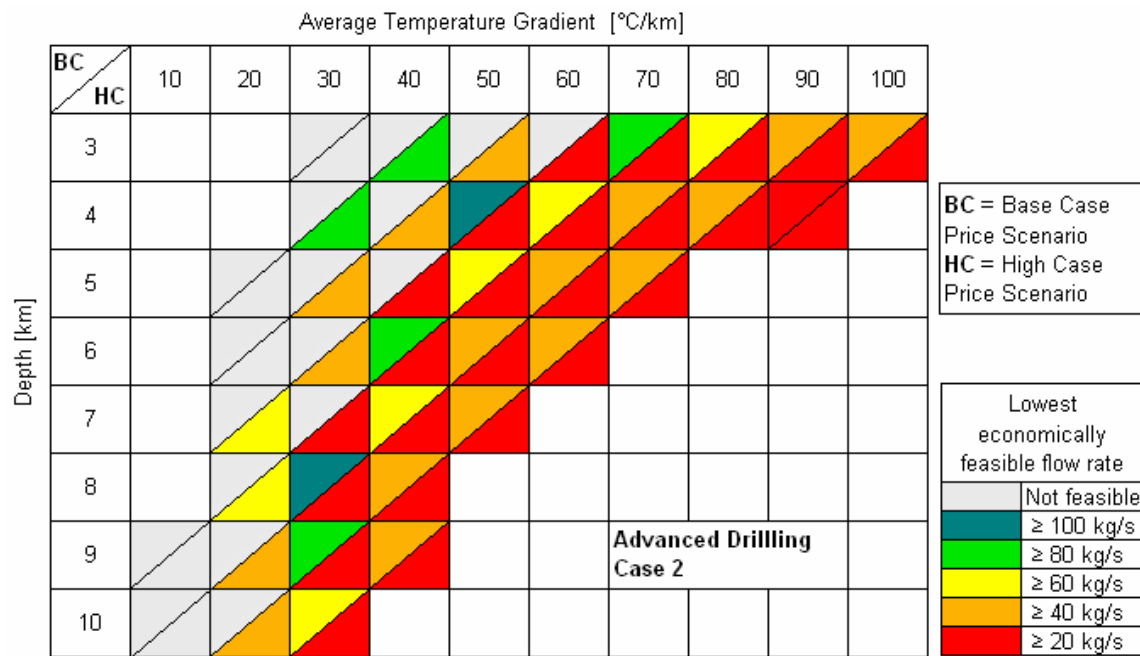
Figure 4.8 Base case and high case price scenario economic feasibility for drilling cost Case 2.
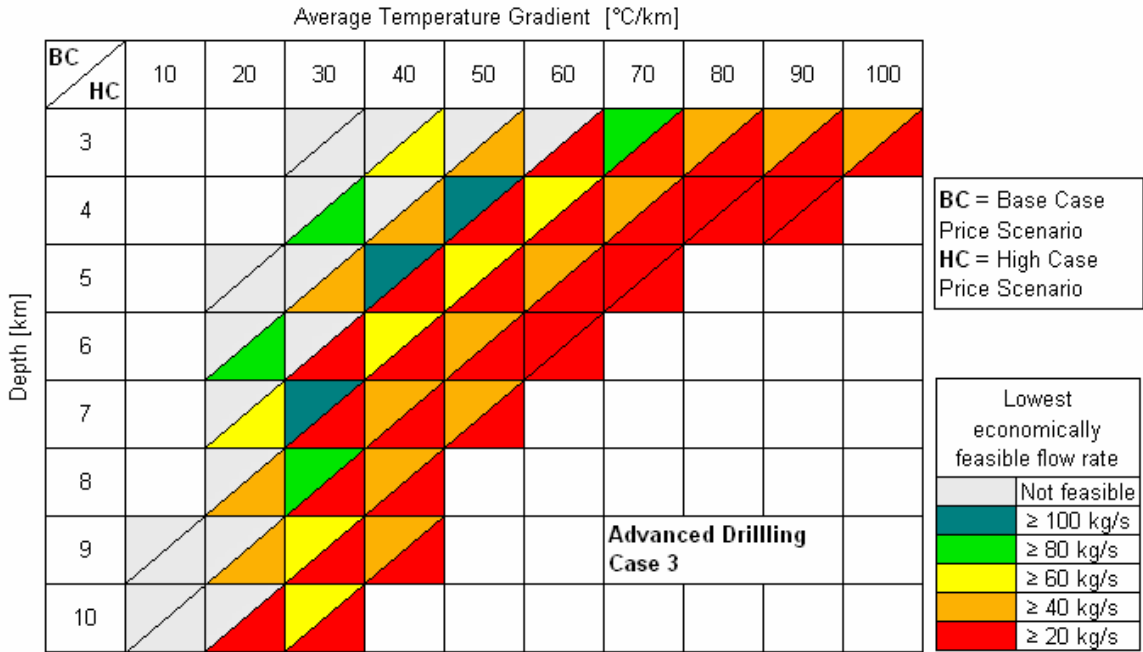
Figure 4.9 Base case and high case price scenario economic feasibility for drilling cost Case 3.

The analysis shows that as drilling costs decrease, lower quality EGS resources can be feasibly developed, or can be developed at lower well production flow rates, as one would expect. Still, even for the lowest drilling cost scenario considered (case 3), the lowest quality EGS resources could still not be economically developed at base case electricity prices, even assuming production well flow rates in excess of 100 kg/s. Advances in stimulating production flow rates beyond the current 20 kg/s per production well will be needed to economically develop high grade EGS resources with mid- and high temperature gradients with today's drilling technology if electricity costs remain low and follow base case, slow growth projections. Even significant drilling advances will still require reservoir stimulation improvements to access mid grade EGS resources. For the high electricity price case, the high- and mid grade resources could be developed using today's technology, and for the most advanced drilling scenario, almost all resources could be developed with modest improvements on today's reservoir stimulation technology.

4.8.1. Effect of Drilling Technology Advances

Figure 4.4 – Figure 4.9 show that economic feasibility increases considerably with drilling cost reductions. For example, EGS electricity production at Wellcost Lite +25% drilling costs is only feasible under the base case electricity price scenario for flow rates of 60-100 kg/s and average temperature gradients of 60°C/km and higher for reservoirs with depths of 5 km and less. However, for advanced drilling technology Case 3, a 20-60 kg/s flow rate is sufficient for base price case feasibility for a wide range of depths and mid- to high-average temperature gradients. Also, as drilling costs decrease, higher flow rates are no longer as required for economic feasibility in mid- to low- grade resource areas.

To more clearly demonstrate the effect of drilling technology advances on LEC estimates, economic feasibility results were correlated with the well and surface plant costs. Conditions were chosen for analysis that would represent different feasibility conditions. Figure 4.10 and Figure 4.11 show the base case price feasibility of the six drilling cases for different flow rates at depths of 5 and 4 km and average temperature gradients of 60°C/km and 80°C/km, respectively. Figure 4.12 shows the high price case feasibility at 10 km depth and an average temperature gradient of 20°C/km.

Within each figure, the reservoir temperature remains constant, so the surface plant costs also remain constant. The figures show that drilling costs make up a significant portion of the initial capital costs, especially for low temperature gradient resources. By comparing the three figures it can be seen that well costs become increasingly dominant as reservoir productivity declines. The effect of decreased drilling costs can be seen as well. For feasible cases, drilling costs tend to make up 30%-70% of capital costs. Conversely, for infeasible cases, the high price of drilling to access the reservoir prevents the resource from being developed. This analysis concludes for most cases that efforts to reduce EGS project costs should focus primarily on decreasing or lowering drilling costs rather than costs associated with the power plant.

5 km well depth and 60°C/km average gradient
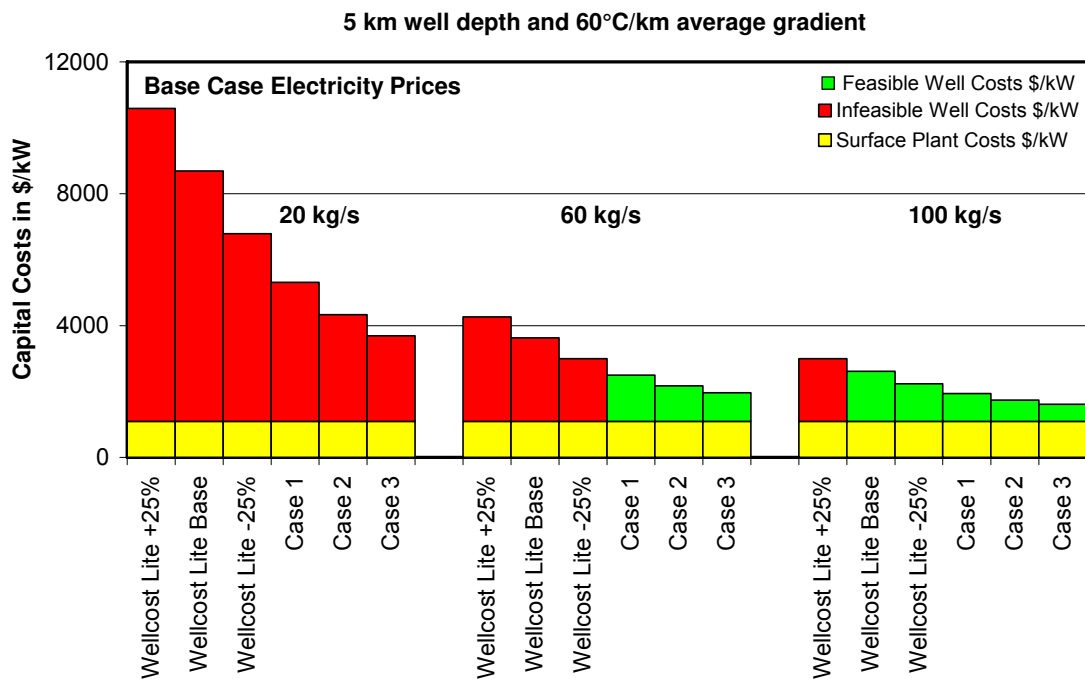
Figure 4.10 Well costs and surface plant costs for different drilling technology cases. Economic feasibility at base case electricity prices indicated by color of bars representing drilling costs.

4 km well depth and 80°C/km average gradient
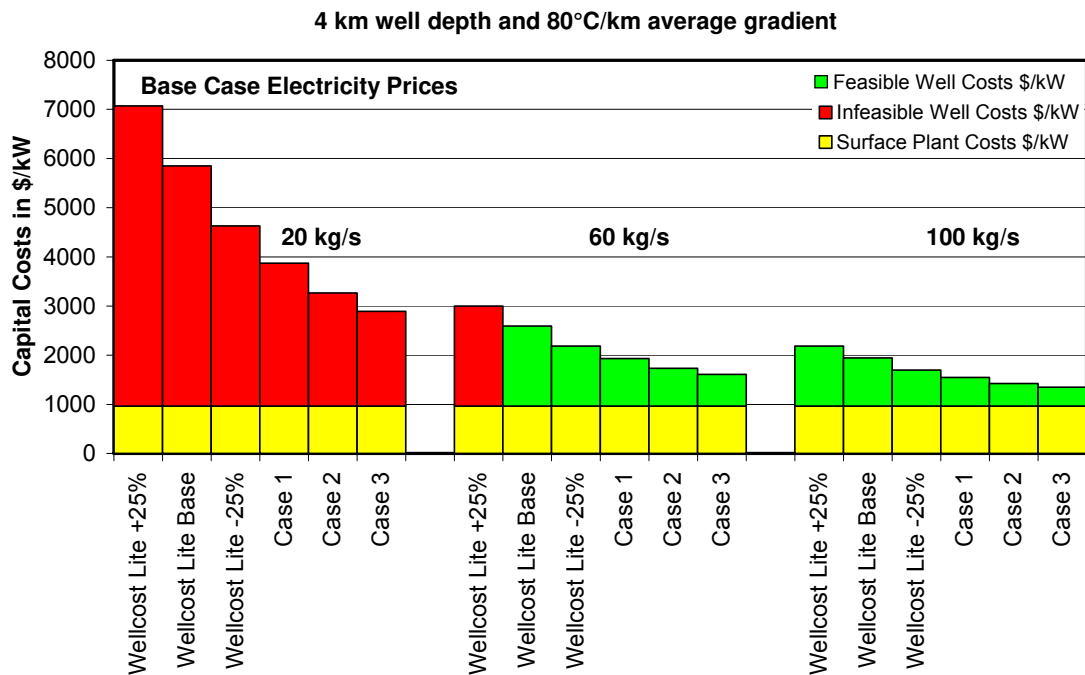
Figure 4.11 Well costs and surface plant costs for different drilling technology cases. Economic feasibility at base case electricity prices indicated by color of bars representing drilling costs.
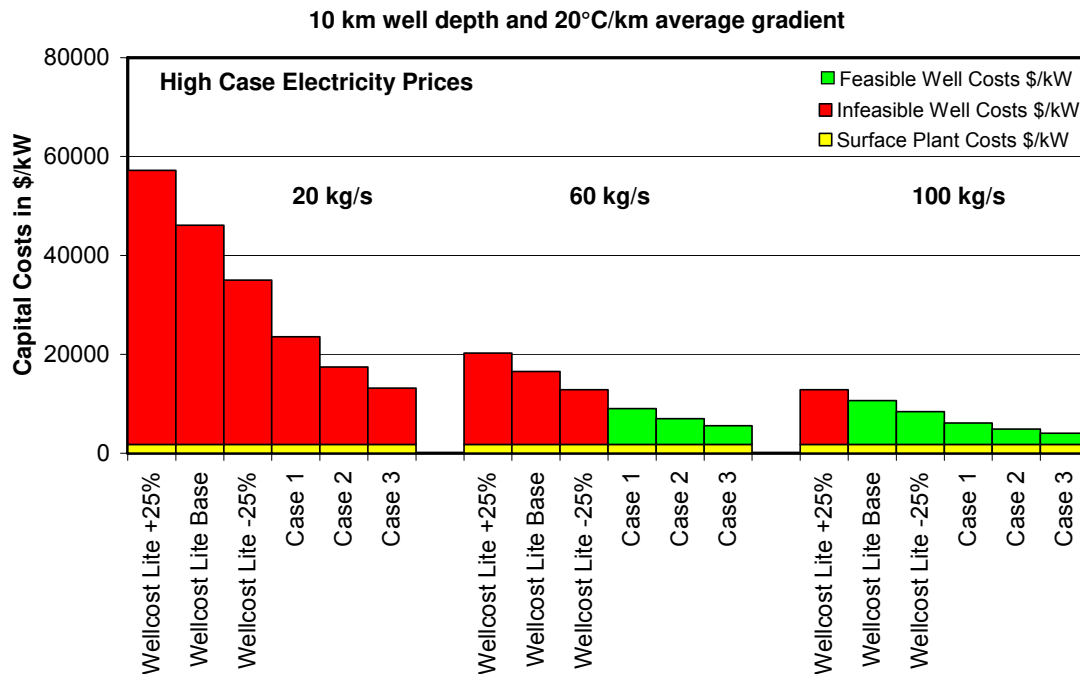
Figure 4.12 Well costs and surface plant costs for different drilling technology cases. Economic feasibility at high case electricity prices indicated by color of bars representing drilling costs.

4.8.2. Effect of Reservoir Technology Advances

Figure 4.10 – Figure 4.12 can also be used to assess the impact of advances in reservoir technology, primarily through increased production flow rates per well, on LEC estimates for EGS. Increased production well flow rates have a significant impact on the economic feasibility of EGS. In fact, even for the highest drilling cost scenario, a production well flow rate of 100 kg/s would permit the higher grade resources to be economically feasible. Increasing well productivity has the same effect as decreasing the number of wells needed to produce a given amount of electricity, which in turn reduces the overall drilling costs. Advances in reservoir technology are needed to provide economically feasible fluid production rates for the full range of EGS resource types. Unlike drilling and well completions, stimulation in EGS reservoirs is still relatively new and untested at a commercial scale, resulting in considerable uncertainty and risk as to its success for enabling sustainable production rates.

4.9. Conclusions

While drilling represents a significant cost component in any EGS development it becomes increasingly important as drilling depths increase for lower gradient resources. Six drilling cost cases with different parameters for flow and resource quality were explored in terms of economic feasibility using an updated version of the MIT EGS model. Three advanced technology drilling cases were developed without a specific technology to study the effects of dramatically lower well costs. The cases cover a range of improvements for mitigating or eliminating some of the factors that lead well costs to increase non-linearly with depth. In the advanced drilling technologies cases, the main cost reducing factors used were single diameter or monobore wells, increased rates of penetration, and reduced casing costs.

To analyze the feasibility of the six drilling cases, two electricity price forecasts to 2050 were developed: a base case scenario and a high price scenario. The base case price scenario predicts 7 cents/kWh in 2050 while the high price scenario predicts 29 cents/kWh, both in year 2007 $. The model runs show that economic feasibility increases considerably with drilling cost reductions. Model results show clearly that drilling costs represent a significant portion of EGS capital costs. As drilling costs are lowered, the ratio between well costs/kW and plant costs/kW decreases, and economic feasibility is achieved.

Well production flow rates are another important performance factor for any EGS project as they are a measure of how well engineered the subsurface is. Field experiments in Soultz, France have achieved flow rates of 25 kg/s (Baria and Petty, 2008) with a clear path to increase them by two to three fold. At a flow of 20 kg/s, economic feasibility is only achieved under high electricity price forecast conditions based on the model. If the flow rate is doubled, base case price feasibility will only be achieved for the very highest grade resources in today's energy markets unless innovation occurs in drilling technology. However, if a three-fold increase in production flow rates is achieved, economic feasibility is attainable under base case price conditions in areas with high average temperature gradients. Accordingly, the first EGS development projects should be focused on those areas.

If the high price scenario proves to be right, then 20-40 kg/s would make it economically feasible to develop EGS resources for a wide range of depths and average temperature gradients. Conversely, only the best EGS resources could be economically developed using today's technology assuming base case electricity costs. Of course, as electricity prices increase, the requirements for economic feasibility are relaxed facilitating wide scale EGS deployment particularly to lower grade areas. As outlined in the high cost electricity scenario, rapidly escalating prices are entirely possible if concerns over global warming caused by fossil fuel emissions continue to increase and lead to enforced energy emissions reductions, if delays occur in the construction of new nuclear facilities, and/or if supply shortages for lower carbon fuels like methane are caused by increasing price and demand. Although not a technical solution, policies that increase electricity costs from conventional fossil fuel and nuclear sources would be beneficial to EGS development.

This analysis shows that capital costs and LECs for EGS power plants can be reduced significantly by advances in drilling technology that decrease drilling costs directly, or by advances in EGS reservoir technology that increase production well flow rates and decrease the number of wells needed. As technology innovations occur to lower cost, and energy and financial markets evolve to lower debt, interest and equity rates of return, it is important to identify and quantify what EGS resource and engineering conditions are likely to produce economic feasibility. Consequently, EGS economic analysis needs to be continually updated with respect to technical advances and project costs.

4.10. References

Augustine, C., J. W. Tester, B. J. Anderson, S. Petty and B. Livesay (2006). "A Comparison of Geothermal with Oil and Gas Well Drilling Costs." Proceedings, Thirty-First Workshop on Geothermal Reservoir Engineering, Stanford University, Stanford, CA, January 30-February 1.

Baria, R. and S. Petty (2008). "Economic and Technical Case for Commercial Exploitation of EGS." Proceedings, Thirty-Third Workshop on Geothermal Reservoir Engineering, Stanford University, Stanford CA, January 28-30.

Cummings, R. G. and G. E. Morris (1979). "Economic Modeling of Electricity Production from Hot Dry Rock Geothermal Reservoirs: Methodology and Analyses." Electric Power Research Institute, Palo Alto, CA, EA-630.

Geddes, C. J. and H. B. Curlett (2006). "Leveraging a New Energy Source to Enhance Oil and Oil Sands Production." GRC Bulletin(January/February): 32-36.

Hardie, R. W. (1981). "BICYCLE II: A Computer Code for Calculating Levelized Life-Cycle Costs." Los Alamos National Laboratory, Los Alamos, NM, (November). LA-8909.

Herzog, H. J., J. W. Tester and M. G. Frank (1997). "Economic Analysis of Heat Mining." Energy Sources **19**(1): 19-33.

Mansure, A. J., S. J. Bauer and B. J. Livesay (2005). "Geothermal Well Cost Analyses 2005." Geothermal Resources Council Transactions **29**: 515-519.

Polizzotti, R. S., L. L. Hirsch, A. B. Herhold and M. D. Ertas (2003). Hydrothermal Drilling Method and System. U.S. Patent No. 20030121701.

Potter, R. M. and J. W. Tester (1998). Continuous Drilling of Vertical Boreholes by Thermal Processes: Including Rock Spallation and Fusion. US Patent No. 5,771,984.

Tester, J. W., B. J. Anderson, A. S. Batchelor, D. D. Blackwell, R. DiPippo, E. M. Drake, J. Garnish, B. Livesay, M. C. Moore, K. Nichols, S. Petty, M. N. Toksoz and R. W. Veatch (2006). "The Future of Geothermal Energy." MIT, Cambridge, MA, INL/EXT-06-11746.

Tester, J. W. and H. J. Herzog (1990). "Economic Predictions for Heat Mining: A Review and Analysis of Hot Dry Rock (HDR) Geothermal Energy Technology." Energy Laboratory, Massachusetts Institute of Technology, Cambridge, MA, MIT-EL 90-001.

Thorsteinsson, H., C. Augustine, B. J. Anderson, M. C. Moore and J. W. Tester (2008). "The Impacts of Drilling and Reservoir Technology Advances on EGS Exploitation." Proceedings, Thirty-Third Workshop on Geothermal Reservoir Engineering, Stanford University, Stanford, CA, Janurary 28-30.

4.11. Appendix

Table A.1 MIT EGS model LEC results: Wellcost Lite +25% Drilling Scenario.

Levelized Electricity Cost (LEC) (cents/kWh): Wellcost Lite +25%						
Depth	Temp Gradient	Production Well Flow Rate (kg/s)				
(km)	(°C/km)	20	40	60	80	100
3	30	249.9	157.6	140.4	155.3	226.9
3	40	115.3	62.4	47.5	41.0	38.2
3	50	60.9	32.6	23.9	20.0	17.8
3	60	35.1	19.6	14.4	12.1	10.8
3	70	23.0	13.3	10.1	8.5	7.7
3	80	16.8	10.1	7.8	6.7	6.1
3	90	13.2	8.1	6.5	5.6	5.1
3	100	11.0	6.9	5.6	4.9	4.5
4	30	165.6	85.6	63.4	53.9	49.3
4	40	70.9	37.6	26.5	21.4	18.6
4	50	36.2	20.0	14.6	11.9	10.4
4	60	22.9	13.1	9.9	8.3	7.3
4	70	16.9	9.9	7.6	6.5	5.8
4	80	13.1	7.9	6.1	5.3	4.7
4	90	10.4	6.4	5.0	4.3	3.9
5	20	350.2	181.5	143.2	131.0	133.3
5	30	111.5	57.9	40.1	31.5	27.2
5	40	46.0	24.9	17.9	14.4	12.3
5	50	26.3	14.8	11.0	9.0	7.9
5	60	18.4	10.6	8.0	6.7	5.9
5	70	13.7	8.0	6.1	5.2	4.6
6	20	262.7	133.7	91.4	74.9	67.2
6	30	76.5	40.3	28.2	22.2	18.6
6	40	34.8	19.1	13.8	11.2	9.7
6	50	22.1	12.4	9.2	7.6	6.7
6	60	15.4	8.9	6.7	5.6	4.9
7	20	199.9	102.2	69.6	53.3	44.3
7	30	57.3	30.5	21.6	17.1	14.4
7	40	29.6	16.3	11.9	9.7	8.3
7	50	18.9	10.7	7.9	6.5	5.7
8	20	151.4	77.8	53.3	41.0	33.7
8	30	46.6	25.0	17.8	14.2	12.0
8	40	25.8	14.2	10.4	8.4	7.3
9	10	883.2	444.2	312.6	292.6	311.0
9	20	117.5	60.8	41.9	32.4	26.7
9	30	40.2	21.6	15.5	12.4	10.5
9	40	22.8	12.6	9.2	7.4	6.4
10	10	750.5	377.7	253.4	199.8	187.7
10	20	94.8	49.3	34.2	26.6	22.0
10	30	36.6	19.7	14.1	11.3	9.6

Table A.2 MIT EGS model LEC results: Wellcost Lite Base Case Drilling Scenario.

Levelized Electricity Cost (LEC) (cents/kWh): Wellcost Lite Base Case						
Depth	**Temp Gradient**	**Production Well Flow Rate (kg/s)**				
(km)	**(°C/km)**	**20**	**40**	**60**	**80**	**100**
3	30	217.3	137.5	122.8	136.3	199.6
3	40	100.6	54.8	41.9	36.3	34.0
3	50	53.3	28.8	21.3	17.9	16.0
3	60	30.9	17.5	13.1	11.0	9.9
3	70	20.4	12.0	9.3	7.9	7.1
3	80	15.0	9.2	7.2	6.3	5.7
3	90	11.8	7.5	6.0	5.3	4.8
3	100	9.9	6.4	5.2	4.6	4.2
4	30	142.4	74.0	55.0	46.9	43.1
4	40	61.2	32.7	23.3	18.9	16.6
4	50	31.5	17.7	13.1	10.8	9.4
4	60	20.1	11.7	8.9	7.6	6.7
4	70	14.9	8.9	7.0	6.0	5.4
4	80	11.5	7.1	5.6	4.9	4.4
4	90	9.2	5.8	4.6	4.0	3.7
5	20	298.8	155.2	122.7	112.5	114.8
5	30	95.5	49.9	34.7	27.4	23.8
5	40	39.7	21.8	15.8	12.8	11.0
5	50	22.8	13.1	9.8	8.2	7.2
5	60	16.1	9.4	7.2	6.1	5.5
5	70	11.9	7.2	5.6	4.8	4.3
6	20	223.4	114.0	78.2	64.3	57.8
6	30	65.4	34.7	24.5	19.4	16.3
6	40	29.9	16.7	12.2	10.0	8.7
6	50	19.1	11.0	8.2	6.9	6.1
6	60	13.4	7.8	6.0	5.1	4.5
7	20	169.6	87.0	59.5	45.7	38.1
7	30	49.0	26.3	18.8	15.0	12.7
7	40	25.4	14.2	10.5	8.6	7.5
7	50	16.3	9.4	7.0	5.9	5.2
8	20	128.3	66.3	45.6	35.3	29.1
8	30	39.8	21.6	15.5	12.5	10.7
8	40	22.1	12.4	9.1	7.5	6.6
9	10	745.0	375.1	264.2	247.6	263.5
9	20	99.5	51.8	35.9	27.9	23.2
9	30	34.3	18.7	13.5	10.9	9.3
9	40	19.5	10.9	8.1	6.6	5.8
10	10	632.4	318.7	214.1	169.0	158.9
10	20	80.4	42.1	29.4	23.0	19.1
10	30	31.2	17.0	12.3	9.9	8.5

Table A.3 MIT EGS model LEC results: Wellcost Lite -25% Drilling Scenario.

Levelized Electricity Cost (LEC) (cents/kWh): Wellcost Lite -25%						
Depth	**Temp Gradient**	**Production Well Flow Rate (kg/s)**				
(km)	**(°C/km)**	**20**	**40**	**60**	**80**	**100**
3	30	184.7	117.4	105.2	117.2	172.3
3	40	85.8	47.1	36.3	31.7	29.8
3	50	45.7	25.0	18.7	15.9	14.3
3	60	26.8	15.4	11.7	10.0	9.0
3	70	17.8	10.7	8.4	7.2	6.6
3	80	13.2	8.3	6.6	5.8	5.3
3	90	10.5	6.8	5.6	4.9	4.6
3	100	8.8	5.8	4.8	4.3	4.0
4	30	119.3	62.3	46.6	40.0	36.9
4	40	51.6	27.9	20.1	16.4	14.5
4	50	26.8	15.3	11.5	9.6	8.5
4	60	17.2	10.3	8.0	6.8	6.1
4	70	12.8	7.9	6.3	5.5	5.0
4	80	10.0	6.3	5.1	4.5	4.1
4	90	8.0	5.2	4.2	3.7	3.5
5	20	247.3	129.0	102.3	94.1	96.3
5	30	79.4	41.9	29.4	23.4	20.4
5	40	33.3	18.6	13.7	11.2	9.7
5	50	19.4	11.3	8.6	7.3	6.5
5	60	13.7	8.3	6.4	5.5	5.0
5	70	10.2	6.3	5.0	4.3	4.0
6	20	184.1	94.4	65.0	53.6	48.4
6	30	54.3	29.2	20.8	16.6	14.1
6	40	25.1	14.2	10.6	8.8	7.7
6	50	16.1	9.5	7.3	6.1	5.5
6	60	11.3	6.8	5.3	4.6	4.1
7	20	139.2	71.8	49.3	38.1	31.9
7	30	40.6	22.1	16.0	12.9	11.1
7	40	21.2	12.1	9.1	7.6	6.6
7	50	13.7	8.0	6.2	5.2	4.7
8	20	105.2	54.7	37.9	29.5	24.4
8	30	33.0	18.2	13.2	10.8	9.3
8	40	18.4	10.5	7.9	6.6	5.8
9	10	606.7	305.9	215.9	202.6	215.9
9	20	81.6	42.8	29.9	23.4	19.6
9	30	28.4	15.7	11.5	9.4	8.2
9	40	16.2	9.3	7.0	5.8	5.1
10	10	514.3	259.6	174.7	138.2	130.1
10	20	65.9	34.9	24.5	19.4	16.3
10	30	25.8	14.3	10.5	8.6	7.4

Table A.4 MIT EGS model LEC results: Advanced Drilling Technology Case 1 Scenario.

Levelized Electricity Cost (LEC) (cents/kWh): Advanced Drilling Case 1						
Depth	Temp Gradient	Production Well Flow Rate (kg/s)				
(km)	(°C/km)	20	40	60	80	100
3	30	166.6	106.2	95.4	106.6	157.1
3	40	77.6	42.8	33.1	29.1	27.4
3	50	41.5	23.0	17.3	14.7	13.4
3	60	24.5	14.3	10.9	9.4	8.5
3	70	16.3	10.0	7.9	6.9	6.3
3	80	12.2	7.8	6.3	5.6	5.1
3	90	9.7	6.4	5.3	4.8	4.4
3	100	8.2	5.5	4.6	4.2	3.9
4	30	95.5	50.4	38.0	32.8	30.5
4	40	41.8	23.0	16.8	13.9	12.5
4	50	22.1	13.0	9.9	8.4	7.5
4	60	14.4	8.9	7.0	6.1	5.6
4	70	10.8	6.9	5.6	4.9	4.6
4	80	8.5	5.6	4.6	4.1	3.8
4	90	6.8	4.6	3.8	3.5	3.2
5	20	184.2	96.7	77.2	71.4	73.5
5	30	59.9	32.1	22.8	18.4	16.3
5	40	25.7	14.8	11.1	9.3	8.2
5	50	15.2	9.2	7.2	6.3	5.7
5	60	10.9	6.8	5.5	4.8	4.4
5	70	8.2	5.3	4.3	3.8	3.6
6	20	131.4	68.0	47.3	39.4	35.8
6	30	39.6	21.8	15.9	12.9	11.2
6	40	18.7	11.1	8.5	7.2	6.4
6	50	12.2	7.5	6.0	5.2	4.7
6	60	8.7	5.5	4.4	3.9	3.6
7	20	96.5	50.4	35.1	27.4	23.2
7	30	28.9	16.3	12.1	10.0	8.7
7	40	15.5	9.2	7.2	6.1	5.5
7	50	10.1	6.3	5.0	4.3	3.9
8	20	71.5	37.9	26.7	21.1	17.7
8	30	23.1	13.2	9.9	8.3	7.3
8	40	13.2	7.9	6.2	5.3	4.8
9	10	397.8	201.5	142.8	134.6	144.0
9	20	54.7	29.4	20.9	16.7	14.2
9	30	19.6	11.4	8.6	7.2	6.4
9	40	11.4	6.9	5.3	4.6	4.1
10	10	332.1	168.5	114.0	90.6	85.7
10	20	43.7	23.8	17.1	13.8	11.8
10	30	17.6	10.2	7.7	6.5	5.8

Table A.5 MIT EGS model LEC results: Advanced Drilling Technology Case 2 Scenario.

Levelized Electricity Cost (LEC) (cents/kWh): Advanced Drilling Case 2						
Depth	**Temp Gradient**	**Production Well Flow Rate (kg/s)**				
(km)	**(°C/km)**	**20**	**40**	**60**	**80**	**100**
3	30	148.1	94.7	85.5	95.8	141.6
3	40	69.3	38.5	30.0	26.4	25.0
3	50	37.3	20.8	15.8	13.6	12.4
3	60	22.1	13.1	10.1	8.8	8.0
3	70	14.9	9.3	7.4	6.5	6.0
3	80	11.2	7.3	6.0	5.3	4.9
3	90	9.0	6.0	5.1	4.6	4.3
3	100	7.6	5.2	4.4	4.0	3.8
4	30	81.2	43.2	32.8	28.6	26.7
4	40	35.9	20.1	14.8	12.4	11.2
4	50	19.2	11.5	9.0	7.7	6.9
4	60	12.6	8.0	6.5	5.7	5.2
4	70	9.5	6.3	5.2	4.6	4.3
4	80	7.6	5.1	4.3	3.9	3.6
4	90	6.1	4.2	3.6	3.3	3.1
5	20	150.9	79.7	63.9	59.5	61.5
5	30	49.5	26.9	19.4	15.8	14.1
5	40	21.6	12.7	9.8	8.3	7.4
5	50	13.0	8.1	6.5	5.7	5.2
5	60	9.3	6.1	5.0	4.5	4.1
5	70	7.1	4.7	4.0	3.6	3.3
6	20	105.3	54.9	38.5	32.3	29.6
6	30	32.2	18.1	13.5	11.1	9.7
6	40	15.5	9.5	7.4	6.4	5.8
6	50	10.2	6.5	5.3	4.7	4.3
6	60	7.3	4.8	4.0	3.6	3.3
7	20	76.0	40.2	28.3	22.3	19.1
7	30	23.3	13.5	10.2	8.6	7.6
7	40	12.7	7.8	6.2	5.4	4.9
7	50	8.4	5.4	4.4	3.9	3.6
8	20	55.8	30.0	21.4	17.1	14.6
8	30	18.5	10.9	8.4	7.2	6.4
8	40	10.7	6.7	5.3	4.7	4.3
9	10	302.4	153.8	109.4	103.5	111.2
9	20	42.4	23.2	16.8	13.6	11.7
9	30	15.6	9.3	7.3	6.2	5.6
9	40	9.2	5.7	4.6	4.0	3.7
10	10	250.1	127.5	86.6	69.2	65.7
10	20	33.7	18.8	13.8	11.3	9.8
10	30	13.8	8.3	6.5	5.6	5.0

Table A.6 MIT EGS model LEC results: Advanced Drilling Technology Case 3 Scenario.

Levelized Electricity Cost (LEC) (cents/kWh): Advanced Drilling Case 3						
Depth	Temp Gradient	Production Well Flow Rate (kg/s)				
(km)	(°C/km)	20	40	60	80	100
3	30	138.0	88.5	80.0	89.9	133.1
3	40	64.7	36.1	28.2	24.9	23.7
3	50	34.9	19.6	15.0	13.0	11.9
3	60	20.8	12.5	9.7	8.4	7.8
3	70	14.1	8.9	7.2	6.3	5.9
3	80	10.6	7.0	5.8	5.2	4.8
3	90	8.5	5.8	4.9	4.5	4.2
3	100	7.2	5.0	4.3	3.9	3.7
4	30	72.4	38.7	29.6	25.9	24.4
4	40	32.2	18.2	13.6	11.5	10.4
4	50	17.4	10.6	8.4	7.2	6.6
4	60	11.5	7.5	6.1	5.4	5.0
4	70	8.8	5.9	4.9	4.4	4.2
4	80	7.0	4.8	4.1	3.7	3.5
4	90	5.7	4.0	3.4	3.2	3.0
5	20	129.3	68.6	55.3	51.7	53.7
5	30	42.8	23.6	17.2	14.1	12.7
5	40	19.0	11.4	8.9	7.6	6.9
5	50	11.5	7.4	6.0	5.3	4.9
5	60	8.4	5.6	4.7	4.2	3.9
5	70	6.4	4.4	3.7	3.4	3.2
6	20	87.9	46.3	32.7	27.6	25.4
6	30	27.4	15.7	11.8	9.9	8.7
6	40	13.4	8.4	6.7	5.9	5.4
6	50	8.9	5.9	4.9	4.4	4.1
6	60	6.5	4.4	3.7	3.4	3.1
7	20	62.2	33.3	23.7	18.9	16.3
7	30	19.5	11.6	9.0	7.6	6.9
7	40	10.8	6.9	5.6	4.9	4.6
7	50	7.2	4.8	4.0	3.6	3.4
8	20	45.0	24.6	17.8	14.5	12.4
8	30	15.3	9.3	7.4	6.4	5.8
8	40	9.0	5.8	4.8	4.3	3.9
9	10	236.9	121.0	86.5	82.2	88.6
9	20	33.9	19.0	14.0	11.5	10.0
9	30	12.8	8.0	6.3	5.5	5.0
9	40	7.6	5.0	4.1	3.6	3.4
10	10	193.4	99.2	67.8	54.4	51.9
10	20	26.8	15.3	11.5	9.6	8.4
10	30	11.3	7.1	5.6	4.9	4.5

Chapter 5: Modeling and Analysis of Surface Power Plants

In Chapter 4, an economic modeling approach was used to determine the relative importance of the different components that make up an EGS electric power plant. From this earlier analysis, it was concluded that drilling costs and reservoir productivity were key parameters in determining the economic feasibility of EGS. In this chapter, the remaining major capital cost component for the surface power plant itself is explored. Since the design, construction and operation of surface power plants for hydrothermal resources is already a commercially mature technology constrained by practical thermodynamic limitations, major advances and cost reductions for the power plant like those discussed for drilling and reservoir stimulation technologies are not expected. Nevertheless, the capital costs for a power plant are large enough that even incremental improvements in costs and efficiencies can have a significant impact on overall electricity costs. Therefore, technical models of power plants likely to be used in EGS projects were developed to analyze their performance characteristics. Since a large part of the EGS resource base has a mid- to low temperature gradient, a binary Rankine cycle power plant was chosen for study.

The objective of the study was to test different working fluids in a binary cycle plant that use geofluids ranging from 100-200 ^{o}C as their heat source to determine the optimum working fluid and operating conditions as a function of temperature. Both subcritical and supercritical binary Rankine cycles were modeled and compared. This work was done in collaboration with Randall Field, Ronald DiPippo, and Jeff Tester and will be reported in a forthcoming paper at the 2009 Geothermal Resources Council Annual Meeting in Reno, NV.

5.1. Power Plant Designs for EGS

5.1.1. Conventional Geothermal Power Plants

The design used in conventional geothermal power plants depends on the type and quality of the geothermal resource. The fluid produced from the geothermal reservoir, or geofluid, can range

anywhere from a single phase dry steam to a liquid-dominated two-phase mixture to a pressurized fluid. The power plant design and working fluid choice are matched as well as possible to the resource's characteristic to optimize power production and minimize capital costs. A brief explanation of the most common power plant designs for conventional geothermal systems follows. A much more in-depth discussion of the design, unit processes, and usage of these systems can be found in (DiPippo, 2005).

Dry Steam Plant

In cases where dry steam is produced from a geothermal reservoir, the steam can be expanded directly in a turbine that is connected to a generator to produce electricity. A simplified schematic of a dry steam plant is shown in Figure 5.1. After passing through the turbine, the steam is condensed in a heat exchanger (condenser) and typically reinjected into the reservoir through an injection well. The type of cooling system used with the condenser depends on the location of the plant. If the plant is located close to a large body of water, such as a river or sea, then it can be used as a source of cooling water for the condenser. Another option is cooling towers, which evaporate part of the steam condensate to generate cooling water, and are very common in dry steam and flash plants. The design for a dry steam plant is the simplest and least expensive of all conventional geothermal plant designs. However, their use is limited, as relatively few dry steam fields exist in the world. Wells at Larderello, Italy, The Geysers, California and Matsukawa, Japan are well known examples of dry steam production and utilization.

Single Flash Steam Plant

A single-stage flash steam plant, shown schematically in Figure 5.2, is very similar in design to a dry steam plant, except that the geofluid feed to the plant is a two-phase liquid-vapor mixture. A two-phase mixture occurs when the pressure of the geofluid drops to its saturation pressure and partially flashes to produce a vapor phase. The flashing can occur in the reservoir formation, in the wellbore, or by isentropic expansion across a valve used to control the pressure and flow rate of the geofluid to the plant. The geofluid is fed to a cyclone separator where the liquid and vapor are separated. The saturated liquid is reinjected while the steam vapor is expanded in a turbine,
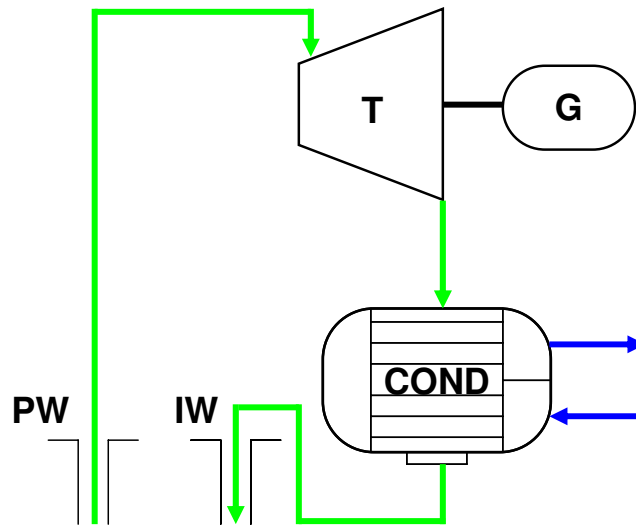
Figure 5.1 Schematic of dry steam plant. Geofluid flow path is shown in green, cooling water in blue (T = turbine, G = generator, COND = condenser, PW = production well, IW = injection well).

condensed and then reinjected into the reservoir as in a dry stream plant. The remainder of the geofluid leaves the cyclone separator as a liquid and eventually rejoins the condensate from the condenser before being reinjected into the reservoir. The single flash steam plant is the most conventional of all the power plant designs and is widely used throughout the geothermal industry.
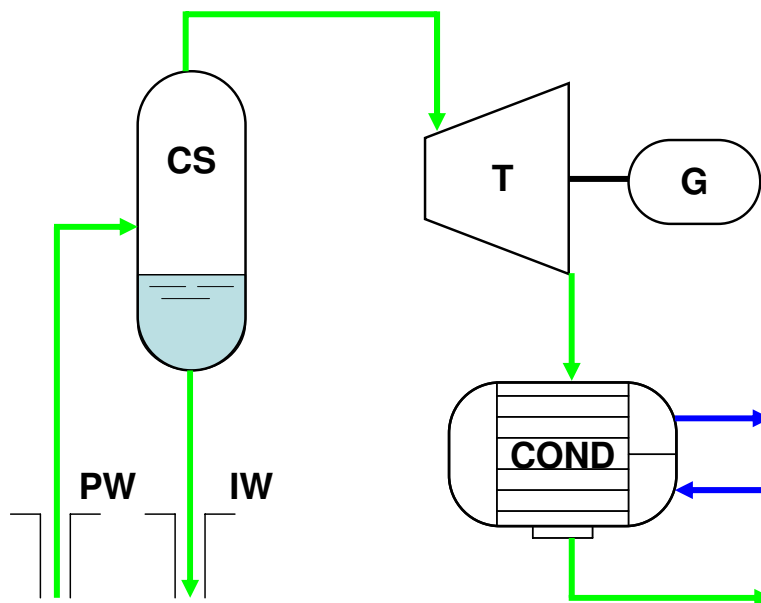

Figure 5.2 Schematic of single flash steam plant. Geofluid flow path is shown in green, cooling water in blue (CS = cyclone separator, T = turbine, G = generator, COND = condenser, PW = production well, IW = injection well).

Double Flash Steam Plant

A double-stage flash steam plant, shown in Figure 5.3, is a single flash steam plant in which the condensate from the cyclone separator is sent to a lower pressure flash tank, where the fluid again flashes into liquid and vapor components. The lower-pressure steam is admitted into the turbine at the appropriate stage and is used to generate more electricity. Because it produces a greater amount of steam, a double flash steam plant is more efficient and produces more power than a single flash steam plant. However, a double flash plant is also more complex, more costly, and requires more maintenance. Another consideration that must be taken into account when choosing a plant design is the amount of minerals, such as silica, dissolved in the geofluid. During the flashing processes, the minerals remain in the liquid phase, so their concentrations increase. At the same time, their solubility decreases as the geofluid temperature decreases. If their concentration becomes too high and/or the geofluid temperature becomes too low, the minerals will precipitate on flash vessels, piping, or other equipment. The number of times the geofluid can be flashed, as well as the flash temperature, can be limited by the presence of minerals.
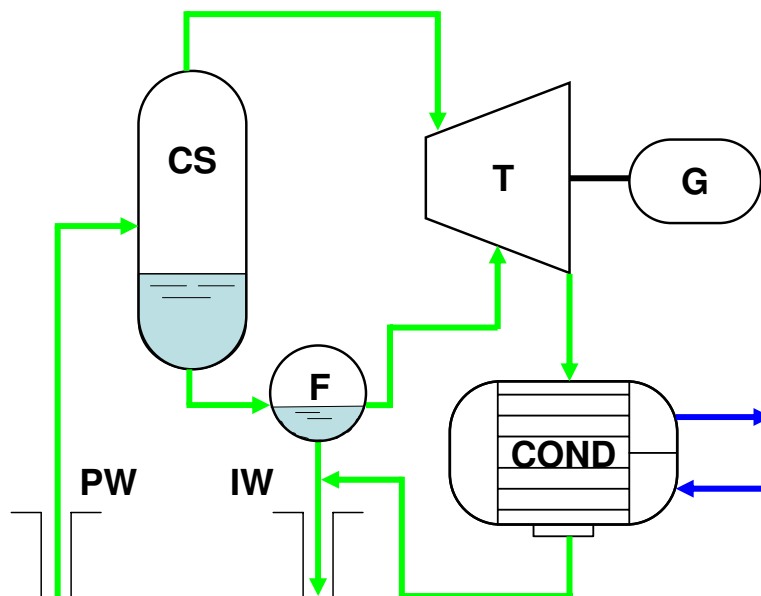

Figure 5.3 Schematic of double flash steam plant. Geofluid flow path is shown in green, cooling water in blue (CS = cyclone separator, F = flash tank, T = turbine, G = generator, COND = condenser, PW = production well, IW = injection well).

Binary Cycle Plant

A binary cycle operates much like a conventional coal or nuclear fired Rankine cycle. The geofluid is not used to power the turbine directly as in a dry steam or flash plant. Instead, a heat exchanger is used to transfer thermal energy from the geofluid to a working fluid circulating in a closed loop cycle. The process is shown in Figure 5.4. A pressurized working fluid evaporates in the heat exchanger, expands in the turbine to produce power in the generator, condenses in the condenser, and is re-pressurized in the condensate feed pump and sent back to heat exchanger. Working fluids are chosen based on how well their thermodynamic properties match the geofluid and heat rejection conditions. Often, a simple hydrocarbon, such as isopentane is used. These systems are often referred to as organic Rankine cycle (ORC) plants.
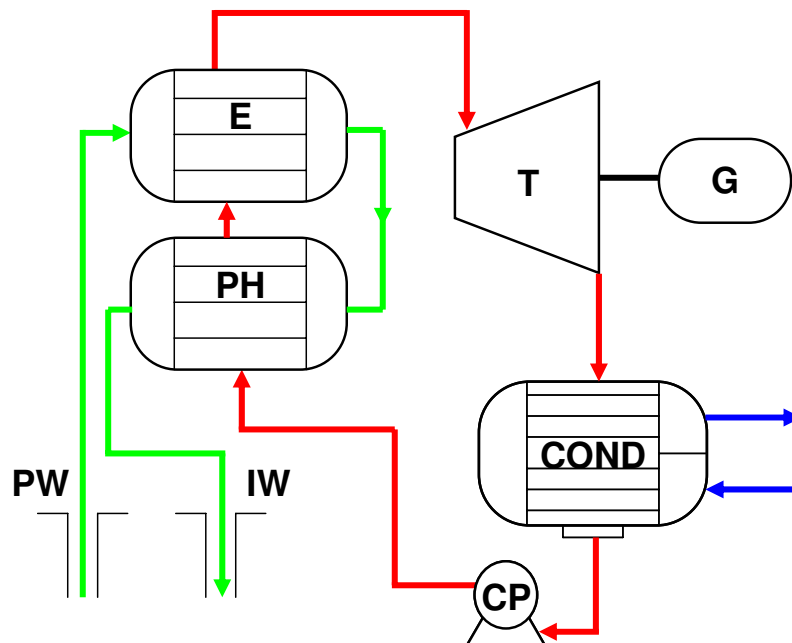
Figure 5.4 Schematic of binary cycle plant. Geofluid flow path is shown in green, working fluid in red, cooling water in blue (PH = preheater, E = evaporator, T = turbine, G = generator, COND = condenser, CP = condensate pump, PW = production well, IW = injection well).

Binary cycle plants are used for mid- to low temperature geothermal resources, generally 150 $^{\circ}$C or less, where flashing the steam is either impractical or economically not viable. They are also used to avoid scaling in a system when the geofluid has a large concentration of dissolved minerals. Typically, the geofluid is produced as a pressurized liquid and does not undergo any phase change while passing through the heat exchanger. Unlike dry steam and flash plants, binary cycle plants do not have steam condensate available for use in an evaporative cooling

tower. If there is a not a cooling water source available for condensing the working fluid, an air cooled condenser is used. The use of air cooled condensers with binary cycle plants is common in arid locations.

In terms of number of units, binary plants are the most widely used type of geothermal power plant. However, they make up a small percentage of total geothermal power produced, due to their smaller sizes and their tendency to be used for lower temperature resources (DiPippo, 2005).

5.1.2. Use of Binary Cycle Plants in EGS

Based on the temperature distribution of EGS resources, it is anticipated that the majority of EGS power plants will use binary cycles. As Figure 1.3 shows, most of the thermal energy stored in the earth's crust to a total depth of 10 km under the U.S. is at a temperature of 200 $^{\circ}$C or less. This is especially true if access to the EGS resource is limited to reservoirs relatively close to the surface at depths of 6 km and less. Geothermal resources at temperatures of 150 $^{\circ}$C and less are too low to use a flash system and will require binary power plants (DiPippo, 2005). The transition from binary to flash plants in terms of overall economics occurs around 200 $^{\circ}$C (Tester et al., 2006). However, when downhole pumps are used, as will likely be the case with many EGS production wells to increase productivity, it generally does not make thermodynamic sense to use the pressurized liquid flow to operate a flash system.

An important feature of any thermal cycle is the heat rejection system. The first EGS resources to be developed will be those in areas that have high temperature gradients, such as the Southwest U.S. In these regions, air cooled condensers will be frequently used to reject heat as cooling water will be too expensive or unavailable. The fans required to force air through the air-cooled condensers require additional power to operate. The high capital costs and parasitic fan power losses associated with air cooled condensers negatively affect the plant's economic performance by lowering power output and increasing busbar costs.
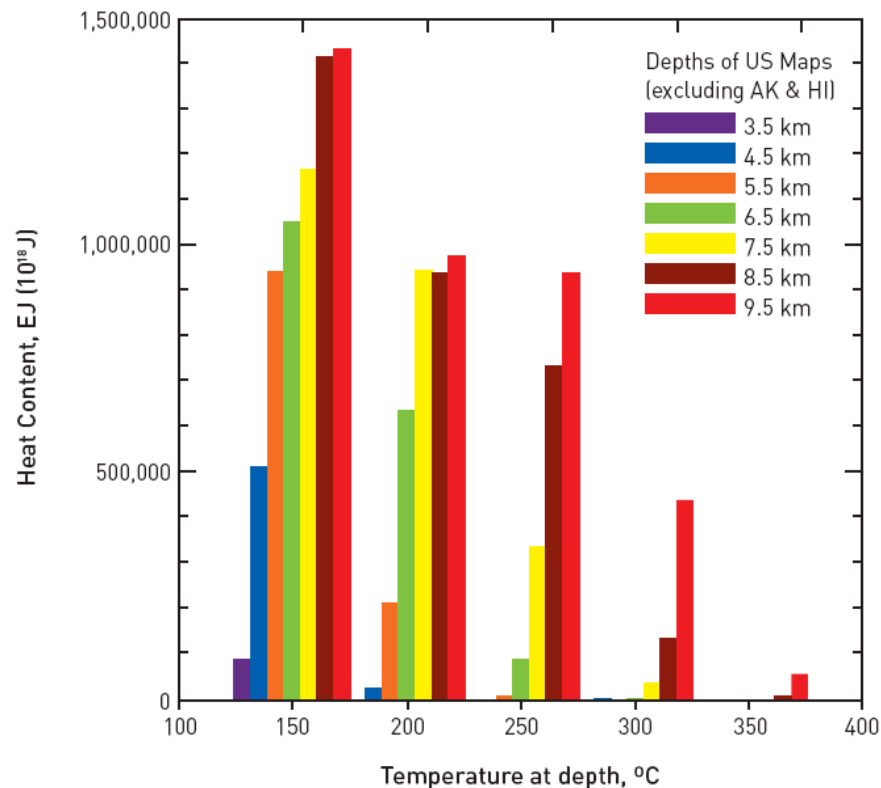
Figure 5.5 Histogram of total heat content as thermal energy contained in 1 km-thick slices over the entire US area (from Tester et al., 2006)

5.2. Study Objectives and Approach

The objective of this study was to optimize binary organic Rankine cycles for use with EGS resources by determining the optimum working fluid and plant operating conditions for electric power plants using geofluids ranging in temperature from 100 to 200 ^{o}C as a heat source.

Models of subcritical and supercritical binary Rankine cycle power plants were developed using Aspen Plus 2006 simulation software. A wide range of candidate working fluids were selected and tested in the model. To reflect the large number of resources in the mid- to low-temperature range, geofluid temperatures ranging from 100-200 ^{o}C were modeled at 10 ^{o}C intervals. The operating conditions for the working fluid in the binary plant were divided into two categories – subcritical and supercritical. In the supercritical case, the working fluid is pressurized above its critical pressure and heated to temperatures above its critical temperature, which gives it a thermodynamic advantage by lowering the average temperature gradient between process

streams in the primary heat exchanger. Air cooled condensers were incorporated into the model to assess their impact on thermodynamic performance. Simulations determined the optimum operating conditions for each working fluid as a function of geofluid (or resource) temperature for both subcritical and supercritical binary Rankine cycle power plants. The best working fluid in the subcritical and supercritical cycles was identified for each geofluid temperature interval, and the results were compared.

5.3. Model Specification and Approach

5.3.1. Efficiency Definitions

The efficiency of any thermal power plant can be defined several different ways. The two most commonly used definitions are the thermal efficiency and utilization efficiency.

Thermal Efficiency

The thermal efficiency, η_{th}, is derived from the First Law of thermodynamics, which states that the heat entering a steady state closed cycle must equal the net work produced plus the heat rejected so that energy is conserved. The thermal efficiency, η_{th}, is defined as the ratio of the net power output from the cycle to the rate of heat input to the cycle:

$$\eta_{th} = \frac{\dot{W}_e}{\dot{Q}_{in}} \qquad\qquad \text{Eq. (5-1)}$$

where:
$$\dot{W}_e = \text{net work from cycle}$$
$$\dot{Q}_{in} = \text{net heat entering cycle}$$

The thermal efficiency represents the amount of thermal energy entering the cycle that is converted to useful work. The limiting value of η_{th} is governed by the second law of thermodynamics based on a reversible cycle. Typical thermal efficiencies for operating binary power plants range from 10-13% (DiPippo, 2005).

Utilization Efficiency

The utilization efficiency is based on the Second Law of thermodynamics and incorporates the exergy, or availability, of the incoming geofluid stream. The geofluid exergy, $\dot{E}_{geo}$, is the maximum amount of useful power that can be derived from the geofluid by an ideal steady state power cycle, operating reversibly and rejecting heat to the ambient (dead state) at temperature and pressure T_o and P_o, respectively:

$$\dot{E}_{geo} = \dot{m}\left[h_{geo} - h_o - T_o\left(s_{geo} - s_o\right)\right] \qquad \text{Eq. (5-2)}$$

where:
$$h = \text{specific enthalpy}$$
$$s = \text{specific entropy}$$
$$\dot{m} = \text{mass flow rate of geofluid}$$

The utilization efficiency, η_u, is defined as the ratio of net power output from the cycle to the exergy of the geofluid entering the plant:

$$\eta_u = \frac{\dot{W}_e}{\dot{E}_{geo}} \qquad \text{Eq. (5-3)}$$

η_u represents how much useful work is derived from the process in relation to the maximum amount of work that is theoretically possible. In practice, the utilization efficiency never exceeds 1.0 or 100%, due to inefficiencies and irreversibilities in the cycle. Inefficiencies result from friction among moving parts, pressure losses in piping and equipment, the irreversible expansion of the working fluid through the turbine, and the irreversible flow of heat across finite temperature differences between streams in the heat exchangers.

5.3.2. Subcritical Rankine Cycle

Figure 5.6 shows the temperature-enthalpy diagram for a basic subcritical binary plant, shown schematically in Figure 5.4. The plant is referred to as subcritical because as the working fluid never exceeds both its critical temperature and pressure during the cycle. An examination of Figure 5.6 reveals some of the irreversibilities that prevent the utilization efficiency defined in Eq. (5-3) from reaching its maximum theoretical value. For example, in the turbine, an isentropic expansion would lead the working fluid cycle path from point 3 to point 4s. In reality, the expansion is not isentropic, and the path terminates at a higher specific enthalpy and entropy

Figure 5.6 Temperature-enthalpy diagram for a basic subcritical binary plant with temperature-heat transfer curves for preheater, evaporator, and condenser included.

at point 4. The ratio of the actual work extracted by the turbine to the work from isentropic expansion is the turbine efficiency, η_t:

$$\eta_t = \frac{h_4 - h_3}{h_{4s} - h_3}$$
Eq. (5-4)

Turbine efficiencies of 85% or better are common for modern turbines.

Further efficiency losses come from the transfer of heat from the geofluid to the working fluid in the preheater and evaporator. Heat transfer from high to low temperatures is an irreversible process. Ideally, heat could be transferred "reversibly" across an infinitely small temperature gradient, δT. This is not possible, not only because it would require an infinitely large heat exchanger, but also because the subcritical working fluid undergoes a constant temperature phase transition from liquid to vapor in the evaporator. Meanwhile, the geofluid decreases in temperature as it transfers heat to vaporize the working fluid. This leads to a minimum temperature difference, or pinch point, where the geofluid exits the evaporator and the working fluid enters, indicated in Figure 5.6. Likewise, a pinch point occurs at the working fluid exit of the preheater. The pinch temperature in the center of the preheater/evaporator system makes large temperature differences, especially at the working fluid exit of the evaporator, unavoidable

for the subcritical binary plant. These large temperature differences lower the cycle's utilization efficiency and the amount of work that can be derived from the geofluid.

5.3.3. Supercritical Rankine Cycle

The critical pressure is the pressure at which the isobar of a pure fluid intersects its saturation curve at only one point. Above this pressure, supercritical fluids do not undergo phase transitions during heating because their isobars do not pass through the saturation curve. Instead, the density transitions continuously from liquid-like to vapor-like as temperature increases.

A supercritical Rankine cycle takes advantage of the properties of supercritical fluids to increase its overall efficiency by lowering the average temperature gradient across process streams in the primary heat exchanger. The temperature-enthalpy diagram for a supercritical Rankine cycle is shown in Figure 5.7. The steps in a supercritical Rankine cycle are identical to those of the subcritical cycle shown in Figure 5.4, except that a separate preheater and evaporator are not needed. Instead, heat transfer occurs inside a single heat exchanger. Because there is no phase change, the temperature change of the working fluid is continuous and the heat exchanger and fluid flows can be designed so that the temperature paths of the geofluid and working fluid are nearly parallel, as illustrated in Figure 5.7. This leads to smaller, more nearly constant temperature difference and reduces the irreversibility of the heat transfer step and should lead to a higher utilization efficiency.
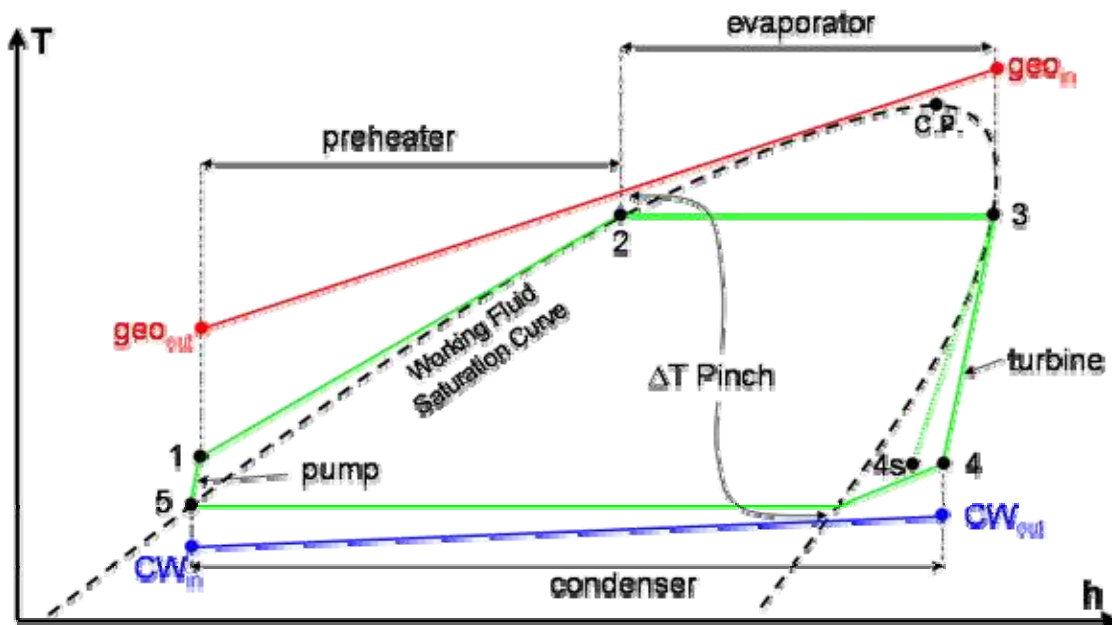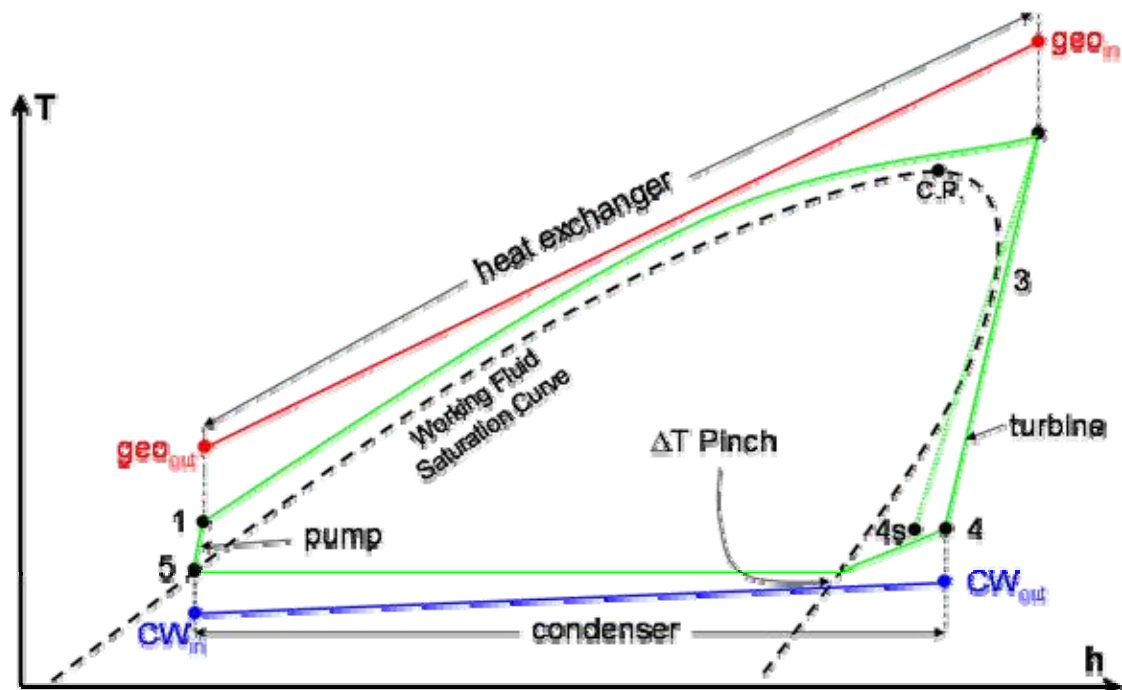
Figure 5.7 Temperature-enthalpy diagram for a basic supercritical binary plant with temperature-heat transfer curves for the primary heat exchanger and condenser included.

Despite its thermodynamic advantages, there are drawbacks to the supercritical cycle. The higher pressures required to achieve supercritical pressures lead to higher parasitic pump power requirements. Also, the pump, heat exchanger, turbine, and connection tubing require thicker walls to contain the pressure, which drive up their costs. Modeling of the process is needed to determine if the advantages of using a supercritical cycle outweigh these disadvantages.

5.4. Model Development

5.4.1. Binary Cycle Designs

The process flow diagrams used in modeling of the sub- and supercritical binary cycles are shown in Figure 5.8 and Figure 5.9, respectively. In the subcritical case, there are two heat exchangers that the working fluid passes through: the pre-heater (PH), where it is heated to a saturated liquid, and the evaporator (E), where it undergoes a phase transition from liquid to vapor. In the supercritical case, only a single heat exchanger (E) is used to transfer thermal energy to the single-phase supercritical working fluid. Since many EGS will be built in areas where water resources are scarce, an air-cooled condenser (ACC) was used in the design. The

Figure 5.8 Process flow diagram for subcritical binary Rankine cycle power plant.

Figure 5.9 Process flow diagram for supercritical binary Rankine cycle power plant.

parasitic power requirements of the ACC fans are subtracted from the gross power output of the turbine/generator, which decreases the overall utilization efficiency of the cycle. In both cases, the designs incorporate a recuperator (RECUP) that is used to transfer heat from the working fluid exiting the turbine/generator (T/G) to working fluid that has been condensed and pressurized in the feed pump (CP) before it enters the preheater. The recuperation step reduces the cooling load on the condenser and improves overall plant performance.

5.4.2. Working Fluid Selection and Properties

Candidate working fluids to be used in the model were selected based on the geofluid temperature and pressure operating conditions in the Rankine cycle using results from a previous study on power cycles (Khalifa and Rhodes, 1985) and the experience of the collaborating researchers. A range of organic fluids conventionally used in binary plants, along with some novel fluids and refrigerants, was desired. The working fluids chosen, along with their critical temperature and pressure, are shown in Table 5.1. Ten fluids were used for the subcritical cycle and seven for the supercritical cycle. Three of the fluids were excluded from supercritical trials because either their critical temperature or pressure was considered too high to be practical.

Table 5.1 Critical temperatures and pressures of candidate working fluids used in Aspen simulations of binary cycle plants utilizing geofluids with temperatures ranging from 100 to 200 °C.

Working fluid	Cycle Type	Critical Temperature (°C)	Critical Pressure (bar)
Propane (C_3H_8)	Sub- & supercritical	96.7	42.5
Isobutane (i-C_4H_{10})	Sub- & supercritical	134.7	36.4
N-Pentane (n-C_5H_{12})	Sub- & supercritical	196.6	33.7
Isopentane (i-C_5H_{12})	Sub- & supercritical	187.3	33.8
R-32	Sub- & supercritical	78.1	57.8
R-134a	Sub- & supercritical	101.0	40.6
R-245fa	Sub- & supercritical	154.1	36.4
Cyclopentane	Subcritical	238.6	45.1
Ammonia	Subcritical	132.4	113.5
Toluene	Subcritical	318.6	41.1

The *PVT* (volumetric) thermodynamic properties of these fluids were based on the Benedict-Webb-Rubin-Starling (BWRS) equation of state (EOS). The BWRS property method in Aspen is based on the Benedict-Webb-Rubin-Starling equation of state with optional pure-component

and binary interaction parameters. The BWRS property model is comparable to Peng-Robinson and Redlich-Kwong-Soave for phase equilibrium calculations, but is more accurate for liquid molar volume and enthalpy calculations. It is suited for reduced temperatures (T/T_{cr}) as low as 0.3 and reduced densities (ρ/ρ_{cr}) as great as 3.0. This EOS has eleven pure-component parameters along with binary interaction parameters. These parameters can be obtained from multi-property (vapor-liquid equilibrium, enthalpy, PVT, etc.) data regressions for higher fidelity. If pure-component parameters are not supplied, they are estimated with correlations proposed by Starling. The primary source for the EOS parameters is the Design Institute for Physical Properties (DIPPR). The geofluid in the model simulations is assumed to be pure water. The Steam Tables were used for water properties and are based on the ASME 1967 steam table correlations.

5.4.3. Model Design Specifications and Parameters

The geofluid mass flow rate used for all simulations was 100 kg/s, so that the results can be compared on a common basis. In the subcritical case, the flow rate of the working fluid is varied so that it leaves the evaporator (E) as a saturated vapor. Superheated vapor turbine inlet conditions were not considered. Likewise, the model requires the working fluid to leave the preheater (PH) as a saturated liquid. The pinch temperature in the evaporator is set at 5 ^{o}C and occurs at the working fluid entrance. It is not known a priori where the pinch temperature in the preheater will occur, so the log-mean temperature difference (LMTD) is restricted 5 ^{o}C or greater. In the supercritical case, the location of the pinch temperature is also unknown a priori, so the main heat exchanger (E) LMTD is set to 10 ^{o}C. Pressure drops in all heat exchangers were assumed to be negligible.

The turbine (T) isentropic efficiency is assumed to be 85%, which is a reasonable value for dry expansions. In practice, when the working fluid exits the turbine as a partially condensed two-phase fluid, the efficiency suffers. The drop in efficiency is estimated using the Baumann rule, which subtracts 1% in efficiency for each 1% of average moisture content in the turbine. Although the turbine can withstand some amount of liquid, the turbine exit vapor fraction is limited to 90% to prevent erosion of the blades. For the supercritical case, the turbine expansion

path was examined to ensure that the working fluid did not pass through the critical point or the saturated liquid line. The generator (G) efficiency is assumed to be 98%.

The recuperator (RECUP) is only useful when the working fluid exiting the turbine is superheated, or above its saturation temperature. The model takes this into consideration, and only "turns on" the recuperator when the temperature of the working fluid exiting the turbine is 10 $^{\circ}$C higher than the temperature of the working fluid leaving the feed pump. The pinch temperature in the recuperator is set to 5 $^{\circ}$C.

The pinch temperature difference in the ACC was set at 10 $^{\circ}$C. The air flow through the air cooled exchanger was specified such that the air temperature rise is exactly half of the temperature difference between the working fluid condensing temperature and the ambient air temperature. This rule was developed based on the results from running multiple cases using the Aspen HTFS heat exchanger design program for air cooled exchangers. It was found that this rule of thumb minimized capital costs for the air cool condenser. Similarly, the parasitic power to run the fans in the air cooled condenser was very nearly constant and equal to 0.25 kW per kg/s of air flow through the ACC. This was used as a fixed parameter during cycle optimization and then validated once the best cycles were determined. The value was sufficiently accurate, in the worst case being only 7% in error. The ambient, or dead state, temperature was assumed to be 20 $^{\circ}$C for all cases. It was also assumed that the ACC sub-cooled the working fluid by 2 $^{\circ}$C. Finally, the efficiency of the condensate pump (CP) was assumed to be 80% for all cases. Parasitic losses from the geofluid injection pump (IP) were not included. A summary of the parameters and design specifications used by the simulation is given in Table 5.2.

5.4.4. Optimization Strategy

The optimum operating conditions for the binary cycle models were found by maximizing the utilization efficiency, η_u, during simulations. The utilization efficiency was chosen as the optimization parameter because η_u measures the extent to which the available thermodynamic potential of the geofluid is put to practical use. For completeness, the cycle thermal efficiency was also calculated and reported.

Table 5.2 Summary of fixed parameters, design specifications, and optimization variable parameters used in sub- and supercritical binary cycle models.

Fixed Parameters/Design Specifications	Value/Range Selected for Study
General	
Geofluid Inlet Temperature	100-200 ^{o}C (10 ^{o}C intervals)
Geofluid Pressure	20 bar
Geofluid mass flow rate	100 kg/s
Ambient Air Temperature	20 ^{o}C
Primary Heat Exchangers – Subcritical Case	
Preheater LMTD	$\geq$5 ^{o}C
Evaporator Pinch	5 ^{o}C
Preheater Working Fluid Exit	Saturated Liquid
Evaporator Working Fluid Exit	Saturated Vapor
Primary Heat Exchangers – Supercritical Case	
Primary Heat Exchanger LMTD	$\geq$10 ^{o}C
Turbine	
Isentropic Efficiency	85% for all vapor <85% when liquid present (Baumann rule)
Exit Vapor Quality	$\geq$95%
Expansion Path (Supercritical Case)	Cannot pass through critical point or saturated vapor curve
Generator Efficiency	98%
Recuperator (used when ΔT hot-cold inlets $\geq 10\ ^{o}C$)	
Pinch Temperature	5 ^{o}C
Condenser	
Pinch Temperature	$\geq$ 10 ^{o}C
Power Requirements	0.25 kW per kg/s air flow
ΔT Air	½ ($T_{WF\ dewpt} - T_{air}$)
Working Fluid Subcooling	2 ^{o}C
Condensate Pump	
Efficiency	80%

Optimization Variable Parameters	Range
Subcritical Case	
Turbine Inlet Pressure	$P_r \leq 0.9$
Condenser Dewpoint Temperature	T_{air} + 10-20 ^{o}C
Supercritical Case	
Turbine Inlet Pressure	$1.1 \leq P_r \leq 3.0$
Condenser Dewpoint Temperature	T_{air} + 10-20 ^{o}C
ΔT hot inlet/cold outlet	5-30 ^{o}C

For the subcritical binary plant cases, the optima were found by varying the turbine inlet and outlet pressures to maximize utilization efficiency. Since there is only one degree of freedom for a pure fluid undergoing a phase change, varying the turbine outlet pressure/condenser pressure is equivalent to varying the dewpoint temperature in the condenser. As mentioned above, the working fluid flow rate is determined by the design specification of saturated vapor exiting the evaporator (E). This is not the case for the supercritical cycles, since no phase transition occurs. In the supercritical cases, in addition to the parameters varied in the subcritical case, the working fluid mass flow rate is used indirectly as an optimization parameter. The temperature difference between primary heat exchanger hot (geofluid) inlet and cold (working fluid) outlet is varied between 5-30 $^{\circ}$C, and then the working fluid flow rate is adjusted to meet the 10 $^{\circ}$C LMTD constraint. Varying the heat exchanger hot inlet/cold outlet temperature difference instead of the mass flow rate directly prevents temperature crossover errors in the heat exchanger calculation and facilitates simulation convergence. For the subcritical case, the turbine inlet pressure was limited to a reduced pressure of $P_r = P/P_c \leq 0.9$, where P_c is the critical pressure. For the supercritical case, the turbine inlet pressure was limited to $P_r \geq 1.1$. These limitations were imposed to avoid calculations in the critical region around $P_r \approx 1.0$, where the thermodynamic properties predicted by the BWRS EOS tend to have large errors. The simulation carries out the optimization strategy using the "Optimization" tool in the model analysis toolbox in Aspen. The optimization strategy is summarized in the bottom of Table 5.2.

5.5. Results – Subcritical Binary Cycle

The operating conditions that yielded the thermodynamic optima for the subcritical binary cycle shown in Figure 5.8 were found for ten candidate working fluids at geofluid temperatures ranging from 100-200 $^{\circ}$C in 10 $^{\circ}$C intervals, subject to the parameters, design specifications, and optimization strategy in Table 5.2 using Aspen simulation software. The resulting maximum utilization efficiency values for these optimum operating conditions are shown Figure 5.10.
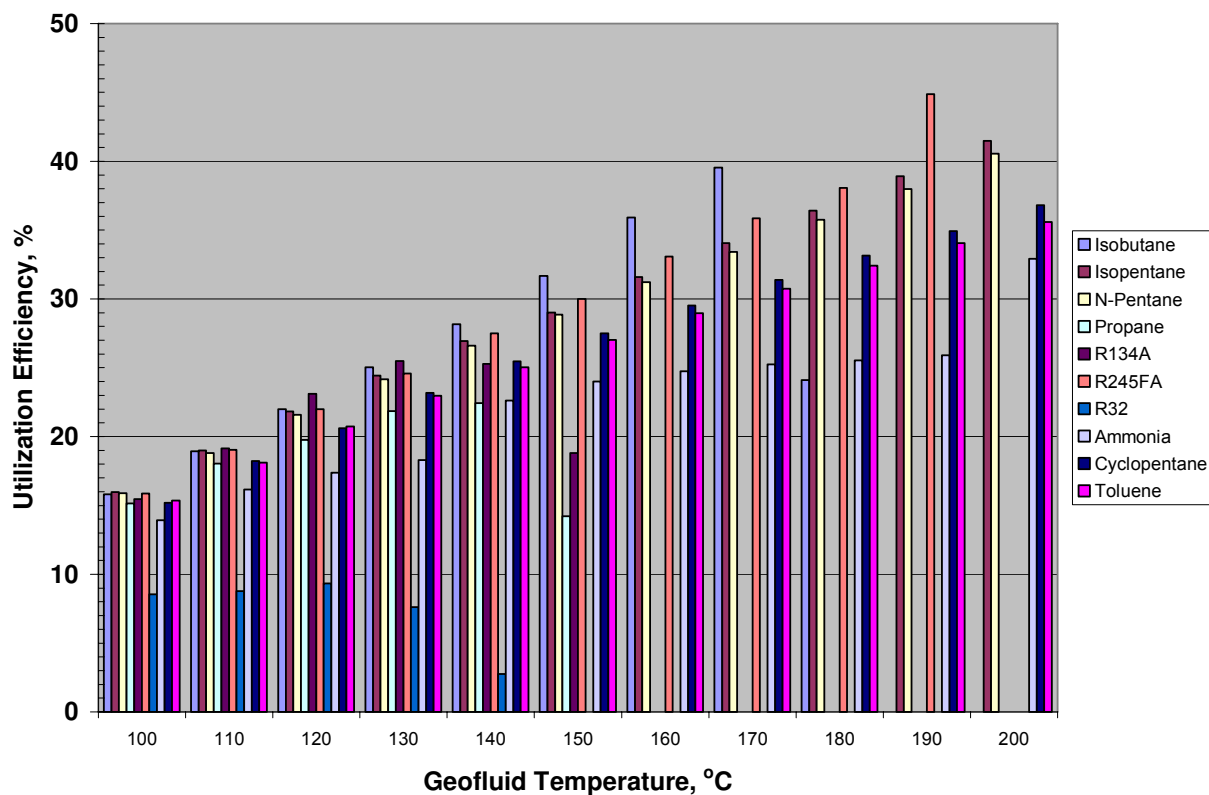
Figure 5.10 Maximum utilization efficiency at optimized operating conditions as a function of geofluid temperature for candidate working fluids in subcritical binary cycle.

Table 5.3 gives a summary of the results for the subcritical turbine inlet pressure cycles for the optimum cycle/working fluid combinations at each geofluid temperature. There are four different working fluids that yield the best utilization efficiency depending on the geofluid temperature. Isopentane is best at 100 and 200 ^{o}C; R134a is best from 110-130°C; isobutane is best from 140-170°C; and R245fa is best at 180-190°C. As the geofluid temperature increases, some cycle simulations of particular working fluids, such as isobutane and R-134a, did not converge to a feasible solution because of the 5 ^{o}C pinch temperature and saturated vapor design specifications on the evaporator (E). As the geofluid temperature increases, it becomes impossible for some fluids to maintain the specified approach temperatures without temperature crossover occurring in the preheater (PH). Either widening the pinch or permitting superheated vapor to enter the turbine would allow the simulations to find solutions for those cases compatible with the laws of thermodynamics. However, this would have required optimizing another degree of freedom in the subcritical simulations. Therefore, analyses were not carried out for those cases.

Table 5.3 Operating conditions and results for optimum cycle/working fluid combinations as a function of geofluid temperature for subcritical binary plant simulations with a 100 kg/s geofluid mass flow rate.

Geofluid Temp.	Working fluid	Turbine inlet pressure		W.F. mass flow rate	Thermal power input	RECUP heat load	Turbine power	Pump power	ACC fan power	Net power	Utilization efficiency	Thermal efficiency
(^{o}C)		(bar)	P_r	(kg/s)	(MW$_t$)	(MW$_t$)	(MW$_e$)	(MW$_e$)	(MW$_e$)	(MW$_e$)	(%)	(%)
100	i-C$_5$H$_{12}$	3.74	0.11	30.9	11.84	0.65	1.03	0.02	0.39	0.62	16.0	5.2
110	R-134a	28.83	0.71	94.7	17.38	0	1.65	0.20	0.53	0.93	19.2	5.3
120	R-134a	29.36	0.72	136.7	25.27	0	2.48	0.30	0.82	1.36	23.1	5.4
130	R-134a	29.61	0.73	180.7	33.31	0	3.27	0.40	1.09	1.78	25.5	5.4
140	i-C$_4$H$_{10}$	18.88	0.52	70.9	26.76	1.47	3.39	0.24	0.84	2.31	28.2	8.6
150	i-C$_4$H$_{10}$	22.19	0.61	82.0	31.43	1.83	4.37	0.34	1.03	3.00	31.7	9.6
160	i-C$_4$H$_{10}$	24.92	0.68	100.0	38.33	2.15	5.50	0.47	1.14	3.89	35.9	10.2
170	i-C$_4$H$_{10}$	24.98	0.69	124.0	47.78	2.72	6.94	0.59	1.50	4.85	39.5	10.2
180	R-245fa	16.06	0.44	220.1	48.63	3.43	6.91	0.29	1.37	5.25	38.1	10.8
190	R-245fa	22.27	0.61	248.9	56.41	4.19	9.09	0.47	1.72	6.90	44.9	12.2
200	i-C$_5$H$_{12}$	14.66	0.43	112.8	48.68	8.17	9.11	0.31	1.73	7.07	41.5	14.5

The simulation results were validated by using a "brute force" sensitivity study to vary the turbine inlet pressure systematically. At each geofluid temperature interval, the simulation maximized the utilization efficiency by varying the turbine outlet pressure. The sensitivity study results were then compared to the optimum results found by the model which varied both the inlet and outlet turbine pressures simultaneously. Isopentane was chosen as the working fluid. The results are shown in Figure 5.11. The sensitivity analysis shows that the utilization efficiency does not vary strongly as a function of turbine inlet pressure near its maximum for each temperature interval, and that the curves become flatter as geofluid temperatures increase. In each case, the optimum operating conditions found by the optimization strategy return utilization efficiencies within tenths of a percent of the maximum indicated by using the sensitivity analysis, but in a single simulation run. The figure validates that the simulation is effective at finding the operating conditions that maximize the utilization efficiency for each geofluid temperature interval for a given working fluid.
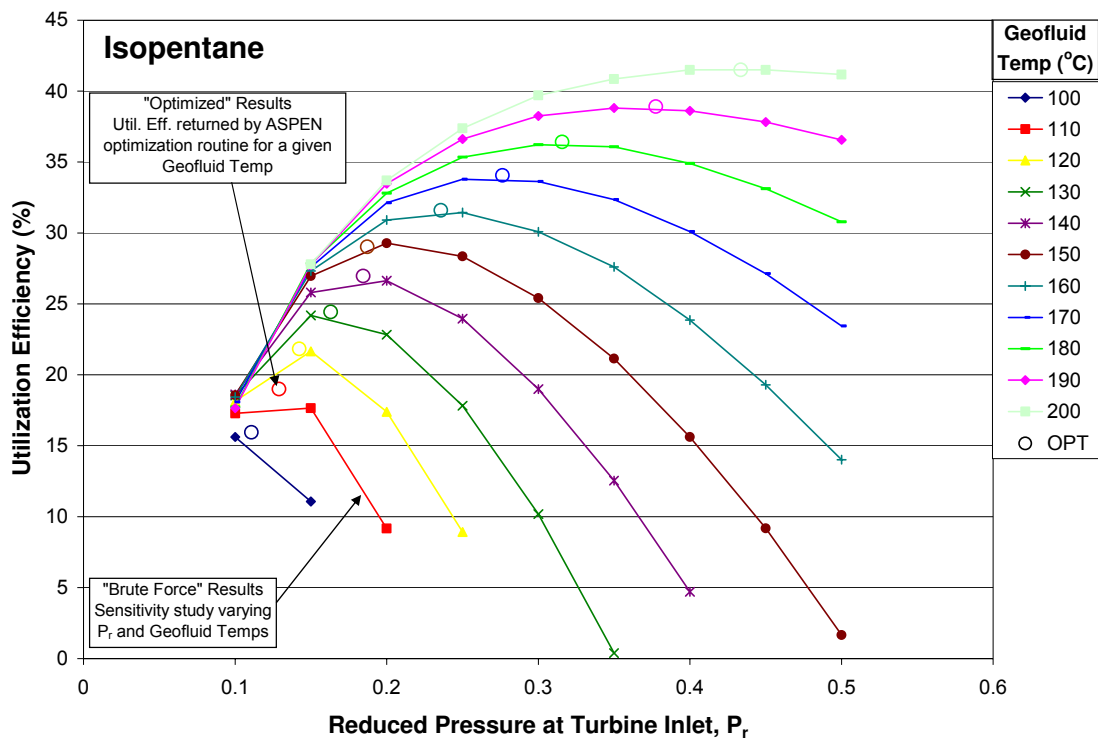
Figure 5.11 Utilization efficiencies determined by sensitivity analysis compared to maximum utilization efficiency found by full optimization strategy simulation for isopentane. The optimum point found by the full simulation is shown as an open circle "○".

The optimum utilization efficiency increases roughly linearly with the geofluid temperature up to 170°C, as shown in Figure 5.12, varying from about 16% at 100 °C to nearly 40% at 170 °C. The peculiar behavior at higher temperatures is caused by changes in the best working fluid that are a consequence of the temperature constraints imposed on the heat exchangers, as explained above.

The various power loads are shown in Figure 5.13. The points represent the optimum conditions for each geofluid temperature and correspond to various cycle working fluids. The condensate pump (CP) power is relatively small since the pressure rise across the pump is small. However, even the best performance is quite poor at low geofluid temperatures since the parasitic power requirements represent a large percentage of the gross turbine power. Table 5.4 shows three representative cases of optimum results. The total parasitic power requirements amount to roughly 40% of the gross power at 100°C, 31% at 150°C, and 22% at 200°C.
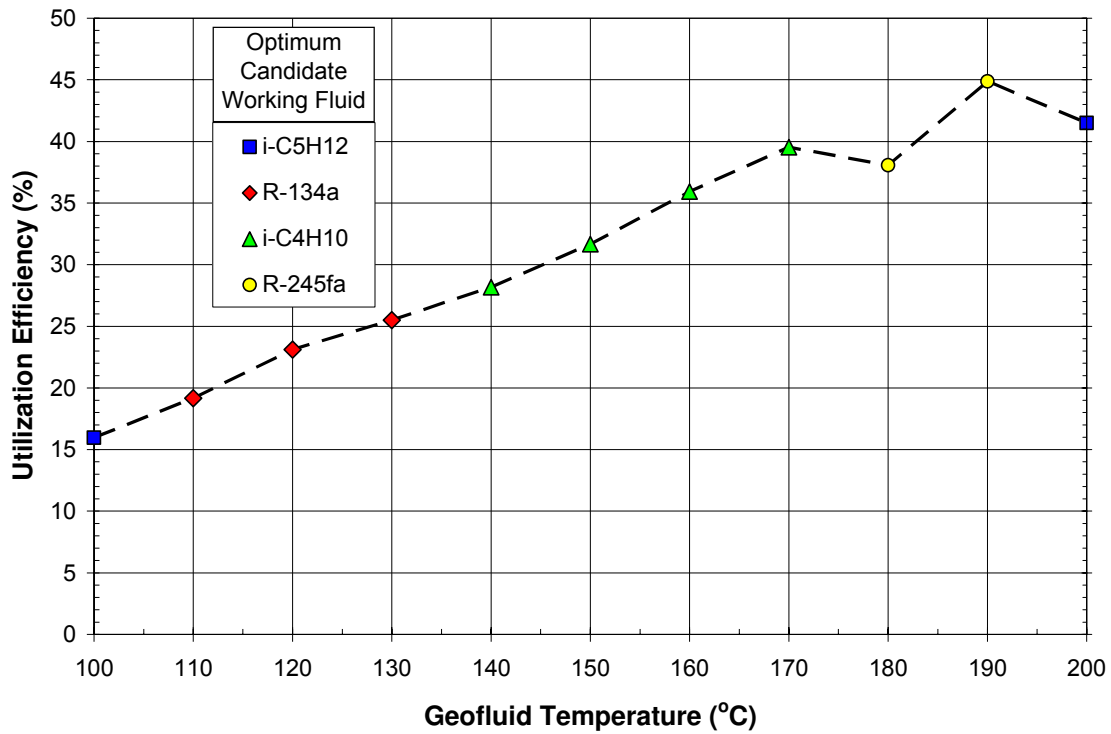
Figure 5.12 Maximum utilization efficiency found for subcritical binary cycle among 10 candidate working working fluids as a function of geofluid temperature.
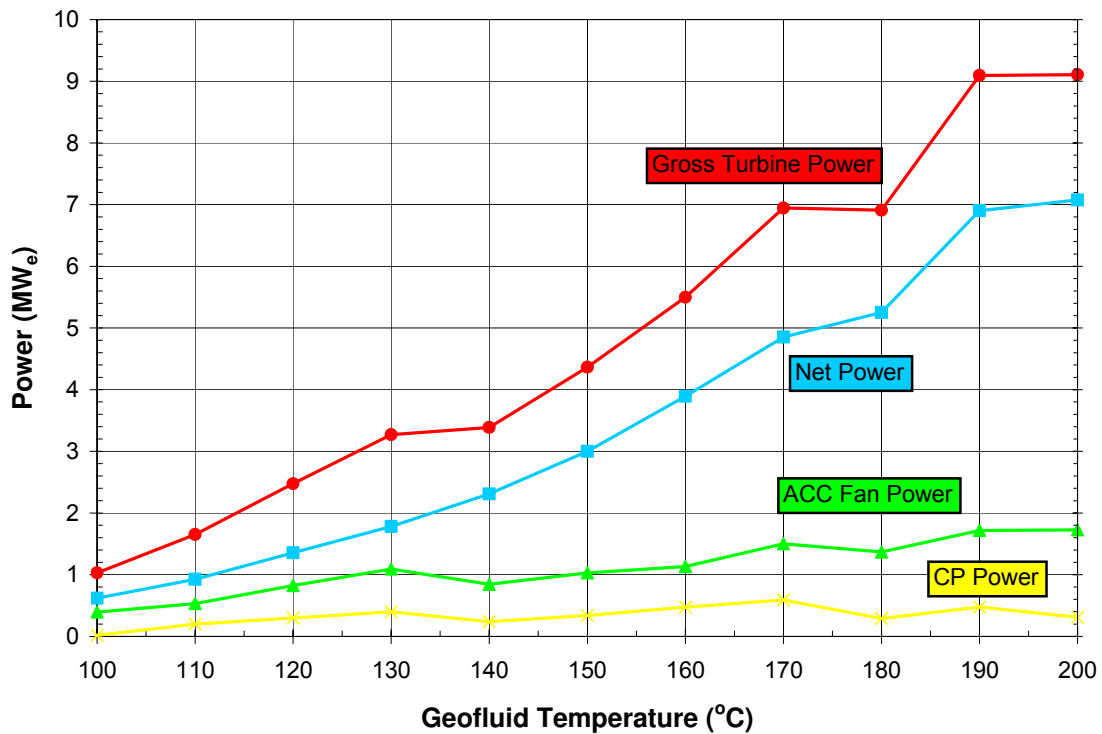

Figure 5.13 Variation of gross turbine power, condensate pump power, ACC fan power, and net power with geofluid temperature for subcritical cycles.

Table 5.4 Effect of parasitic power requirements on net power for subcritical cycles.

Power	Working Fluid/Geofluid Temperature		
(MW$_e$)	i-C$_5$H$_{12}$ @ 100°C	i-C$_4$H$_{10}$ @ 150°C	i-C$_5$H$_{12}$ @ 200°C
Gross	1.028	4.366	9.108
Pump	0.016 (1.6%)	0.338 (7.7%)	0.309 (3.4%)
ACC fans	0.394 (38.3%)	1.028 (23.5%)	1.725 (18.9%)
Net	0.619	3.000	7.074

Lastly, the thermal efficiency for the subcritical case was examined. It was found that the best thermal efficiency often occurred with working fluids other than those that produced the best utilization efficiency at a given geofluid temperature. Except for isopentane at 100 and 200 °C, the working fluids that yielded the best thermal efficiency were different from those that gave the best utilization efficiency. The thermal efficiency results are depicted in Figure 5.14.
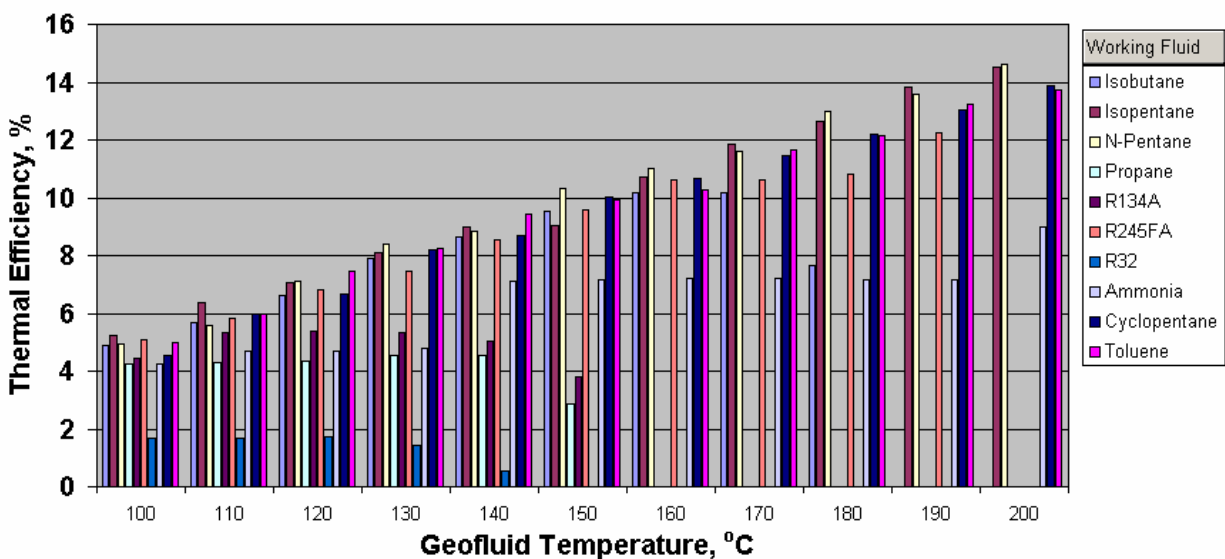
Figure 5.14 Thermal efficiency as a function of geofluid temperature for subcritical cycles using ten different candidate working fluids.

5.6. Results – Supercritical Binary Cycle

The operating conditions that yielded the thermodynamic optima for the supercritical binary cycle shown in Figure 5.9 were found for seven candidate working fluids at geofluid temperatures ranging from 100-200 °C in 10 °C intervals, subject to the parameters, design specifications, and optimization strategy in Table 5.2 using Aspen simulation software. The

resulting maximum utilization efficiency values for these optimum operating conditions are shown in Figure 5.15.

Figure 5.15 Maximum utilization efficiency at optimized operating conditions as a function of geofluid temperature for candidate working fluids in supercritical binary cycle.

Table 5.5 presents a summary of the results for the supercritical turbine inlet pressure cycles for the optimum cycle/working fluid combinations at each geofluid temperature. As in the subcritical case, no single working fluid emerges as the best one over the entire temperature range. Instead, the simulations show that the refrigerant R-32 is the best working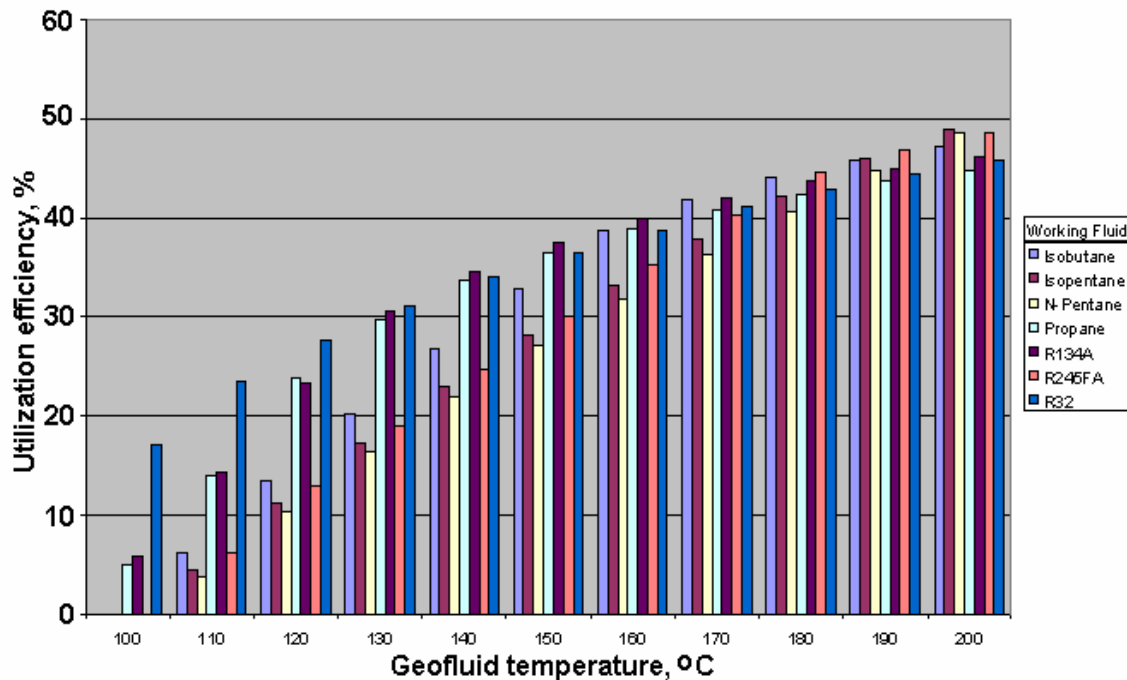 fluid for geofluid temperatures of 100-130 $^{\circ}$C; R-134a is best for 140-170 $^{\circ}$C; isobutane is best for 180 $^{\circ}$C; and R-245fa is best for 190-200 $^{\circ}$C. For the 180 and 200 $^{\circ}$C cases, R245fa and isopentane, respectively, yielded the highest utilization efficiency but they failed the turbine quality criterion by either crossing through the saturated liquid line or near the critical point during expansion in the turbine. However, the differences between the maximum utilization efficiencies for those working fluids and the ones shown in Table 5.5 are very small.

As for the subcritical binary cycle, the optimum utilization efficiency is a strong function of the geofluid temperature, as can be seen from Figure 5.16, varying from about 17% at 100°C to nearly 49% at 200°C.

Table 5.5 Operating conditions and results for optimum cycle/working fluid combinations as a function of geofluid temperature for supercritical binary plant simulations with a 100 kg/s geofluid mass flow rate.

Geofluid Temp.	Working fluid	Turbine inlet pressure		W.F. mass flow rate	Thermal power input	RECUP heat load	Turbine power	Pump power	ACC fan power	Net power	Utilization efficiency	Thermal efficiency
(^{o}C)		(bar)	P_r	(kg/s)	(MW$_t$)	(MW$_t$)	(MW$_e$)	(MW$_e$)	(MW$_e$)	(MW$_e$)	(%)	(%)
100	R-32	63.6	1.10	53.8	14.64	NA	1.41	0.29	0.45	0.66	17.1	4.5
110	R-32	63.6	1.10	72.4	21.3	NA	2.21	0.40	0.68	1.13	23.5	5.3
120	R-32	70.6	1.22	87.0	26.15	NA	3.02	0.56	0.84	1.62	27.6	6.2
130	R-32	80.1	1.39	100.6	30.59	NA	3.93	0.78	0.97	2.17	31.1	7.1
140	R-134a	45.8	1.13	148.7	31	1.98	4.43	0.58	1.02	2.83	34.5	9.1
150	R-134a	52.5	1.29	168.3	35.36	2.73	5.43	0.78	1.10	3.56	37.5	10.1
160	R-134a	57.4	1.41	186.9	39.99	3.96	6.61	0.96	1.32	4.33	40.0	10.8
170	R-134a	69.2	1.70	204.9	44.26	4.36	7.85	1.30	1.39	5.16	42.0	11.7
180	i-C$_4$H$_{10}$	48.6	1.34	128.9	51.28	2.24	9.04	1.32	1.64	6.08	44.1	11.9
190	R-245fa	43.4	1.19	247.7	56.81	1.44	9.93	0.96	1.76	7.21	46.9	12.7
200	R-245fa	47.8	1.31	253.5	59.21	4.07	11.23	1.09	1.84	8.30	48.7	14.0
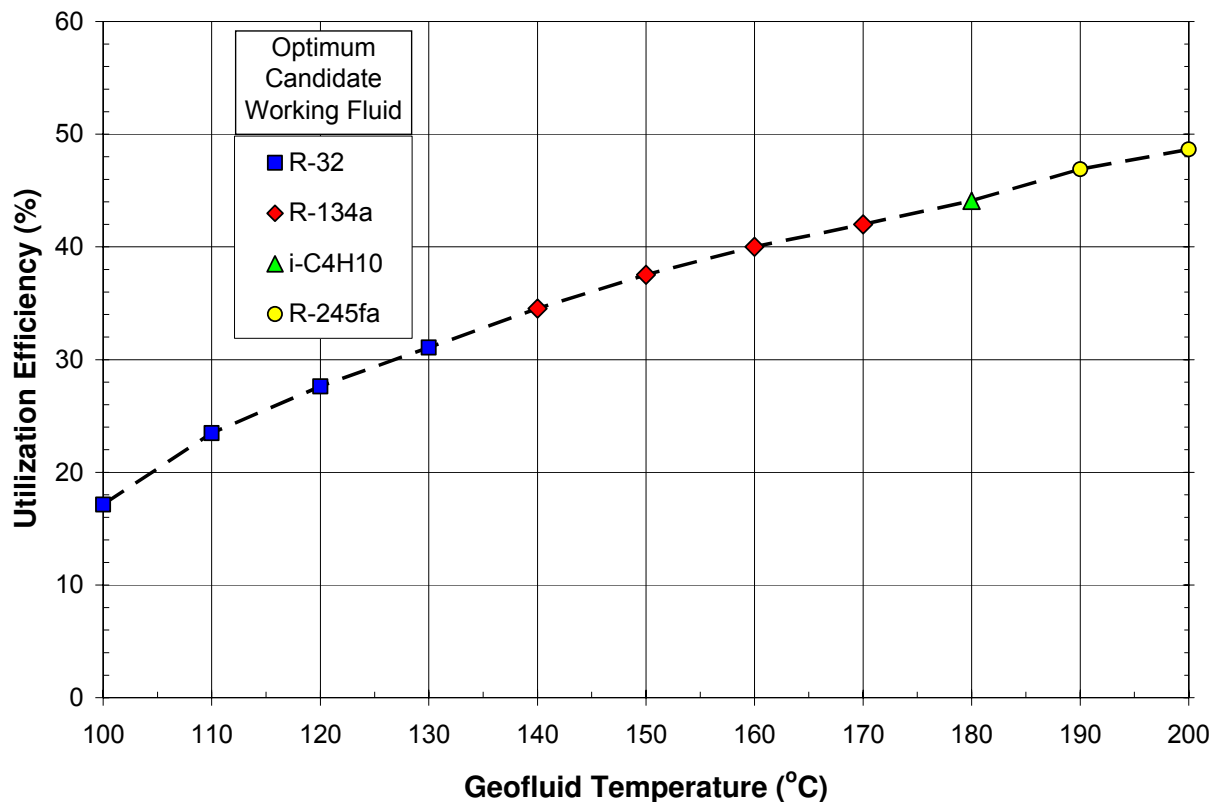
Figure 5.16 Maximum utilization efficiency found for supercritical binary cycle among 10 candidate working working fluids as a function of geofluid temperature.

The various power terms are shown in Figure 5.17. The points represent the optimum conditions for each geofluid temperature and correspond to various cycle working fluids. Compared to the subcritical case, the condensate pump requirements are much higher, requiring almost as much power as the ACC fans. Once again, parasitic power requirements as a fraction of gross power generated leads to poor overall performance at the low end of the temperature spectrum. Table 5.6 shows three representative cases of optimum results. The total parasitic power requirements amount to 53% of the gross power at 100°C, 34% at 150°C, and 26% at 200°C. These are significantly higher than for the subcritical case (Table 5.4), due almost entirely to the condensate pump requirements.
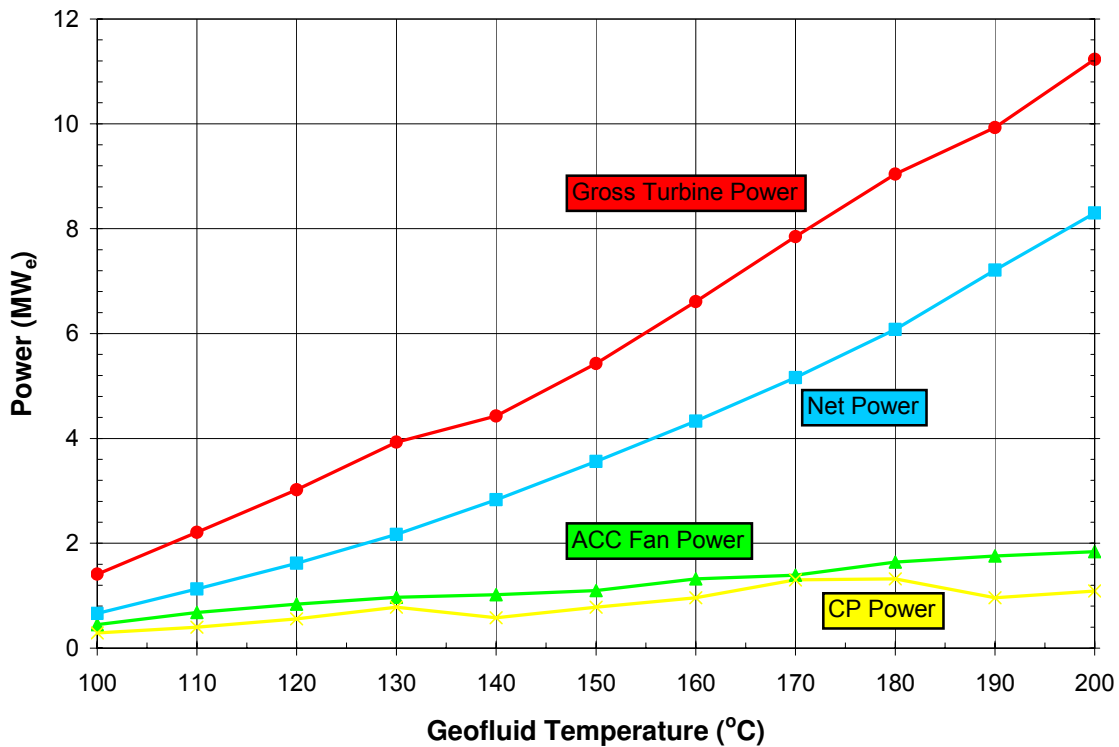
Figure 5.17 Variation of gross turbine power, condensate pump power, ACC fan power, and net power with geofluid temperature for supercritical cycles.

Table 5.6 Effect of parasitic power requirements on net power for supercritical cycles.

Power	Working Fluid/Geofluid Temperature		
(MW$_e$)	R32 @ 100C	R134a @ 150C	R245fa @ 200C
Gross	1.41	5.43	11.23
Pump	0.29 (21%)	0.78 (14%)	1.09 (10%)
ACC fans	0.45 (32%)	1.10 (20%)	1.84 (16%)
Net	0.66	3.56	8.30

The thermal efficiency for each of the simulations in Figure 5.15 is shown in Figure 5.18. It should be emphasized that the results shown in Figure 5.18 were not obtained by maximizing the thermal efficiency, but are a consequence of maximizing the utilization efficiency. As with the utilization efficiency, the thermal efficiency is also a strong function of the geofluid temperature, varying from about 4.5% at 100 $^{\circ}$C to slightly over 14% at 200 $^{\circ}$C. In terms the thermal efficiency, R-32 is the best working fluids from 100-110 $^{\circ}$C, and either R-124a or propane has the highest thermal efficiency at all other temperatures considered. Isobutane becomes nearly as good as propane and R134a as a working fluid at the highest end of the temperature range.
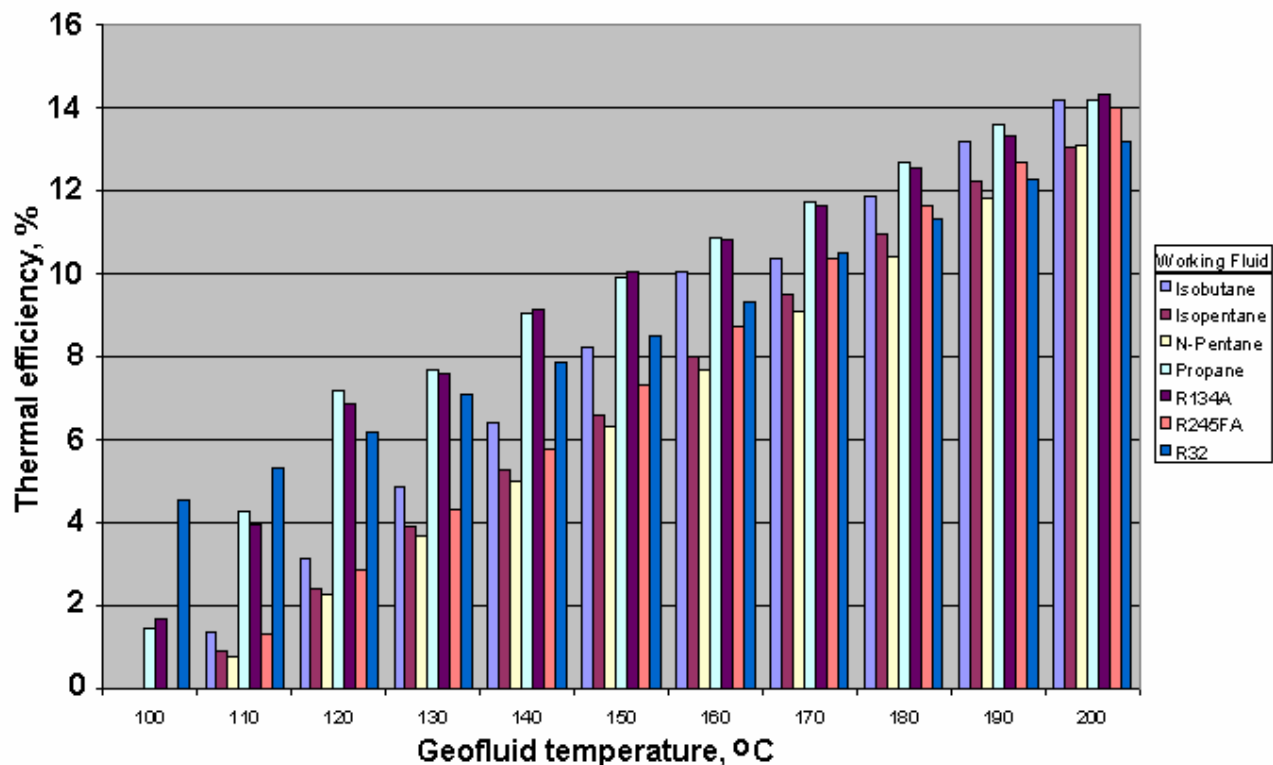
Figure 5.18 Thermal efficiency as a function of geofluid temperature for supercritical cycles using seven different candidate working fluids.

5.7. Discussion

5.7.1. Thermal vs. Utilization Efficiency

In both the sub- and supercritical cases, the working fluid that gave the highest utilization efficiency at each temperature interval did not necessarily have the highest thermal efficiency. The justification for choosing the utilization efficiency as the optimization parameter is

illustrated by Figure 5.19, which shows the thermal and utilization efficiencies, net power, and thermal heat input to a subcritical isopentane binary cycle with a geofluid temperature of 150 °C as a function of turbine inlet pressure. The thermal efficiency is only evaluated on the amount of thermal energy the cycle removes from the geofluid stream and is not discounted for available thermal energy left behind in the geofluid by the cycle. The thermal efficiency increases with pressure because the definition of thermal efficiency favors a high vaporization temperature in the evaporator that allows the cycle to preferentially take a smaller amount of thermal energy at a higher temperature and leaves the rest in the geofluid so that the thermal heat input into the cycle in the denominator of Eq. (5-1) decreases faster than the work output in the denominator. The utilization efficiency, defined in Eq. (5-3), is highest when the net power is highest since the exergy of geofluid is constant for all cases – the cycle is "judged" on a consistent basis at all possible operating conditions. In this example, the thermal efficiency maximum occurs at the minimum net power output. Since the purpose of the power plant is to generate the most electric power possible for a fixed thermal resource (i.e. 100 kg/s of geofluid), the utilization efficiency is an obvious choice for optimization criteria.
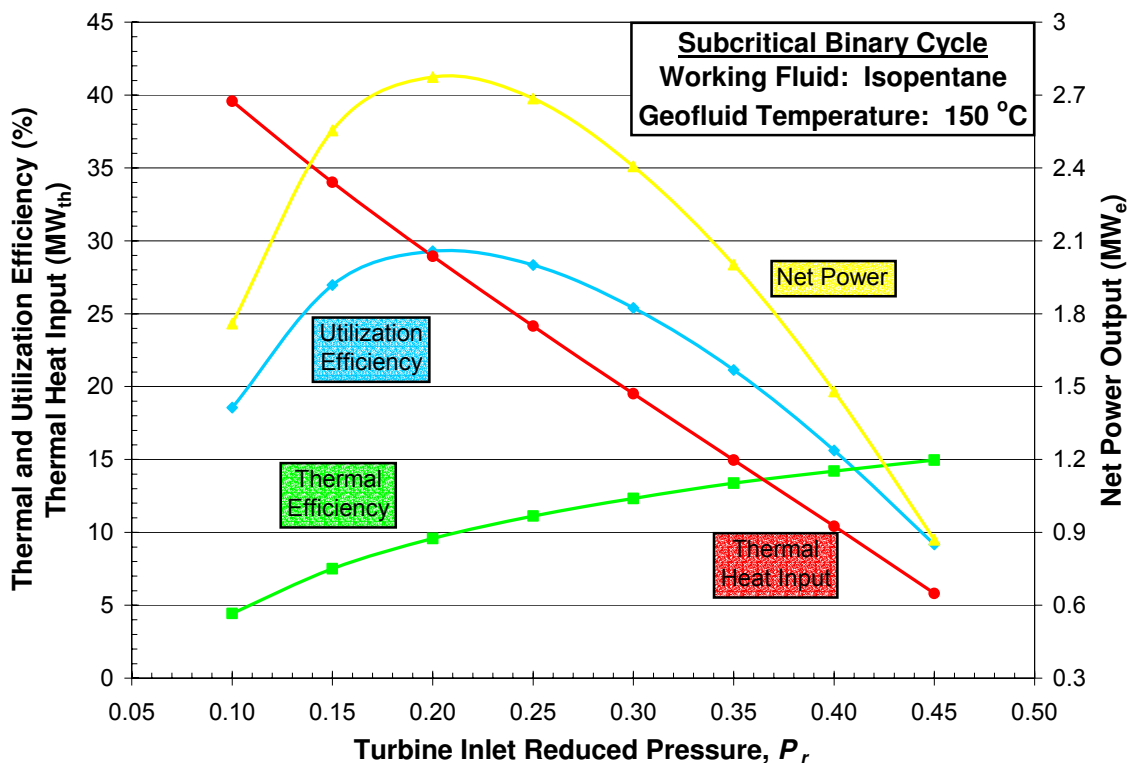

Figure 5.19 Utilization efficiency, thermal efficiency, net power, and thermal heat input as a function of turbine inlet pressure for a subcritical binary cycle using isopentane as working fluid and a 150 °C geofluid.

5.7.2. Comparison of Sub- and Supercritical Cycles

Table 5.7 presents a comparison of optimum net power and utilization efficiency from the analysis of the two types of power cycles. The supercritical cycles hold an advantage over the subcritical cycles for all geofluid temperatures from 100-200 ^{o}C, resulting in a 4% to 23% increase in net power. These results validate the theoretical argument that a supercritical binary Rankine cycle is inherently more efficient than a subcritical one for low-enthalpy heat sources like geothermal because it lowers the irreversible losses in the primary heat exchange step.

Table 5.7 Comparison of optimum net power and utilization efficiencies for sub- and supercritical turbine inlet pressures, optimized for utilization efficiency.

	Subcritical Cycles			Supercritical Cycles			Comparisons
Geofluid Temp.	Working fluid	Net power	Utilization efficiency	Working fluid	Net power	Utilization efficiency	Efficiency ratio: Super/Sub
(^{o}C)		(MW$_e$)	(%)		(MW$_e$)	(%)	
100	i-C$_5$H$_{12}$	16.0	16.0	R-32	0.66	17.1	1.07
110	R-134a	19.2	19.2	R-32	1.13	23.5	1.23
120	R-134a	23.1	23.1	R-32	1.62	27.6	1.20
130	R-134a	25.5	25.5	R-32	2.17	31.1	1.22
140	i-C$_4$H$_{10}$	28.2	28.2	R-134a	2.83	34.5	1.22
150	i-C$_4$H$_{10}$	31.7	31.7	R-134a	3.56	37.5	1.19
160	i-C$_4$H$_{10}$	35.9	35.9	R-134a	4.33	40.0	1.11
170	i-C$_4$H$_{10}$	39.5	39.5	R-134a	5.16	42.0	1.06
180	R-245fa	38.1	38.1	i-C$_4$H$_{10}$	6.08	44.1	1.16
190	R-245fa	44.9	44.9	R-245fa	7.21	46.9	1.04
200	i-C$_5$H$_{12}$	41.5	41.5	i-C$_5$H$_{12}$	8.30	48.7	1.18

Table 5.8 displays the turbine inlet and outlet pressures and their ratios for the optimum cases. The pressure ratios increase dramatically as the resource temperature increases. Table 5.9 shows how the turbine power generation and pump and ACC fan parasitic power losses compare for the two types of cycle. The supercritical cases have consistently higher turbine generation powers at each temperature interval. However, these are partially offset by higher pumping costs. The higher turbine inlet pressures in the supercritical case lead to 2-3 times higher pumping power needs (ignoring the 100°C case where the pumping power is 18 times higher) than the subcritical case. Similarly, the supercritical cycle ACC fans tend to consume between 4 and 23% more power, on average 9% more, with a few exceptions.

Table 5.8 Comparison of optimum turbine inlet and outlet pressures for sub- and supercritical turbine inlet pressures, optimized for utilization efficiency.

Geofluid Temp.	Subcritical Cycles			Supercritical Cycles			Comparison
	Turbine inlet pressure	Turbine outlet pressure	Ratio: Inlet/outlet	Turbine inlet pressure	Turbine outlet pressure	Ratio: Inlet/Outlet	Ratio of inlet pressures: Supercritical/Subcritical
(°C)	(bar)	(bar)		(bar)	(bar)		
100	3.74	1.21	3.09	63.63	24.20	2.63	17.01
110	28.83	9.01	3.20	63.63	23.85	2.67	2.21
120	29.36	8.73	3.36	70.64	23.71	2.98	2.40
130	29.61	8.77	3.38	80.08	23.69	3.38	2.71
140	18.88	4.39	4.30	45.80	8.60	5.33	2.43
150	22.19	4.30	5.16	52.49	8.76	5.99	2.37
160	24.92	4.48	5.56	57.44	8.53	6.73	2.30
170	24.98	4.36	5.73	69.16	8.67	7.97	2.77
180	16.06	2.09	7.68	48.61	4.31	11.29	3.03
190	22.27	1.99	11.19	43.36	1.99	21.84	1.95
200	14.66	1.13	12.97	47.85	1.96	24.36	3.26

Table 5.9 Comparison of optimum CP and ACC power for sub- and supercritical turbine inlet pressures, optimized for utilization efficiency.

Geofluid Temp.	Subcritical Cycles			Supercritical Cycles			Comparison		
	Pump power	ACC fan power	Turbine power	Pump power	ACC fan power	Turbine power	Pump: Super/Sub	ACC: Super/Sub	Turbine: Super/Sub
(°C)	(MW$_e$)	(MW$_e$)	(MW$_e$)	(MW$_e$)	(MW$_e$)	(MW$_e$)			
100	0.016	0.394	1.029	0.294	0.452	1.41	18.13	1.14	1.37
110	0.198	0.530	1.653	0.398	0.676	2.21	2.02	1.28	1.34
120	0.297	0.823	2.476	0.564	0.836	3.02	1.89	1.02	1.22
130	0.397	1.091	3.27	0.784	0.971	3.93	1.96	0.89	1.20
140	0.237	0.844	3.389	0.582	1.021	4.43	2.45	1.21	1.31
150	0.338	1.028	4.366	0.775	1.099	5.43	2.31	1.07	1.24
160	0.472	1.135	5.5	0.960	1.319	6.61	2.03	1.16	1.20
170	0.590	1.501	6.944	1.305	1.385	7.85	2.20	0.93	1.13
180	0.290	1.369	6.91	1.315	1.642	9.04	4.53	1.20	1.31
190	0.474	1.716	9.094	0.963	1.755	9.93	2.03	1.03	1.09
200	0.309	1.725	9.108	1.093	1.843	11.23	3.54	1.07	1.23

At most of the geofluid temperatures studied, the working fluid that gave the maximum utilization efficiency differed for the sub- and supercritical cycles, making direct comparisons difficult. However, at 190 ^{o}C, R-245fa was found to be the optimum working fluid for both cycles. The operating conditions for the optimized sub- and supercritical binary cycles using R-245fa as a working fluid and 190 ^{o}C geofluid are shown in Table 5.10. Many of the operating conditions, such as the mass flow rate and turbine outlet pressure (and therefore condenser temperature) are nearly identical, making the results at this temperature interval a good example for comparison of the sub- and supercritical cases. The turbine inlet pressure in the supercritical case is twice that of the subcritical case. This leads to a ~10% higher turbine power output for the supercritical case, which is in turn offset by a higher pumping power requirement. In the end, the supercritical case has only a 2% higher utilization efficiency, which represents a 4.4 % improvement in net power output over the subcritical case. This example confirms many of the generalizations made above.

Table 5.10 Comparison of operating conditions for sub- and supercritical cases for a geofluid temperature of 190 ^{o}C. For both cycles, R-245fa was found to be the optimum working fluid.

Cycle Type	Turbine inlet pressure	Turbine outlet pressure	W.F. mass flow rate	Thermal power input	RECUP heat load	Turbine power	Pump power	ACC fan power	Net power	Utilization efficiency	Thermal efficiency
	(bar)	(bar)	(kg/s)	(MW$_t$)	(MW$_t$)	(MW$_e$)	(MW$_e$)	(MW$_e$)	(MW$_e$)	(%)	(%)
Subcritical	22.27	1.99	248.9	56.41	4.19	9.09	0.47	1.72	6.90	44.9	12.2
Supercritical	43.40	1.99	247.7	56.81	1.44	9.93	0.96	1.76	7.21	46.9	12.7

Although the supercritical binary plants were shown to be more thermodynamically efficient than their subcritical counterparts for the range of geofluid temperatures considered, they may not be superior on an economic basis. Table 5.8 shows the optimum supercritical binary plants to consistently have turbine inlet pressures 2-3 times higher than the subcritical plants. When the primary heat exchangers are designed, they will require a heavier gauge, more costly tubing and thicker walled flanges and manifolds to safely operate at the higher pressures. Turbine and pump casings will require a greater wall thickness as well. Also, because the LMTD in the primary heat exchanger is typically lower for supercritical cycles, a greater surface area will be required and will also increase costs. Given these factors, the 4-23% increase in net power output from supercritical cycles compared to subcritical cycles may be negated when component costs are

factored in, and the "best" cycles on an economic basis may differ from the best ones based on thermodynamics alone.

5.7.3. Refrigerant Working Fluids

In these simulations, refrigerants performed very well as working fluids. Refrigerants were found to be the best working fluids for 5 of the 11 temperature intervals in the subcritical cycles and 9 in the supercritical cycles. They were especially impressive in the low temperature range, where small improvements in utilization efficiency lead to large increases in net power output. However, environmental considerations may preclude the use of some of the best candidate working fluids. R-32, R-134a and R-245fa all have a high Global Warming Potential (GWP): R-32 = 600, R-134a = 1,300, and R-245fa = 950, relative to CO_2 = 1.0. All turbine outlet pressures are above atmospheric pressure which will likely cause a loss of working fluid to the surroundings through leaks in the system. Although these working fluids are contained in closed loop cycles, their potential release may lead to regulatory and permitting issues. Their use may become problematic should they be banned by international protocols, as happened for example with R114, a very good binary cycle working fluid, because of its high Ozone Depletion Potential (ODP). Currently there are no restrictions on their use.

5.7.4. Effect of Air Cooled Condensers

Air cooled condensers were incorporated into the model to reflect the likely use of binary power plants for geothermal resources in areas that do not have water available for cooling, such as in the U.S. Southwest. Figure 5.13 and Figure 5.17 illustrate the parasitic power losses incurred by using fans for air cooling. Since the power requirements for fans do not increase as quickly as the power generated by the turbine, as a function of geofluid temperature, the use of ACC for higher temperature geothermal resources is acceptable. For low temperature cases though, the parasitic fan load is high – up to a third of the power generated by the turbine in the binary cycle for both the sub- and supercritical cases. For applications where site conditions permit the use of water-cooling, it is strongly recommended to employ wet-cooling instead of dry-cooling to reduce the parasitic power demand, especially for low temperature resources. Considering the

size of the low temperature resource base for EGS, investment in research and development for heat rejection technology is warranted.

5.8. Conclusions

Models of sub- and supercritical binary Rankine power cycles using a number of working fluids and a range of geofluid temperature resources were successfully developed and simulated using Aspen Plus 2006 software. The models were used to determine the optimum working fluid/operating conditions combination that maximized the utilization efficiency as a function of geofluid temperature at 10 ^{o}C intervals from 100-200 ^{o}C. Over this temperature range and for the model design specifications considered, supercritical binary cycles were more efficient than subcritical cycles, producing 4-23% more net power. This was despite having parasitic pumping losses 2-3 times higher than the subcritical cases due to the need to boost the working fluids to supercritical pressures. The higher pressures also require thicker-walled, more expensive equipment. An economic analysis of the plant construction costs on a per kW net power output basis is needed to determine if the efficiency gains from the supercritical cycle justify the increased capital costs.

For both the sub- and supercritical cases, refrigerants were often found to be the best working fluids, especially for lower temperature geothermal resources. The use of these working fluids to boost net power output should be explored. Ironically, their high global warming potential may limit their use in the carbon-free production of electricity from geothermal binary cycle plants. Heat rejection is also an important consideration in designing ORC plants. The need for greater efficiencies at low geofluid temperatures is underscored by the effect of parasitic power losses from air cooled condensers. At the lowest geofluid temperatures explored, ACC fan use can account for up to a third of gross power generation. The model results show that power losses from ACC systems is significant, and wet-cooling should be used wherever site conditions permit.

5.9. References

DiPippo, R. (2005). <u>Geothermal power plants : principles, applications and case studies</u>. Oxford ; New York, Elsevier.

Khalifa, H. E. and B. W. Rhodes (1985). "Analysis of Power Cycles for Geothermal Wellhead Conversion Systems." Electric Power Research Institute, Palo Alto, CA, (June). AP-4070.

Tester, J. W., B. J. Anderson, A. S. Batchelor, D. D. Blackwell, R. DiPippo, E. M. Drake, J. Garnish, B. Livesay, M. C. Moore, K. Nichols, S. Petty, M. N. Toksoz and R. W. Veatch (2006). "The Future of Geothermal Energy." MIT, Cambridge, MA, INL/EXT-06-11746.

Chapter 6: Review of Hydrothermal Flame Experiments and Modeling

A primary goal of this thesis was to examine the feasibility of using thermal spallation drilling in a deep borehole environment for the purpose of lowering the costs associated with developing a geothermal resource. Thermal spallation drilling consists of heating the rock surface so quickly that thermal stresses induced in the rock cause it to fail forming spalls that are ejected from the surface. In order to achieve this, heat fluxes on the order of $0.5 - 10$ MW/m^2 (Rauenzahn and Tester, 1989) are typically applied. This process has been used for decades in the mining industry for drilling shallow blast holes using supersonic flame jets. However, if thermal spallation is to be applied in deeper boreholes encountered while drilling injection and production wells for geothermal, water or hydrocarbon fluids, the ability to produce and utilize combustion flames in a high pressure, high density, aqueous environment is needed. Flames in produced in these environments are called hydrothermal flames.

This chapter presents an in-depth review of the previous hydrothermal flame studies to assess the technologies and techniques used to produce and characterize hydrothermal flames. A shortened version of this review was published in the *Journal of Supercritical Fluids* (Augustine and Tester, 2009).

6.1. Thermal Spallation Drilling in a Deep Borehole Environment

6.1.1. Conditions in a Deep Borehole Environment

The downhole environment encountered in drilling deep boreholes (> 3 km) is much different than atmospheric conditions in shallow boreholes where thermal spallation drilling has been traditionally used. Deep boreholes usually employ a drilling fluid, or liquid water or an aqueous"mud," to aid in the drilling process. In conventional rotary drilling, the drilling mud serves three purposes: 1.) it cools and lubricates the drill bit, 2.) it sweeps rock chips away from the bottom of the hole and transports them to the surface, and 3.) it generates a hydrostatic head

pressure that stabilizes the borehole. The hydrostatic head from the column of drilling fluid balances the lithostatic pressure of the formation and prevents the well bore from collapsing. It also prevents the influx of formation fluids into the wellbore. If left unchecked, fluid formation inflow can cause well collapse at the point of entry, upset the balance of fluids in the wellbore and lead to formation collapse, or increase the pressure in the well and lead to a blow out at the surface. Conversely, too high of a hydrostatic head can cause drilling fluid to flow freely into the formation, a condition known as lost circulation. Collectively, the management of drilling fluids and hydrostatic pressure is known as well control. Developing an effective mud plan is the job of the mud engineer, and is one of the most important roles on a drilling rig.

From the discussion above, it is clear that any deep borehole thermal spallation drilling system will require a liquid drilling fluid with sufficient density to maintain the hydrostatic head needed, for well control and for chip removal. Conventional flame jet spallation systems are not designed to operate under such conditions. While drilling a test hole in a granite formation in Conway, NH, Browning (1981) noted that his open-hole spallation drilling system could tolerate some influx of fluids from the formation, but the rate of penetration slowed markedly when water bearing zones were encountered in the rock. The maximum depth reached during drilling was only 330 m (1,000 ft). Wells deeper than 3 km (10,000 ft) will require the drilling equipment to operate in a fluid-filled hole. In addition to aqueous conditions, much higher pressures will be encountered. Mud engineers achieve well control by using various fluids (aqueous or oil based) and additives, such as clays and chemicals, to control the density of fluid in the borehole. Figure 6.1 shows the hydrostatic pressure as function of depth in the wellbore assuming pure water is used as the drilling fluid.
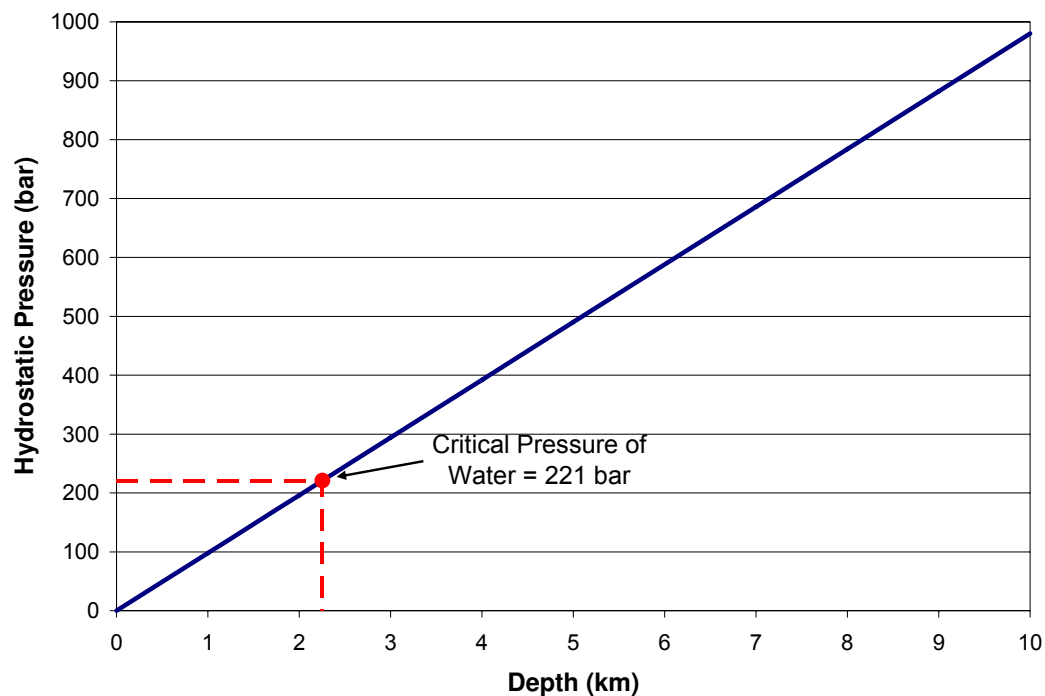
Figure 6.1 Hydrostatic pressure in well as a function of depth assuming water used as a drilling fluid.

6.1.2. The Need for Hydrothermal Flame Research

If jet flames are to be used in a deep borehole environment to generate the heat fluxes needed to induce thermal spallation, then the technology to make flames in a high pressure, high density environment is needed. Figure 6.1 shows that if the drilling fluid is assumed to be pure water or water-based, the bottom hole pressure will be above the critical pressure of water. Therefore, the ability to produce stable, hydrothermal flames in supercritical water will be needed.

Hydrothermal flames are combustion flames produced in aqueous environments at conditions above the vapor pressure of water ($P_c = 221$ bar and $T_c = 374$ $^{\circ}$C). The study of hydrothermal flames began over 20 years ago after a series of studies on the thermodynamic properties of binary systems of various gases and water at high temperatures and pressures "opened up the possibility to study combustion and flames at very high pressures in unusual environments" (Schilling and Franck, 1988). At conditions sufficiently above the critical temperature and pressure of water, light gases such as hydrogen, oxygen and methane are completely miscible in

water, forming a single homogeneous phase that can be ignited and combusted, producing luminous flames in a supercritical environment.

Initially, hydrothermal flames were regarded as interesting phenomena that occurred in for high reactant and oxidant concentrations, resulting in fast oxidation rates and temperatures $>1000\,^{o}C$. However, soon after their discovery, researchers quickly realized that hydrothermal flames could be used to solve two of the major obstacles confronting the practical application of supercritical water oxidation (SCWO) to the treatment of aqueous waste streams – metal corrosion and salt precipitation and plugging. Near its critical temperature, aqueous solutions can be highly corrosive, particularly at acidic conditions when chlorine or other halogen ions are present, requiring materials that have special corrosion-resistance properties. Additionally, because most ionic salts are not soluble in supercritical water due to its lower density and dielectric constant, they rapidly precipitate and can plug reactors and heat exchangers. Recent research has focused on engineering efficient and economical processes that used hydrothermal flames as an internal heat source to destroy organic compounds in various concentrated wastewater streams faster and with less pre-heating than conventional SCWO, while at the same time protecting the reactor walls from the corrosion and salt formation that often plague SCWO reactors.

Even though they were first demonstrated in Franck's laboratory over 20 years ago, the study of hydrothermal flames is still very much in its infancy. Most studies have consisted of phenomenological demonstrations showing the range of organic compounds that can be combusted and proving the feasibility of the technology under different hydrothermal operating conditions. Only a few investigators have conducted in-depth quantitative studies of hydrothermal flame behavior,

Although our research group at MIT has a long history of performing research in supercritical water, the application of hydrothermal flames to thermal spallation drilling goes beyond the regime we have investigated which was limited to 700 ^{o}C and 400 bar. Therefore, a comprehensive review of hydrothermal flame research was performed focusing on three main elements: 1.) a categorization of hydrothermal flame demonstrations and characterization of

experiments for comparison and reference, 2.) a review of the state of the art in equipment, instrumentation and techniques developed to assist researchers interested in carrying out research in this field, and 3.) an evaluation of results from both experimental and modeling studies to summarize what is known about the behavior of hydrothermal flames.

The review began with a description of the properties of supercritical water and its mixtures that give hydrothermal flames their unique properties. A working definition of what constitutes a hydrothermal flame was developed. The remaining discussion was then divided into a review on the experimental and modeling studies performed on hydrothermal flames. The experiments reported to date were separated by flow regime, and the apparatuses used to generate hydrothermal flames by different research groups were reviewed. Next, the current state of the art of instrumentation used by researchers to characterize hydrothermal flames was evaluated along with the results of experiments characterizing hydrothermal flames. Modeling efforts to describe hydrothermal flame behavior was also evaluated. To conclude, future opportunities and challenges in the study of hydrothermal flames were outlined. A proposed mechanism for applying hydrothermal flames to thermal spallation drilling was briefly discussed.

6.2. Background and Origins of Hydrothermal Flames

6.2.1. Properties of Supercritical Water and Supercritical Water Mixtures

The thermophysical and transport properties of water near and above its critical point ($T_c = 374\ ^\circ$C and $P_c = 221$ bar) differ greatly from its properties at ambient conditions. At near and supercritical conditions water has densities that are intermediate between those of ambient liquid and gaseous water. At these conditions, the density and other properties can be rapidly tuned by varying the temperature or pressure. For example, the variation of several properties of water as a function temperature at $P = 250$ bar is shown in Figure 6.2. The viscosity, dielectric strength, surface tension and other physical properties of the supercritical combustion environment can be greatly varied by adjusting the pressure, temperature, and composition of the system. For example, the viscosity at 400 $^\circ$C is about one-tenth of that of liquid water at ambient
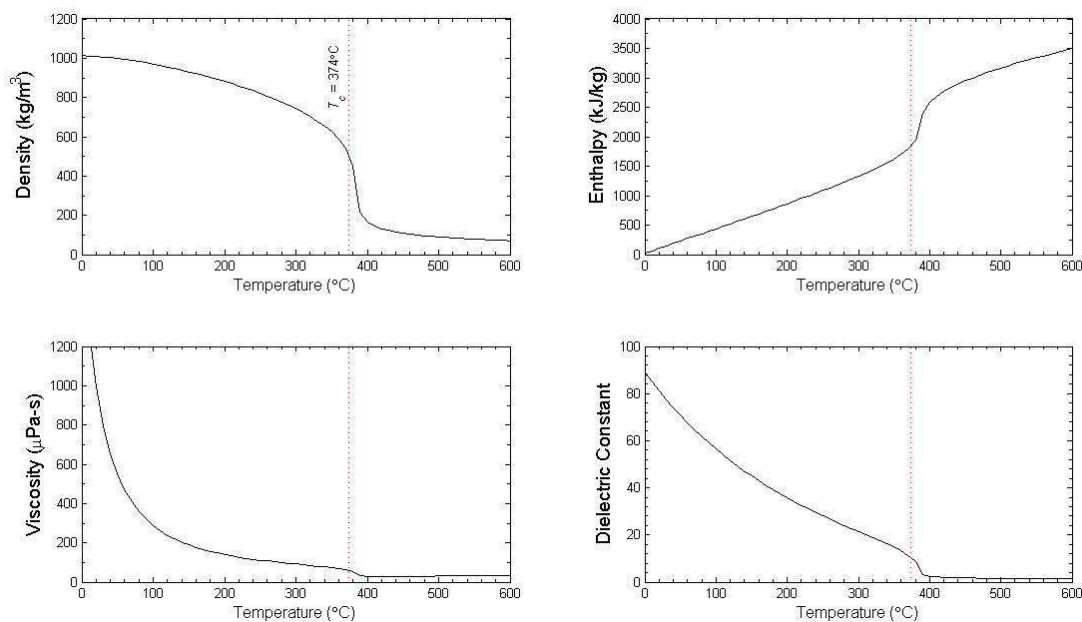
Figure 6.2 Properties of water as a function of temperature at *P* = 250 bar (Wagner and Pruss, 2002). temperatures, leading to higher diffusion coefficients. This causes chemical reactions that are diffusion limited in liquid water to become faster in supercritical water, even at high densities.

Rather small changes in temperature or pressure near the critical point can cause dramatic changes in the solvation character of water – causing it to transition from a very polar, hydrogen bonding solvent at subcritical conditions that easily dissociates and dissolves ionic salts to a non-polar solvent at supercritical conditions that solubilizes gases and light hydrocarbons and provides an attractive environment for treating heterogeneous wastes by oxidation.

More specifically, the dielectric constant of water at a pressure of 250 bar decreases from about 80 at ambient conditions to less than 2 at 400 $^{\circ}$C. These effects, correlated with the decrease in water density, reduces water's hydrogen bonding power, making supercritical water behave like a non-polar solvent such as hexane. Above a temperature of about 375°C, gases such as N_2 (Japas and Franck, 1985a),O_2 (Japas and Franck, 1985b), H_2 (Seward and Franck, 1981), and CO_2 (Mather and Franck, 1992), as well as non-polar organic compounds such as methane (Shmonov et al., 1993), ethane (Danneil et al., 1967), and benzene (Alwani and Schneider,

1967), are completely miscible with water. The critical locus curves of many of these binary aqueous systems, given in Figure 6.3, illustrate the large temperature-pressure region where a single supercritical phase exists. Under supercritical conditions, only a single phase exists and interfacial mass transfer resistances typical of two-phase systems are absent.

Because of the substantial decrease in dielectric strength and loss of hydrogen bonding effectiveness of the supercritical water state, ionic salts have extremely low solubilities (Bischoff and Pitzer, 1989; Armellini and Tester, 1993; DiPippo et al., 1999) and tend to rapidly precipitate out of supercritical water mixtures (Armellini et al., 1994).
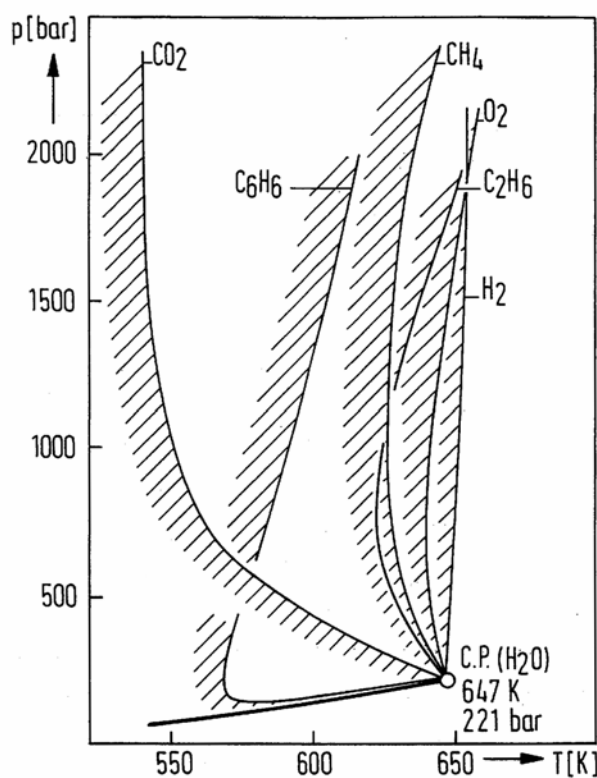

Figure 6.3 Critical curves of gaseous and non-polar organic aqueous binary systems. C.P. indicates the critical point of water (from Hirth and Franck, 1993).

6.2.2. Supercritical Water Oxidation (SCWO)

Supercritical water oxidation (SCWO) takes advantage of the complete miscibility of oxygen and non-polar organic compounds in supercritical water to destroy hazardous, toxic, or non-biodegradable aqueous organic waste. Compared to hydrothermal flame combustion, SCWO is a

moderate temperature process that is usually carried out at temperatures between 450-650 $^{\circ}$C and at supercritical pressures of 230 bar or higher. At these conditions, oxidation reactions take place in a homogenous, single-phase environment. To facilitate isothermal kinetic studies or to prevent thermal runaway in industrial applications, the concentration of reactive species in the aqueous mixture is kept low. Although high reaction rates can be achieved, to completely oxidize organic compounds to conversions of 99.9% or more, residence times, ranging from seconds to minutes, are needed. A range of model compounds and waste streams, including municipal sludges and chemical and biological warfare agents, have been studied. Extensive reviews of the fundamental research and process engineering aspects of SCWO are available from several authors (Tester et al., 1993; Tester and Cline, 1999; Schmieder and Abeln, 1999).

Despite its attributes, SCWO has two well known technical drawbacks– 1.) corrosion and 2.) plugging of the reactors and process equipment due to precipitating solids. Corrosion is caused by the presence of reactive ions such as Cl^- and F^- often present in wastewater streams, particularly those that are acidic. These, combined with supercritical water and oxygen, can lead to severe corrosion over a large range of hydrothermal temperatures and pressures. Metal alloys with a high nickel content, such as Inconel and Hastelloy, are usually used as materials of construction due to their corrosion resistance and strength at high temperatures. Corrosion behavior in SCWO systems has been well documented (Kritzer et al., 2000; Mitton et al., 2001). Equipment fouling and plugging is caused by the precipitation of salt particles in the wastewater as it transitions from the sub- to supercritical conditions (Kritzer and Dinjus, 2001).

Another often overlooked disadvantage of SCWO is that the maximum operating temperature of the process is often limited by the pressure rating of the reactor vessel, which decreases with increasing temperature. Even using high-temperature nickel alloys, the temperature of the reactor wall under stress must usually be kept below ~650 $^{\circ}$C to ~700 $^{\circ}$C to avoid creep and failure. This limits the temperature at which the SCWO reaction can be carried out. Since the rate of the decomposition reactions follow an Arrhenius temperature dependence, the reaction temperature must be kept quasi-isothermal to prevent thermal runaway. The lower kinetic rate

results in required residence times on the order of seconds to minutes, requiring large reaction vessels to process a given volumetric flow rate of waste water (La Roche et al., 1995).

6.2.3. Definition of Hydrothermal Flames

The term "hydrothermal combustion" was first used by Franck to describe oxidation processes taking place in dense aqueous environments (Franck, 1992; Franck and Wiegand, 1996). Although not strictly defined, for the purposes of this review the term hydrothermal flame refers to an oxidation process occurring in a supercritical aqueous environment at sufficient temperature and rate to produce a luminous flame. Because the reaction environment is supercritical, the oxidation process occurs in a single phase with oxygen and the combustible reactant (e.g. methane) mutually soluble in water, thus eliminating any interfacial mass transport limitations. Compared to SCWO processes, hydrothermal flames are characterized by high temperatures, usually in excess of 1000 $^\circ$C, and extremely fast reaction rates, with residence times on the order of only 10-100 ms needed for complete oxidation of reactants. Hydrothermal flames operate in the regime of thermal runaway (La Roche et al., 1995), in which species enter the reaction zone at significantly lower temperatures before being heated to the reaction temperature and undergoing the combustion process.

In practice, a hydrothermal flame is produced by pre-heating the fuel and oxidant streams to a high enough temperature that auto-ignition occurs when they are mixed. Ignition can be induced by other means, such as a heated wire filament (Steinle and Franck, 1995) or spark ignition. In most experiments, the fuel stream is dissolved in the aqueous phase, usually consisting of a single phase supercritical mixture of fuel and water, while the oxidant stream is typically either pure oxygen or air. Flames have been produced in which supercritical water containing a dissolved oxidant was mixed with a pure organic phase. (Sato et al., 2001; Serikawa et al., 2002). There is no reason that a hydrothermal flame cannot be produced by combusting streams in which both fuel and oxidant are mixed in supercritical water or in a single pre-mixed supercritical aqueous phase. The single phase requirement is relaxed somewhat for turbulent diffusion flames in continuous processes, in which the goal is often to decrease the temperature of the incoming fuel (or oxidant) stream below its critical point to reduce the amount of pre-

heating required and to prevent the pre-heater section from plugging with salts that would otherwise precipitate out of solution. Instead, the reaction is autothermal, generating heat of reaction sufficient to increase the temperature of the incoming streams to the point that auto ignition occurs. Since the streams are heated to a single, supercritical phase immediately before combusting, the definition of a hydrothermal flame given above still applies. Also, hydrothermal flames do not always achieve sufficient luminosity to be visible to the naked eye. Steeper and co-workers (1992b) noted in their studies of methanol flames in supercritical water that even after methanol concentrations were insufficient to produce a visible flame, the thermal plume associated with the flame remained visible using a shadowgraph to identify density differences, and elevated temperatures were detectable from thermocouple measurements. Once the methanol concentration was depleted to the point where the hydrothermal flame could not be sustained, the thermal plume structure lifted off the injection nozzle and all evidence of combustion disappeared.

6.3. Industrial Applications of Hydrothermal Flames

The design and construction of equipment for study of continuous hydrothermal flames is not trivial, and have been the focus of much of the recent research. The application of hydrothermal flame technology to the remediation of the same hazardous, toxic, and non-biodegradable aqueous wastes proposed for SCWO processes has been the primary motivation behind hydrothermal flame research. Hydrothermal flames have the potential to solve some of the operational problems associated with SCWO processes. Once ignited, hydrothermal flames provide an internal heat source for the continuous heating and combustion of concentrated wastewater streams that are introduced into the reactor. The inlet streams would not require pre-heating to reaction temperatures as in traditional SCWO processes, eliminating the problems of corrosion and plugging in the pre-heating section. Because of the high flame temperatures, the combustion reaction would proceed very quickly, requiring residence times of only 10-100 ms, to completely oxidize organic compounds. By comparison, traditional SCWO processes require residence times on the order of 25 to 120 seconds or longer to achieve high destruction efficiencies. The design and operation of several hydrothermal flame reaction systems for waste remediation are discussed in Section 6.4.2.

Hydrothermal flames might also be useful for upgrading sub-standard fuels, such as the heavy oils from tar sands and oil shale, by utilizing fuel rich conditions for the flame, and carrying out chemical reforming reactions to break down high molecular weight constituents. These reactions would take advantage of the highly tunable properties of the supercritical water environment and, in principle, be carried out *in situ.* This application would require in-depth understanding of the kinetics and fluid dynamics that control hydrocarbon reforming reactions in hydrothermal flames, and much research would be required to realize this goal.

6.4. Classification of Experiments

Almost all hydrothermal flame experiments performed to date can be divided into one of two categories – 1.) laminar inverse diffusion flames in semi-batch processes and 2.) turbulent diffusion flames in continuous processes. Laminar diffusion flame studies dominated the early period of research in this area, when the phenomena was first identified and being explored. Continuous turbulent diffusion flames in supercritical water were developed as a means to process aqueous waste streams, and have been the primary focus of hydrothermal flame research for over a decade. A much larger number of compounds have been tested as fuels in laminar diffusion flame studies under a wider range of operating conditions, while the majority of turbulent diffusion flame studies have chosen methanol as the fuel of choice. The reason for this disparity is that laminar diffusion studies have focused on the range of compounds that can be used with hydrothermal flames, while turbulent diffusion studies have focused on demonstrating the feasibility of the hydrothermal flame reactor system. The hydrothermal flame experiments that were reviewed including these primary operating conditions are summarized for both laminar inverse diffusion flames (Table 11) and turbulent diffusion flames (Table 12). A description of each of these flow regimes for hydrothermal flame experiments and the apparatuses used to produce them is given below.

Table 11. List of laminar inverse diffusion flame studies with primary operating conditions.

PI Affiliation	Source	Fuel Mixtures			Oxidant		Pressure (bar)	Main Goal of Study
		Fuel(s)	Mole%	Mass%	Oxygen/ Air	Flow Rate[a] (mm³/s)		
Franck, Karlsruhe University	(Schilling and Franck, 1988)	Methane	30	27.6	Oxygen	1-6	200-2000	Demonstration
	(Franck, 1992)	Methane Ethane, higher alkanes, toluene, hydrogen	30	27.6	Oxygen	1-6	100-2000	Demonstration
	(Hirth and Franck, 1993)	Methane Ethane N-Heptane Toluene	10-30 5-20 25 25	9-27.6 8.1-29.4 63.0 65.0	Oxygen	1-5	300-1000 730 600 600	Reaction Products Soot Formation
	(Pohsner and Franck, 1994)	Methane H₂ Methane (with Ar) H₂ (with Ar)	30 30 30 30	27.6 4.6 14.7 2.1	Oxygen	2-5	50-1000	Flame Temperature via OH Spectra
	(Steinle and Franck, 1995)[b]	Methane	30	27.6	Air	Stoichio-metric	50-1100	Ignition Temperature
Steeper, Sandia National Laboratories	(Steeper et al., 1992a)	Methane Methanol	1-50 1-50	0.9-47.1 1.8-64	Oxygen	16.7-50.0	275	Ignition Temperature
Kozinski, McGill University	(Sobhy et al., 2007)	Methanol	11.2-32.3	18.3-45.9	Air	0.5-1.5	230	Demonstration, Reaction Products

[a]Flow rate assumes oxidant is at room temperature and system pressure
[b]Pre-mixed fuel and oxidant ignition experiment.

Table 12. List of turbulent diffusion flame studies with primary operating conditions. *P* = 250 bar for all studies.

PI Affiliation	Source	Reactor	Fuel Mixture				Oxidant	
			Fuel(s)	Mole%	Mass%	Flow Rate (g/s)		Flow Rate (g/s)
von Rohr, ETH	(La Roche, 1996)	WCHB-1	Methane Methanol	11.1-32.5 5.9-19.4	10-27	0.93-2.17	Oxygen	0.56-1.5
	(Weber, 1997)	WCHB-1	Methanol	2.3-15.8	4-25	2.1	Oxygen	1.1
	(Weber et al., 1999)	WCHB-2	Methanol	10-19.4	16.5-30	3.2	Oxygen	1.5
	(Wellig, 2003)	TWR w/o transpiring walls	Methanol	3.5-17.9	6.-28	1.5 + 2.0	Oxygen	1.2 x Stoich.
	(Wellig, 2003; Wellig et al., 2005)	TWR w/ transpiring walls	Methanol Methanol (in secondary fuel stream)	9.7 + 13.7 0 or 3.5	16 + 22 0 or 6	1.5 1.0	Oxygen Oxygen (in secondary O₂ stream)	1.2 x Stoich. 0.2-0.25
	(Príkopský, 2007; Príkopský et al., 2007)	TWR w/ transpiring walls + salts	Methanol Methanol (in secondary fuel stream)	9.7 + 13.7 0 or 3.5	16 + 22 0 or 6	1.5 1.0	Oxygen Oxygen (in secondary O₂ stream)	1.2 x Stoich. 0.2-0.25
	(Príkopský, 2007; Narayanan et al., In Press)	WCHB-3	Methanol	7.1 or 9.7	12 or 16	1.8 + 2.0	Oxygen	0.64 + 0.62
Serikawa, Ebara Research Company	(Sato et al., 2001; Serikawa et al., 2002)	Vertical SCWO reaction tower	2-Propanol	0.8-2.4	2.5-7.5	~0.83	Air	1.1-2.2 x Stoich.
	(Serikawa et al., 2002)	Vertical SCWO reaction tower	Hexane Dioxins	0.6	3.0	~0.83	Air	2 x Stoich.
Tester, MIT	(this study)	WCHB-1	Methanol H₂	25 21.7+27.1	15.8 3+4	1.25-1.5	Oxygen	1.5 x Stoich.

6.4.1. Laminar Inverse Diffusion Flames in Semi-Batch Processes

Description

Laminar inverse diffusion flames in semi-batch systems were the first type of flames in supercritical water studied (Schilling and Franck, 1988). They were made using a 30/70 mole% mixture of methane and water, respectively. The supercritical mixture and reaction vessel was pressurized to between 200-2000 bar and pre-heated to a pre-determined temperature. Oxygen was injected into the reaction vessel. Spontaneous ignition occurred at temperatures of 400 $^{\circ}$C and higher, depending on system pressure. Stationary, cone-shaped flames about 3 mm in height could be seen through sapphire windows built into the reaction vessel. At lower temperatures, flameless oxidation occurred.

Later researchers used this same method to generate laminar inverse diffusion flames in which fuel/water mixtures were injected into the reaction vessel and then pressurized and pre-heated to operating conditions, usually to supercritical pressures and temperatures. Sometimes, the fuel was added after the water had been pressurized and pre-heated, and adequate time allowed for mixing to produce a single supercritical phase. An oxidant, either pure oxygen or air, was injected through a nozzle into the quiescent supercritical fuel/water mixture at low enough flow rates to ensure laminar flow. The oxidant stream may or may not be pre-heated, depending on the reaction system set-up. If temperatures were high enough, spontaneous ignition occurred and an inverse diffusion flame was formed.

In a laminar diffusion flame, the reaction is mixing limited and occurs at the flame front, so that the ratio of reactant to oxidant mass flux into the flame front corresponds to its stoichiometric ratio in the overall reaction. Since the chemical reaction time scale is much smaller than the mass diffusion time scale, the concentration of reactants at the flame front is nearly zero.

The flames are referred to as "inverse" diffusion flames because the oxidant is injected into the fuel, whereas in typical diffusion flames the fuel is injected into the surrounding oxidant rich environment. The process is semi-batch because although oxidant is continuously being injected

into the reaction vessel, fuel is not. As the flame burned, the concentration of the fuel in the system decreased while reaction products accumulated, until the fuel concentration was too low to support continued combustion and flame combustion ceases. Even though the reaction systems are designed to vent or remove products to maintain a constant pressure, that fact that the flames cannot be produced indefinitely but instead are limited by the initial concentration of fuel in the vessel makes the term "semi-batch" the most appropriate description of the operating system. The times during which stable flames are produced experimentally typically range from 10-30 minutes.

Experimental Apparatuses

The apparatus used by Shilling and Franck (1988) to first study inverse laminar diffusion hydrothermal flames, shown in Figure 6.4, consists of an 80 mm OD by 30 mm ID horizontally mounted cylindrical body constructed of corrosion-resistant, high strength nickel-based superalloy. Their reactor has a sample volume of about 30 mL and is capable of withstanding pressures of up to 2000 bar at 500 $^{\circ}$C. There are four ports around the circumference of the vessel, and sapphire windows at opposite ends of the vessel permit visual access into the vessel. The burner is introduced through the bottom port. Oxygen is injected through the burner, creating a laminar jet with a Reynolds number of ~200. The other three ports serve as inlets for a sheathed thermocouple and two stainless steel capillaries that are used to take samples of the reaction products and connect to feed autoclaves that control the pressure inside the vessel. During combustion, oxygen is introduced from stainless steel bellows contained inside a pressurized autoclave. A motor with specialized gearing slowly compresses the bellows. As oxygen enters the reaction vessel, reaction products leave it and enter the space in the autoclave surrounding the bellows, creating a quasi-circular flow that keeps the pressure constant.

The apparatus used at Sandia National Laboratories to study laminar inverse diffusion flames is smaller (14.7 mL), but similar in design to the one used by Franck's group, with a few important modifications. For example, the reaction vessel has 3 sapphire windows instead of two. The third window allows Raman scattering to be used to identify major species and measure fuel concentration. Also, in place of a bellows system, oxygen is fed to the vessel by stainless steel
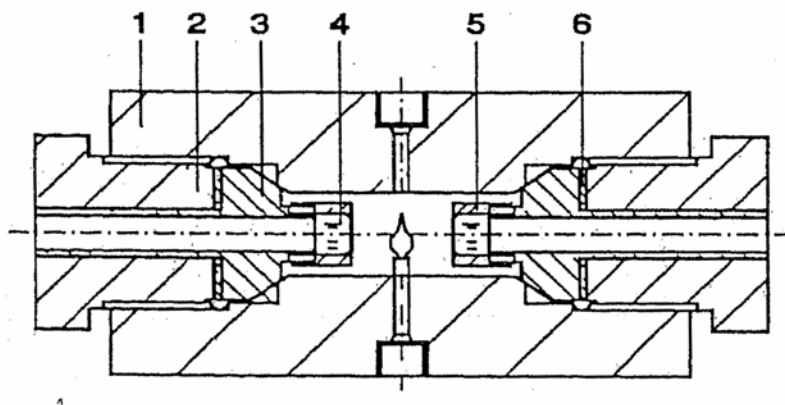
Figure 6.4 High pressure combustion cell with sapphire windows for inverse laminar diffusion flame experiments. 1.) Cell body (Nickel-based alloy) 2.) Gland 3.) Cone sealing plug 4.) Sapphire window 5.) Cap to hold window in place 6.) Slide ring (from Franck and Wiegand, 1996).

cylinders fitted with pistons and driven by water from an HPLC pump. Pressure in the vessel is controlled by a back pressure regulator. Like Franck's, the Sandia system is semi-batch in the sense that fuel is not continuously added to the vessel during reaction, so the concentration of fuel continually decreases as combustion proceeds. A detailed description of the reactor, fluid handling system, the Raman spectroscopic measurement system, and experimental procedure are described in Steeper et al. (1992a).

A recent study of laminar inverse diffusion flames was reported by Sobhy et al. (2007) using the apparatus shown in Figure 6.5, which is similar in principle and operation to those discussed above. Their apparatus has an internal volume of 15 mL and a single sapphire window viewing port. During experiments, air is injected into the nozzle, and the back pressure regulator opens as needed to maintain pressure.
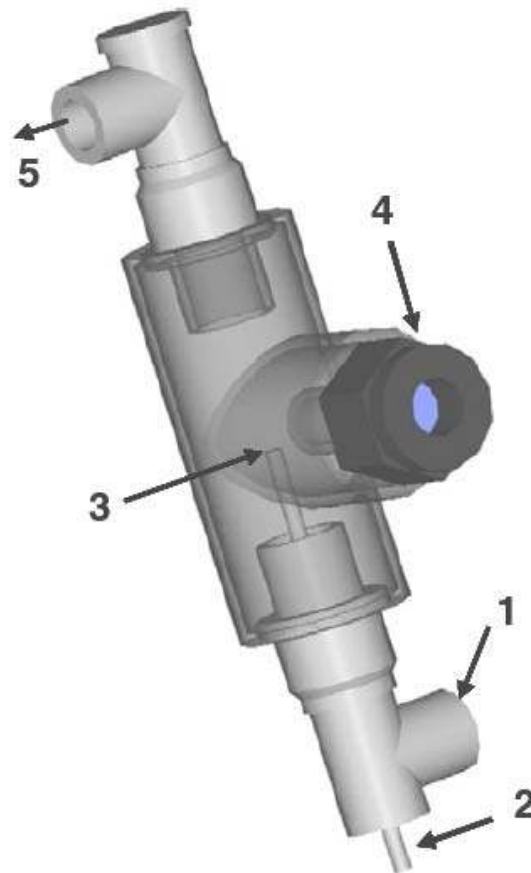
Figure 6.5 Visual flame cell (VFC) used to produce laminar inverse diffusion flames. 1.) Supercritical water/fuel inlet 2.) Air inlet 3.) Nozzle tip 4.) Sapphire window port 5.) Reaction product exit to cooling circuit, back pressure regulator, and sample collection (Sobhy et al., 2007).

6.4.2. Turbulent Diffusion Flames in Continuous Processes

Description

Turbulent diffusion flames are produced by the turbulent mixing and combustion of separated fuel and oxidant streams. In typical turbulent diffusion flames, a turbulent jet of fuel is injected through a nozzle into a quiescent environment containing the oxidant. Due to turbulent mixing, the mixing and combustion process is inherently an unsteady process that does not occur at a well defined flame front. The flame front develops where the oxidant is entrained into the moving jet. In hydrothermal flame studies, the fuel and oxidant are usually both continuously injected as co-axial jets and reaction products are removed from the reactor exit. Consequently, these experiments are not limited by the initial conditions or concentrations and can be operated

for an indefinite period of time and over a range of operating conditions. Often, the purpose of these studies was to demonstrate the feasibility of the continuous hydrothermal flame process rather than study the characteristics of the hydrothermal flame itself. In turbulent diffusion flame experiments, methanol has been the fuel of choice because it is completely miscible with water, allowing the fuel/water mixture to be pre-mixed under ambient conditions and avoiding the complication of an additional high pressure delivery line for fuel.

Experimental Apparatuses

The high temperatures, continuous operation, and ability to use aqueous fuel mixtures make turbulent diffusion hydrothermal flames ideal for remediation of hazardous wastewater streams. As mentioned previously, two major drawbacks of using SCWO processes for aqueous waste remediation are corrosion and salt-plugging. With a proper process engineering design, a high pressure reactor that confines the hydrothermal flame reaction zone to the interior of the vessel while protecting the reactor walls could eliminate corrosion and plugging entirely. Such a design was first proposed by La Roche et al. (1995) in the form of a reactor with a flame recirculation zone and wall cooling. The reaction zone would operate as a turbulent diffusion flame jet in the thermal runaway regime, and an internal recirculation zone would be used to induce back mixing of the hot reaction products with the incoming cooler subcritical streams to heat them to the ignition temperature. The wastewater and oxidant would be introduced coaxially. At the same time, a co-flowing outer stream of subcritical water would confine the flame and protect the walls of the reactor from high temperatures, corrosion, and plugging. La Roche and co-workers originally proposed film cooling to protect the reactor walls, but noted that convective cooling or transpiration cooling could be used as well.

These design criteria were incorporated into a reaction vessel in which the first reported turbulent diffusion hydrothermal flames in a continuous system were produced. The vessel, later known as the 1st Generation Wall-Cooled Hydrothermal Burner (WCHB-1), is shown in Figure 6.6, with a close-up of the reactor burner configuration shown on the left in Figure 6.7. Fuel, usually a methane or methanol and water mixture, flows through the innermost tube (fuel nozzle) and enters through the bottom entrance of the reactor. Oxygen enters through a port on the radius of

the vessel and flows in the annulus surrounding the fuel nozzle. Sub-critical cooling water enters though a radial port and through the outermost annulus, cooling the walls of the reactor and protecting them from corrosion and plugging. The nozzle is configured to provide a mixing and combustion chamber shielded from the cooling water stream to stabilize the flame. The combustion products are quenched by the outer cooling water stream and exit the outlet of the reactor. The WCHB-1 is also equipped with four thermocouple ports at various positions around the burner configuration and one thermocouple port near the exit. Two, 20 mm sapphire windows provide optical access to the reactor. An elaborate system of pumps, gas boosters, flow indicators, heating units, a pressure control system, and instrumentation, similar in scale to a small pilot plant, are required to supply the reaction vessel with fuel, oxygen, and cooling water and control operating conditions. A detailed description of the design and construction of the WCHB-1 reactor and the ancillary equipment used in its operation is given in (La Roche, 1996). The same apparatus, with modifications to the burner nozzle configuration, was used in our lab at MIT to study the application of hydrothermal flames for thermal spallation drilling.

Later, the ETH group built a second generation wall-cooled hydrothermal burner (WCHB-2) designed to allow better optical access of hydrothermal flames (Weber et al., 1999). The WCHB-2 had two sapphire windows 165 mm in length that allowed the nozzle configuration and flame to be easily viewed. The size and position of the windows altered the reactor cross section, so a long cylindrical glass tube was used to separate the reaction zone from the sapphire windows and keep its cross section circular and constant. A long transparent quartz tube was used to separate the flame from the surrounding cooling water but still allow visual access. The nozzle configuration is shown on the right in Figure 6.7. They found that radial burners, which are closed at the end and have small holes drilled around the radius at the tip to promote mixing of the fuel with the co-annular oxygen stream, would impinge against and quickly destroy the quartz tube. Coaxial burners, in which the nozzle is a simple tube open at the end, had to be used instead. Except for the longer quartz tube confining the hydrothermal flame, the burner design and geometry was similar to that used in the WCHB-1.
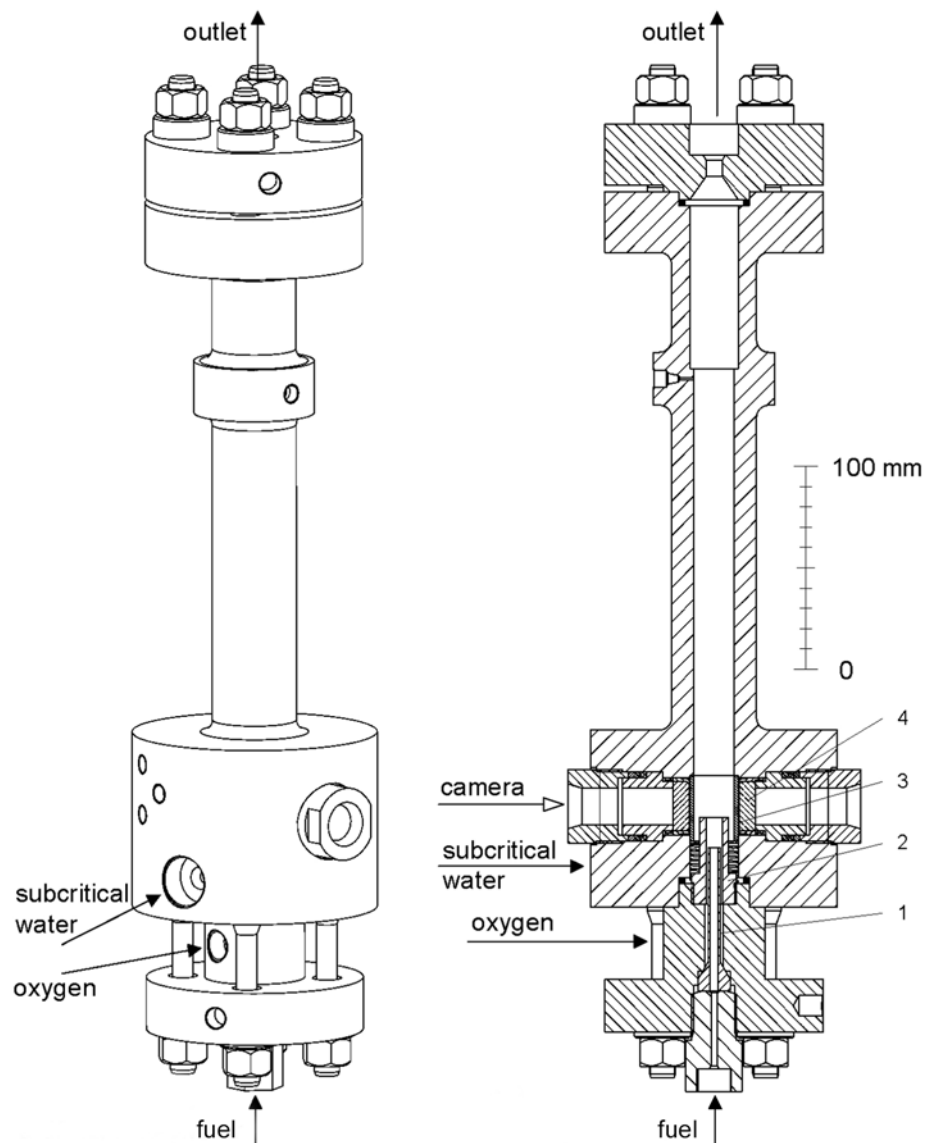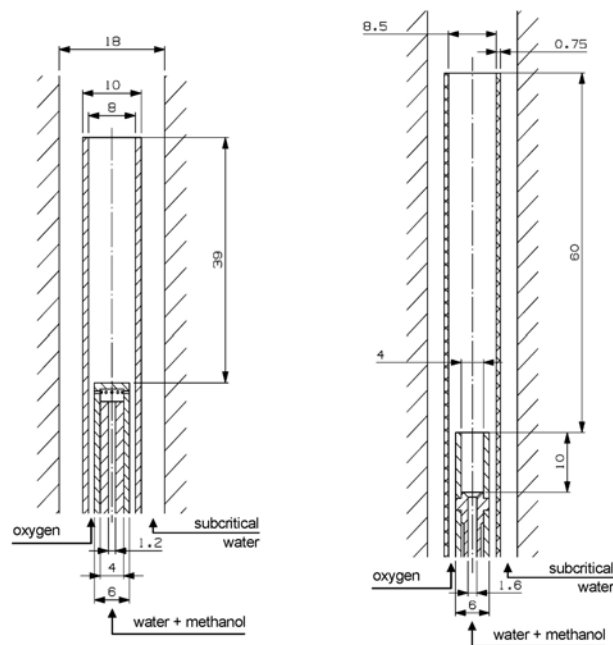
Figure 6.6 First generation ETH wall-cooled hydrothermal burner (WCHB-1) reactor. 1.) Core tube of burner/fuel inlet 2.) Coaxial tube/oxygen inlet 3.) Cylindrical glass tube (keeps cross section constant) 4.) Sapphire windows (adapted from Wellig, 2003).

Figure 6.7 Close-up schematics of a typical burners used in wall-cooled hydrothermal burners at ETH. Radial burner used in WCHB-1 experiments (left) and coaxial burner used in WCHB-2 experiments (from Príkopský, 2007). Dimensions are in mm.

The next ETH hydrothermal flame reactor design, referred to as the Transpiring Wall Reactor (TWR), utilized transpiring walls as the means to prevent corrosion and plugging of the reactor walls. The transpiring wall consisted of highly-porous sintered Inconel 625 tubes. Sub-critical water flowing through the porous tube wall forms a film that prevents contact by the corrosive reacting mixture and inhibits precipitation of salts on the walls. The reaction zone was divided into 4 sections fed by cooling water flows that could be separately controlled to study the effect of transpiring intensity in different parts of the reactor. Additional changes were made to the nozzle geometry so that secondary waste water and oxygen inlet streams, co-annular to the primary ones, could be accommodated. With these secondary streams, a hydrothermal flame burning a "clean" fuel/water mixture could provide internal heat to the reactor, eliminating the need for high pre-heating temperatures, while a second wastewater stream with dissolved salts could be introduced with additional oxidant. The heat from the hydrothermal flame would be used to destroy the contents of the wastewater stream, while the transpiring walls prevented corrosion and plugging. The TWR was not equipped with sapphire windows and lacked visual access. The ignition, extinction, and presence of flames was inferred by thermocouple measurements, pressure variations, and other indicators recognizable as evidence of flames from

previous experimental experience. More details about the design and construction of the TWR can be found in (Wellig, 2003).

The third-generation ETH Wall-Cooled Hydrothermal Burner (WCHB-3) currently in use at ETH was based on the design of the WCHB-2 and was intended to be used to study different optical diagnostic techniques for characterizing hydrothermal flames. This design includes four large sapphire windows, each 85 mm in length, with a combustion chamber formed by a quartz glass tube 8.5 mm ID x 10 mm OD that runs the length of the reactor, completely confining the flame (Figure 6.8). A second quartz glass tube 22 mm ID x 24 mm OD encases the combustion chamber, and two separately controlled cooling water streams are circulated around the outside of both tubes. The design allows optical access of the entire length of the combustion chamber from four directions. For details see (Príkopský, 2007).
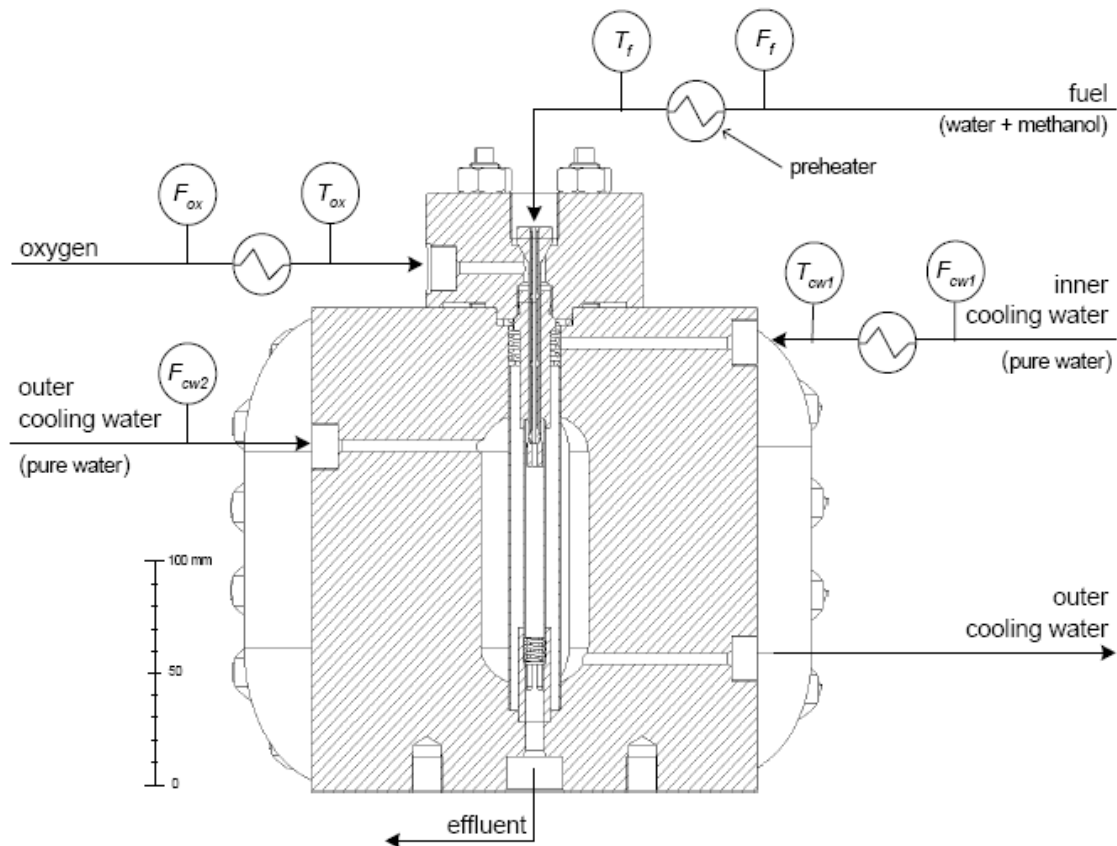

Figure 6.8 Schematic of WCHB-3 reactor, showing inlet and outlet stream flows (Príkopský, 2007).

Hydrothermal flames were also produced in a vertical continuous reactor by the Ebara Research Company in Japan (Sato et al., 2001; Serikawa et al., 2002). The constructed apparatus, shown in Figure 6.9, is 2600 mm in length, has an internal diameter of 50 mm, and an internal volume of 4800 mL. The Ebara system was fitted with a single sapphire window for optical observation of oxidation reactions. The operation of the reactor was unique in several ways. First, air was used as the oxidant instead of oxygen. Second, water was injected into the oxidant feed stream and pre-heated to form a supercritical oxidant/water mixture rather than a fuel/water mixture. Fuel and oxidant are injected co-axially and a special nozzle was designed to enhance mixing of the streams at the nozzle outlet. The air-water mixture was pre-heated and injected through the center of the nozzle, while an unheated pure fuel stream was injected into the nozzle annulus. The upper section of the reactor walls are heated to achieve desired reactor temperatures, while the lower section is air-cooled and then water-cooled, well after the reaction zone. It appears that the initial production of hydrothermal flames was an unintended consequence of using high fuel concentrations in SCWO studies. Flames ranging from intermittent to continuous were produced by increasing the amount of fuel fed to the reaction nozzle. Unlike the ETH reactor designs, the Ebara design does not use sub-critical water to protect or cool the reactor walls, and lacks any active cooling scheme for the reactor walls in the upper section, where flames are produced. Consequently, hydrothermal flames were produced with fuel concentrations equivalent to a 2.4/97.6 mol% fuel/water mixture, very low in comparison to other studies. If they used higher fuel concentrations, wall temperatures in excess of 600 $^{\circ}$C would have been encountered which would have caused temperatures to exceed design limits for the vessel and could have resulted in mechanical failure of the reactor walls. As a result only these low feed concentrations were studied (Serikawa et al., 2002). The Ebara reactor design illustrates the importance of incorporating proper wall cooling and protection strategies into the design and construction of continuous hydrothermal flame apparatuses.
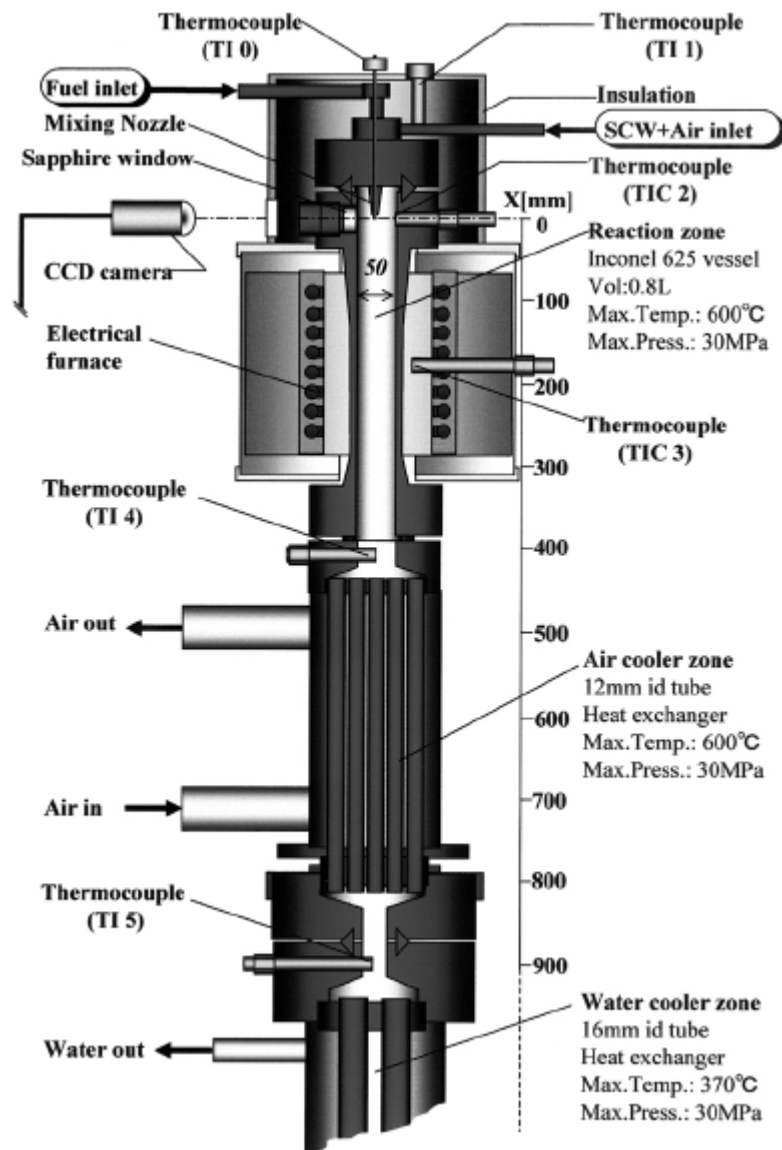
Figure 6.9 Schematic illustration of vertical SCWO reaction tower used by Ebara Research Company, Japan (Serikawa et al., 2002).

6.4.3. Spontaneous Ignition of Pre-Mixed Flames

The only notable experiments that deviated from the laminar or turbulent diffusion flame studies typical of hydrothermal flame research were spontaneous ignition studies of high pressure mixtures of methane or ethane with oxygen or air (Steinle and Franck, 1995). Three different vessels, similar to bomb calorimeters, were used in the study, two cylindrical (internal volumes of 3.87 and 10.18 cm^3) and one spherical (internal volume of 20.58 cm^3). Several ignition methods were applied, such as forced ignition with heated wires and rapid injection into a pre-

heated vessel, but the preferred method was determined to be gradual heating of the vessel and gas mixture simultaneously at a rate of 6-19 K/min until ignition occurred. Pressure and temperature in the vessel were measured continuously to determine the ignition temperature and pressure. Hydrothermal flames were not the primary focus of this study, and most of the experiments were performed in the absence of water. Only a few experiments under hydrothermal conditions, using mixtures of 30/70 mole% methane and water, respectively, with stoichiometric air at pressures of 50-1000 bar were performed. The results of their ignition temperature studies are presented in Section 6.6.1.

6.5. Experimental Instrumentation

As with any combustion process, there are two experimental variables that are of primary interest – the temperature and fuel-oxidant-solvent composition. The ability to measure these quantities as a function of position or residence time is imperative for characterizing hydrothermal flames and describing the combustion process. The measurement of these quantities is made especially difficult in hydrothermal flames due to the high pressures encountered and high gradients in the reaction zone. The tools and instrumentation used to study flames at ambient, low density conditions are often not suited for or applicable to the high pressure, high density hydrothermal flame environment. Hydrothermal flame researchers have attempted to adapt conventional instrumentation and techniques to cope with these challenges with limited success. Instrumentation and techniques that have been developed that are capable of measuring temperature, composition, and other variables of interest in hydrothermal flame systems while still maintaining system pressure are presented below.

6.5.1. Temperature measurement

System and inlet temperature measurement

System and stream temperatures before and during hydrothermal flame ignition have been measured almost exclusively using metal-sheathed thermocouples inserted through a port on the reaction vessel and sealed using a compression-type fitting. The thermocouples are typically Type-K, with a temperature range up to 1375 $^{\circ}$C, and are sheathed in a high-nickel alloy such as Inconel 600. The compression fittings lock the thermocouple in place, so the thermocouple can

only record temperatures at a single position within the reaction vessel. The pressure rating of the compression fitting varies by design and manufacture, but ratings of up to 1000 bar are common.

Brown and Steeper (1991) demonstrated that the temperature of mixtures encountered in supercritical water oxidation could be measured using CO_2 Raman spectroscopy. Over the temperature range of 400-650 $^{\circ}$C, hot bands in the Raman spectrum of CO_2 appear with sufficient intensity that temperature can be determined based on intensity ratios. A nearly linear intensity ratio dependence with temperature was found, making temperature determinations with accuracies of ±6% possible. In systems with visual access, the technique could be used to measure the system temperature just prior to ignition in laminar inverse diffusion flame studies. The researchers had planned on testing their proposed method to measure flame temperatures in future experiments (Steeper et al., 1992b), but results were never published.

Flame temperature measurement

The determination of flame temperatures, even under atmospheric conditions in open reaction vessels, is difficult, requiring specialized techniques and is even more challenging because of restricted access the combustion region at high pressures. In addition, the decreased thickness of the flame fronts increases the temperature gradient. Pohsner and Franck (1994) discussed the shortcomings of most traditional flame temperature determination techniques. Thermocouples interfere with the flame and are either melted by the intense temperatures within the hydrothermal flame or are quickly corroded by the hydrothermal environment. Pyrometric techniques require black body radiation, but the radiation from hydrothermal flames in the visible region is mostly of non-thermal origin and is caused by chemiluminescence. The sodium D-line reversal method, in which the characteristic spectra from a small amount of sodium salt introduced to the flame, is measured to determine flame temperature, can quickly corrode and etch the inner surface of the sapphire windows of the reactor apparatus, inhibiting visual access. The feasibility of the sodium D-line method should be revisited with the advent of wall-cooled hydrothermal burners, in which the flame is confined by subcritical water, protecting the reactor

windows and walls. Despite these inherent challenges, techniques to measure hydrothermal flame temperatures have been developed and teste, with varying degrees of success.

Pohsner and Franck (1994) attempted to use the intense rotational emission of OH-radicals in the near UV to measure hydrothermal flame temperatures. This emission can be found in all flames containing O and H radicals as combustion components. Laminar inverse diffusion flames of dense mixtures of methane or hydrogen in either supercritical water or argon were studied. The study used a least squares method to determine rotational temperatures from (0-0) and (0-1) transitions of the $A^2\Sigma–X^2\Pi$ electronic transition by fitting theoretical curves to experimental spectra. The temperatures determined from the analysis did not follow trends predicted by theory, and were 1000 K higher than calculated adiabatic flame temperatures at a system pressure of 1000 bar. Self-absorption of quanta by the surrounding high-density media and non-equilibrium among molecular degrees of freedom were cited as possible sources of error in the temperature measurement.

Thermocouples can be used to measure hydrothermal flame temperatures if they are properly positioned and flame temperatures are within the operating range of the thermocouples, such as when the overall concentration of fuel in the aqueous mixture is low. For example, thermocouples have been used successfully to measure the temperature of continuous turbulent diffusion flames. A Type-S thermocouple with platinum sheathing was used to measure the temperature of hydrothermal flames inside its combustion chamber made using 12, 16, and 20 mass% (7.1, 9.7 and 12.3 mole%) methanol fuel mixtures and oxygen (Wellig, 2003; Príkopský, 2007). The 20 mass% methanol fuel mixture damaged the thermocouple probe. More conventional Type-K thermocouples sheathed in Inconel, readily available from industrial suppliers, have been used to measure the temperature of methanol flame jets issuing into subcritical waters immediately outside the combustion chamber (Wellig, 2003)(authors, unpublished).

When measurements are made with thermocouples, the temperature at the thermocouple junction is not necessarily the flame temperature due to heat losses via radiation from the thermocouple,

conduction through the thermocouple itself, and catalytic effects induced by the thermocouple sheathing. Care must be taken to account for these effects when reporting flame temperatures measured by thermocouples.

When using any of the above techniques to measure flame temperature, estimates of the adiabatic flame temperature are useful for providing an upper bound and determining the validity of measurements. Adiabatic calculations estimate flame temperatures by balancing the heat liberated from the combustion process with the thermal capacity of combustion products to determine their final temperature. Heat losses due to convective transport and radiation are not considered, so the actual flame temperature will always be cooler than the adiabatic flame temperature. Numerous researchers have performed adiabatic flame calculations as part of their analysis (Saur et al., 1993; Pohsner and Franck, 1994; Wellig, 2003; Narayanan et al., 2008).As an example, the estimated adiabatic flame temperature for a 30/70 mole% methane/water mixture initially at 500 $^{\circ}$C and 270 bar combusted with stoichiometric amounts of oxygen was 2920 $^{\circ}$C

6.5.2. Flame position determination

Chemiluminescence can be used to identify hot reaction zones and the position of flame fronts in oxidation reaction systems. Chemiluminescence is light emitted by electronically excited molecules as they transition from a high energy state to a lower one. The light emitted ranges from the UV to the IR spectrum. Since the wavelength of the light emitted is specific to the type of molecule and the transition it is undergoing, chemiluminescence can be used to identify regions of high concentrations of a particular species. While large molecules have complex emission spectra, diatomic molecules usually exhibit emission spectra with a major peak that can be used to identify the species and a few secondary peaks of lower intensity.

The research group headed by von Rohr at ETH has recently explored the use of chemiluminescence for determining flame front positions. Príkopský (2007) measured the position of the flame front in continuous turbulent diffusion hydrothermal flames by measuring the chemiluminescence of OH and CH radicals as well as overall flame luminosity. An

intensified CCD camera was used to capture "line of sight" images of the flame. For overall flame luminosity, no filter was used. Bandpass filters for 313 nm wavelengths and 431 nm wavelengths were used to image chemiluminescence of OH and CH radicals, respectively. The images were processed using an algorithm to segment the image into burnt and unburnt zones and derive a contour of the flame front. A large number of these images for a single condition were then analyzed to determine the probable position of the flame front. By extracting a single line profile along the reactor axis, referred to as the centerline intensity profile, a similar process was used to determine the start and end points of the flame front zone at the centerline.

The group at ETH also set up a laser-induced fluorescence (LIF) system to visualize specific regions of the flame. LIF uses a laser sheet tuned to the specific absorption wavelength of a species. The laser excites the species to a higher energy level. The species emits light at a characteristic wavelength as it returns from the higher energy level. This emission is captured using a CCD camera. LIF gives much higher spatial and temporal resolution than chemiluminescence visualization systems. Although the LIF system was described in (Príkopský, 2007), results from experiments using the technique were not presented, but are reported to be published at a later date.

Sobhy et al. (2007) used Near Infrared (NIR) imaging to obtain qualitative measures of temperature in their vessel during experiments and to identify hot regions in the reactor to develop a better understanding of the ignition process they observed. The NIR spectra has been considered as a region from which flame temperatures could be measured, based on theoretical calculations (Michelfelder et al., 1996), but no quantitative measurement of temperature has been reported attempted using NIR.

6.5.3. Temperature profile determination

Probing the structure of hydrothermal flames is challenging because of the high pressures at which they operate. Any diagnostic tool used to make measurements of the flame must pass through a port on the reaction vessel and form a seal capable of holding pressures well in excess of 200 bar. Temperature measurements have been accomplished using metal-sheathed

thermocouples positioned at various positions throughout the reaction vessel. The inability to dynamically move a probe within the reaction zone requires that the researcher have some prior knowledge of the flow and temperature fields in order to position thermocouples to make useful measurements. This severely limits the quality of the resulting temperature profile. Fitting the reaction vessel with sapphire windows to gain visual access to the hydrothermal flame has proven successful, but optical techniques used to characterize the flame are complex and have yielded mixed results.

A special device that allows vertical displacement of a thermocouple in the combustion chamber during an experiment has been designed by ETH and successfully used in the WCHB-3 reactor (Narayanan et al., 2008). The ETH design is based on the working mechanism of a valve. The thermocouple enters the reaction vessel through the fuel nozzle along the axis of the reactor, and has 100 mm of free travel. Using a single thermocouple, the axial temperature profile of the hydrothermal flame along the entire length of the combustion chamber can be obtained (Príkopský, 2007). Researchers at ETH have recently developed a second probe that can be mounted at the exit of the WCHB-3 reactor instead of the inlet, which should minimize disturbance of the flame during experiments. Our group at MIT has also designed and constructed a movable probe for use in hydrothermal flame studies with the WCHB-1 reactor. The design and operation of the movable probe is discussed in Chapter 7.

6.5.4. Species identification and quantification

The study of compounds formed during and after reactions in hydrothermal flames is mostly limited to identifying components in the reactor effluent or present in the vessel after the experiment. Standard gas (GC) and high-pressure liquid chromatography (HPLC) techniques are used to identify combustion products such as CO, CO_2, O_2, NO_x, and residual fuel. The reaction products from turbulent diffusion flame studies can be quickly quenched by surrounding cooling upon exiting the reaction chamber, effectively "freezing" the reaction. On the other hand, in laminar diffusion studies, the reaction products remain in a high temperature, fuel rich aqueous environment long after leaving the flame front reaction zone, so reactions between the flame combustion products and surrounding medium are highly likely. Analysis of species in the bulk

fluid exiting reactor vessels under such conditions in laminar flame studies should take this effect into consideration.

Steeper et al. (1992b) measured species *in-situ* in laminar inverse diffusion flames both qualitatively and quantitatively using Raman spectroscopy. For experiments of laminar inverse diffusion flames using methane and methanol, calibration curves of signal intensity versus component density were made. Density measurements were then converted to mole fractions using an equation-of-state tailored to supercritical water mixtures (Christoforakos and Franck, 1986). Methane and methanol concentrations in supercritical water prior to ignition could be measured to within ±6 mole% (95% CI) using this method. After the flame experiments, the presence of combustion products such as CO, CO_2, and H_2 could be detected using Raman measurements as well. Chemiluminescence and the use of LIF, as described above, also shows promise in identifying intermediate species present during hydrothermal flame reactions.

6.6. Characterization of Hydrothermal Flame Processes

The goals of hydrothermal flame experiments vary with the type of flow regime and the intended application of the technology. Laminar inverse diffusion flame studies focus on flame ignition characteristics and the effect of operating conditions on reaction products, while continuous turbulent diffusion flame studies deal primarily with the conditions that lead to flame extinction and the effect of operating conditions on flame stability, fluid flow patterns, and destruction efficiency.

6.6.1. Ignition Temperature

Temperature data have been used to identify conditions where hydrothermal flames spontaneously ignite going back to the original laminar diffusion flame experiments. In these studies, performed by injecting oxygen into a pre-heated 30/70 mole% methane/water fuel mixture, variations of ignition temperatures with pressure were characterized. Schilling and Franck (1988) found that the temperature required for ignition decreased as the system pressure increased, from 420 °C at 200 bar to as low as 400 °C at 1000 bar. These ignition temperatures

were significantly below the ignition temperature of 550 $^\circ$C required for methane under ambient conditions.

Later experiments conducted by Hirth and Franck (1993) in the same apparatus varied both pressure and concentration to see what effect it would have on ignition temperatures. Pressure was varied from 300-1000 bar for a 30/70 mole% methane-water mixture, and composition was varied from 10-30 mole% methane at 600 bar. As before, ignition temperature decreased with increasing pressure. Not surprisingly, the ignition temperature increased as methane concentration decreased. A similar trend was found for the ignition of mixtures of ethane and water at 730 bar over a range of 5-20 mole% ethane. 20 mole% mixtures of ethane could be ignited at temperatures as low as 350 $^\circ$C.

Steeper and co-workers (1992b) at Sandia quantitatively mapped the ignition limits for a laminar inverse diffusion flame over a wider range than Franck's group. They studied the ignition temperature of methane-water and methanol-water fuel mixtures ranging in concentration from 1-50 mole% methane or methanol by pre-heating it to 380-510 $^\circ$C and injecting oxygen at a system pressure of 275 bar. If spontaneous ignition was observed, the experiment was repeated at a lower initial temperature until no ignition was observed. The resulting ignition maps for both methane and methanol diffusion flames in supercritical water with interpolated ignition limits is shown in Figure 6.10. At temperatures above 450 $^\circ$C, flames readily ignited for fuel mixtures as low as 6 mole% methane or methanol. At lower temperatures, higher organic concentrations are needed to induce ignition. The variability in ignition temperatures around the interpolated ignition limit illustrates the sensitivity of ignition to variations in the oxygen injection rate. Higher ignition temperatures could not be studied due to pyrolysis of the organic compound in the fuel mixture. When burned to extinction, between 1-5 mole% of the organic fuel remained uncombusted.
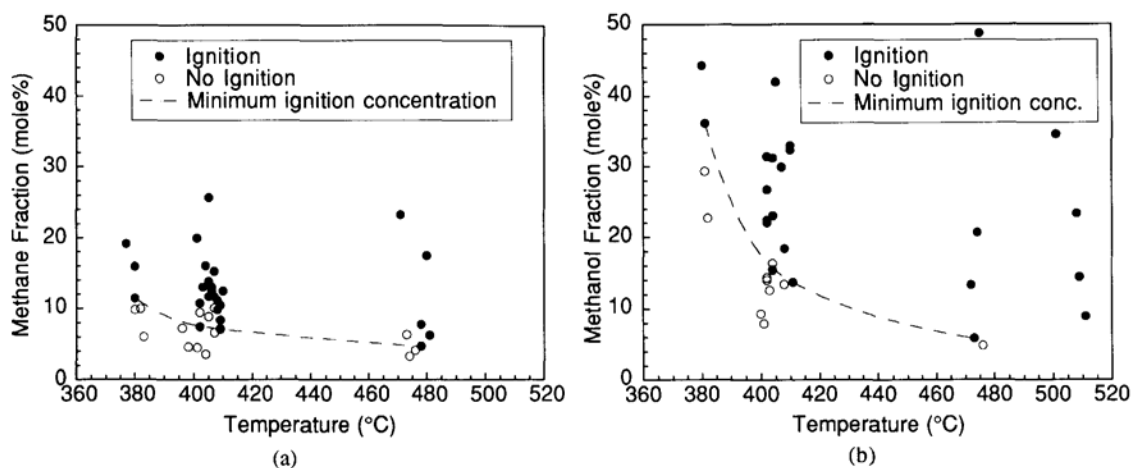
Figure 6.10 (a) Spontaneous ignition limits for methane in supercritical water upon injection of oxygen. (b) Spontaneous ignition limits for methanol in supercritical water upon injection of oxygen. Pressure is 275 ± 5 bar, oxygen injection rate is 1-3 mL/min, and concentration measurement error is ± 6% (95% CI) (Steeper et al., 1992b).

Steinle and Franck (1995) determined ignition temperatures for pre-mixed mixtures of methane or ethane with oxygen or air from 50-1000 bar using an apparatus very similar to a bomb calorimeter. Reaction mixtures, along with the vessel, were slowly heated until spontaneous ignition occurred. Most experiments were done in the absence of water. Ignition temperatures were found to decrease dramatically with pressure, dropping from 600 $^{\circ}$C at 1 bar to 390 $^{\circ}$C at 1000 bar for mixtures of methane and stoichiometric air. The ignition temperature decreased quickly with increasing pressure initially, dropping by 160 $^{\circ}$C at 100 bar. The rate of ignition temperature depression then leveled off, decreasing only an additional 60 $^{\circ}$C after additional pressurization to 1000 bar. The presence of water on ignition temperatures was only explored briefly. Experiments performed under hydrothermal conditions using a 30/70 mole% methane/water fuel mixture with stoichiometric air showed an increase in ignition temperatures of 15-20 $^{\circ}$C compared to water-free tests, as shown in Figure 6.11. Semenov plots, which approximate the effective activation energy of an overall nth order combustion reaction based on the pressure and temperature at the time of ignition, showed that activation energies for methane-air systems with and without water were similar, indicating that the presence of supercritical water has little effect on the ignition process. Activation energies for the ignition process were also estimated assuming a 2nd order global reaction mechanism. Unfortunately, since the ignition experiments were performed using air as the oxidant, they can not be directly compared to results from other researchers performing laminar inverse diffusion flame experiments with pure

oxygen. Conceivably this method, using homogeneous mixtures, would give the most accurate measure of ignition temperatures since it is not as dependent on reactor configurations, flow rates, or other fluid dynamic effects.
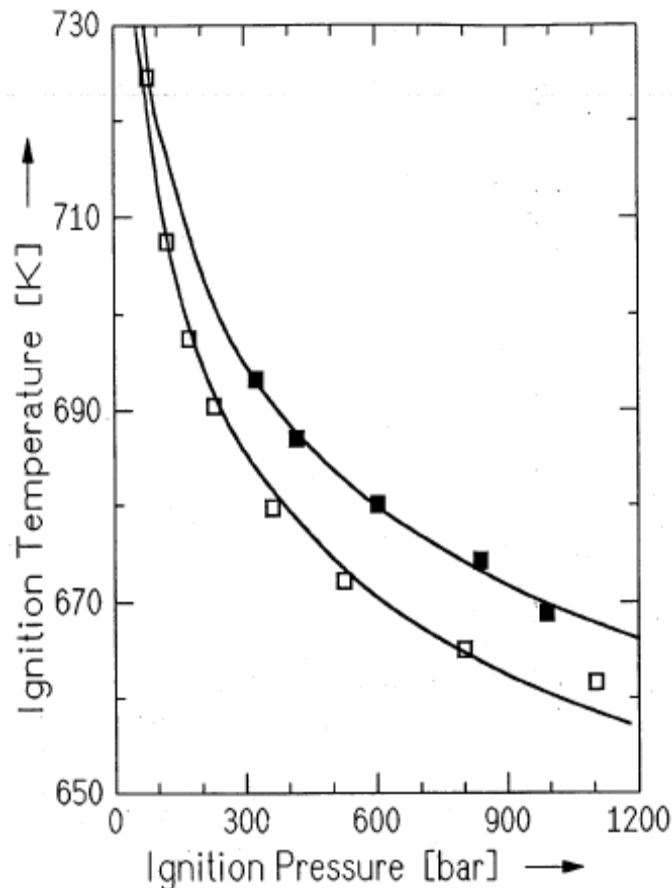
Figure 6.11 Ignition temperatures vs. pressure for stoichiometric methane-air and methane-air-water mixtures. White squares (□): methane-air only. Black sqaures (■): Methane-water (mole-ratios 3:7) fuel – air (from Steinle and Franck, 1995).

Sobhy et al. (2007) reported ignition temperatures for laminar inverse diffusion flames made by injecting air into mixtures of methanol (15-40 vol%/vol or 11.2-32.3 mole%) and water at 230 bar significantly lower than previous researchers. Precise ignition temperatures as a function of methanol concentration are not given, but ignition is reported for temperatures from 400 ^{o}C to as low as 350 ^{o}C. For comparison, Steeper (1992b) reported ignition temperatures of 380 ^{o}C for methanol concentrations over 35 mole% using oxygen as fuel, and Steinle and Franck (1995) found 30/70 mole% methanol/water mixtures ignited at around 410 ^{o}C using air as an oxidant at similar pressures. Sobhy and co-workers reported that the flames did not appear instantly upon injection of air. Instead, using NIR imaging, they noted that after air injection began, a hot

reaction zone formed near the reactor wall. This zone expands toward the center of the vessel and caused ignition upon reaching the nozzle tip. This process takes about 10 seconds. Moreover, the duration of the flame is very short, only 10 seconds or less depending on methanol concentration, even though the reactor volume and therefore quantity of fuel available for combustion is similar to that of Steeper et al., whose flames consistently lasted about 15 minutes. Given these discrepancies, it is likely that the ignition temperatures reported by Sobhy et al. are not representative of true spontaneous ignition of the hydrothermal flame at the reported temperature, but instead are the result of more complex phenomena, such as a wall-catalyzed reaction that then extends to the center of the reaction vessel to trigger flame ignition.

Continuous turbulent diffusion flames are poorly suited for measuring ignition temperatures because the ignition process is highly dependent on the nozzle configuration, reactor geometry and operating conditions. Ignition temperatures observed by researchers in different apparatuses, or even in the same apparatus with different injection nozzle configurations, vary greatly, and are significantly higher than those observed by Steeper et al. (1992b). For example, Weber (1997) began many of his experiments by igniting a 16.5 mass% (10 mole%) methanol fuel mixture at an inlet temperature of 520 $^{\circ}$C in the WCHB-1, whereas Wellig (2003) was able to ignite 16-20 mass% (9.7-12.3 mole%) methanol flames in the TWR (without the transpiring walls in place) at temperatures ranging from 460-490 $^{\circ}$C. Ignition temperatures as low as 452 $^{\circ}$C have been reported for the WCHB-3 reactor using only a 12 mass% (7.1 mole%) methanol fuel (Narayanan et al., 2008). In recent experiments in our laboratory at MIT, a 25 mass% (15.8 mole%) methanol fuel that ignited easily in the WCHB-1 reactor at inlet temperatures around 500 $^{\circ}$C using one nozzle configuration failed to ignite at all when a smaller diameter nozzle was used, even at fuel inlet temperatures over 550 $^{\circ}$C.

6.6.2. Extinction Temperature

One of the primary goals of continuous turbulent diffusion flame research is to demonstrate the ability to feed a sub-critical aqueous waste stream into the reaction vessel to minimize or totally avoid corrosion and plugging. In order to do this, the system must be designed with nozzle injectors that can handle two-phase flow, accommodate recirculation zones with adequate back

mixing to pre-heat, and ignite the cold feed injection and maintain stable flame combustion (LaRoche et al., 1997). The extinction temperature refers to the minimum temperature of fuel injected into the reactor at which flame combustion can be maintained. Experimentally, extinction is achieved by slowly lowering the inlet fuel temperature for a given set of operating conditions (fuel type, fuel concentration, pressure, etc.) until the flame is extinguished. Since the temperature at which flame extinction occurs is a complicated function of mixing, reaction rates, phase behavior, and flow dynamics, its study has not progressed far beyond measuring the temperature where flame extinction occurs for different reactor configurations.

Preliminary extinction temperature studies of continuous turbulent diffusion flames made by combusting methane and methanol aqueous fuel mixtures ranging in concentration from 10-30 mass% combusting with oxygen were first measured at ETH in the WCHB-1. The methane fuel inlet temperature could be lowered to 250 $^{\circ}$C before extinction occurred. Comparison of methane fuel extinction temperatures with the bimodal surface of the methane-water system (Shmonov et al., 1993) suggests that flame extinction may have been due to separation of the water-methane fuel into two phases. Methanol-water fuel mixtures, which are completely miscible even at ambient conditions, could be fed at temperatures below 100 $^{\circ}$C before flame extinction occurred (La Roche, 1996). In recent experiments in our laboratory, extinction temperatures below 100 $^{\circ}$C for methanol flames in the WCHB-1 were confirmed in later experiments by the authors. Preliminary experiments using 3 and 4 mass% (21.7 and 27.1 mole%) hydrogen fuel mixtures show much higher extinction temperatures of 335 $^{\circ}$C and 320 $^{\circ}$C, respectively.

Systematic extinction experiments as a function of fuel concentration for methanol flames were carried out in the WCHB-1 (Weber and Trepp, 1996; Weber, 1997). Flames were ignited using a 16.5 mass% (10 mole%) aqueous methanol fuel, and then the fuel concentration was changed to experimental conditions. Mixtures ranging from 4-25 mass% (2.3-15.8 mole%) methanol were tested. The nozzle geometry is shown on the left-hand side of Figure 6.7. The fuel stream temperature was systematically lowered until extinction occurred, and the temperature immediately before extinction was recorded. Multiple experiments at a given fuel concentration

showed extinction temperatures were repeatable to within 10 ^{o}C. The results are shown in Figure 6.12. Extinction temperatures ranged from 550 ^{o}C for a 4 mass% methanol fuel mixture to less than 100 ^{o}C for a 25 mass% mixture. Results from similar extinction experiments with methanol fuel performed in the WCHB-2 and TWR reactors are also shown. Figure 6.12 illustrates how widely extinction temperature measurements can vary with different reactor designs and nozzle configurations.
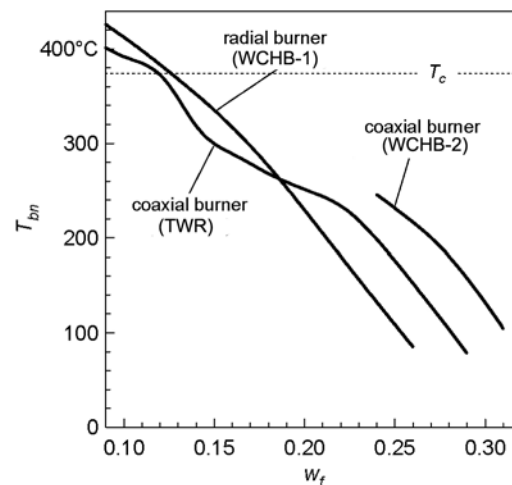

Figure 6.12 Extinction temperatures (T_{bn}) as a function of mass fraction of methanol in fuel (W_f) for hydrothermal flames in the WCHB-1 (Weber, 1997), WCHB-2 (Weber et al., 1999), and TWR (without transpiring walls in place) (Wellig, 2003). T_c is the critical temperature of water (374 ^{o}C) (adapted from Wellig, 2003).
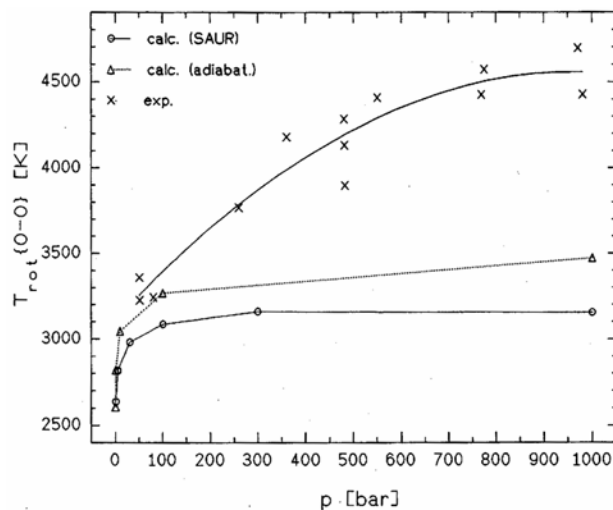
6.6.3. Flame Temperature

The flame temperature of laminar inverse diffusion flames of dense mixtures of methane or hydrogen in either supercritical water or argon were determined by measuring the spectra from OH radicals in the flame (Pohsner and Franck, 1994). The mixtures consisted of 30 mole% fuel and were pre-heated to temperatures of 450-500 ^{o}C at pressures ranging from 50-1000 bar. When oxygen was injected into the system, flames spontaneously appeared and would burn until the fuel was depleted, around 10 minutes for hydrogen and 30 minutes for methane. Rectangular slit nozzles, measuring 2 mm in length and 0.1 mm in length, were used to give a larger area from which to gather emission spectra. The resulting rotational temperature measurements, described in Section 6.5.1, were compared to adiabatic flame temperature calculations and results from models of 1-D counter flow diffusion flames (Saur et al., 1993). For flames in water, the spectroscopic rotational temperatures from the (0-0) transition increased with pressure.

The trend goes against thermodynamic theory, and resulted in temperatures at 1000 bar that were about 1000 $^{\circ}$C higher than predicted by adiabatic flame temperatures (see Figure 6.13). Spectroscopic measurements of flames in argon were in better agreement with adiabatic and model predictions, but followed a similar trend. Rotational temperature measurements from the (1-0) transition were lower than adiabatic and model calculations. Self-absorption of quanta from highly excited transitions in the cooler zones of the dense media was cited as one possible source for the high temperature predictions. Higher or incorrect rotational temperatures can also be reported if all the molecular degrees of freedom are not in equilibrium (Franck and Wiegand, 1996).

Figure 6.13 Pressure dependence of rotational flame temperature derived from analysis of OH-(0-0) transition emission spectra for 30/70 mole% methane/water mixture, compared to adiabatic flame temperature calculations and model predictions from Saur (1993) (from Pohsner and Franck, 1994).

Measurements of flame temperatures for low fuel concentration, continuous turbulent diffusion flames using thermocouples have had more success. For instance, Wellig (2003) measured the temperature in the combustion chamber of a continuous turbulent diffusion hydrothermal flame for a 16 mass% (9.7 mole%) methanol fuel mixture as a function of inlet temperature using two Type-S thermocouples. The thermocouple tips were positioned on the axis of the 50 mm by 9 mm ID cylindrical combustion chamber 27 mm and 50 mm (at the chamber exit) away from the fuel nozzle exit. Type K thermocouples were also positioned in the fuel nozzle (ID 2.1 mm) to measure inlet temperature and 12 mm after the exit of the combustion chamber where it began mixing with a subcritical cooling water stream. The fuel inlet temperature was varied from 275-450 $^{\circ}$C, so the transition from a sub-critical to a supercritical feed could be studied. The results

are shown in Figure 6.14. Flame temperatures from 800-1200 ^{o}C were measured and were consistently 150-200 ^{o}C less than the calculated adiabatic flame temperature. When the fuel is injected into the combustion chamber, it must mix with the co-annular oxygen stream and be heated to auto-ignition temperature. The chamber can be divided into a mixing zone, where these events occur, and a reaction zone, where high temperature combustion takes place. From the measurements, it can seen that the mixing zone increases in size as the inlet temperature decreases, pushing the flame front closer to the exit of the combustion chamber. For the particular nozzle configuration and operating conditions in this experiment, a fuel inlet temperature of about 360 ^{o}C causes the flame front to move past the point 27 mm away from the fuel nozzle exit. Whether the flame front moves gradually as the inlet temperature is decreased or shifts suddenly due to the fuel inlet stream transitioning from a supercritical to sub-critical phase is not clear since the entire axial temperature profile of the combustion chamber cannot be determined with the fixed position thermocouples.

Similar experiments (Narayanan et al., 2008) were carried out in the WCHB-3 reactor, this time using a thermocouple that could be vertically displaced during the experiment to measure the axial temperature profile over the entire length of the combustion chamber (see Section 6.5.3). Fuel mixtures of 12 and 16 mass% (7.1 and 9.7 mole%) methanol at inlet temperatures of 402 and 383 ^{o}C, respectively, were combusted with oxygen at a system pressure of 250 bar. The temperature along the axis was measured every 4 mm. Corrections to the measured temperature to account for radiative heat losses were made. The results are shown in Figure 6.15. Large flame fluctuations caused the temperature measurements to vary widely for a given location. Simulations using a numerical model of the hydrothermal flame combustion process, discussed in Section 6.7.2, were also performed. The mixing and reaction zones can be easily identified from the axial temperature profile.
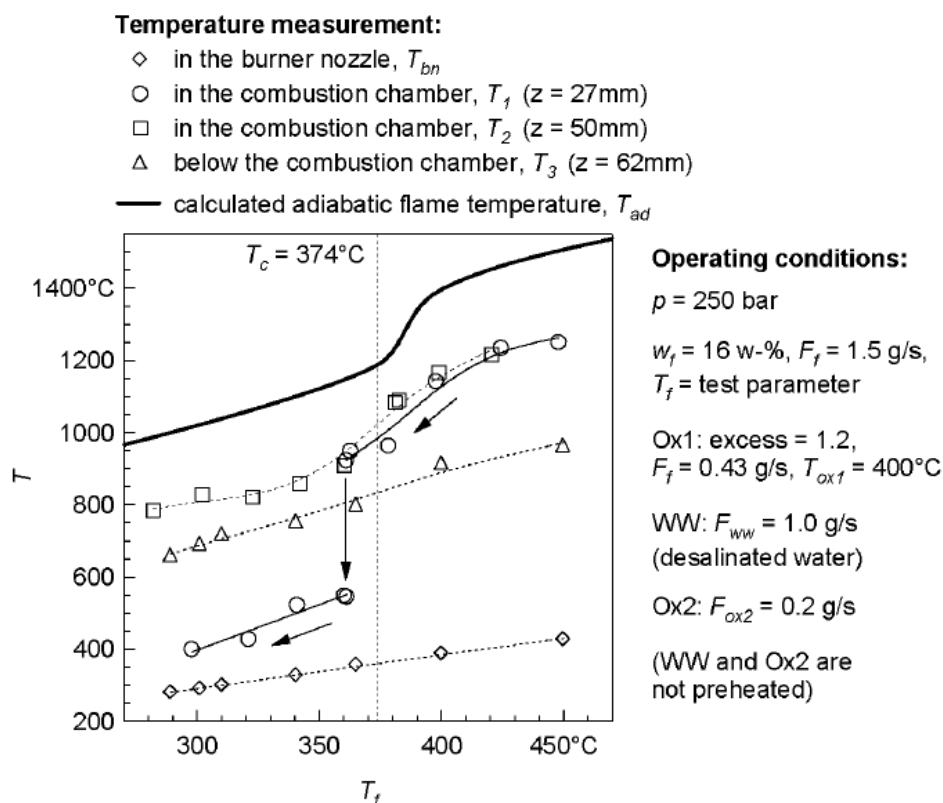
Temperature measurement:

◇   in the burner nozzle, T_{bn}
○   in the combustion chamber, T_1 (z = 27mm)
□   in the combustion chamber, T_2 (z = 50mm)
△   below the combustion chamber, T_3 (z = 62mm)
──   calculated adiabatic flame temperature, T_{ad}

Operating conditions:

p = 250 bar

w_f = 16 w-%, F_f = 1.5 g/s,
T_f = test parameter

Ox1: excess = 1.2,
F_f = 0.43 g/s, T_{ox1} = 400°C

WW: F_{ww} = 1.0 g/s
(desalinated water)

Ox2: F_{ox2} = 0.2 g/s

(WW and Ox2 are
not preheated)

Figure 6.14 Temperatures in combustion chamber as a function of fuel inlet temperature for a 16 mass% methanol fuel mixture in a continuous turbulent diffusion hydrothermal flame. The temperature immediately outside of the combustion chamber is also given (Wellig, 2003).
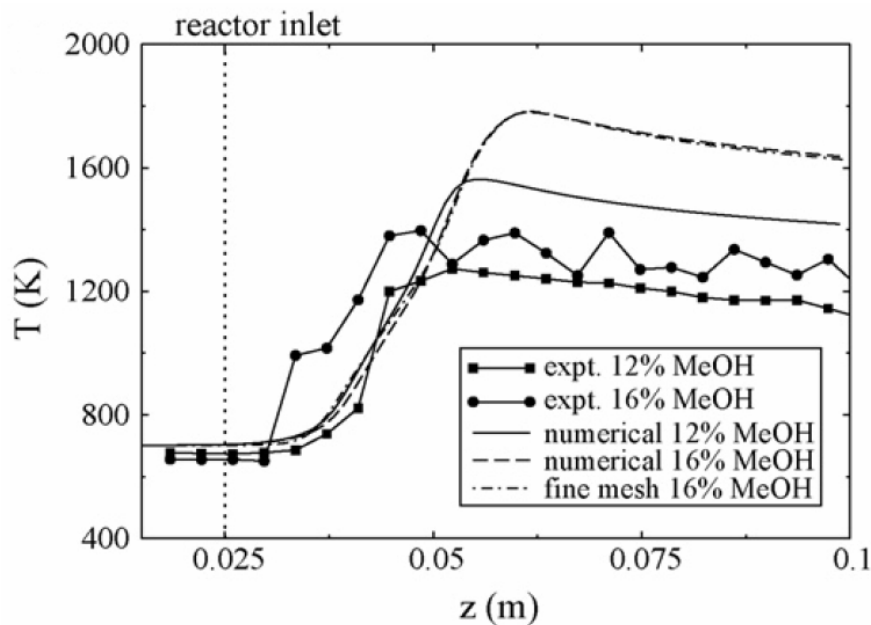
Figure 6.15 Variation of temperature along reactor axis for hydrothermal flames made with 12 and 16 mass% methanol mixtures. Experimental measurements and model results are shown for each case (Narayanan et al., 2008).

Further experiments studying the effect of inlet temperature and fuel inlet flow rate on the axial temperature profile were performed (Príkopský, 2007). Generally, low fuel concentrations, low fuel inlet temperatures, and high fuel flow rates displaced the reaction zone farther down the length of the combustion chamber. Visual observations of the flame showed that the presence of the thermocouple had a large effect on the flame. The thermocouple changed the flame shape and the flame appeared to be "attached" to the thermocouple, moving with it as it traversed the combustion chamber.

Other attempts to measure flame temperatures using fixed thermocouples have not had much success. Sobhy et al. (2007) reported maximum temperatures from 970 to almost 1300 $^{\circ}$C from a thermocouple positioned 4 mm directly above the air injection nozzle for laminar inverse diffusion methanol flames in supercritical water, depending on methanol concentration. The flame was large enough to reach and envelop the thermocouple tip for some of these runs, but the position of the thermocouple with respect to the flame front in each run is not stated, so it is doubtful that the reported temperatures are accurate measures of actual flame temperatures.

Similarly, Serikawa et al. (2002) reported questionable flame temperature measurements for turbulent diffusion flames in their reaction vessel from an Inconel 600 sheathed Type-R thermocouple inserted along the reactor axis through the injection nozzle, with the thermocouple tip fixed at a position 5 mm from the exit of the nozzle. A supercritical water/air mixture was injected through the central nozzle and pure, unheated isopropyl alcohol was injected co-annularly. Isopropyl alcohol and water were injected at 3 mL/min and 47 mL/min, respectively, equivalent to a 6 mol% fuel mixture. The air flow rate was varied over a stoichiometric air/fuel ratio of 1.1-2.2. The measured temperature oscillated by ~250 $^{\circ}$C at regular 20-30 s intervals, indicating large variations in either fuel or air feed flow rates, but no explanation for the oscillations could be found. The maximum measured temperature increased from ~800 $^{\circ}$C at an air ratio of 1.1 to ~1100 $^{\circ}$C at an air ratio of 2.2, even though analysis of effluents indicated over 99.9% destruction efficiency at all conditions, indicating complete combustion had occurred. These results were contrary to those expected, and the researchers attributed the temperature rise to air having a low specific heat capacity, making it possible to heat the mixture to a higher

temperature. However, since the mass flow rate of isopropyl alcohol and water did not change, it is unlikely that the total heat capacity of the mixture would have changed in a way that large decreases in the flame temperature would be seen. A more likely explanation is that rapid mixing and quenching of the flame by the surrounding ambient fluid lowered the mixture temperature at the thermocouple position, and increasing the air ratio had the effect of increasing the initial velocity of the turbulent jet, giving it a higher momentum flux and allowing the jet to penetrate farther into the reactor.

6.6.4. Flame Front Visualization

Príkopský (2007) confirmed his observations from axial temperature profiles of the effect that fuel concentration and inlet temperature had on the position of the flame front by determining its position via imaging the overall luminescence and chemiluminescence of OH and CH radicals. For these studies, the axial temperature probe was not present in the combustion chamber. He also found that varying the excess O_2 fed to the hydrothermal flame and the system pressure had no significant effect on the position of the flame front. However, the fuel stream flow rate had no significant effect on the position of the flame front, contrary to observations made with the axial temperature probe. The difference was attributed to the presence of the thermocouple, noting that the flame would attach itself to the thermocouple when it was present. It was also observed that the mere presence of thermocouple inside the fuel inlet nozzle significantly affected flame front position, even though the thermocouple was not in the combustion chamber. This effect was attributed to an increased velocity profile for the incoming fuel stream.

6.6.5. Combustion Products

Hirth and Franck (1993) studied oxidation of methane both with and without flames in supercritical water, and reported the presence of CO, CO_2, H_2, and CH_3OH as major combustion products. The formation of formaldehyde, a major reaction product at lower pressures, was insignificant and higher alkanes were not detected. Similar results were found for the flame oxidation of ethane, with minor traces of alcohols, aldehydes, and carbonic acids detected. Hirth studied methanol selectivity ($[CH_3OH]/([CH_4]_{initial} - [CH_4]_{final})$) and the CO_2/CO ratio for reactions for excess methane in both flameless and flame oxidation and found that while

methanol selectivity increased as the amount of surplus methane increased for both flame and flameless oxidation, the presence of flames considerably lowered the methanol selectivity. The reaction zones for the cases of flame and flameless oxidation differ greatly. The reaction zone in laminar flames consists of a thin, hot flame front. A mole balance requires that the molar diffusion flux of reactants to the flame front be stoichiometric, so the amount of "surplus methane" in the system should have little effect on laminar diffusion flame combustion products. The hydrothermal flame effect Hirth and Franck observed was likely a combination of flame combustion followed by interactions between leftover oxygen after flame extinction and/or the reaction products with methane in the surrounding high temperature supercritical water environment to produce methanol.

Hirth and Franck also studied the formation of soot from inverse diffusion hydrothermal flames using supercritical aqueous mixtures of n-heptane and toluene as fuel. They found that the presence of supercritical water suppresses the formation of soot by performing similar experiments replacing water with argon. They also concluded that increased pressure suppresses soot formation from hydrothermal flames due to increased temperatures based on spectroscopic investigations, but future studies indicate that these spectroscopic measurements overestimated the actual flame temperature (Pohsner and Franck, 1994), so it is possible that some other pressure effect is responsible for soot suppression.

In Raman measurements of combustion products from studies of methane and methanol laminar inverse diffusion flames in supercritical water with oxygen showed significant amounts of CO_2 produced, regardless of whether flames were present or not. Measurable quantities of CO and H_2 were detected from methanol flames, but these amounts were not quantified (Steeper et al., 1992b).

When air is used as the oxidant, nitrogen is present in large quantities and the formation of NO_x in hydrothermal flames is possible. Sobhy et al. (2007) reported the formation of NO_x at concentrations ranging from 18-52 ppm in supercritical water using methanol as a fuel for both flame- and flameless oxidation. Significant amounts of CO (800-12,000 ppm) were also

detected, and the amount of CO produced was always proportional to the amount of CO_2 produced. These results run contrary to those from the Ebara Research Company in Japan, who detected CO concentrations as low as 1 ppm and no traces of NO_x for continuous turbulent diffusion flames made using isopropyl alcohol and air (Sato et al., 2001; Serikawa et al., 2002). Príkopský also only detected CO_2 and O_2 after analyzing the reactor gas exhaust from a methanol/oxygen turbulent diffusion hydrothermal flame with a gas chromatograph, although CO was not looked for specifically (Príkopský, 2007). It is possible that the production of NO_x and CO in laminar diffusion flames was characteristic of the type of the flame. Laminar diffusion flames consist of a thin flame front at close to adiabatic flame temperatures dividing fuel rich and oxidant rich regions, which could favor the production of CO and NO_x. Turbulent flames could undergo sufficient mixing before combustion to result in a fuel-lean mixture that promotes complete combustion to CO_2 at low enough temperatures to avoid the formation of NO_x. Further studies are needed to confirm how flow conditions affect reaction products.

6.6.6. Destruction Efficiency

The destruction efficiency, defined as the percentage of fuel fed to the reactor that is oxidized, is very high in turbulent diffusion hydrothermal flame processes. Destruction efficiency is measured by analyzing the reaction products and performing a species balance, usually a carbon balance, to account for all the fuel fed to the reactor. Since destruction efficiencies of over 99% for residence times of less than 100 ms are common for hydrothermal flame processes, the destruction efficiency is usually measured and reported as a process parameter of secondary interest. No in-depth studies attempting to maximize destruction efficiency have been performed. Destruction efficiencies are not relevant to laminar diffusion flame studies since the flames extinguish long before all the fuel in the reactor is used up in the reaction.

LaRoche (1996) reported destruction efficiencies of methane and methanol feeds ranging from 80-96% for estimated residence times and flame temperatures of 20-50 ms and 900-1100 ^{o}C, respectively. The measure of destruction efficiency was highly uncertain in these early experiments due to heavy dilution from cooling water flow in the reactor. Wellig (2003) achieved destruction efficiencies of methanol at subcritical inlet temperatures of over 99.8% in

50-100 ms in the transpiring wall reactor (TWR) without transpiring walls in place, and over 99% with transpiring walls. Príkopský (2007) reported similar methanol conversion ratios of 97.85-99.99% for studies in the WCHB-3 reactor.

Sato et al. (2001) achieved destruction efficiencies of over 99.9% for reactions between isopropyl alcohol and a water/air mixture at 250 bar, regardless of whether or not flames were present. Serikawa et al. (2002) studied the oxidation of dioxins diluted in hexane using in the same experimental set-up. The sapphire window was removed and plugged for safety reasons, but the researchers assumed that hydrothermal flames were present based on the operating conditions. However, the previous studies in which hydrothermal flames had been observed had used isopropyl alcohol as a fuel and in greater molar concentrations than in the hexane/dioxin study. Also, no temperature measurement data supporting the presence of flames were reported. It was not clear whether flames were actually generated in this study. Despite this, destruction efficiencies of greater than 99.9% were observed for the dioxins. With claimed residence times of over 1 minute, the SCWO kinetics may have been sufficient to result in such high destruction efficiencies.

6.6.7. Corrosion and Salt Plugging Studies

Several studies on the effect of salts added to fuels on reactor corrosion and plugging in continuous turbulent diffusion flames have been reported. In these studies, the temperature profiles and flow fields inside the reactor were of primary importance, and the hydrothermal flame was seen only as an internal heat source to avoid the need to pre-heat waste streams to supercritical conditions.

The TWR reactor was designed specifically to test the concept of transpiring walls as a means to inhibit corrosion and plugging from salts in hydrothermal flame reaction systems. Experiments without salts present were performed first to characterize the axial and radial temperature profile of the flow field in the reactor as a function of transpiration intensity through the reactor walls. Temperature measurements were made using thermocouples inserted through ports throughout the reactor. Profiles indicated buoyancy-driven eddies developed downstream of the

hydrothermal flames in the transpiration zone in the absence of reactions, but that the flow field was stabilized when an additional 6 mass% methanol wastewater stream was injected co-annularly so that reactions persisted into the transpiration zone. In all cases, the temperature near the transpiring wall was well below the critical temperature of water (Wellig et al., 2005).

The experiments that included a 6 mass% methanol wastewater stream were repeated, this time with either 1 or 3 mass% sodium sulfate added to the wastewater stream. Transpiration intensity was varied to determine its effect on salt precipitation at the reactor walls. The amount of salt deposition in the reactor was determined by measuring the conductivity of the reactor effluent. Ionic chromatography was used to measure sodium ion concentrations as well. About 65% of the salt introduced into the reactor was detected in the effluent, regardless of transpiration intensity, type of transpiring wall, or salt content. Although no plugging occurred in the reactor, salt did collect on thermocouple tips, and salt residues did form in the upper flame/hot zone of the reactor, between the burner chamber and outer insert. This area was above the wall-protecting transpiration zone. Severe corrosion occurred along the outer diameter of the combustion chamber, but this non-load bearing component was easily replaced. The rest of the reactor operated without any visible signs of corrosion for 500 h, demonstrating the feasibility of using hydrothermal flames for remediation of salt-containing aqueous waste streams (Príkopský et al., 2007). Numeric modeling of the salt studies was carried out and is discussed in Section 6.7.2.

6.7. Modeling

Modeling reactive flow systems is difficult due to inadequacy of the sub-models that must be incorporated to fully describe the system. Reactive flow systems require a fluid dynamics model to describe fluid flow and behavior, a chemical kinetics model to describe reactions between species, and an equation of state (EOS) to describe mixture thermodynamic state variables and behavior, and models of the transport properties of the mixture. The task is made more difficult for hydrothermal flame systems because simplifying assumptions normally applied to reactive transport models can not be used. In hydrothermal systems, a constant density assumption cannot be made due to the large changes in density that occur near the critical temperature. The

presence of varying density complicates both the fluid dynamics model and the choice of a mixture equation of state. Assuming ideal gas properties also leads to large errors near the critical point, so robust, more accurate equations of state for supercritical mixtures are needed. Models for transport properties are also necessary since experiments data is not usually available at supercritical temperatures and pressures, especially for mixtures. The situation is worse for systems in which fluids transition from sub-critical to supercritical phases, often referred to as transcritical processes, especially if separate phases need to be accounted for at sub-critical conditions. The difficulties that arise and the special models and assumptions that must be made in modeling transcritical mixing and combustion processes in general has been addressed by the aerospace community in order to describe combustion in high pressure rocket engines, including subcritical droplet behavior in a supercritical environment and combustion and transcritical shear and mixing layers, jets, and sprays. Excellent review articles of the stud of these phenomena are available (Bellan, 2000; Yang, 2000). The discussion of these general phenomena is beyond the scope of this article. We will instead review the relatively few number of studies that focus specifically on modeling hydrothermal flame systems.

The defining traits of a hydrothermal system are high pressure and an aqueous environment in near critical or supercritical state over a significant portion of the flow field. Near the critical point, aqueous mixture properties deviate significantly from ideal behavior. As pressure increases, molecular transport mechanisms transition from translational motion in dilute gases gives way to collision-dominated in dense fluids. This causes the viscosity and thermal conductivity of the fluid to increase, while diffusion coefficients decrease. An equation of state capable of estimating the large density and enthalpy deviations from ideal behavior near the critical point of water is a necessary component of any hydrothermal flame model. Transport property models that accurately represent the dense fluid phases are also required. Often, simplifying assumptions about the fluid dynamics and kinetic mechanisms of the reactive flow are necessary to make the problem tractable. The assumptions and models, especially equations of state and transport models, commonly used in simulation studies of hydrothermal flames are presented here.

6.7.1. Laminar diffusion flame models

Saur et al. (1993) created a model for 1-D hydrogen and methane counter-diffusion flames in supercritical water based on an existing 1-D counter-diffusion flame model at ambient pressures. The model was extended from 1 bar to 3000 bar by incorporating models for fluid properties at the high temperatures and pressures encountered in hydrothermal diffusion flames. Thermodynamic properties such at density, heat capacity, fugacity, and molar enthalpy were estimated using a modified version of the pressure-explicit cubic equation of state developed by Christoforakos and Franck (1986), replacing the square-well potential with the Leonard-Jones potential to describe the attractive term, but keeping the Carnahan-Starling equation to describe the repulsive term. Correlations for transport coefficients (diffusivity, viscosity, and thermal conductivity) at supercritical temperatures and pressures were determined using the Chapman-Enskog theory for dense gases of hard spheres. The detailed kinetic reaction mechanism was not updated due to a lack of experimental data on the influence of pressure on the elementary free radical reactions. The reaction mechanism for the oxidation of methane contained 97 elementary reactions for 16 different reacting species. Most of the reactions were equilibrium reactions. The system of discretized differential equations was solved using an implicit method developed especially to handle stiff systems of equations.

The resulting model was used to simulate the oxidation of CO, CH_4, and H_2 in both supercritical water and argon. Mixtures of 30 mole% fuel were assumed. The inlet temperature of both fuel mixture and oxygen was set at 400 ^{o}C to ensure single, supercritical phase behavior at all times. The pressure was varied from 1 to 3000 bar. The results show that the width of the flame zone decreases significantly as pressure increases, narrowing to 5% of its original size as the pressure is increased from 1 to 1000 bar. The flame narrowing was attributed to low diffusion coefficients (high viscosity) at high pressures, which confine oxygen consumption to a smaller region. Maximum flame temperatures were predicted to increase with pressure up to about 1000 bar, at which point they leveled off and began to decline. The non-ideal behavior of the fluid properties increases. However, at the center of the flame where temperatures are highest, the fluid properties approach ideality.

6.7.2. Turbulent diffusion flame models

Simulations of turbulent diffusion flames require a turbulence model. There are several well known, mature commercial computational fluid dynamics (CFD) software packages that offer a variety of turbulent flow models, as well as modules to describe reactions and fluid properties. Several studies on turbulent diffusion flame models have taken advantage of these simulation tools to model hydrothermal flame processes.

Michelfelder et al. (1996) used a program named CAST (Computer Aided Simulation of Turbulent Flow) to create an early model of oxidation of a dilute methanol/water fuel mixture initially at 500 ^{o}C and 500 bar. The program could model two-dimensional laminar or turbulent flow using the finite volume method. Thermodynamic properties were calculated using a high-pressure PVT-EOS with mixing rules for the mixture components(Christoforakos and Franck, 1986), although above 625 ^{o}C it was noted that an ideal mixing assumption gave nearly identical results. The simplified kinetic model assumed a diffusion dominated system in which instantaneous reaction upon mixing of fuel and oxygen occurred. Although temperature and velocity profiles for the axi-symmetric injection of fuel were calculated, a discussion of the results was not included.

A Three-Environment Model (3EM) was used to determine the shape of the extinction temperature of a turbulent diffusion hydrothermal flame with respect to extinction temperature as a function of methanol concentration in the aqueous fuel stream for a given nozzle configuration (Weber and Trepp, 1996). The 3EM is a Lagrangian model that combines turbulent flow, mixing, and chemical reactions. Since the model is developed from the viewpoint of an observer moving with a fluid particle, it does not translate back to a Eulerian reference frame from which temperature or concentration profiles as a function of position can be extracted. Instead, the two inlet streams are divided into entering environments, while the exit separated into leaving environments. The model is a theoretical representation of how the environments age and mix, and can be thought of as tracking when and how many fluid particles go from the entering environment (inlet streams) to the leaving environment (exiting stream), where reactions can occur. An Arrhenius type reaction is used to describe the system kinetics, with the reaction

assumed to take place at the adiabatic flame temperature. By lowering the inlet stream temperature, the temperature at which flame extinction theoretically occurs can be found. The 3EM model was modified by adding an enthalpy term to account for the energy required to heat and "dissolved" from subcritical to supercritical conditions. The enthalpy term is based on heating a fluid droplet. Despite the many simplifying assumptions made in the model, correspondence between theoretical and experimental results, both described in (Weber, 1997) in detail, was satisfactory. Criteria and operating conditions that would allow lower fuel concentrations to be used in stable turbulent diffusion hydrothermal flames were identified using the model. Despite its apparent success, the 3EM model was abandoned in future studies for CFD simulations that could be easily related to reactor geometries and operating conditions.

Lieball (2003) performed computational fluid dynamics (CFD) simulations of flow and reactions in a simplified axi-symmetric geometry representing the TWR used by Wellig (2003) in order to determine the optimal flow conditions that would prevent the deposition of salt particles on the reactor wall and result in a favorable temperature field in the reactor. The software package CFD-ACE+ 6.4, developed by CRFDC (Zhou et al., 1999; Zhou et al., 2000), was used to perform the simulations. The parameters studied were the temperatures and flow rates of the bulk flow and the transpiration flow. The analysis was carried out by first considering a simulation in which no reaction was carried out. Due to turbulence, flow was modeled using the Farvre-averaged Navier-Stokes equations using the standard k-ε turbulence model. The density and enthalpy of the reactor mixture was calculated using the Peng-Robinson equation of state with constant volume translation and ideal gas state heat capacity correlations. Viscosities and thermal conductivities were approximated using a modified Chapman-Enskog theory for dense gases. An accurate correlation for the self-diffusion of water was used, and a general correlation valid for supercritical fluids was used for all other species. Simulations found that natural convection effects were always present in the system, leading to a less favorable flow field and wall protection than desired, but that with properly selected operating parameters good reactor performance could be expected. The temperature and intensity of the transpiring flow were found to have the largest effect on the flow field.

CFD calculations were validated through experimental measurements of the temperature field and residence time distribution (RTD) inside the TWR. For measurement of the RTD, a special sensor capable of detecting salt tracers and able to withstand the high temperature, corrosive environment was constructed and used. Finally, reactive CFD simulations were performed, assuming a one-step global reaction model, and compared against experimental data. Both qualitative and some quantitative agreement were found between the model and the experiments. Although the model correctly predicted the length of the supercritical region in the reactor, the predicted radial temperature profiles did not match experimental results.

Most recently, the steady-state combustion of supercritical methanol fuel mixtures with oxygen at inlet concentrations of 12 and 16 mass% in the WCHB-3 was modeled (Narayanan et al., 2008), this time using Ansys CFX software. As before, inlet temperatures were kept well above the critical temperature of water to ensure a single supercritical phase throughout the system. The standard k-ε turbulence model was used to model fluid flow, and the Peng-Robinson EOS with constant volume translation and ideal mixing rules were used. Transport coefficients were calculated in the same manner as used by (Lieball, 2003). The rate of combustion was assumed to be controlled by the rate of mixing by means of a simple eddy dissipation model, in which the reaction rate was assumed to be inversely proportional to the mixing time scale. Modeling results were compared to experimental results performed under identical operating conditions. The model did a reasonable job of predicting the flame position, but overestimated flame temperatures by 15-18%, as seen in Figure 6.15. However, significant variations were also observed in the experimental temperature measurements. The presence of the temperature probe, which enters through the fuel nozzle and occupies the axis of the reaction zone during operation, was also simulated. As observed experimentally, the presence of the thermocouple moves the flame significantly closer to the fuel inlet in the model results.

6.8. Conclusions

Existing literature covering experimental equipment and procedures and theoretical methods for understanding the behavior of hydrothermal flame processes served as a basis for this review. Hydrothermal flame experiments were divided into either studies of either laminar inverse

diffusion flame in a semi-batch system, or turbulent diffusion flames in continuous processes. Laminar inverse diffusion flame studies made up the bulk of early hydrothermal flame research, and focused on demonstrating the range of pressures, temperatures, and reactant concentrations under which they could be produced. The studies showed that a wide range of hydrocarbons could be used to produce flames in supercritical water. Turbulent diffusion flame studies occurred later, and focused on the application of hydrothermal flame to the remediation of aqueous waste streams by using the flame as an internal heat source, along with its fast kinetics, to avoid corrosion and salt plugging that plagues traditional SCWO processes. Methanol was the fuel of choice for these studies, due to its miscibility with water.

Experimental instrumentation and techniques used to carry out hydrothermal flame studies have been specifically adapted to the high pressure, high temperature environment. Because of high pressures, gaining access to probe flames inside the reactor vessel is very difficult. As a result, experimental techniques have mostly been limited to measuring bulk properties during and after the flame reaction. Temperature measurements are made mostly with metal-sheathed thermocouples, which have been successful in measuring system and stream temperatures before ignition and outside the flame. They have been used on a more limited basis for measuring low concentration, low temperature continuous, turbulent diffusion flames, but are not capable of withstanding high temperatures encountered in high concentration flames. Attempts to measure flame temperature using spectra from OH radicals had limited success, with significant measurement errors likely due to self absorption of quanta by surrounding media and non-equilibrium among molecular degrees of freedom.

Species identification and quantization is performed using gas- and high pressure liquid chromatography of reactor bulk effluents. Experimental results gathered in this manner must be scrutinized for effects caused by reactions that continue after the flame region, especially in semi-batch laminar flame systems. Some optical techniques have been developed to identify species *in situ*, but these are not yet capable of making quantitative measurements. Optical techniques have also been developed for identifying radical species in the flame and have been used to identify flame position. Given the difficulties in accessing high pressure chamber, along with small flame sizes, high temperature gradients, and the disruptive effects intrusive

instruments have on the flame structure, future experiments should focus on optical techniques for measuring temperature and composition.

Hydrothermal flame studies have been successful in characterizing flame ignition temperatures using several compounds as fuels. Studies done with laminar inverse diffusion flames or pre-mixed mixtures show ignition temperatures for supercritical mixtures are significantly lower than under ambient conditions and decrease with pressure. The characterization of flame extinction temperatures is not definitive at this time. These studies, performed with continuous turbulent diffusion flame jets, demonstrate that flame extinction depends heavily on the reactor and nozzle configuration, and operating conditions. Turbulent diffusion flame studies have demonstrated that the destruction efficiencies for reaction compounds is high, even for reaction times of only 100 ms or less.

The ability of these reaction systems to avoid plugging from salts included in inlet streams has also been demonstrated, but more quantitative studies are needed to demonstrate the feasibility of using hydrothermal flames to avoid corrosion and plugging in remediation of aqueous waste streams. This will require the coupling of experimental studies with CFD models of the reaction process. Current modeling studies of hydrothermal flame processes show qualitative agreement with experiments, but more development is needed to get to the point where quantitative validation can be achieved and realistic predictive models can be developed. These will require better sub-models, especially kinetic, turbulent, and mixture equation of state and transport models. These models will become even more important as hydrothermal flames are applied to new fields, such as thermal spallation drilling and the *in-situ* upgrading and conversion of heavy crude oils.

6.9. Proposed Mechanism for Use of Hydrothermal Flames in Thermal Spallation Drilling

Figure 6.16 depicts the likely conditions that will be found in a deep borehole environment. As the literature review above demonstrates, hydrothermal flame systems are ideally suited for the high pressure, high density aqueous conditions that will be encountered in the deep borehole

environment. The proposed mechanism for applying hydrothermal flames to thermal spallation drilling is to create turbulent diffusion hydrothermal flames, as has been done in the study of waste remediation.
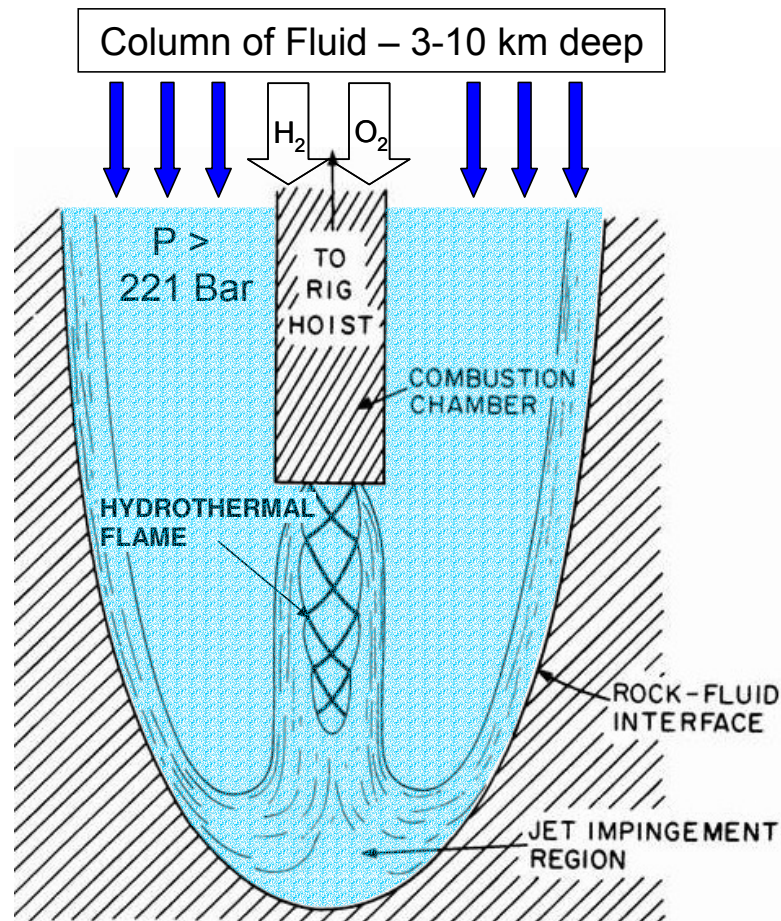

Figure 6.16 Depiction of conditions in deep borehole environment (adapted from Rauenzahn, 1986).

Based on the lessons learned from the literature review, two fuels will be used to create hydrothermal flames during experimental studies. Like most turbulent diffusion hydrothermal flame experiments performed to date, early experiments will use methanol. Since the downhole production of carbon dioxide has the potential of creating gas bubbles and wellbore control problems, later experiments will use hydrogen as a fuel since the only combustion products will be water. The experiments will still use mixtures of water and combustant as fuel rather than pure combustant for several reasons. First, the resulting lower temperature flames will be safer and easier to handle and less likely to lead to failures in the reaction vessel. Second, by varying the amount of water in the fuel mixture, the adiabatic flame temperature can be controlled. This

approach may have advantages when attempting to spall rocks that are traditionally considered non-spallable because they melt when a flame is applied to the surface. Being able to control the jet temperature would also be useful for regulating the heat flux to the rock surface. The remaining chapters describe these concepts and the mechanism by which hydrothermal flames can be used to spall rock in greater detail.

6.10. References

Alwani, Z. and G. M. Schneider (1967). "Druckeinfluss auf die Entmischung Flussiger Systeme 6. Phasengleichgewichte und Kritische Erscheinungen im System Benzol-H_2O Zwischen 250 Und 368 Degrees C bis 3700 bar." Berichte Der Bunsen-Gesellschaft fur Physikalische Chemie **71**: 633.

Armellini, F. J. and J. W. Tester (1993). "Solubility of Sodium-Chloride and Sulfate in Subcritical and Supercritical Water-Vapor from 450-550-Degrees-C and 100-250 Bar." Fluid Phase Equilibria **84**: 123-142.

Armellini, F. J., J. W. Tester and G. T. Hong (1994). "Precipitation of Sodium-Chloride and Sodium-Sulfate in Water from Sub- to Supercritical Conditions - 150 to 550-Degrees-C, 100 to 300 Bar." Journal of Supercritical Fluids **7**(3): 147-158.

Augustine, C. and J. W. Tester (2009). "Hydrothermal Flames: From Phenomenological Experimental Demonstrations to Quantitative Understanding." The Journal of Supercritical Fluids **47**(3): 415-430.

Bellan, J. (2000). "Supercritical (and Subcritical) Fluid Behavior and Modeling: Drops, Streams, Shear and Mixing Layers, Jets and Sprays." Progress in Energy and Combustion Science **26**(4-6): 329-366.

Bischoff, J. L. and K. S. Pitzer (1989). "Liquid-Vapor Relations for the System NaCl-H_2O - Summary of the P-T-X Surface from 300-Degrees-C to 500-Degrees-C." American Journal of Science **289**(3): 217-248.

Brown, M. S. and R. R. Steeper (1991). "CO_2-Based Thermometry of Supercritical Water Oxidation." Applied Spectroscopy **45**(10): 1733-1738.

Browning, J. A. (1981). Flame-Jet Drilling in Conway, N.H. Granite, University of California, Work Order Number 4-L10-2889R-1.

Christoforakos, M. and E. U. Franck (1986). "An Equation of State for Binary Fluid Mixtures to High-Temperatures and High-Pressures." Berichte Der Bunsen-Gesellschaft-Physical Chemistry Chemical Physics **90**(9): 780-789.

Danneil, A., T. Todheide and E. U. Franck (1967). "Vaporisation Equilibria and Critical Curves for Systems Ethane/Water and N-Butane/Water at High Pressures." Chemie Ingenieur Technik **39**: 816.

DiPippo, M. M., K. Sako and J. W. Tester (1999). "Ternary Phase Equilibria for the Sodium Chloride-Sodium Sulfate-Water System at 200 and 250 bar up to 400 ^{o}C." Fluid Phase Equilibria **157**(2): 229-255.

Franck, E. U. (1992). "Combustion and Flames in Supercritical Fluids to 2000 bar." Recent Trends in High Pressure Research: Proceedings of the XIII AIRAPT International Conference on High Pressure Science and Technology, 7-11 October 1991, New Delhi, October 7-11, Oxford & IBH Pub., 501-506.

Franck, E. U. and G. Wiegand (1996). "High Pressure Hydrothermal Combustion." Polish Journal of Chemistry **70**(5): 527-543.

Hirth, T. and E. U. Franck (1993). "Oxidation and Hydrothermolysis of Hydrocarbons in Supercritical Water at High-Pressures." Berichte Der Bunsen-Gesellschaft-Physical Chemistry Chemical Physics **97**(9): 1091-1098.

Japas, M. L. and E. U. Franck (1985a). "High-Pressure Phase-Equilibria and PVT-Data of the Water-Nitrogen System to 673-K and 250 MPa." Berichte Der Bunsen-Gesellschaft-Physical Chemistry Chemical Physics **89**(7): 793-800.

Japas, M. L. and E. U. Franck (1985b). "High-Pressure Phase-Equilibria and PVT-Data of the Water-Oxygen System Including Water-Air to 673-K and 250-MPa." Berichte Der Bunsen-Gesellschaft-Physical Chemistry Chemical Physics **89**(12): 1268-1275.

Kritzer, P., N. Boukis and E. Dinjus (2000). "Review of the corrosion of nickel-based alloys and stainless steels in strongly oxidizing pressurized high-temperature solutions at subcritical and supercritical temperatures." Corrosion **56**(11): 1093-1104.

Kritzer, P. and E. Dinjus (2001). "An assessment of supercritical water oxidation (SCWO) - Existing problems, possible solutions and new reactor concepts." Chemical Engineering Journal **83**(3): 207-214.

La Roche, H. L. (1996). Wandegkühlter Hydrothermal-Brenner (WHB) für die überkritische Nassoxidation. Doctoral Thesis, Swiss Federal Institute of Technology (ETH).

La Roche, H. L., M. Weber and C. Trepp (1995). "Rationale for the Filmcooled Coaxial Hydrothermal Burner (FCHB) for Supercritical Water Oxidation (SCWO)." Proceedings of the 1st International Workshop on Supercritical Water Oxidation, Jacksonville, Florida, USA, February 6-9, WCM Forums, 125-133.

LaRoche, H. L., M. Weber and C. Trepp (1997). "Design rules for the Wallcooled Hydrothermal Burner (WHB)." Chemical Engineering & Technology **20**(3): 208-211.

Lieball, K. S. (2003). Numerical Investigations on a Transpiring Wall Reactor for Supercritical Water Oxidation. Doctor of Technical Sciences Thesis, Swiss Federal Institute of Technology (ETH), Available online at Available from: www.e-collection.ethz.ch.

Mather, A. E. and E. U. Franck (1992). "Phase-Equilibria in the System Carbon-Dioxide Water at Elevated Pressures." Journal of Physical Chemistry **96**(1): 6-8.

Michelfelder, B., B. Noll, M. Weindel, W. Eckl, N. Eisenreich and M. M. Herrmann (1996). "A High Pressure Combustion Cell Based on Numerical Flow Simulation and Reaction Zone Radiation Modelling." Proceedings of High Pressure Chemical Engineering. P. R. von Rohr and C. Trepp. Amsterdam, New York, Elsevier**:** 559 - 564.

Mitton, D. B., N. Eliaz, J. A. Cline and R. M. Latanision (2001). "An overview of the current understanding of corrosion in SCWO systems for the destruction of hazardous waste products." Materials Technology **16**(1): 44-53.

Narayanan, C., C. Frouzakis, K. Boulouchos, K. Príkopský, B. Wellig and P. Rudolf von Rohr (2008). "Numerical Modelling of a Supercritical Water Oxidation Reactor Containing a Hydrothermal Flame." Journal of Supercritical Fluids **46**(2): 149-155.

Pohsner, G. M. and E. U. Franck (1994). "Spectra and Temperatures of Diffusion Flames at High-Pressures to 1000 Bar." Berichte Der Bunsen-Gesellschaft-Physical Chemistry Chemical Physics **98**(8): 1082-1090.

Príkopský, K. (2007). Characterization of Continuous Diffusion Flames in Supercritical Water. Doctor of Technical Sciences Thesis, Swiss Federal Institute of Technology, Available online at Available from: www.e-collection.ethz.ch.

Príkopský, K., B. Wellig and P. R. von Rohr (2007). "SCWO of salt containing artificial wastewater using a transpiring-wall reactor: Experimental results." Journal of Supercritical Fluids **40**(2): 246-257.

Rauenzahn, R. M. (1986). Analysis of Rock Mechanics and Gas Dynamics of Flame-Jet Thermal Spallation Drilling. Doctoral Thesis, Massachusetts Institute of Technology.

Rauenzahn, R. M. and J. W. Tester (1989). "Rock Failure Mechanisms of Flame-Jet Thermal Spallation Drilling - Theory and Experimental Testing." International Journal of Rock Mechanics and Mining Sciences & Geomechanics Abstracts **26**(5): 381-399.

Sato, H., S. Hamada, R. M. Serikawa, T. Nishimura, T. Usui and H. Sekino (2001). "Continuous flame oxidation in supercritical water." High Pressure Research **20**(1-6): 403-413.

Saur, A. M., F. Behrendt and E. U. Franck (1993). "Calculation of High-Pressure Counterflow Diffusion Flames up to 3000 Bar." Berichte Der Bunsen-Gesellschaft-Physical Chemistry Chemical Physics **97**(7): 900-908.

Schilling, W. and E. U. Franck (1988). "Combustion and Diffusion Flames at High-Pressures to 2000 Bar." Berichte Der Bunsen-Gesellschaft-Physical Chemistry Chemical Physics **92**(5): 631-636.

Schmieder, H. and J. Abeln (1999). "Supercritical water oxidation: State of the art." Chemical Engineering & Technology **22**(11): 903-908.

Serikawa, R. M., T. Usui, T. Nishimura, H. Sato, S. Hamada and H. Sekino (2002). "Hydrothermal flames in supercritical water oxidation: investigation in a pilot scale continuous reactor." Fuel **81**(9): 1147-1159.

Seward, T. M. and E. U. Franck (1981). "The System Hydrogen - Water up to 440 ºC and 2500 bar Pressure." Berichte Der Bunsen-Gesellschaft-Physical Chemistry Chemical Physics **85**(1): 2-7.

Shmonov, V. M., R. J. Sadus and E. U. Franck (1993). "High-Pressure Phase-Equilibria and Supercritical PVT Data of the Binary Water Plus Methane Mixture to 723-K and 200-MPa." Journal of Physical Chemistry **97**(35): 9054-9059.

Sobhy, A., I. S. Butler and J. A. Kozinski (2007). "Selected profiles of high-pressure methanol-air flames in supercritical water." Proceedings of the Combustion Institute **31**: 3369-3376.

Steeper, R. R., S. F. Rice, M. S. Brown and S. C. Johnston (1992a). Methane and Methanol Diffusion Flames in Supercritical Water. SAND92-8474.

Steeper, R. R., S. F. Rice, M. S. Brown and S. C. Johnston (1992b). "Methane and Methanol Diffusion Flames in Supercritical Water." Journal of Supercritical Fluids **5**(4): 262-268.

Steinle, J. U. and E. U. Franck (1995). "High-Pressure Combustion - Ignition Temperatures to 1000 Bar." Berichte Der Bunsen-Gesellschaft-Physical Chemistry Chemical Physics **99**(1): 66-73.

Tester, J. W. and J. A. Cline (1999). "Hydrolysis and oxidation in subcritical and supercritical water: Connecting process engineering science to molecular interactions." Corrosion **55**(11): 1088-1100.

Tester, J. W., H. R. Holgate, F. J. Armellini, P. A. Webley, W. R. Killilea, G. T. Hong and H. E. Barner (1993). "Supercritical Water Oxidation Technology - Process-Development and Fundamental Research." Acs Symposium Series **518**: 35-76.

Wagner, W. and A. Pruss (2002). "The IAPWS Formulation 1995 for the Thermodynamic Properties of Ordinary Water Substance for General and Scientific Use." Journal of Physical and Chemical Reference Data **31**(2): 387-535.

Weber, M. (1997). Apparate einer SCWO-Anglage und deren Leistungsfähigkeit. Doctoral Thesis, Swiss Federal Institute of Technology (ETH).

Weber, M. and C. Trepp (1996). "Required Fuel Contents for Sewage Disposal by Means of Supercritical Wet Oxidation (SCWO) in a Pilot Plant Containing a Wall Cooled Hydrothermal Burner (WCHB)." Proceedings of High Pressure Chemical Engineering. P. R. von Rohr and C. Trepp. Amsterdam, New York, Elsevier**:** 565-574.

Weber, M., B. Wellig and P. Rudolf von Rohr (1999). "SCWO Apparatus Design - Towards Industrial Availability." Corrosion/NACE 1999, 54th Annual Conference & Exposition, San Antonio, Texas, USA, April 25-30, NACE International, Paper No. 258.

Wellig, B. (2003). <u>Transpiring Wall Reactor for Supercritical Water Oxidation</u>. Doctor of Technical Sciences Thesis, Swiss Federal Institute of Technology, Available online at Available from: www.e-collection.ethz.ch.

Wellig, B., K. Lieball and P. R. von Rohr (2005). "Operating characteristics of a transpiring-wall SCWO reactor with a hydrothermal flame as internal heat source." <u>Journal of Supercritical Fluids</u> **34**(1): 35-50.

Yang, V. (2000). "Modeling of supercritical vaporization, mixing, and combustion processes in liquid-fueled propulsion systems." <u>Proceedings of the Combustion Institute</u> **28**: 925-942.

Zhou, N., W. A. Peters, K. A. Smith and J. W. Tester (1999). "Chemical Process Models for Supercritical Water Oxidation of Toxic Organic Materials." U.S. Army Research Office, Research Triangle Park, (December).

Zhou, N., W. A. Peters, K. A. Smith and J. W. Tester (2000). "Chemical Process Models for Supercritical Water Oxidation of Toxic Organic Materials." U.S. Army Research Office, Research Triangle Park, (March).

Chapter 7: WCHB Reaction System Design and Construction

7.1. WCHB Reaction System Overview

In order to carry out experimental studies on the feasibility of thermal spallation in a deep borehole environment, an autoclave reactor system that could create a hydrothermal flame jet under simulated downhole conditions was designed and constructed. The design was based on the experimental reaction system described by Wellig (2003) that was used to perform hydrothermal flame research by the von Rohr group at ETH Zurich. The reaction vessel that forms the core of the system is a Wall-Cooled Hydrothermal Burner (WCHB), shown in Figure 6.6. This vessel was donated to MIT by the von Rohr group and was the first generation reactor (WCHB-1) they used in their initial hydrothermal flame studies (La Roche, 1996; Weber, 1997). The WCHB utilizes of three co-axial feed streams: the fuel feed, which travels down the center of the reactor, the oxygen feed, which is in the annulus surrounding the fuel feed and combines with the fuel in the combustion chamber, and the cooling water feed, which flows through the outermost annulus and forms a sub-critical thermal barrier that protects the reactor walls from the flame. The WCHB also has two sapphire windows for optical observations.

To operate the WCHB requires a large amount of auxiliary equipment. Figure 7.2 shows a process and instrumentation scheme of the overall system that is equipped to create hydrothermal flames using either methanol or hydrogen as a fuel. Liquid methanol is pressurized and fed by a pulseless flow plunger-type metering pump, while gaseous hydrogen is pressurized by a gas booster. In either case, the pure fuel is mixed with water delivered by another plunger-type metering pump to create a fuel mixture. Oxygen is pressurized by a gas booster. The fuel mixture and oxygen are heated to reaction temperature by custom-designed and constructed electrical resistance preheaters before entering the WCHB, where they mix in the combustion chamber and react, creating a continuous turbulent diffusion flame. The flame is quenched by cooling water inside the WCHB which is supplied by a triplex plunger piston pump. After leaving the WCHB, the effluents pass through a heat exchanger, where they are cooled to a
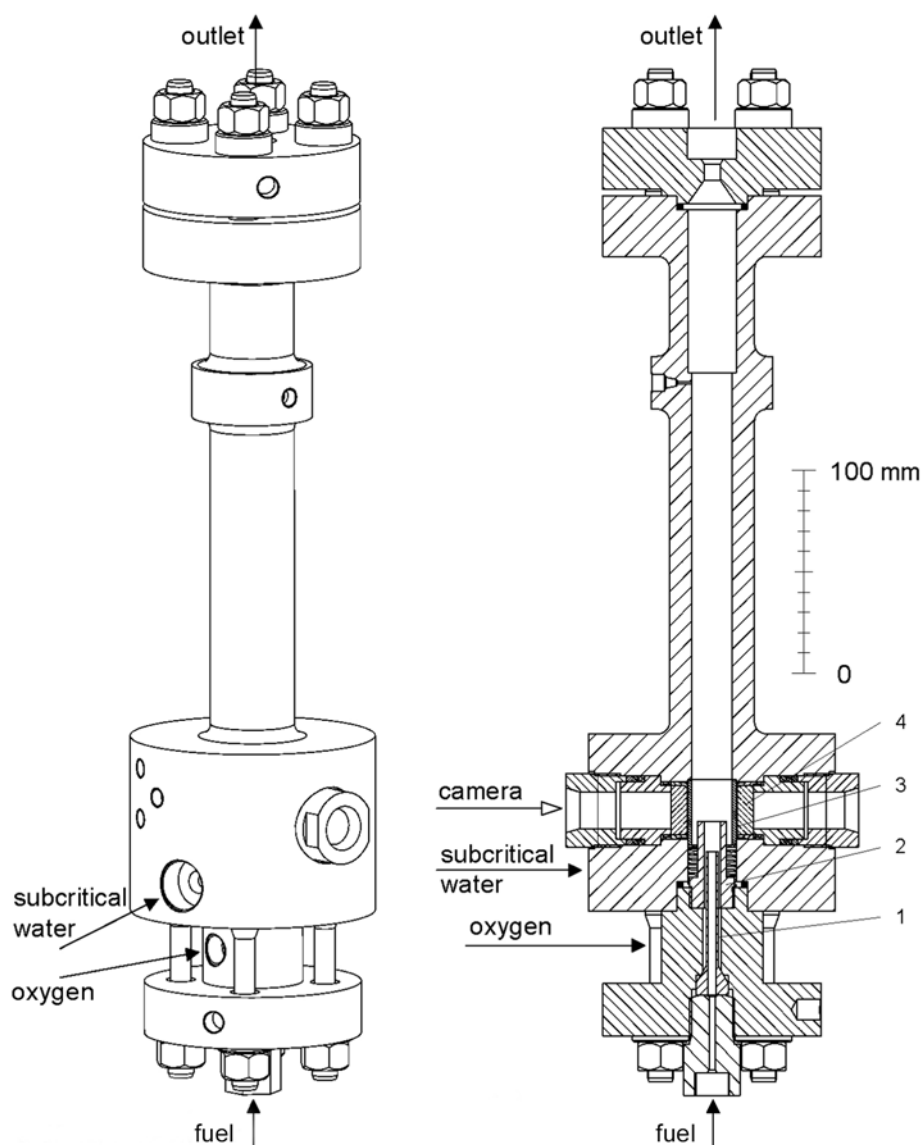
Figure 7.1 Wall-cooled hydrothermal burner (WCHB) donated to MIT by von Rohr group at ETH Zurich. 1.) Core tube of burner/fuel inlet 2.) Coaxial tube/oxygen inlet 3.) Cylindrical glass tube (not used in MIT experiments) 4.) Sapphire windows (adapted from Wellig, 2003).

temperature of 40 $^{\circ}$C or less. The effluent stream pressure is reduced to atmospheric through a back pressure regulator, which uses feedback control to maintain the system pressure. Pressure, temperature, and flow rate measurements are taken throughout the system by a data acquisition system and stored on a PC for later analysis. The WCHB reaction system is designed and calibrated to carry out all reactions at 250 bar, well in excess of the critical pressure of water. Safety systems are installed throughout the WCHB system to ensure a safe and controlled experimental environment. Stainless steel 316 (SS316) high pressure tubing is used throughout,
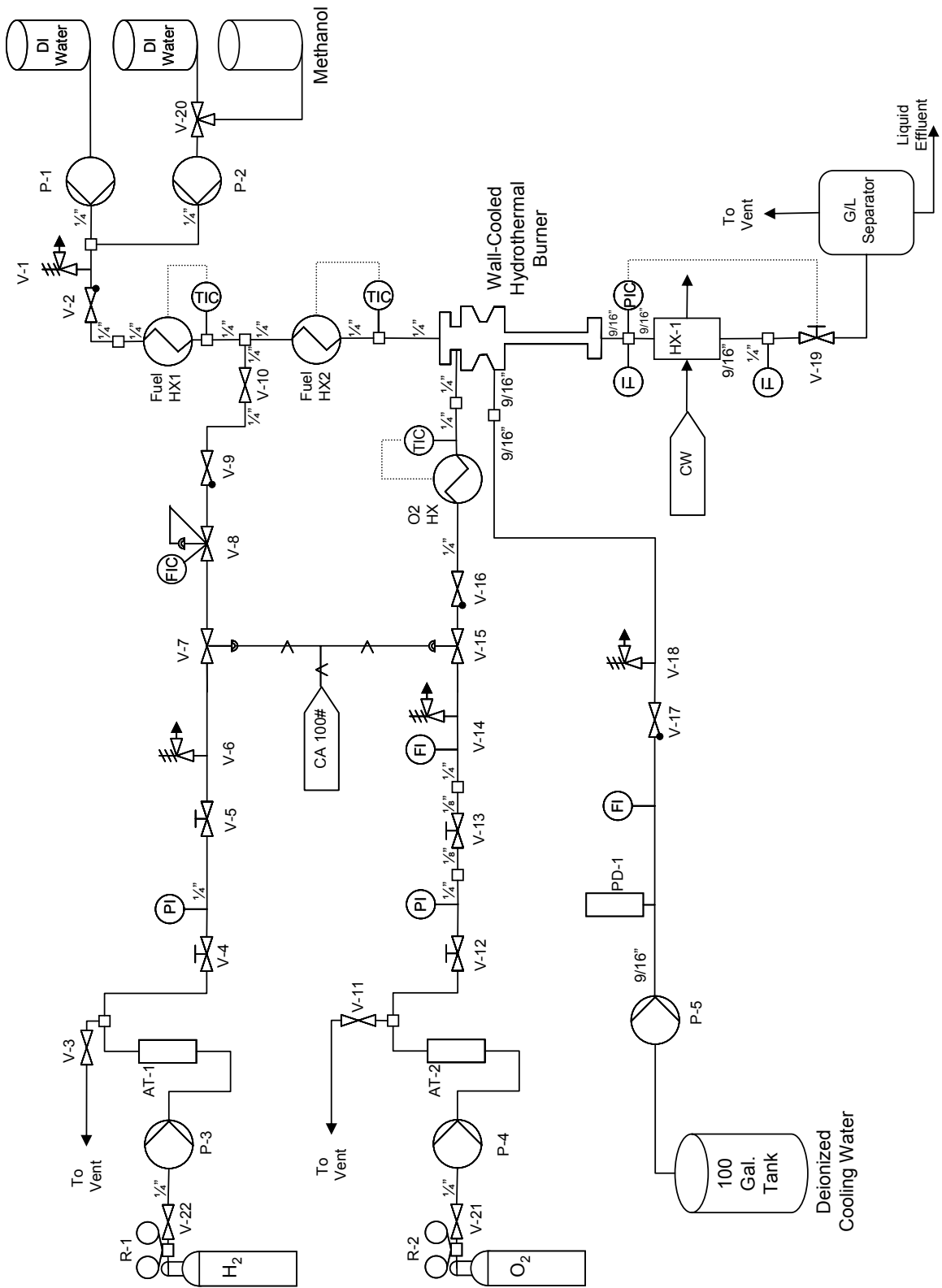
Figure 7.2 Process and instrumentation scheme of WCHB reaction system (see Table 7.1 for symbol key).

Table 7.1 Process and instrumentation diagram (Figure 7.2) symbol key.

| Symbol	Label	Description
Valves		
	V-7, V-15	Diaphragm pneumatic valve
		Fail Closed Air-Operated Isolation Valve
	V-5, V-13	1/16" Micro-metering Valve Cv = 0.004
	V-4, V-12	Forward Pressure Regulator
	V-19	Back Pressure Regulator
	V-1, V-6, V-14, V-18	Pressure Relief Valve
	V-2, V-9, V-16, V-17	Check Valve
	V-8	Flow Indicator and Controller
	V-20	Three-Way Valve
	V-3, V-10, V-11, V-21, V-22	Needle Valves
	R-1, R-2	Compressed Cylinder Pressure Regulator
Instrumentation and Control		
		Temperature Indicator
		Temperature Indicator Controller
		Pressure Indicator
		Flow Indicator Controller
Vessels		
n/a	AT -1, AT-2	Accumulator Tank
	n/a	Tank/Carboy
Miscellaneous Equipment, Fittings and Symbols		
	P-1, P-2,	SD-1 HPLC Pumps
	P-3, P-4	Haskel Gas Boosters
	P-5	Triplex Plunger Cooling Water Pump
	Fuel HX1, Fuel HX2	Fuel Preheaters
	O2 HX	Oxygen Preheater
n/a	HX-1	Process Fluid Cooling Heat Exchanger
n/a	PD-1	Pulsation Dampener
n/a	CA	Compressed Air
n/a	CW	House Cooling Water
	n/a	Pneumatic Line
	n/a	Instrumentation Signal Line

except in the preheaters and in connections to the WCHB, where either Hastelloy (HC-276) or Inconel 625 is used. The entire system is housed in an enclosure built of double-walled Lexan shielding to permit visual access during operation while protecting the operator from potential equipment failure.

7.2. Subsystems

The WCHB reaction system consists of several subsystems, which are described in detail below. Figure 7.2 can be used to follow the subsystem descriptions and identify equipment.

7.2.1. Fuel Mixture Delivery Line

The WCHB reaction system is designed to use either methanol or hydrogen as a fuel. The fuel is mixed with water to form a fuel mixture. The operation of the system varies depending on which fuel is used.

Methanol Delivery

Anhydrous methanol (>99.8% purity) is stored in a 4 L plastic carboy and is connected to a Dynamax SD-1 HPLC pump by plastic tubing with an inline HDPE filter. A 20 L plastic carboy filled with deionizied (DI) water is also connected to this SD-1 pump by plastic tubing with an inline HDPE filter. The DI water is used during startup, shutdown, and in experiments where pure water is desired to be the process fluid. A three-way valve is used to toggle between methanol and DI water during operation.

The methanol is pressurized and fed to the WCHB reactor by a Dynamax model SD-1 HPLC pump. The SD-1 pump is driven by dual independent linear piston drives, coordinated to deliver continuous pulseless flow. The SD-1 is fitted with 200 mL titanium pump heads and is capable of delivering up to 200 mL/minute of fluid at a pressure of 4,500 psi (310 bar), increasing to 6,000 psi (414 bar) at flow rates of 150 mL/min and less. The pump delivers flowrates accurate to <1%. The calibration of the SD-1 pumps is verified frequently. Because of the high accuracy of these metering pumps, separate flow rate measurement instrumentation is not required.

After the pump, the methanol is conveyed inside ¼" SS316 tubing to a tee where it is mixed with DI water to form the fuel mixture. The DI water is stored in a 20 L carboy and delivered by a second SD-1 pump. Fuel mixtures used vary, but a 25 wt% methanol/75 wt% DI water fuel mixture is typical. A pressure release valve set at 4500 psi (310 bar) is situated after the tee. The fuel mixture passes through a check valve, which permits flow in one direction only and prevents backflow of the fuel mixture to the SD-1 pumps.

The fuel mixture then passes through two electrically heated preheaters, labeled Fuel HX1 and Fuel HX2 in Figure 7.2 (9 kW and 6 kW nominal rating, respectively), where they are brought to reaction temperature before entering the WCHB reactor. The preheaters are described in detail in Section 7.3.

Hydrogen Delivery

Hydrogen (High Purity Grade 4.5) is stored in high pressure cylinders outside the system enclosure and connected to a manifold. This allows empty cylinders to be replaced during the course of an experiment. A dual stage pressure regulator on the manifold delivers hydrogen at a pressure of ~500 psi (~35 bar) to a Haskell AGT-32/62 dual stage gas booster. The gas booster is driven by compressed "house" air delivered from the building process plant at a pressure of about 90 psi (~6 bar). The gas booster can deliver hydrogen pressurized to 4500 psi (310 bar) at flow rates of up to 13 scfm (0.55 g/s). However, the pumping speed of the gas booster is not easily controlled or adjusted during operation. Instead, the hydrogen is delivered to a 20 in^3 (330 cm^3) SS316 accumulator tank. The gas booster operates until the accumulator tank reaches a pressure of about 4,500 psi (~310 bar) and then cuts out. It starts operation again when the accumulator pressure has dropped 200 to 300 psi (14 to 21 bar). The on/off operation of the gas booster is controlled by an adjustable air pilot switch.

The accumulator tank serves as a reservoir for the pressurized hydrogen and also reduces pulsations from the gas booster. A Tescom Model 26-1063D24-551 forward pressure regulator (FPR) reduces the pressure of hydrogen flowing from the accumulator tank to about 3800 psi

(~260 bar) and maintains this constant pressure to eliminate oscillations in flow downstream. The hydrogen then passes through a "fail-closed" air-operated safety isolation valve.

Next, a Bronkhorst EL-Flow Model F-133M thermal mass flow meter and controller is used to both measure the flow of hydrogen and control its flow rate. The meter has been calibrated to measure/control hydrogen flow at a system pressure of 3625 psi (250 bar) over a range of 0-5.65 scfm (0 - 160 L_n/min or 0- 0.24 g/s) at an accuracy of ± 1 % or less. The flow meter/controller is operated using software installed on the data acquisition PC. Under some operating conditions, the performance of the controller has been less than satisfactory. For this reason, flow can also be manually controlled using a Tescom Model CC-B16A21APV 1/16" micrometering valve with a flow coefficient of $C_v = 0.00125$ installed inline and using the Bronkhorst meter used to measure the flow rate. When not in use, the micrometering valve is left fully open.

After the flow meter, the hydrogen goes through a check valve that prevents flow reversal from the reactor and heat exchangers from damaging upstream equipment. The hydrogen mixes with DI water supplied by the SD-1 pumps and heated above its critical temperature by preheater Fuel HX1 (9 kW nominal rating). Above the critical point of water, hydrogen and water are completely miscible (Seward and Franck, 1981). The fuel mixture then enters preheater Fuel HX2 (6 kW nominal rating) where it is heated to its reaction temperature before entering the WCHB reactor.

7.2.2. Oxygen Delivery Line

Oxygen (Extra Dry $\geq$99.8% Purity) is stored in high pressure cylinders outside the system enclosure and connected to a manifold. A dual stage pressure regulator on the manifold delivers hydrogen at a pressure of ~500 psi (~35 bar) to a Haskell AGT-30/75 dual stage gas booster capable of delivering the oxygen at pressures of over 5000 psi. The gas booster operates periodically, boosting the feed gas to an operator set pressure, and then cutting out automatically until the oxygen pressure drops several hundred psi. Oxygen from the booster is collected in a stainless steel accumulator tank which also acts to reduce pressure pulsations from the gas booster. Oxygen from the tank flows through a Tescom Model 26-1012-24-387 forward

pressure regulator (FPR) which regulates the pressure at which oxygen flows to the reactor. The oxygen flows through an Autoclave Engineering Model 10VRMM ⅛" micrometering valve with a flow coefficient of $C_v = 0.004$. The micrometering valve, coupled with the set pressure from the FPR, is used to manually control the feed rate of oxygen to the system. The flow rate of oxygen is measured by a Thermal Instrument Co. Model 600-9 thermal mass flowmeter. The flowmeter is calibrated to read oxygen flow rates from 0 to 4.4 g/s at a system pressure of 250 bar to within ±2%. The oxygen then passes through a "fail-closed" air-operated safety isolation valve and a check valve before entering preheater O2 HX (3 kW nominal rating) where it is heated to reaction temperature and before entering the WCHB reactor.

7.2.3. Cooling Water Delivery Line

DI water is used as both cooling water and in the fuel mixtures throughout the system to decrease corrosion from the presence of ions such as Cl⁻ and F⁻, especially under supercritical conditions. House supplied DI water is used as cooling water in the WCHB system. Cooling water is stored in a 100 gallon (~400 L) carboy inside the system enclosure to ensure an adequate supply is available during experiments. The tank supplies cooling water to a Giant Co. Model P-57 triplex ceramic plunger pump, capable of delivering 1.4 gallons per minute (gpm) (5.3 liters per minute) at a pressure of 6,500 psi (450 bar). The pump is powered by a Reliance Electric Model P18G7403 5-HP electric AC induction motor controlled by a Reliance Electric Model MD60 variable frequency drive. The variable frequency drive is used to control the speed of the electric motor, up to 1750 rpm, that drives the triplex plunger pump. The flow rate is easily controlled with the variable frequency drive during the course of an experiment and once set to a value, remains fairly constant.

A FlowGuard USA Model DS-10 pulsation dampener is installed immediately after the triplex plunger pump to reduce pulsations from the pump. The pulsation dampener is a bladder charged with nitrogen to about 80% of the system operating pressure. During operation, pulsations from the triplex plunger pump compress the bladder, greatly decreasing the magnitude of the pressure pulse downstream. An analysis of the pulsation dampener performance is given in the following subsection. The cooling water flow rate is measured using a Flowmetrics, Inc. Model FM-4-8

turbine flow meter calibrated to measure flow rates of 0 to 95.4 g/s at 250 bar system pressure with an accuracy of ±0.5%. The cooling water then passes through a check valve and into the WCHB reactor.

Pulsation Dampener Performance

An analysis of the pulsation dampener performance was performed to determine its effectiveness in eliminating pulsations from the triplex plunger pump. The pressure in the cooling water line directly after the triplex plunger pump with and without the pulsation dampener in place was measured as a function of time at a sampling rate of 1000 Hz over a range of flow rates. Table 7.2 shows the measured cooling water pressure pulsation frequency and magnitude as a function of flow rate without the pulsation dampener in place. The calculated pulsation frequency is based on the pump rated capacity of 1.4 gpm (5.3 L/min)at 1420 rpm. For each revolution, each of the three plungers in the pump deliver one pulse of fluid. Therefore, the frequency of oscillations at full rated capacity is 71 Hz. The calculated pulsation frequency is scaled by flow rate from this number. The results show that not having a functioning pulsation dampener results in high frequency pressure fluctuations on the order of 200 psi (14 bar) in magnitude. Figure 7.3 shows the pressure pulsations from the triplex plunger pump with and without the pulsation dampener in place. The amplitude of the pressure pulsations with the pulsation dampener in place is greatly diminished and has no discernible frequency. Given the resolution of the data acquisition board is 8 psi, most of the pressure fluctuations are within system noise. The analysis shows that the pulsation dampener is very effective at virtually eliminating pulsations from the triplex plunger pump.

Table 7.2 Cooling water pressure pulsation frequency and magnitude as a function of flow rate with no pulsation dampener in place.

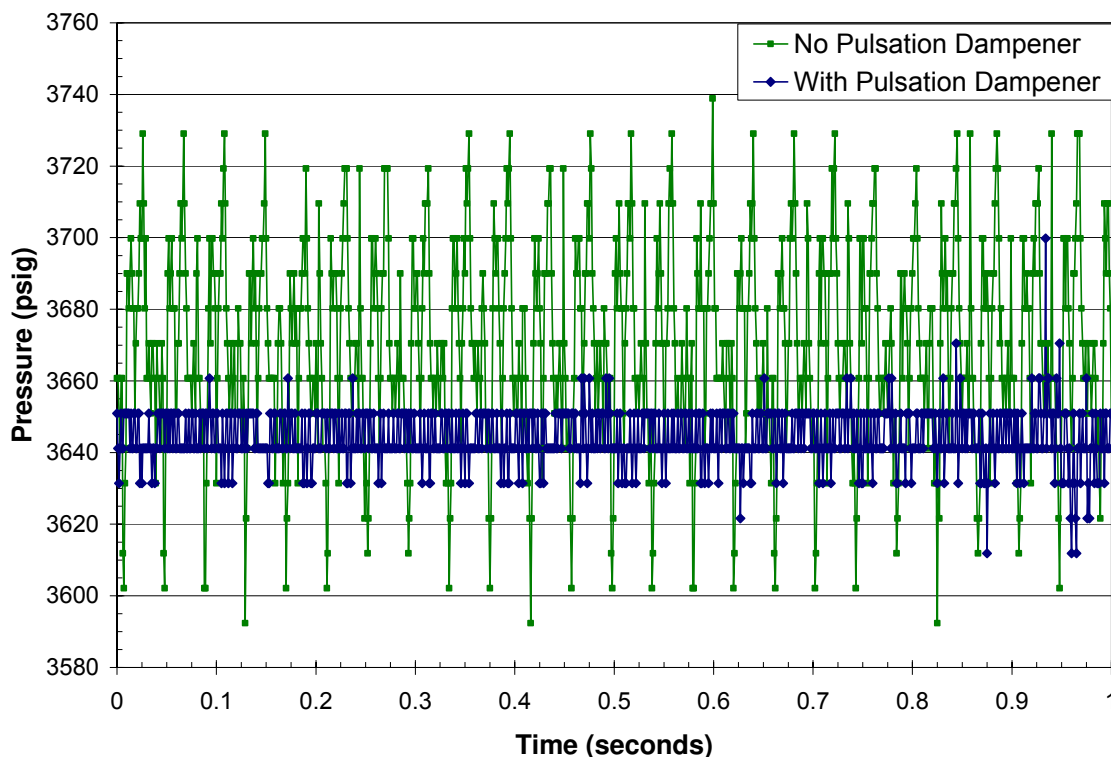| Cooling Water Flowrate (g/s)	Calculated Pulsation Frequency (Hz)	Measured Pulsation Frequency (Hz)	Measured Pressure Pulsation Amplitude (psi)
20	14.5	13	100
35	26	25	130
50	37.2	35	230
65	48.3	46	200
80	59.5	56	230

Figure 7.3 Pressure pulsations from triplex plunger pump with and without pulsation dampener in place. Cooling water flow rate = 35 g/s.

7.2.4. WCHB Reactor

The WCHB reactor, shown schematically in Figure 6.6, is a cylindrical vessel, about 0.5 m in length, constructed out of Inconel 625 with an internal diameter of 20 mm, which expands to 24 mm near the vessel entrance. Two sapphire viewing windows are located near the entrance. The vessel has an internal volume of 0.14 L, a maximum pressure rating of 420 bar, and a maximum temperature rating of 600 $^{\circ}$C.

The vessel is mounted vertically in the WCHB system as depicted in Figure 6.6, so that fuel, oxygen and cooling water enter the bottom of the reactor and flow upwards towards the reactor outlet. This orientation is necessary because if the reactor is inverted so that oxygen enters from the top, the vessel fills with oxygen during operation. If fuel were to ignite in an enriched high pressure oxygen environment, there is a possibility the reactor metal itself could melt or even ignite and result in vessel failure.

The fuel and oxygen inlet ports are located on the reactor head, which is attached to the vessel body by 4 bolts which are threaded into the face of the reactor entrance. A spring energized C-seal forms the high pressure seal between the reactor head and body. The same arrangement attaches the base, where the exit port is located, to the body. The cooling water port is located on outer radius of the vessel body, close to the entrance and near the window ports. Four small instrumentation ports, situated for the insertion of thermocouples to monitor temperatures at the outlet of the combustion chamber, are also located near the vessel entrance. Three of these are visible in Figure 6.6. Another small port is located on the body near the reactor exit. Because the WCHB was manufactured in Germany, the ports on the reactor require metric fittings. The fuel and oxygen inlet ports have female M16x1.5 threads designed to accept 6.35mm (equivalent to ¼") OD tubing, while the cooling water entrance and reactor exit ports have female M26x1.5 threads designed to accept 14.3 mm (equivalent to 9/16") OD tubing. The technical details of the small thermocouple ports could not be determined, but it was found that low pressure fittings Autoclave Engineering compression fittings (gland – SMN(10), sleeve – SSL(10), plug – SP(10)) could be used to seal them. Hastelloy (HC-276) fittings and tubing were used for all ports on the reactor due to their high temperature performance properties and tendency to resist galling. The fittings were sized and ordered through local vendors where possible, or purchased from companies in Europe when necessary (e.g. Sitec), or were custom machined at MIT. The fuel port adapter that forms the seal between the fuel inlet and fuel burner was specially fabricated by a firm in Germany.

7.2.5. Reactor Outlet Line

After exiting the WCHB reactor, the effluents pass through a Norman Filter Company 4100 Series 75 micron filter to remove any large debris resulting from rock spallation experiments. The effluent is then cooled in a counter-flow heat exchanger constructed out of three approximately 30" (0.75 m) lengths of ½" (12.7 mm) OD SS316 high pressure tubing inside ¾" (19.1 mm) OD tubing connected in series. Tap water is used as the cooling medium. A 0.5 micron filter then removes any fine particulates before the fluid is depressurized using a Tescom Model 26-1762-24-417A air actuated Back Pressure Regulator (BPR) coupled to a Tescom ER3000 Electronic Pressure Controller with PID feedback control. Feedback control is

necessary to control the system pressure during operation and prevent pressure spikes during flame ignition (Wellig, 2003). The ER3000 works by controlling the air pressure signal to the BPR based on the system pressure, set point pressure, and PID parameters input by the user. Compressed air at 100 psi (7 bar) is provided to the ER3000 by a compressed air cylinder with a regulator. The ER3000 is operated using software on the data acquisition PC. After being depressurized, the reactor effluent enters a tank which acts as a gas-liquid separator.

7.2.6. Data Acquisition

Temperature, pressure, and flow rate measurements from instrumentation in the WCHB system are recorded on a data acquisition (DAQ) PC using National Instruments (NI) Labview software. Voltage signals are acquired from the WCHB system via a NI BNC-2110 Board connected to a NI PCI-6023E DAQ card installed in the DAQ PC. Two Measurement Computing Company USB-TC thermocouple data acquisition devices connected to the DAQ PC were used for temperature measurements.

Flow measurement signals from the hydrogen, oxygen, and cooling water lines are all fed to Omega DP25B-S display meters mounted on a panel display. The display meters then condition the inputs to a 0-10 V signal and relay them to the NI DAQ board.

The pressures after the FPR's on the hydrogen and oxygen lines are measured by Omega Model PX906-5KGV pressure transducers and displayed on Dynisco Model 1290 panel displays, but are not collected by the DAQ system. The system pressure in the WCHB reactor is measured by a Setra Model 206-5000G pressure transducer with an accuracy of ±0.13% of full scale. The 0.1-10.1 V output signal is read by both an Omega DP25B-S display meter, which displays the system pressure and then passes the value along to the NI DAQ board, and the ER3000. The response time of the transducer to pressure changes is 5 ms. The fast response and high accuracy are needed so the ER3000 can respond quickly to system pressure changes.

Omega Type-K thermocouples were mounted in each of the preheater blocks as well as in the inlet feed streams after each of the preheaters. The thermocouples measuring the feed inlet

temperatures are placed as far into the reactor as possible in order to measure the feed stream temperatures just before they combine and combust. A thermocouple is also located at the outlet of the reactor to give a temperature of the mixed reactor effluents. A final temperature measurement is acquired just before the BPR to ensure the temperature does not exceed $70^{\circ}C$. Otherwise, damage to some of its components could occur. For some experiments, additional temperature measurements were made using Type-K thermocouples as appropriate.

7.2.7. Safety Systems

Safety is a top priority of the WCHB reactor system due to the inherent dangers of working at high pressures with pure oxygen and combustibles. Because of this, the WCHB pilot system is equipped with several safety features. Each feed line is equipped with a check valve to prevent the back flow of reactor fluids into delicate upstream equipment and a pressure relief valve to prevent the system pressure or any of the line pressures from becoming over-pressurized. The pressure relief valve on the cooling water line is located after the check valve so that a pressure buildup in the WCHB reactor itself can also be relieved. All tubing and equipment in the oxygen line were specially cleaned to remove any traces of oil or grease to mitigate the risk of an oxygen fire. Additionally, all valves on the oxygen line are slow-acting needle valves. Fast-acting ball valves can not be used in pure oxygen lines because of the risk of fires caused by adiabatic compression ignition downstream of the valve when opened.

The system is also equipped with an emergency shutdown system. Four events can trigger an emergency shutdown: 1.) low cooling water flow alarm from the turbine flow meter, 2.) high temperature alarm before the BPR, 3.) high pressure alarm in the WCHB reactor, or 4.) operator initiated shutdown via a "kill" switch. An energized circuit is connected in series to each of these alarms. The energized circuit is the signal to a solid state relay device that provides power to the SD-1 pumps and two self-venting solenoid valves. One solenoid valve provides an air pressure signal to air-operated "fail-closed" safety valves located on the oxygen and hydrogen feed lines. The other solenoid valve is installed on the ~90 psi (~6 bar) house air line that drives the hydrogen and oxygen Haskell gas boosters. If any of the alarms are triggered, the energized circuit is opened, killing the signal to the solid state relay device and resulting in a loss of power

to the SD-1 pumps and solenoid valves.   The SD-1 pumps are turned off. Likewise, the safety valves on the oxygen and hydrogen lines fail closed, preventing oxygen and hydrogen from entering the reactor and stopping further reactions. Drive air to the Haskell gas boosters is also stopped, preventing additional flow of pressurized hydrogen or oxygen to the system. The "kill" switch cuts power to the solenoid valves and SD-1 pumps directly.

The preheaters are equipped with their own separate safety system. The temperatures of the preheater blocks are monitored and have a cut out temperature, above which power is no longer delivered to the units to prevent them from overheating.

In the case of catastrophic tubing or other equipment failure, the entire system is enclosed in two layers of Lexan bulletproof sheeting. The first layer is intended to slow down any high velocity projectiles and the second layer to stop them completely. Ballistics tests performed off-site confirmed that the double layer Lexan design could stop a 9 mm projectile fired from a handgun at a distance of ~20 meters (Boettger, 2005). The enclosure is vented at the rate of 100 ft^3/min by the building fume hood system to prevent the buildup of oxygen, carbon monoxide or combustible gases.

7.3. High Pressure Preheaters

A great deal of effort was expended in the design and construction of the high pressure preheaters (Fuel HX1, Fuel HX2, and O2 HX in Figure 7.2). The preheaters heat the fuel and oxygen inlet streams to the point where auto-ignition occurs when the feed streams meet in the reactor, and are essential to operation of the WCHB reaction system. Three preheaters with nominal power ratings of 3, 6, and 9 kW were constructed in all.

7.3.1. Design

The preheaters were based on the design used at ETH Zurich in their hydrothermal flame reactor system (Wellig, 2003). The ETH preheaters were fabricated by casting a coil of high pressure Inconel 625 tubing in a bronze block and machining holes for the insertion of electrical resistance heating elements. The metal casting fabrication method proved to be difficult, costly,

and prone to tubing failure, mostly due to problems with liquid metal embrittlement. Therefore, an alternative design method in which high pressure tubing is coiled around a cylindrical block of highly conductive metal was developed. To maximize the heat transfer contact surface area between the block and high pressure tubing, the block was machined with a spiral groove for the high pressure tubing to rest in. As in the ETH experiments, the preheaters were designed to carry out experiments at a pressure of 3625 psi (250 bar).

Hydrothermal flame studies at ETH showed that the fuel and oxygen feed streams had to be heated to approximately 500 $^{\circ}$C for autoignition to occur in the WCHB combustion chamber. Therefore, the ability to preheat the feeds to a temperature of 600 $^{\circ}$C was desired. Typical flow rates in those experiments were 2 g/s fuel mixture and 1.5 g/s oxygen. Assuming the fuel to be pure water, and that the feeds entered the preheaters at 25 $^{\circ}$C, then 6.7 and 0.94 kW of heating were required for the fuel and oxygen feeds, respectively. These values represented the minimum system outlet temperature and power requirements.

The design of the preheaters was the result of a compromise between system requirements and limitations on material performance and system facilities. The greatest limitation was the tubing strength at high temperatures. Inconel 625 was chosen as the high pressure tubing material due to its high tensile strength at elevated temperatures. Inconel 625 high pressure tubing is available commercially in tubing sizes of 0.25" (6.4 mm) OD x 0.125" (3.2 mm) ID in 20 ft (6.09 m) lengths. Smaller diameter tubing was considered, but it was calculated that the pressure drop in the tubing would be prohibitively high. Based on the ANSI B31.3-1983 standard, the pressure rating for the ¼" (6.4 mm) tubing was found to be 3700 psig (255 bar) at 625 $^{\circ}$C. Above this temperature, the pressure rating decreases quickly, so 625 $^{\circ}$C was set as the upper limit for the preheater blocks during operation.

Copper (UNS C11000, 99.9% purity) was chosen as the material of construction for the preheater block due to its superior thermal conductivity ($k_c = 354$ W/m-K) and a high melting temperature of 1065 $^{\circ}$C. The design of the copper block is shown in Figure 7.4. The preheater block was designed with a left hand spiral thread ¼" (6.4 mm) deep and circular in cross section

for the high pressure tubing to rest in, maximizing the heat transfer contact surface area between the block and tubing. A spacing of 3 threads per inch (tpi) was chosen to allow a gap so that the tubing would rest flush with the outer surface of the preheater block when coiled into the thread. A major thread diameter of 4.5" (114 mm) and minor diameter of 4" (102 mm) were chosen to allow room for 6 Watlow firerod heating elements -¾" (19 mm) OD- in the block. Allowing for 5" (127 mm) of tubing length on each end of the block, this resulted in a preheater block length of 6" (152 mm) for a 20 ft (6.09 m) length of tubing. The center of the block is made hollow to reduce the thermal mass of the block and increase response time.
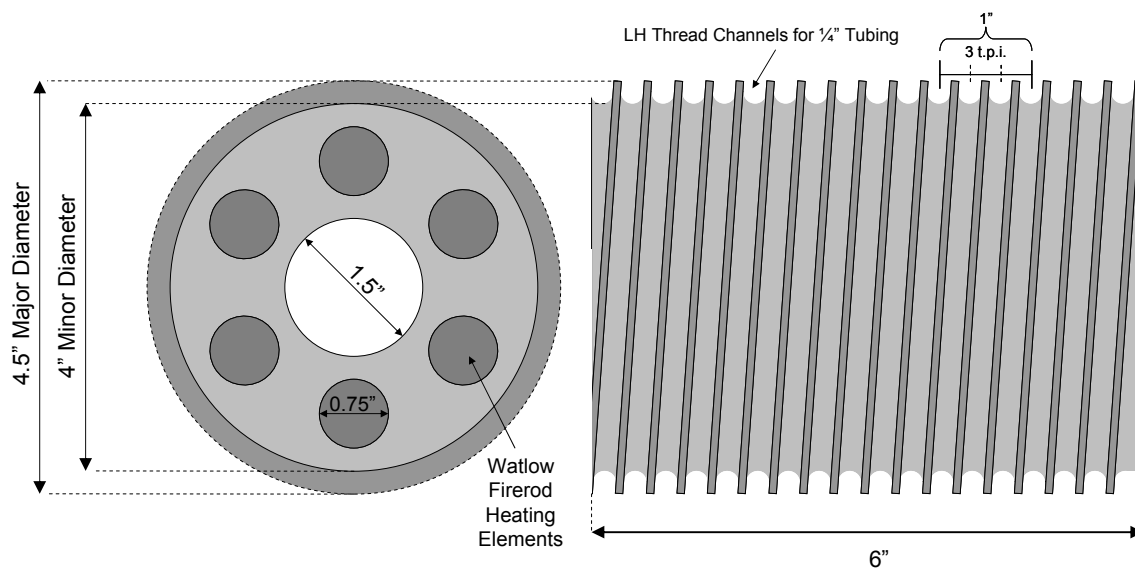
Figure 7.4 Design for copper preheater blocks.

The amount of thermal energy that the Watlow Firerod heating elements can deliver to the copper block depends on the temperature of the block during operation, the closeness of fit between the block and heating elements, and the total surface contact area for heat transfer. According to the manufacturer, as the operating temperature of the block increases, the maximum heat flux that can be generated at the surface of the heating elements decreases. Assuming a clearance of 0.006" (0.15 mm) between the heating element and block and 13 in^2 (84 cm^2)of heating element surface area, Table 7.3 shows that for a block temperature of 650 $^{\circ}$C, only about 6 kW of thermal energy can be delivered to the preheater block by the heating elements. This left little room for error to meet the system requirements for heating the fuel mixture feeds. Therefore, it was decided to have two preheaters in series for the fuel mixture line. The first would have six heating elements rated at 1.5 kW each for a total of 9 kW of

heating power, and the second would have six elements rated at 1.0 kW each for a total of 6 kW of heating power. As Table 7.3 indicates, the first preheater could take advantage of relatively low block temperatures to deliver a high heat flux, and the second would finish heating the fluid to its final temperature. The heating requirements of the oxygen preheater can be easily met by using six elements rated at 0.5 kW each for a total of 3 kW of heating power. The selected power ratings would allow much higher flow rates than the minimum requirements discussed above, giving the system a greater range of capabilities.

Table 7.3 Maximum heat flux per heating element and total heating power of heating elements used in preheater design.

	Max Heat Flux at Element Surface	Wattage per Heating Element	Wattage per 6 Heating Elements
Copper Block Temperature	W/in^2	kW	kW
T = 540 ^{o}C	150	1.95	11.7
T = 650 ^{o}C	82	1.06	6.3
T = 760 ^{o}C	42	0.54	3.3

7.3.2. Heat Transfer Model

The preheater design described in Section 7.3.1 only considers First Law energy balances between the heating elements and process fluid. It does not take into consideration heat transfer processes. The heating elements and copper block will be hotter than the exiting process fluid due to thermal resistance in the preheater. If these resistances are too large, the temperature difference could cause the electrical resistance heating elements to overheat and be damaged, or conversely, could prevent the process fluid from reaching its desired exit temperature when the copper block is raised to its maximum allowed temperature. To ensure that these events do not occur, a model of steady state heat transfer in the preheaters was developed.

Modeling heat transfer in the preheater was made difficult by the complex 3-D geometry of the preheater design. A tractable model was developed by making simplifying, conservative assumptions. Since the primary variable of concern was temperature difference between the

reactor block and process fluid, the model was developed by dividing the heat transfer pathway into three steps. Thermal resistance in three sections of the preheater was modeled:

- Conduction of heat through copper block from heating element to tubing wall,

- Conduction of heat through tubing wall from outer diameter to inner diameter,

- Convection of heat to process fluid from inner tube wall.

Conductive heat transfer in the copper block was modeled by treating the 6 electrical resistance heat sources in the block as a single cylindrical heating element at the center of the block. Temperature variation along the outer radius was assumed to be negligible, and each coil segment in the preheater was treated separately, so heat transfer along the length of the block was ignored. Although not realistic, this is a conservative estimate, since the actual block temperature at the entrance of the preheater will likely be much higher than in the model due to axial thermal conduction. This would lead to higher rates of heat transfer into the tubing and fluid. Assuming constant heat flux along the length of the heating element and applying boundary conditions, an energy balance results in the following equation:

$$\frac{Q}{2\pi L}\frac{\ln\left(r_o/r_i\right)}{k} = \Delta T \qquad\qquad \text{Eq. (7-1)}$$

where:

$$Q = \text{total heat input}$$
$$L = \text{length of heating element}$$
$$r_i, r_o = \text{inner and outer cylinder diameter, respectively}$$
$$k = \text{thermal conductivity}$$
$$\Delta T = \text{temperature change in block}$$

Simulations were performed using FLUENT software to determine the effective diameter ($r_{i,eff}$) of the simplified heat source. The heat flux from the heating elements was assumed to be constant around their perimeters, and the outer radius (in contact with tubing) was assumed to be at a constant temperature of 600 $^\circ$C. Figure 7.5 shows the resulting temperature profile in the copper block for the 3 kW preheater case, and Table 7.4 lists the results for the three different maximum heat inputs. The temperature profile near the outer radius is nearly concentric, indicating that approximating the heating elements as a single unit is a reasonable assumption. The effective diameter of the lumped heating element closely approximates the diameter of a

circle that would fit within heating element arrangement. Results for $r_{i,eff}$ from Table 7.4 do not vary much with heat input. To be conservative, the smallest value was chosen for the model.
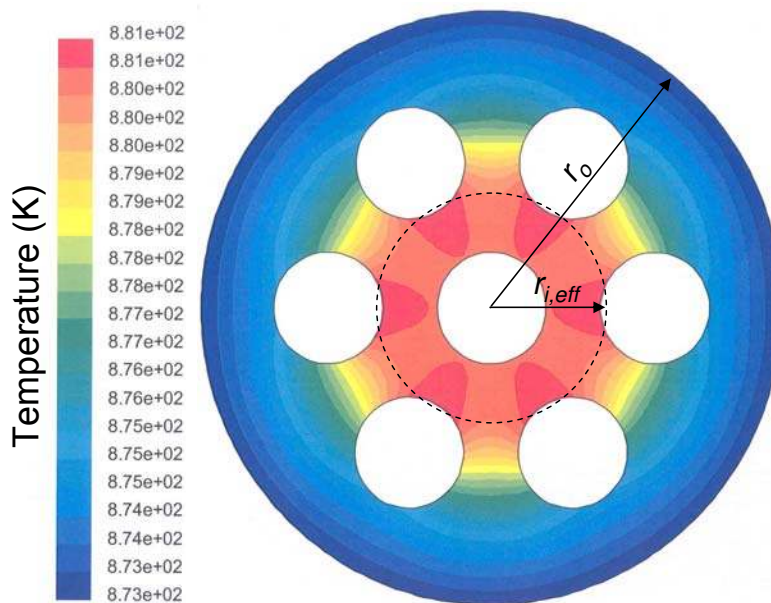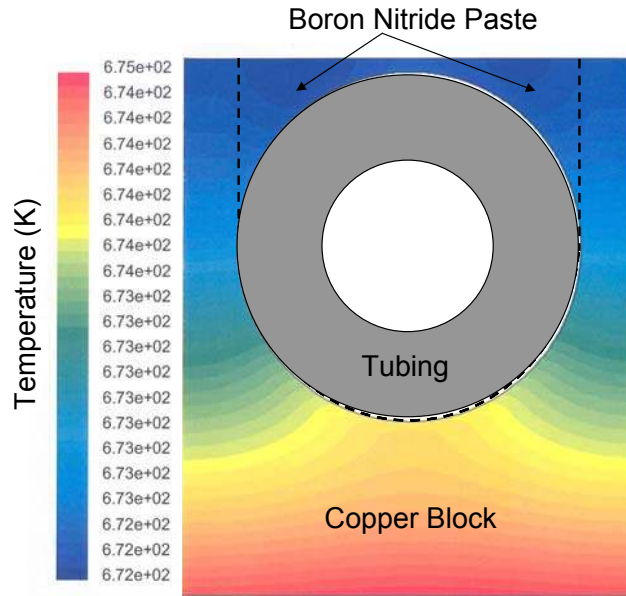

Figure 7.5 2-D temperature profile in copper block assuming constant heat flux from 500 W heating elements.

Table 7.4 Temperature differences and effective inner diameter of copper block from FLUENT simulation results.

Q (kW)	T_{max} (^{o}C)	T_{o} (^{o}C)	ΔT (^{o}C)	$r_{i,eff}$ (m)
3	608	600	8	0.22
6	617	600	17	0.21
9	627	600	27	0.20

The copper block is only in direct contact with the lower half of the tubing surface. Since the thread is ¼" (6.4 mm) deep, it completely envelops the tubing. The space above the tubing was filled with thermally conductive boron nitride paste. A Fluent model of the geometry in the near-tube region was made. Heat transfer from adjacent tube coils was ignored, since heat losses to the colder coil on one side would be partially offset by the hotter coil on the other side. The simulation results in Figure 7.6 show a temperature variation of only 3 ^{o}C in this region. Inconel 625 has a relatively low thermal conductivity, about 1/3 of that of the paste and 1/30th of that of the copper. It was found that the lower conductive resistances in the copper and paste and small

length scales allowed faster heat transfer in these regions than into the tube, so that the temperature around the perimeter of the tube could be treated as being essentially isothermal.

Figure 7.6 Temperature profile in near-tube region of preheater from FLUENT simulations.

Based on the simulation results, the outer tube diameter was assumed to be isothermal and at the same temperature as the outer radius of the copper block. Eq. (7-1) can be used to estimate the temperature drop in the tube wall, with appropriate values for Q, L, k, and the radii substituted.

Finally, for convective heat transfer from the inner tube wall to the process fluid:

$$q = \frac{Q}{2\pi r_{ID} L_T} = h\Delta T \qquad\qquad \text{Eq. (7-2)}$$

where:

$$q = \text{heat flux into fluid}$$
$$L_T = \text{tube length}$$
$$r_{ID} = \text{tube inner diameter}$$
$$h = \text{heat transfer coefficient}$$
$$\Delta T = \text{temperature change in block}$$

As a result of earlier assumptions in the model, Eq. (7-2) assumes a constant heat flux through the tube wall for the length of the reactor. Although this is not likely to be the case in reality, again it represents a conservative assumption. As mentioned earlier, heat fluxes into the tubing near the reactor inlet will likely be higher due to higher copper block temperatures than the

model assumes. By conservation of energy, the local heat flux into the tube near the tube exit would be lower than the model assumes, so the preheater-averaged heat flux will give a lower, more conservative estimate for the temperature difference between the block and exiting process fluid. Several correlations for the heat transfer coefficient were considered. The most conservative heat transfer coefficient values came from Gnielinski (1976):

$$Nu = \frac{(f/2)(\mathrm{Re}-1000)\mathrm{Pr}}{1+12.7(f/2)\left(\mathrm{Pr}^{2/3}-1\right)}$$

Eq. (7-3)

where:
Nu = Nusselt number
f = Fanning friction factor
Re = Reynolds number
Pr = Prandtl number

The constant heat flux assumption along the 20 ft (6.09 m) length of the tubing was used with the submodels to determine the process fluid and block temperature profile as a function of position for the three preheaters. The 9 and 6 kW preheaters were placed in series and used to heat the fuel mixture, which was assumed to be pure water. The 3 kW preheater was used to heat the oxygen inlet. A finite difference method was used to solve the model, with convergence insured by changing the grid interval spacing and checking that the solution did not change. The model results for 5 g/s of pure water at a pressure of 250 bar are shown in Figure 7.7. The model predicts a temperature difference of 70 °C between the process fluid and copper block at the preheater exit. For the oxygen preheater, the temperature difference is even smaller. The models indicate that the preheaters should deliver the desired fluid temperatures without overheating, especially given that the model makes conservative assumptions regarding heat transfer, and that flow rates used in practice (and therefore the heating required) will generally be much lower than those used in the model.
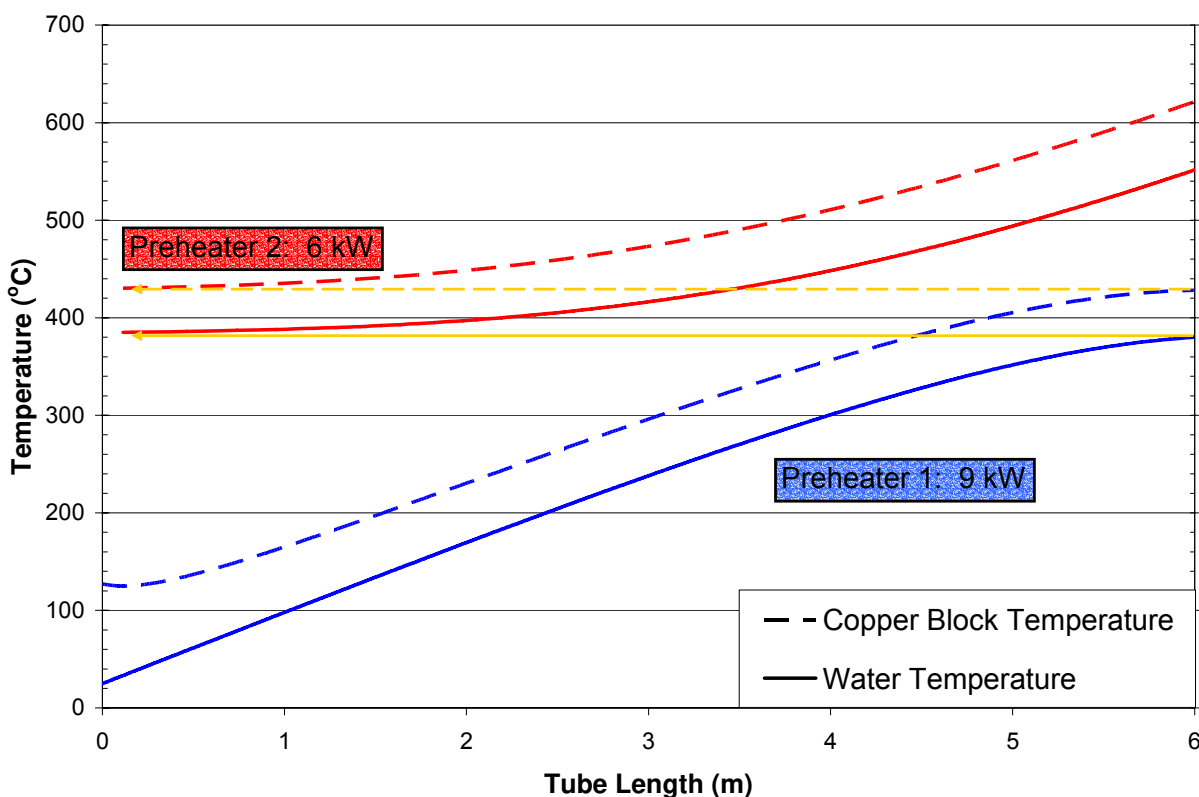
Figure 7.7 Model predictions of process fluid and copper block temperatures as a function of tube length for 9 and 6 kW preheaters.   Process fluid is 5 g/s water at P=250 bar.

7.3.3. Construction

Photographs of the preheater construction process are shown in Figure 7.8. Cylindrical copper blocks 4.75" (121 mm) in diameter and 7" (178 mm) in length were purchased. These blocks were turned down on a lathe to 4.5" (114 mm) and a 1.5" (38.1 mm) diameter hole drilled through the center. A thread with a 3 tpi pitch was then grooved to a depth of ¼" (6.4 mm) along entire length of the block using a ¼" (6.4 mm) diameter circular carbide bit. A left hand thread was required to allow the tool bit to "run out" the end of the block and avoid striking the lathe chuck. A sacrificial end where the copper block had been held in the lathe was removed with a horizontal bandsaw, and the copper block was moved to a milling machine where six undersized holes for the heating elements were drilled lengthwise through the block. The holes were reamed to their final diameter of 0.750" (19 mm). This minimized the clearance between the copper block and the Watlow Firerod heating elements (0.746"±0.002", 18.9 mm±0.05mm)to ensure a

tight fit and good heat transfer. A shallow hole for a 1/16" (1.6 mm) thermocouple element was also drilled into the end of the block to monitor the block temperature during operation.

A 20 ft (6.09 m) length of high pressure ¼" (6.4 mm) Inconel 625 tubing, coned and threaded at the ends, was then wrapped around the block. A special lathe set up was required to provide enough torque to bend the tubing while guiding it into the thread on the copper block. The threads were covered in a high thermal conductivity boron nitride paste to further enhance heat transfer between the block and tubing. The tubing was secured on the copper block by high temperature steel alloy clamps while still under tension on the lathe to prevent "springback" from the bent tubing from popping it out of the threads.

The heating elements were inserted into the ¾" (19 mm) holes in the block. A 1/16" (1.6 mm) Type K thermocouple was inserted into the end of the block. This end was designated the preheater exit so that the thermocouple would measure the block temperature at its hottest point. High pressure HC-276 tees were installed on the tubing at the exit of the preheater, and the tees fitted with Type K thermocouples to monitor the process fluid temperature. The finished preheaters were wrapped in insulation and installed inside a protective casing. The preheaters were then mounted in the WCHB reaction system next to the reactor entrance. Tubing lengths between the preheater exit and reactor entrance were kept as short as possible to mitigate heat losses.

Figure 7.8 Photographs of preheater construction process. From upper left: drilling center hole; grooving thread; drilling and reaming heating element holes; wrapping high pressure tubing around block into threads; block with tubing wrapped and secured with clamps; finished preheater with heating elements inserted.

7.3.4. Performance

The performance of the preheaters was evaluated during WCHB reaction system operation. After installation, it was discovered that the voltage in the system was only 208V. The nominal power rating on the heating elements assume a 240V electricity supply. The lower voltage has the effect of decreasing the maximum thermal output of the preheaters by about 25%. Fortunately, the preheaters had been designed with extra heating capacity, so this did not affect their performance in the system. Fuel mixture temperatures of over 500 ^{o}C in the reactor combustion chamber could be achieved for flow rates as high as 3 g/s while keeping the block temperature below its maximum allowed operating temperature of 625 ^{o}C.

Figure 7.9 shows the performance of the 9 kW preheater (Fuel HX1) compared to predictions of the model in Section 7.3.2 for various flow rates. The small difference between model and experimental values for the process fluid indicate that heat losses from the preheater are small. The model predictions for the copper block temperature at the reactor exit are much higher than experimental values, showing that the model was sufficiently conservative in its estimates as had been intended.

7.4. Movable Probe Assembly

7.4.1. Design and Construction

Data collection from the WCHB reactor as it was originally designed is limited by the number of ports available in the head of the vessel for instrumentation. Moreover, once instrumentation is installed via these ports, it is fixed in position, severely limiting the regions of the vessel that can be measured. A means of measuring or sampling a range of positions in the WCHB reactor space during operation was desired. For example, the ability to measure the temperature of the flame as a function of its position or to insert rock samples and other heat flux measurement equipment directly into the flame would greatly enhance the type and quality of experiments that can be performed with the WCHB system. Therefore, an apparatus capable of positioning a probe dynamically in the WCHB reactor during the course of an experiment while still
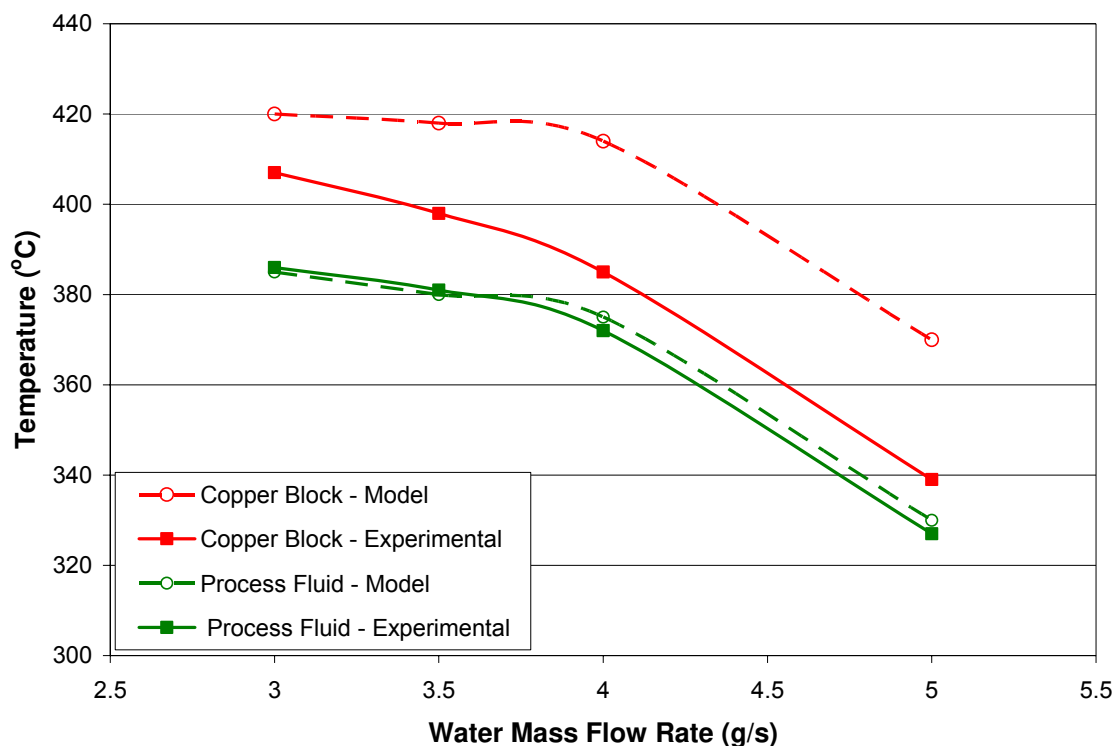
Figure 7.9 Experimental and model temperatures for copper block and process fluid for Fuel HX1 (9 kW nominal rating) preheater. Process fluid was water at P=250 bar.

maintaining system pressure was designed and constructed.   The apparatus was named the movable probe assembly.

The movable probe assembly consists of a piston mounted on a ¼" (6.35 mm) OD tube mounted inside a special cylindrical housing (Figure 7.10). The movable probe assembly is mounted at the WCHB reactor outlet, while the tube extends the length of the vessel to the combustion chamber. The piston has two Viton O-rings that center it and separate the process fluid from the hydraulic fluid used to move the piston. During operation, high pressure hydraulic fluid is injected or removed to move the piston, traversing the probe tip along the axis of the reaction vessel. The piston has about 3.25" (80 mm) of travel inside the housing. Another Viton O-ring at the exit of the cylindrical housing forms a high-pressure seal while allowing the rod to slide into and out of the assembly.
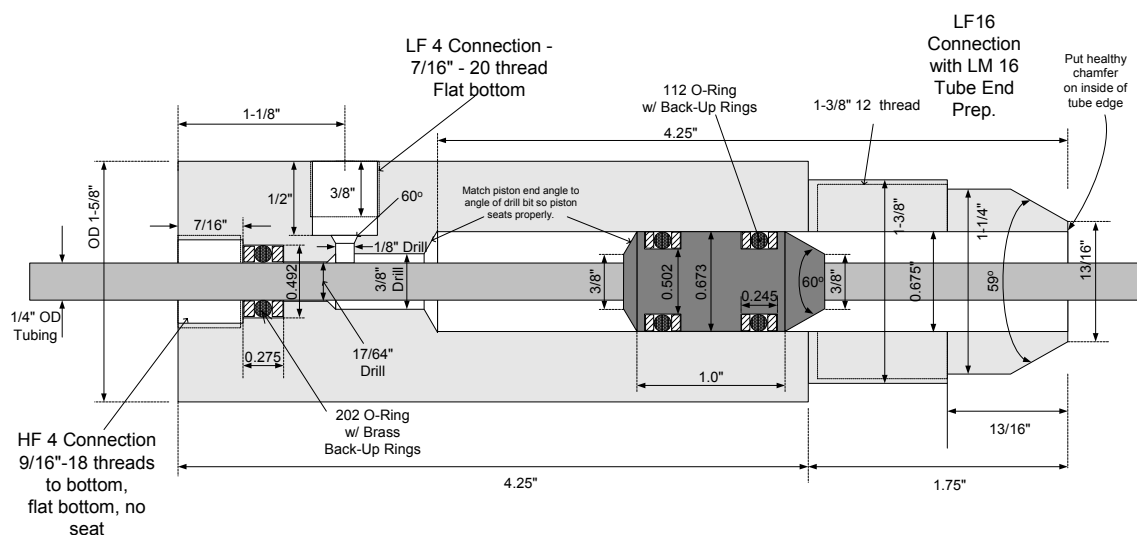
Figure 7.10 Technical drawing of movable probe assembly cylindrical housing and tube-mounted piston, as assembled. All dimenstions are in inches (″). Connection types (ex. – HF4) refer to details for HIP pressure connections (High Pressure Equipment Company, 2009).

The cylindrical housing is connected to a tee with a High Pressure Equipment Company (HIP) adapter fitting. A 9/16" (14.3 mm) OD nipple connects the tee to the reactor outlet port of the WCHB-1 reactor to seal and maintain the reactor system pressure. The cylindrical housing and piston were fabricated by the MIT Central machine shop. SS316 was used as the material of construction. The piston was welded to the ¼" (6.4 mm) HP tubing. Photographs of the finished components and their accompanying HIP fittings are shown in Figure 7.11.

Figure 7.11 Photograph of movable probe assembly. Clockwise from upper right are HIP fittings (nipple, tee, and adapter, assembled), cylindrical housing, and tubing with piston welded in place.

7.4.2. Operation and Performance

The movable probe assembly was mounted on the reactor outlet port of the WCHB reactor. A manual pressure generator was connected to the cylindrical housing and used to operate the piston using DI water as the hydraulic fluid. The movable probe assembly was tested up to operating pressures of 4500 psi (310 bar) without showing any signs of leaking. The relative position of the probe tip was measured using a digital indicator with a resolution of 0.01 mm (or 0.001 in, depending on selected units) mounted on the cylindrical housing. The rod movement is smooth and precise, repeatable axial position control was possible.

The movable probe assembly enables several possible experiments to be carried out. The rod is hollow, so that a thermocouple can be passed through the rod into the reactor. The probe can then be moved through a hydrothermal flame during operation so that temperature as a function of axial position can be determined. A heat flux meter can also be mounted at the end of the probe to determine heat flux from the hydrothermal flame to a flat surface as a function of stand-off distance. Finally, a rock sample can be mounted on the probe to determine if hydrothermal flames are capable of spalling rock at conditions simulating a deep borehole environment. These experiments were carried out and are discussed in Chapters 8, 9 and 10.

7.5. References

Boettger, K. (2005). "Field Ballistics Tests on Lexan Shielding Using 9mm Handgun and Twenty Caliber Rifle". Personal Communication to C. Augustine, Field Test, December 27. Harlan, IA.

Gnielinski, V. (1976). "New Equations for Heat and Mass-Transfer in Turbulent Pipe and Channel Flow." International Chemical Engineering **16**(2): 359-368.

High Pressure Equipment Company. (2009). "Valves, Fittings & Tubing."   Retrieved January 22, 2009, from http://www.highpressure.com/valves.asp.

La Roche, H. L. (1996). Wandegkühlter Hydrothermal-Brenner (WHB) für die überkritische Nassoxidation. Doctoral Thesis, Swiss Federal Institute of Technology (ETH).

Seward, T. M. and E. U. Franck (1981). "The System Hydrogen - Water up to 440 ^{o}C and 2500 bar Pressure." Berichte Der Bunsen-Gesellschaft-Physical Chemistry Chemical Physics **85**(1): 2-7.

Weber, M. (1997). Apparate einer SCWO-Anglage und deren Leistungsfähigkeit. Doctoral Thesis, Swiss Federal Institute of Technology (ETH).

Wellig, B. (2003). Transpiring Wall Reactor for Supercritical Water Oxidation. Doctor of Technical Sciences Thesis, Swiss Federal Institute of Technology, Available online at Available from: www.e-collection.ethz.ch.

Chapter 8: Hydrothermal Flame Experiments using Methanol and Hydrogen

8.1. Objectives

As discussed Chapter 6, the feasibility of making flames in a high pressure, high density aqueous environment has been repeatedly demonstrated by different researchers. Nonetheless, production of stable hydrothermal flames under well-defined conditions is not trivial, and requires a certain degree of experience and expertise. The work described below is the first generation study of hydrothermal flames by our group at MIT. There were two main goals: 1.) to prove and assess the ability to produce hydrothermal flames in the WCHB reactor system, and 2.) to demonstrate that the hydrothermal flames can produce temperatures and heat fluxes at a rock surface sufficient to induce thermal spallation in a deep borehole environment. The experimental approach had three main objectives:

1.) To demonstrate that hydrothermal flames could be produced methanol and hydrogen as fuel in the WCHB reactor system,

2.) To characterize the capabilities and limitations of the WCHB system for producing hydrothermal flames, such as the stability of the flames (ignition and extinction temperatures) in the system, and

3.) To demonstrate that hydrothermal flames can be used to spall rock.

8.2. Motivation

The overall motivation for exploring the application of hydrothermal flames to spallation drilling has been discussed in detail in Chapters 1 and 6. Basically, it is one of necessity. Thermal spallation at practical rates require heat fluxes on the order of 0.5-10 MW/m^2 (Rauenzahn and Tester, 1989). In open air thermal spallation drilling, these fluxes have been achieved by applying high velocity flame jets with nozzle temperatures of 2000-2500 $^{\circ}$C to the rock surface. In the high pressure, high density aqueous environment found in deep boreholes, hydrothermal flames must produce both the necessary temperatures and heat fluxes needed to induce rock spallation.

Although the deep borehole environment necessitates the use of hydrothermal flames, their unique properties also give them some advantages. For example, flame temperature and heat flux control are important factors in spallation. Despite the high jet flame temperatures used in open-air thermal spallation, previous studies found that the rock surface temperature during spallation was only 350-900 ^{o}C, depending on the rock type and applied heat flux (Rauenzahn and Tester, 1989; Wilkinson and Tester, 1993). Lowering the flame jet temperature has been reported to improve the spallability of some types of sedimentary rocks (Williams et al., 1996). For hydrothermal flames, the amount of water in the fuel mixture can easily be varied to control the flame temperature. Changes in the flame temperature also affect the heat flux to the surface, thereby allowing experimental study of its effect with relative ease. On a more practical note, a common problem with designing flame jet burners is producing high temperature flames without melting or destroying burner components. Being able to produce low temperature flames partially mitigates this problem, which is especially advantageous given the inherent danger of performing experiments at elevated pressures.

Methanol and hydrogen were chosen for study as fuels for several reasons. First, methanol has been used in the majority of continuous turbulent diffusion hydrothermal flame studies (as discussed in Chapter 6). Methanol-water fuel mixtures are known to ignite readily, produce stable combustion, and its ignition and extinction behavior has been characterized. Methanol is an ideal fuel to use to gain experience in operating the WCHB reactor system and as a benchmark for comparing WCHB performance to previous studies.

Second, demonstration of thermal spallation in a deep borehole environment is only the first step in developing an advanced drilling technology. If found to be feasible, the thermal spallation mechanism must still be integrated into an entire drilling system. Although the design and testing of such a drilling system are beyond the scope of this study, both methanol and hydrogen have attributes that would be advantageous in a full scale drilling system. Methanol is a good candidate for use as a fuel because it is completely miscible with water, which would make it easy to deliver downhole. Once combusted though, there is some concern about the effect of combustion products on wellbore stability. If a hydrocarbon such as methanol is used as fuel, the

CO_2 produced by combustion would form a separate gas phase as it travels back to the surface in the borehole. As pressure drops with decreasing depth the density of the highly compressible CO_2 decreases, and its volume fraction relative to liquid water would increase. Handling two-phase mixtures at the surface could present difficulties with well pressure control, or could upset well control by altering the average density of the drilling fluid at points in the wellbore. Hydrogen is an interesting fuel choice because it combusts with oxygen to produce water as the only product, so potential problems caused by two-phase mixtures in the wellbore would be avoided. Delivering hydrogen to the bottom of the hole presents its own problems, but the task of delivering hydrogen, oxygen, and water using separate delivery lines could prove easier to solve than separating gas/liquid products downhole. Methanol and hydrogen provide the two extreme cases for delivering fuel downhole and handling the combustion products. Demonstrating that either can be used in a deep borehole environment would give future engineers the greatest number of options in developing a complete thermal spallation drilling system.

8.3. Experimental Setup

8.3.1. Reactor Configuration

Figure 8.1 shows the reactor configuration used in the hydrothermal flame studies. For these initial hydrothermal flame studies, the reactor was configured to replicate hydrothermal flame experiments performed at ETH. Several fuel and oxygen nozzles were donated to MIT by ETH along with the WCHB reactor vessel. The nozzles for the hydrothermal flame stability experiments were chosen from this set based on their demonstrated performance in previous studies at ETH (La Roche, 1996). The reactor is oriented so that fuel, oxygen, and cooling water enter the bottom of the reactor and exit out the top of the reactor. The fuel mixture is introduced to the reactor through the very bottom and enters the combustion chamber through the fuel nozzle. The fuel nozzle is 62.5 mm in length, has an inner diameter of 4.0 mm and an outer diameter of 6.0 mm at its exit. The oxygen nozzle (8 mm ID x 16 mm OD, 42 mm length) threads into the reactor head and separates the oxygen from the cooling water entering at the base of the reactor vessel. Oxygen enters through the side port on the reactor head and flows coaxially with the fuel mixture to the combustion chamber.
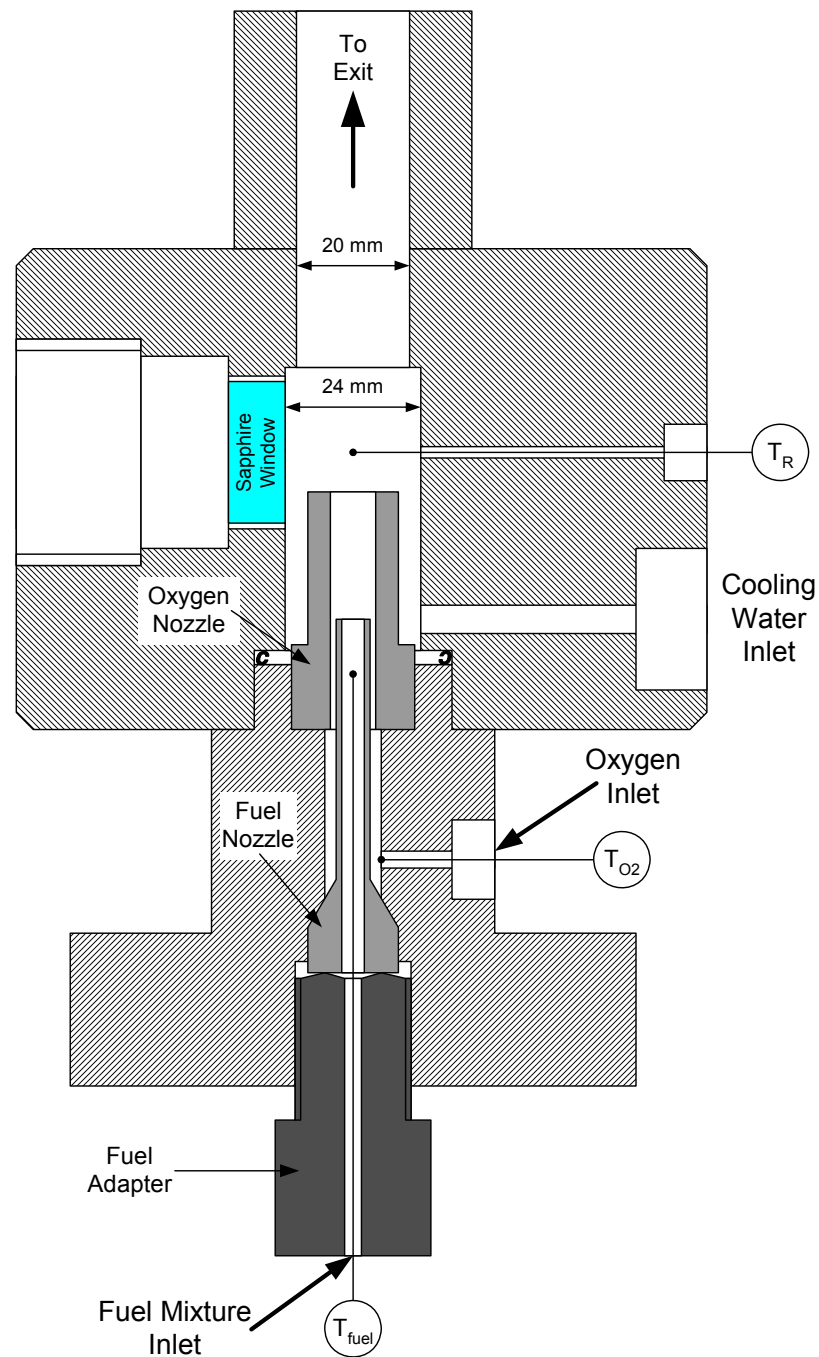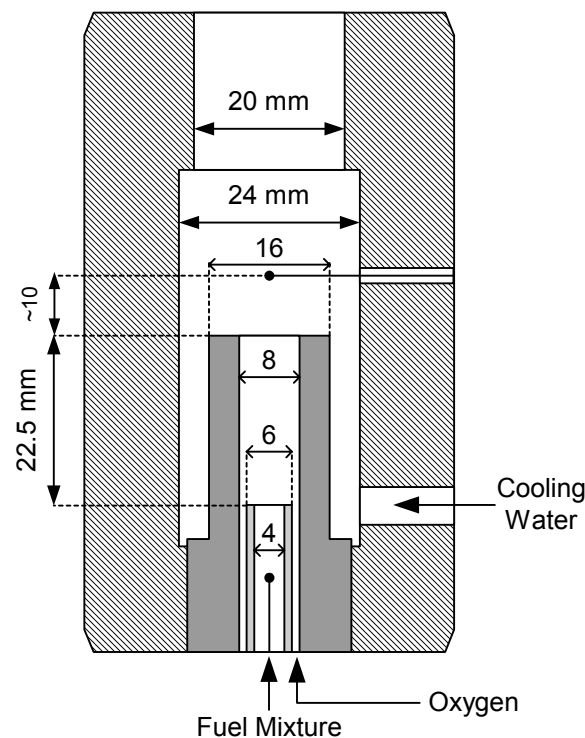
Figure 8.1 Reactor configuration used in hydrothermal flame studies.

The oxygen co-annular nozzle extends up past the fuel nozzle to form the combustion chamber. A close up of this region is shown in Figure 8.2. The combustion chamber is roughly defined as the region between the fuel nozzle exit and oxygen nozzle exit. It is 22.5 mm in length and has a diameter of 8.0 mm. It is here that the preheated fuel and oxygen mix and combust. Ignition is

achieved by heating the fuel mixture and oxygen to the point of autoignition. Cooling water

enters from a port at the bottom of the reactor vessel body and flows upward through the

outermost co-annular channel formed between the oxygen nozzle and reactor walls towards the

reactor exit. Upon entering the vessel, the cooling water flows between the outer wall of the

oxygen nozzle and the reactor wall in the outermost annulus of the vessel to protect the reactor

walls from the high temperatures of the hydrothermal flame. After the oxygen nozzle, the

cooling water mixes with the flame combustion products and quenches the reaction.

Figure 8.2 Detailed drawing of nozzle configuration used in methanol and hydrogen flame studies.

Type K thermocouples 1/16" (1.6 mm) OD are used to measure the temperatures of the fuel

mixture and oxygen inlets to the reactor. The approximate locations of the thermocouples are

indicated in Figure 8.1 and Figure 8.2. The thermocouples were placed as close as possible to

the combustion chamber so the fuel mixture (T_{fuel}) and oxygen (T_{ox}) inlet temperatures just prior

to entering the combustion chamber could be measured. The fuel thermocouple was inserted

through the fuel adapter and positioned in the fuel nozzle at point where the reactor head ends so

that different nozzle lengths could be used in the future without fear of the thermocouple being

exposed to the combustion chamber. The placement of the oxygen thermocouple was limited by

geometry of the oxygen inlet. The annular space between the fuel nozzle and reactor head wall was too narrow to insert the thermocouple any farther.

Four Type K thermocouples were also positioned in the reactor vessel above the exit of the combustion chamber to measure the flame temperature. The thermocouples are introduced through small ports on the reactor vessel body. The thermocouple closest to the combustion chamber exit (T_R) was positioned on the centerline axis of the reactor and ~10 mm above the exit of the combustion chamber. A precise measurement of its position was not possible due to the confined geometry inside the reaction vessel.

8.3.2. Operating Conditions

To study flame stability, the conditions at which the flame ignites and extinguishes are observed as a function of the concentration of fuel in the fuel mixture and the fuel mixture flow rate. For the complete oxidation of methanol by oxygen to carbon dioxide and water:

$$CH_3OH + \frac{3}{2}O_2 \rightarrow CO_2 + 2H_2O \qquad \text{Eq. (8-1)}$$
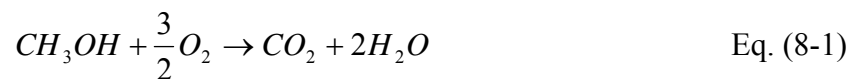
the stoichiometric flow rate of oxygen on a mass basis is:

$$\dot{m}_{O_2} = \dot{m}_{CH_3OH} \cdot \upsilon_{O_2} \cdot \frac{M_{O_2}}{M_{CH_3OH}} \qquad \text{Eq. (8-2)}$$

where:
$\dot{m}_i$ = mass flow rate of component i (g/s)
M_i = molecular weight of component i (moles/g)
v_i = stoichiometric coefficient of component i

When hydrogen is used as a fuel, the corresponding equations are:

$$H_2 + \frac{1}{2}O_2 \rightarrow H_2O \qquad \text{Eq. (8-3)}$$

$$\dot{m}_{O_2} = \dot{m}_{H_2} \cdot \upsilon_{O_2} \cdot \frac{M_{O_2}}{M_{H_2}}$$

To ensure that adequate oxygen is present in the combustion chamber for complete combustion, the mass flow rate of oxygen was set to be 150% of stoichiometric for all experiments. The coling water flow rate was varied between runs, but was not seen to have any effect on ignition

or extinction temperatures or on the fuel mixture or oxygen inlet temperatures prior to ignition. The cooling water inlet temperature was 25 ^{o}C. The operating pressure for all experiments was 250±3 bar.

The calculated adiabatic flame temperatures of both methanol and hydrogen hydrothermal flames at various fuel mixture concentrations are shown in Figure 8.3. Chemkin EQUIL software was used to estimate the flame temperatures. The adiabatic flame temperature is shown as a function of the mass% and mole% of fuel in the fuel/water mixture. Pure oxygen at 150% of stoichiometric is the oxidant. The simulations were carried out assuming a pressure of 250 bar and inlet temperatures of 400 ^{o}C for all components. Methanol concentrations of 25 mass% were typically used during ignition. Higher concentrations were avoided to decrease the risk of damaging the fuel and oxygen nozzles or the reactor walls. Because hydrogen has a much lower molecular weight than methanol, hydrogen fuel mixtures with much lower hydrogen mass fractions were used. Hydrogen fuel concentrations used in the study were limited to 3-6 mass% to avoid excessive temperatures. The figure shows that 3-6 mass% hydrogen-water fuel mixtures should result in similar flame temperatures as 25 mass% methanol flames, which previous studies have demonstrated can be produced safely. Additional analysis confirmed that the total energy released from the heat of reaction for this range of hydrogen fuel mixtures would also be within levels produced in previous studies.
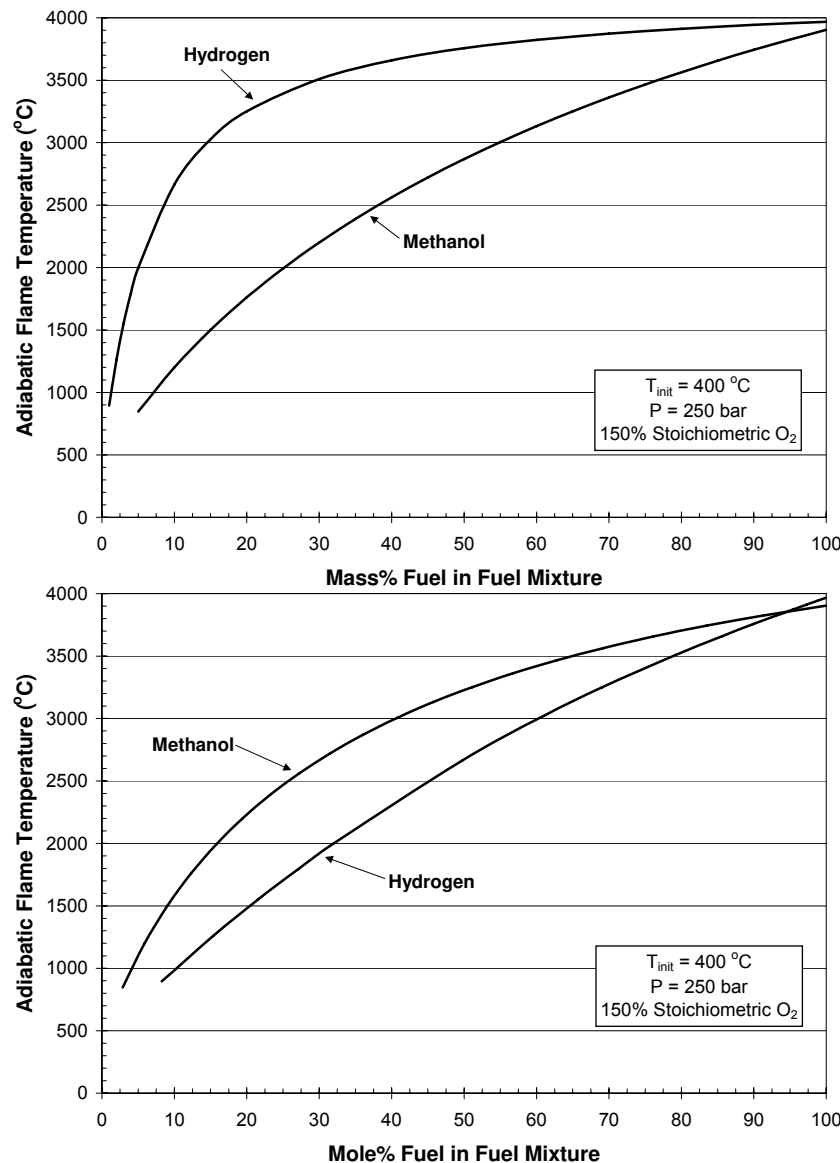
Figure 8.3 Adiabatic flame temperatures of methanol and hydrogen as a function of mass% (top) and mole% (bottom) fuel in the fuel-water mixture. 150% stoichiometric oxygen is assumed.

8.3.3. Procedure

Before an experiment could be started, the reactor configuration had to be assembled, with the appropriate fuel and oxygen nozzles installed, and pressure tested to ensure there were no leaks in the system. A pressure test consisted of starting up the system using only water and oxygen as feeds and increasing the operating pressure to 250 bar. The pressure was held there for several minutes, the system pressure decreased, and then all fittings in the WCHB system were checked

for signs of leaks. Once the system was determined to be pressure tight, an experiment could be started. The general procedure for hydrothermal flame experiments was as follows:

Start-Up

1.) Turn on all meters, temperature controllers, and sensors. These equipment generally require ½ hour to warm up and achieve their maximum accuracy.
2.) Check that there are adequate process fluids for the entire experiment:
    a. De-ionized (DI) cooling water in the cooling water tank,
    b. Full O_2 cylinders in manifold and on reserve,
    c. Fuel (either H_2 cylinders or methanol),
    d. Fuel water in SD-1 pump feed carboy.
3.) Check initial valve positions (feeds to pumps open, bleed valves closed, etc.).
4.) Open necessary programs on DAQ PC:
    a. NI Labview,
    b. ER3000 controller software,
    c. Bronkhorst H_2 flow control software (if using H_2),
5.) Close forward pressure regulators (FPR's) on O_2 and H_2 lines.
6.) Turn "Emergency Shutdown" switch to "On" position – this applies power to the SD-1 pumps and solenoid valves in emergency shutdown system.
7.) Apply 100 psig (6.9 barg) compressed air to BPR and air-operated valves.
8.) Open valves on O_2 (and H_2 if used) cylinders, set outlet pressures on regulators to ~500 psig (~35 barg).
9.) Slowly turn on house drive-air supplies to Haskell gas boosters. O_2 (and H_2 if used) feed lines and accumulator tanks will pressurize, but flow will not go past closed FPR's.
10.) Set initial flow rates:
    a. CW triplex plunger pump to ~20 g/s flowrate,
    b. SD-1 pumps to low flow rate (~25 mL/min), pumping DI water only,
    c. Slowly open O_2 FPR to allow small flow of O_2 through system.
11.) Increase system pressure to final operating pressure in ~15 bar increments, adjusting O_2 FPR to maintain small O_2 flow.
12.) Turn on house water flow through heat exchanger located after the reactor.
13.) Increase fuel mixture and O_2 inlet temperatures:
    a. Increase copper block temperature of Fuel HX1, Fuel HX2, and O2 HX to 350 ^{o}C in 25 ^{o}C increments, waiting 3 minutes between increases.
    b. Continue to increase Fuel HX2 and O2 HX copper block temperature to ~500 ^{o}C in 15 ^{o}C increments, waiting 2 minutes between increases. Additional waiting time may be needed as the fuel mixture flow reaches supercritical temperatures, since increases in fuel mixture inlet temperature occur quickly around pseudo-critical point.

Flame Ignition

1.) Begin data acquisition.
2.) Increase cooling water, fuel mixture, and oxygen flow rates to desired starting experimental values.
3.) Turn on fuel flow:
   - a. If methanol is used as fuel, toggle 3-way valve on SD-1 pump feed to begin flow of methanol,
   - b. If hydrogen is used as fuel, slowly open H_2 FPR and set flow rate to desired value.
4.) Increase fuel mixture and oxygen inlet temperatures in step-by-step manner (5-10 ^oC increments) until auto-ignition is achieved. Record inlet temperatures at time of ignition.

Flame Extinction

1.) Decrease fuel mixture and oxygen inlet temperatures in step-by-step manner (5-10 ^oC increments) until flame extinguishes itself. Record inlet temperatures at time of ignition.
2.) End data acquisition.

Shut Down

1.) Turn off flow of fuel to reactor.
   - a. If methanol is used as fuel, toggle 3-way valve on SD-1 pump feed to switch to DI water flow,
   - b. If hydrogen is used as fuel, set flow rate to zero and close H_2 FPR.
2.) Decrease fuel mixture and oxygen flow rates to startup values.
3.) Slowly decrease temperature of fuel and oxygen inlets.
   - a. Decrease Fuel HX1 and Fuel HX2 copper block temperatures by 15 ^oC every 2 minutes until fuel mixture inlet temperature is below critical temperature. Take special care near critical temperature. Then, decrease block temperature by 25 ^oC every 3 minutes.
   - b. Decrease O2 HX copper block temperature by 25 ^oC every 3 minutes.
4.) Once fuel mixture inlet temperature is below 100 ^oC, close O_2 FPR and slowly decrease system pressure in ~15 bar increments.
5.) Turn off SD-1 pumps, cooling water pump, and house cooling water flow.
6.) Turn off drive air to gas boosters. Close valves on all gas cylinders.
7.) Turn off computer software.
8.) Bleed O_2 and H_2 lines.
9.) Turn off meters, temperature controllers, and sensors.

Even for simple flame ignition and extinction experiments, the preparation, operation, and shut down of the WCHB reaction system is a complex procedure. A typical run takes at minimum 6 hours to complete, requiring at least 1 hour of system preparation, 1.5 hours to start up, 1.5 hours to shut down, and several hours of operation during which fuel mixture and oxygen inlet temperatures are slowly increased or decreased.

The majority of the startup and shutdown time is dedicated to preheating and cooling the heat exchangers at a controlled rate. Experience with operating the system has shown that slow rates of heating and cooling are required to avoid leaks in the system around the reactor vessel. These leaks are believed to be caused by differential heating of the components and fittings, and most often occur at the fuel or oxygen inlet connection, or in the fittings on the preheater tees. Slow rates of heating and cooling prevent excessive differences in expansion of the fittings and have greatly decreased the incidence of experiments halted due to leaks in the system.

Another important and time consuming step in the operation of the reaction system is cooling the system down to fuel mixture inlet temperatures of less than 100 ^{o}C before decreasing the system pressure. Failure to follow this procedure results in flashing of the fuel mixture from liquid to vapor in the preheaters, which can damage the C-seals in the reactor vessel (Wellig, 2003), among other reactor components.

8.4. Methanol Flames

The WCHB reaction system was built in stages, starting with the WCHB reactor, two SD-1 pumps, the oxygen gas booster, and preheaters as the primary components. Preliminary experiments were carried out using methanol as fuel for several reasons. First, it was proven to be an effective fuel in hydrothermal flame experiments at ETH. Based on their studies, it was known that methanol fuel mixture inlet temperatures of 450-550 ^{o}C should be sufficient to cause autoignition of the hydrothermal flame (La Roche, 1996; Weber, 1997; Wellig, 2003). Second, methanol is completely miscible with water, which meant the fuel mixture could be mixed and then metered and pressurized by one of the SD-1 pumps. The other SD-1 pump, operating at its maximum flow rate, was used to deliver cooling water. In June 2006, after much trial and error, the first successful ignition of a hydrothermal flame in our laboratory at MIT was achieved. A 25 wt% methanol fuel mixture was used. The flame had to be quickly extinguished though due to rising temperatures in the reactor outlet, as the cooling system in use at the time was inadequate to handle the heat of combustion released by the hydrothermal flame.

Many lessons were learned from these initial trials. Larger cooling capacity was needed, so the triplex plunger piston cooling water pump was added to enable the cooling water to quench the reaction products to a lower temperature. A larger heat exchanger was also added after the reactor. The liberation of the SD-1 pump from its cooling water duty made it available for fuel delivery. This was advantageous, since the preliminary studies also showed that the reactor head acts as a large heat sink for the fuel mixture and oxygen inlets, decreasing their temperature before they reach the combustion chamber. Parametric studies showed that for a given preheater block temperature, higher flow rates resulted in higher inlet temperatures into the combustion chamber. The higher cooling capacity and fuel mixture pumping capacity would allow the WCHB to operate at higher feed flow rates and to handle the resulting higher heat release as well.

Installation of the new components produced the WCHB system as shown in Figure 7.2. Preliminary experiments with methanol continued using fuel mixture flow rates of 1.0-1.5 g/s to gain further experience in using the WCHB reaction system to produce hydrothermal flames. As the experiments proceeded, further refinements were made to the system to increase its performance and reliability. Although systematic experiments were not carried out, experimental data about the stability of the flame, such as ignition and extinction characteristics, were gathered.

8.4.1. Flame Ignition

During preliminary experiments using methanol as a fuel, the inlet temperatures of the fuel mixture and oxygen just prior to ignition were measured to characterize the conditions under which the hydrothermal flame ignites. The burner geometry, operating conditions and procedure described in Section 8.3 were used for all experiments. Table 8.1 shows the operating conditions at the point of flame ignition for all experiments performed using methanol as a fuel. The point of flame ignition was determined by a sudden increase in temperatures measured by the thermocouples positioned above the combustion chamber exit and at the reactor outlet.

Table 8.1 Operating conditions at point of autoignition for hydrothermal flames using methanol as fuel.

Date	Mass % Methanol	Fuel Mixture			O₂	CW	T_fuel	T_O2
		Methanol	**Water**	**Total**				
	(%)	(g/s)	(g/s)	(g/s)	(g/s)	(g/s)	(°C)	(°C)
6/19/06[1]	25	0.200	0.60	0.8	0.45	3.17	538	413
8/21/06	25	0.375	1.13	1.5	0.84	35	506	454
11/6/06	25	0.313	0.94	1.25	0.70	45	547	409
12/12/06[2]	21.2-23.2	0.30-0.31	1.00-1.17	1.48	0.56[3]	40	547	439
7/30/07	25	0.375	1.13	1.5	0.84	40	497	428
7/30/07	25	0.375	1.13	1.5	0.84	30	507	440
9/7/07	25	0.375	1.13	1.5	0.90	40	532	417
9/17/07	28.1	0.367	0.94	1.31	0.65[3]	35	545	448
9/18/07	35.8	0.419	0.75	1.17	0.84[3]	35	539	423

[1]First successful ignition, performed using SD-1 pump to provide cooling water.
[2]Ignition occurred during increase in methanol flow rate, actual methanol flowrate unknown.
[3]Oxygen flow rates not 150% stoichiometric at time of ignition.

Figure 8.4 shows the fuel mixture temperature at the point of ignition as a function of the percent mass of methanol in the fuel mixture. Ignition temperatures ranged from about 500-550 °C. These temperatures are higher than those reported by Steeper and Rice (1992). They observed that laminar diffusion flames readily ignited above temperatures of 450 °C for methanol fuel mixtures of 10 mass% and higher at similar pressures. However, for continuous turbulent diffusion flames, the ignition temperature depends not only on the fuel mixture in use, but is also sensitive to the reactor configuration. Typical ignition temperatures for Weber (1997) using a 16.5 mass% methanol fuel mixture were 520 °C, while Wellig (2003) reported ignition temperatures from 460-490 °C in his studies. The ignition temperatures observed in this study's experiments, shown in Figure 8.4, are often higher than these values, but are comparable.

Most of the experiments used a fuel mixture of 25 mass% methanol because it was easily ignited but did not result in excessively high flame temperatures. Several attempts were made to ignite 20 mass% methanol fuel mixtures, but were unsuccessful. For example, the experiments on Nov. 6 and Dec. 12, 2006 both began as unsuccessful attempts to ignite 20 mass% methanol fuel mixtures. When ignition could not be achieved, the methanol flow rate and/or the total fuel mixture flow rate were increased to achieve ignition. For the Nov. 6 run, the methanol mass fraction was increased to 25%. Later, on Dec 12, the methanol flow rate only needed to be
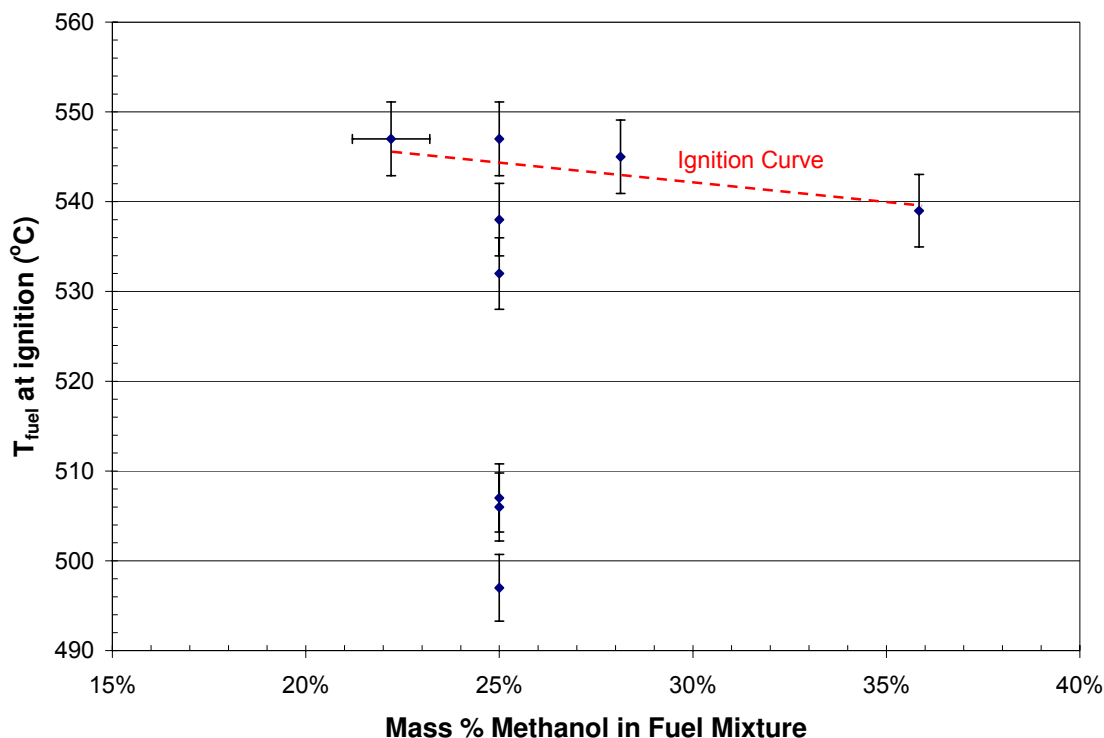
Figure 8.4 Temperature of fuel mixture at point of ignition vs. methanol mass fraction in fuel mixture. increased slightly. The precise methanol mass flow rate is unknown during ignition, since ignition occurred shortly after the mass flow rate was ramped up. Similar events occurred on Dec. 17 and 18, 2007, except then, a 25 mass% mixture would not ignite, so the methanol content of the fuels was increased.

The observed ignition temperatures for 25 mass% fuel span a range of about 50 ^{o}C. However, the ignition is divided into two groups: one at around 505 ^{o}C and the other at around 540 ^{o}C. Two of these observations occurred on the same day – July 30, 2007. During that run, the flame ignited immediately when the SD-1 pump was switched over from DI water to methanol. The fuel inlet temperature did not have to be increased incrementally. It was extinguished when the cooling water flow rate was lowered too far and the emergency shutdown system was activated, and had to be reignited. To reignite the flame a second time, the fuel inlet temperature had to be increased, indicating that $T_{fuel} = 497$ ^{o}C was not the true ignition temperature, but probably the result of some small perturbation to the flow in the reactor. Wellig (2003) reported ignition

temperatures that spanned 30 $^{\circ}$C for a given methanol concentration, so this phenomenon is not an anomaly and may be a common occurrence in continuous turbulent diffusion flames. Following Wellig's criteria, an ignition curve was added to Figure 8.4 based only on the highest measured ignition temperatures as a function of fuel concentration. Similar to the ETH studies, the data indicates a small negative slope, meaning ignition becomes easier as fuel concentration increases.

The oxygen inlet temperature was not increased incrementally during ignition as the fuel mixture inlet temperature was. Instead, it was set between 400-450 $^{\circ}$C and left constant while the fuel mixture inlet temperature was increased. The response of the O2 HX preheater is slow, so matching the fuel mixture inlet temperatures during the course of the reaction would have been difficult. The thermal capacity is higher for the fuel mixture than for the oxygen stream, so it should have a greater effect on the mixing temperature in the combustion chamber. To check that the oxygen inlet temperature does not significantly impact flame ignition, the fuel inlet temperature was plotted against the oxygen inlet temperature at the point of ignition in Figure 8.5. Although the oxygen inlet temperature tends to be higher for lower fuel mixture inlet temperature ignitions, high fuel inlet temperatures were also recorded for high oxygen inlet temperatures as well. The variation in oxygen inlet temperature does not appear to significantly affect the fuel mixture temperature at the point of ignition in any discernible fashion.

8.4.2. Flame Extinction

Once the flame is ignited, the inlet temperatures can be decreased and the flame will persist. The degree to which the inlet temperatures can be decreased is a measure of the flame stability. Flame extinction temperatures were measured for methanol flames, but only a few successful data points were recorded. During several of the experiments, the flame had to be extinguished prematurely due to either equipment malfunction or unsafe operating conditions. For the last two methanol flame ignitions in Table 8.1, the experimental plan called for a different procedure that precluded methanol flame extinction, as will be discussed below.
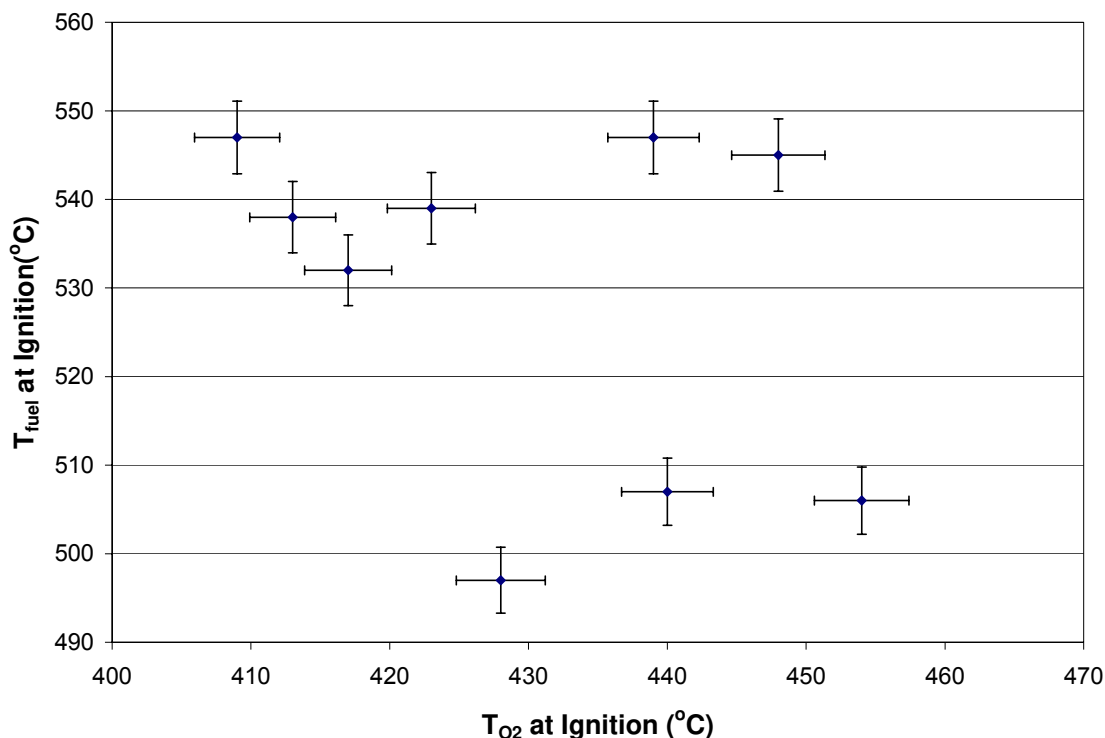
Figure 8.5 Fuel mixture inlet temperature vs. oxygen inlet temperature at point of ignition for methanol hydrothermal flame experiments.

Table 8.2 lists the observed operating conditions at the point of extinction for the methanol flame experiments in which flame extinction was either not intentional or the result of some experimental error. Some of the data in the table are still questionable. For example, in the Aug. 21, 2006 experiment, extinction was believed to be caused by an air bubble that was observed in the methanol feed line to the SD-1 pump. In the Nov. 6, 2006 run, extinction occurred at a high fuel mixture temperature for a 20 mass% methanol fuel. The recorded oxygen temperature was rather low. A review of the data acquisition logs from the run indicated that the oxygen inlet

Table 8.2 Operating conditions at point of extinction for hydrothermal flames with methanol fuel.

Date	Mass % Methanol	Fuel Mixture			O_2	CW	T_{fuel}	T_{O2}
		Methanol	Water	Total				
	(%)	(g/s)	(g/s)	(g/s)	(g/s)	(g/s)	(^{o}C)	(^{o}C)
8/21/06[1]	25	0.375	1.13	1.5	0.84	42.5	258	196
11/6/06	20	0.313	0.94	1.25	0.45	45	428	260
7/30/07	25	0.375	1.13	1.5	0.84	45	85	360

[1]Extinction believed to be caused by air bubble in methanol feed line.

temperature fluctuated between ~260 ^{o}C and ~ 400 ^{o}C. This behavior is common for lower oxygen flow rates, but its source has not been determined. It is likely that the oxygen temperature is higher than that recorded at the time of extinction. The last recorded methanol flame extinction on July 30, 2007 occurred at a fuel mixture temperature of 85 ^{o}C. This value is more in line with those reported by Weber (1997) in his systematic study of methanol flame extinction temperatures where the oxygen inlet temperature was also held at ~400 ^{o}C. A lower fuel extinction temperature may have been possible, but the WCHB system ran out of methanol fuel and ended the experiment prematurely.

8.4.3. Flame Temperature

Type K thermocouples (1/16" OD) inserted into the WCHB reactor were used to measure the temperature in the region around the exit of the combustion chamber. The positions in which the thermocouples could be placed were limited by the reactor geometry. The thermocouple closest to the combustion chamber exit was positioned with the tip along the centerline axis of the reactor, about 8-10 mm above the exit. Despite its proximity to the hydrothermal flame, the thermocouple temperature would only increase by ~100 ^{o}C (from ~200 to ~300 ^{o}C, typically) upon ignition of the flame.

A high speed camera was used to photograph the methanol hydrothermal flame through the sapphire glass viewports on the WCHB reactor. Figure 8.6 shows several consecutive images of the flame. Upon close inspection, the reflection of the flame off the thermocouple can be seen in the fourth image, to the right of the flame. The images show that the flame does not penetrate far into the cooling water after leaving the combustion. It also shows highly turbulent mixing between the flame and the surrounding cooling water, with large eddies present. The rapid entrainment of low enthalpy ambient fluid could explain the low temperature measurements by the thermocouple. (Subsequent studies of the axial temperature decay of high temperature, low density jets injected into low temperature, high density fluid is the subject of Chapter 9, and confirmed that entrainment of the surrounding fluids does lead to rapid temperature decay within several diameters of the nozzle exit).
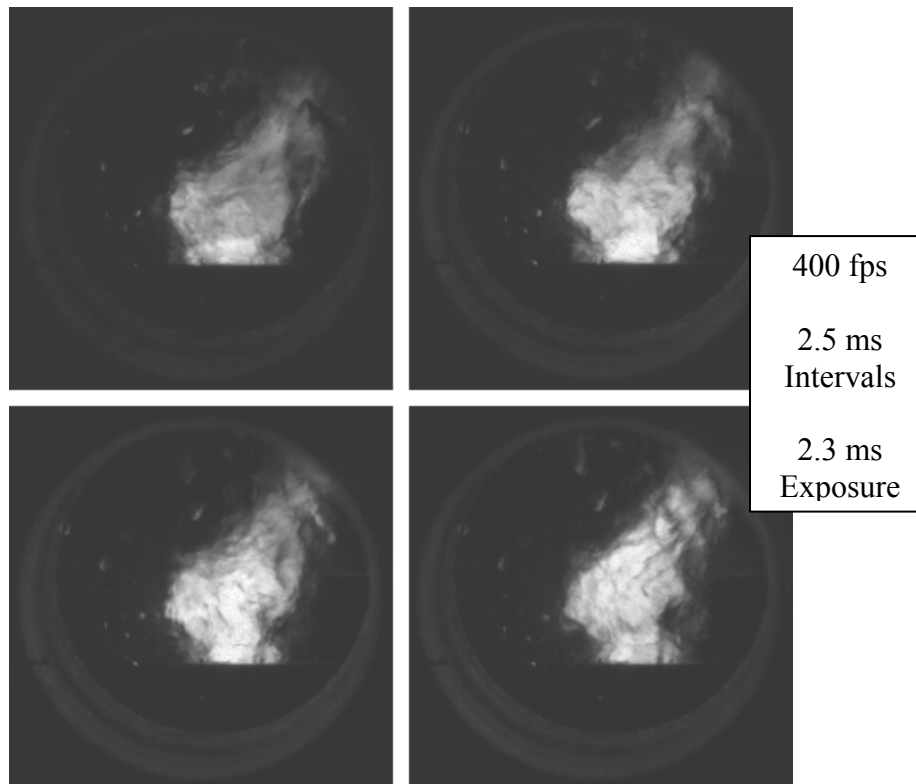
400 fps

2.5 ms
Intervals

2.3 ms
Exposure

Figure 8.6 Four consecutive images (from upper left to lower right) of hydrothermal flame taken using high speed video camera at 400 frames per second (fps). A 25 mass% methanol fuel mixture was used.

8.5. Hydrogen Flames

Having gained considerable experience from producing methanol flames, experiments using a mixture of water and hydrogen as fuel were performed to create continuous turbulent diffusion hydrothermal flames for the first time. The same reactor configuration, burner geometry, operating conditions and procedures described in Section 8.3, including oxygen flow rates 150% of stoichiometric levels, were used for all runs.

8.5.1. Flame Ignition

Despite numerous attempts, flame ignition could not be achieved in the WCHB reactor by systematically increasing the hydrogen-water mixture inlet temperature. In one attempt, a 5.0 mass% (32 mole%) hydrogen fuel mixture with inlet temperatures of 585 $^{\circ}$C failed to result in autoignition. In another, 4.0 mass% (27 mole%) at 550 $^{\circ}$C failed to ignite. The concentration of hydrogen in the fuel mixture was increased to 10.7 mass% (52 mole%) by lowering the water flow rate in the fuel mixture, but even at an inlet temperature of 540 $^{\circ}$C, this highly concentrated

mixture failed to ignite. In laminar diffusion flame studies, 4.6 mass% (30 mole%) hydrogen fuel mixtures were observed to autoignite at temperatures of 450-500 ^{o}C (Pohsner and Franck, 1994), so the failure of the flames to ignite must be due to the nozzle configuration. There was a similar, isolated occasion when a hydrogen flame did ignite in the WCHB reactor shortly after the hydrogen fuel had been switched on. Ignition occurred while the hydrogen flow rate was being increased. The data show that the fuel mixture was roughly 2 mass% (14 mole%) hydrogen at the time of ignition. The fuel inlet temperature was 491 ^{o}C, and the oxygen inlet temperature 355 ^{o}C. It is believed that a perturbation in the system led to the ignition. Subsequent experiments attempted to repeat the ignition by ramping the hydrogen flow rate up and down at increasingly higher inlet temperatures, but the autoignition event could not be replicated.

With no means of reliably igniting a hydrothermal flame using hydrogen fuel, a system was developed in which the flames were ignited using a methanol fuel mixture, and then the fuel source was slowly switched over from methanol to hydrogen. The methanol flow rate was incrementally decreased while the hydrogen flow rate was increased, so for a time a mixed methanol/hydrogen/water mixture fueled the hydrothermal flame. Using this method, hydrogen flames could successfully and reliably be established.

8.5.2. Flame Extinction

The extinction properties of hydrogen hydrothermal flames were studied by igniting methanol flames, switching to hydrogen fuel, and then incrementally decreasing the fuel inlet temperature to the point of flame extinction. The conditions at the point of extinction for three successful experiments are shown in Table 8.3. The fuel inlet temperature at the point of extinction is very similar for the three experiments. This indicates that the experiments are both repeatable and representative of true extinction behavior.

The extinction temperatures observed for hydrogen flames are much higher than those observed for methanol flames of similar molar fuel concentration both in these studies and by ETH. Unlike methanol, which is completely miscible with water at all conditions, hydrogen is only

Table 8.3 Operating conditions at point of extinction for hydrothermal flames with hydrogen fuel.

Date	Mass % H_2	Mole % H_2	Fuel Mixture			O_2	CW	T_{fuel}	T_{O2}
			H_2	Water	Total				
	(%)	(%)	(g/s)	(g/s)	(g/s)	(g/s)	(g/s)	(^{o}C)	(^{o}C)
9/17/07	4.0	27.1	0.050	1.20	1.25	0.60	35	322	321
9/18/07	4.0	27.1	0.060	1.44	1.25	0.71	35	317	301
9/20/07	3.0	21.7	0.038	1.21	1.25	0.45	35	335	360

completely miscible with water above the critical point of water (Seward and Franck, 1981). La Roche (1996) reported extinction temperatures ranging from 320 to 360 ^{o}C for 10-25 mass% (11-33 mole%) methane-water fuel mixtures. These extinction temperatures are close to those observed for hydrogen-water flames produced with a similar mole% fuel mixture. La Roche suggested that the methane flame extinguishes as a result of demixing of the gaseous methane/aqueous water phases below the critical temperature of water (Shmonov et al., 1993). The high extinction temperatures observed for hydrogen fuel mixture flames may indicate that a similar mechanism could be functioning in the hydrogen flames as well.

8.5.3. Flame Temperature

Similar to the methanol experiments, the hydrogen hydrothermal flame was quickly quenched by the surrounding cooling water upon exiting the combustion chamber. Temperatures recorded by the thermocouple positioned just above the combustion chamber exit ranged from 253-285 ^{o}C at the time of extinction.

8.6. Methanol and Hydrogen Flames Discussion

Hydrothermal flame studies carried out in the WCHB pilot system show that flames can be stably formed at high pressures found in a deep borehole using both methanol and hydrogen as fuels. This work was the first demonstration that hydrogen can be used to produce continuous turbulent diffusion hydrothermal flames

The ignition temperatures observed for methanol flames using the nozzle configuration shown in Figure 8.2 was higher than those observed in studies done at ETH. For continuous turbulent diffusion flames, the ignition temperature is a characteristic of the nozzle configuration and

geometry as much as it is of the fuel type and concentration being used. In the initial studies done at ETH using the WCHB-1 reactor (the same one used in this study), methanol fuel mixture inlet temperatures of 520 $^{\circ}$C were needed to cause autoignition (Weber, 1997). Later studies done with a different reactor called the transpiring wall reactor (TWR) could achieve ignition using inlet temperatures of 460-490 $^{\circ}$C (Wellig, 2003). In their most recent reactor design (WCHB-3), ignition temperatures as low as 452 $^{\circ}$C have been reported for the WCHB-3 reactor using only a 12 mass% (7.1 mole%) methanol fuel (Narayanan et al., 2008). Continuing improvements in design, such as the addition of flow stabilizers, swirl generators, and the use of insulated nozzles, have led to lower ignition temperatures. The same is true for extinction temperatures. (see Sections 6.6.1-6.6.2 for a more in-depth discussion).

For flames using hydrogen as fuel, the same nozzle configuration used for methanol flames was not able to achieve reliable autoignition. Instead, a method for producing hydrogen flames using methanol to achieve ignition was developed. It is likely that with a different nozzle configuration, a different type of fuel nozzle, or higher inlet temperatures, flame ignition induced by preheating alone could be achieved. In one experiment, spontaneous ignition of a hydrogen flame was observed, but was likely due to by a system perturbation and could not be replicated. Nonetheless, the random autoignition event indicates that flames can be made using hydrogen alone as fuel if the conditions are correct. The focus of these studies was not to sort out the underlying causes of ignition in hydrogen flames through systematic ignition/extinction studies, but to prove that flames can be made in the deep borehole environment simulated by the WCHB system and to use these flames to spall rock. Since both methanol and hydrogen flames had been successfully produced in the WCHB system, it was decided to move forward and apply these flames to thermal spallation drilling.

The studies also showed that data from temperature probes statically positioned in the reactor are useful in determining when a flame ignition or extinction has occurred, but do not provide any useful information about the flame once it is ignited. A means of being able to probe flame structure is needed. Both the rock spallation and flame property objectives were addressed in the next set of experiments performed.

8.7. Rock Spallation Experiments

Experiments attempting to spall rock under deep borehole conditions using hydrothermal flames were carried out using the WCHB. The stagnation temperature of the flame, defined as the jet temperature at the point of impingement against a surface, was measured as a function of stand-off distance using the movable probe assembly to select the optimum setup for the thermal spallation feasibility tests. Rock samples were then placed on the end of the movable probe assembly and inserted at a specified standoff distance into a hydrothermal flame produced under the same operating conditions as in the stagnation temperature experiments. The experimental setup, procedures used, and experimental results are described below.

8.7.1. Experimental Setup

Operating conditions for the spallation experiment are the same as described in Section 8.3.2. The cooling water flow rate was set to 50 g/s for all experiments. Slight modifications were made to the operating procedure in Section 8.3.3, since ignition/extinction temperature data were not the primary concern of these experiments, and are described below for each experiment. The start-up and shutdown procedures remain the same.

Several changes were made to the reactor configuration described earlier in Section 8.3.1. Rock spallation relies on heating a small portion of the rock surface that is confined by the cooler surrounding rock. The maximum size of rock samples that can be used in the WCHB reactor was 19 mm, which was limited by the narrowest point of the inner diameter of the vessel (20 mm). It was feared that the 8 mm inner diameter of the oxygen nozzle/combustion chamber used in earlier hydrothermal flame experiments was too large relative to the available area of the rock surface, an would prevent spallation from occurring. New fuel and oxygen nozzles were constructed to minimize the diameter of the combustion chamber (henceforth, the "jet") exit. As shown in Figure 8.7, the fuel nozzle has an inner diameter of 2.4 mm, an outer diameter of 3.2 mm at the exit, and an overall length of 62 mm. The inner diameter had to be made large enough to accept the fuel inlet temperature probe. The oxygen nozzle has an inner diameter of 4.8 mm, and outer diameter of 6.4 mm at its exit, and an overall length of 40 mm. Both nozzles were constructed from SS316, and were made by welding tubing into a base machined to fit inside the
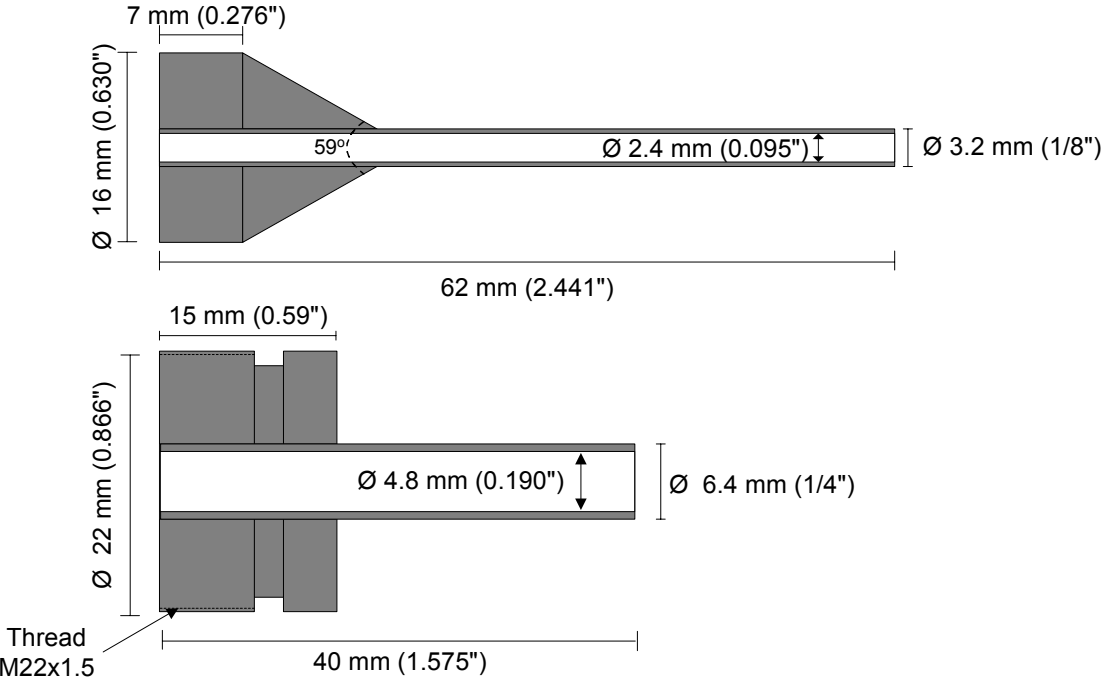
Figure 8.7 Design drawing of fuel (top) and oxygen (bottom) nozzles (SS316) used in hydrothermal flame rock spallation experiments.
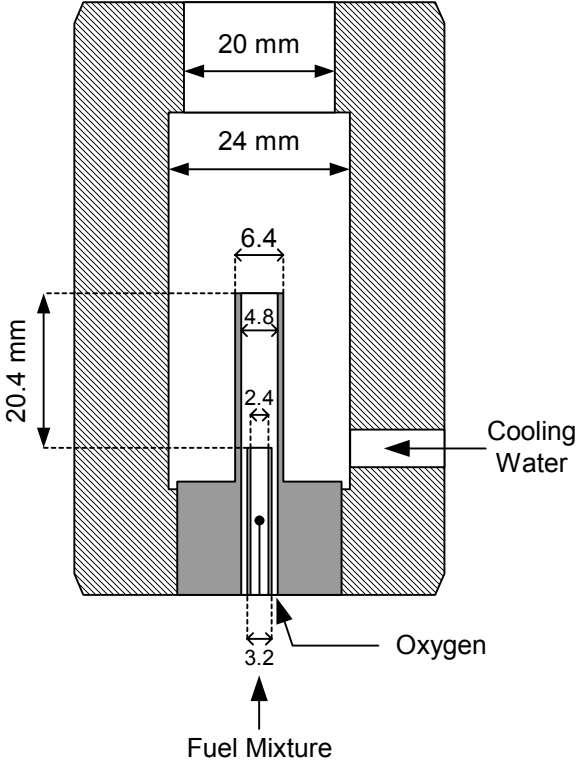

Figure 8.8 Detailed drawing of nozzle configuration used in flame stagnation temperature and flame spallation studies.

WCHB reactor head. Once installed, the nozzle configuration, shown in Figure 8.8, resulted in a combustion chamber 6.4 mm in diameter and 20.4 mm in length. The thermocouple probes previously mounted through ports on the reaction vessel as shown in Figure 8.1 were removed.

The movable probe assembly described in Section 7.4 was used to position the thermocouple probes and rock sample relative to the flame jet nozzle exit along the length of the reactor. In order to ensure that the thermocouple was properly centered, the device shown in Figure 8.9, dubbed the "rock carrier," was designed and constructed. The device is threaded onto the tip of the movable probe. Two O-rings on the rock carrier center the probe in the 20 mm diameter cross-section area of the reactor while still allowing it to slide along the reactor. Holes drilled around the radius of the rock carrier allow cooling water and reaction products to pass through it to the reactor exit. A center hole in the device permits the insertion of the thermocouple down the center of the movable probe assembly rod and through the device, so that temperature measurements of the flame along its central axis can be made. A high pressure seal is made between the thermocouple and a compression fitting at the entrance of the movable probe rod. The rock sample or similar equipment is attached to a nut by epoxy and is threaded onto the end of the rock carrier, which is mounted on the end of the movable probe inside the WCHB as shown in Figure 8.10.
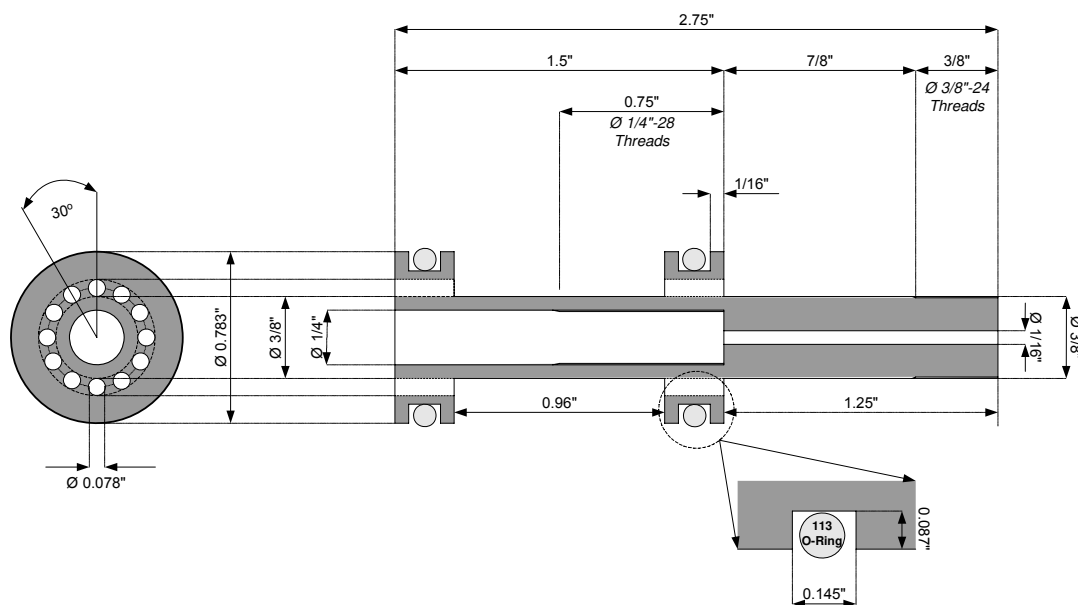

Figure 8.9 Design drawing of "rock carrier" (SS316) used to center probe in reactor and hold rock samples.
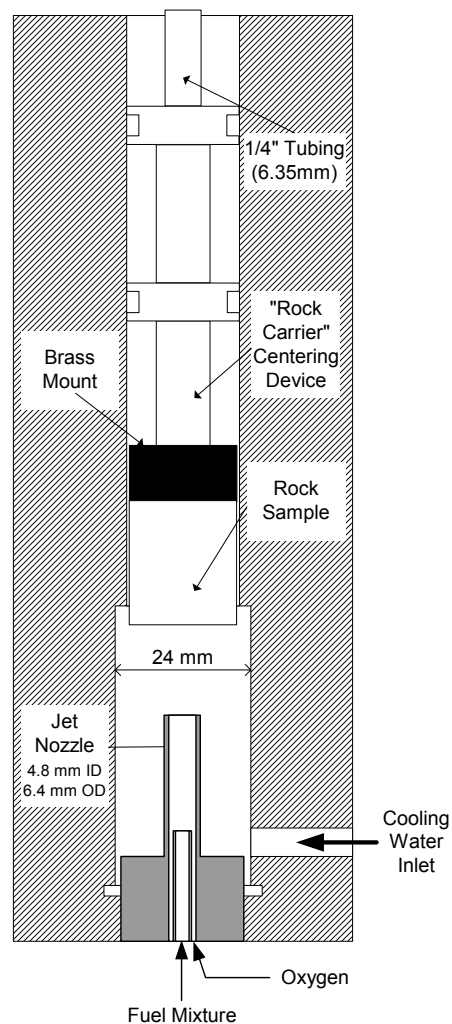
Figure 8.10 Schematic show rock sample attached to brass mount and affixed to rock rock carrier on movable probe as assembled inside the WCHB.

8.7.2. Stagnation Temperature

The stagnation temperature is defined as the temperature of a jet at a point of stagnation, where its velocity is zero. At the stagnation point, all of the kinetic energy of the jet has been converted to internal energy. For compressible supersonic flows, a considerable portion of the enthalpy of the jet can be in the form of kinetic energy, so that its stagnation temperature can differ from its static temperature while flowing. For these experiments, the average jet velocity at the nozzle exit is approximately 2 to 3 m/s, so these effects will not be a factor. Therefore, in these experiments, the stagnation temperature refers to the temperature at the point of jet impingement

on a surface, and will vary with stand-off distance due to entrainment of the surrounding cooling water.

For the stagnation temperature experiments, a 0.75" (19 mm) OD x 1" (25 mm) long cylindrical Macor block was attached to a nut using epoxy and threaded onto the end of the rock carrier. Macor is a machinable ceramic that was chosen because its thermal conductivity (1.4 W/m-K) (Corning Incorporated, 2009) is similar to that of Westerly granite (2.4 W/m-K) (Clark, 1966). The Macor block had a 1/16" (1.6 mm) center hole drilled through the center. A 1/32" (0.8 mm) Type K thermocouple was inserted down the center of the probe rod, through the rock carrier, and then through the Macor block. The tip of the thermocouple was exposed ~1 mm above the face of the Macor block to measure the stagnation temperature of the hydrothermal flame jet impinging on its surface.

A hydrothermal flame was ignited in the WCHB system using methanol as fuel. It was difficult to ignite the flame using the new nozzle configuration in Figure 8.8. In the first attempt, ignition could not be achieved by either increasing the fuel-water mixture inlet temperature to the maximum allowed by the preheaters, or by increasing the concentration of methanol in the fuel mixture. A second attempt succeeded by using a fuel-water mixture inlet temperature of 550 °C and by varying the water content in the fuel mixture to induce a perturbation that led to ignition. After ignition, the plant operating conditions were adjusted to their desired experimental values. Table 8.4 shows the range of methanol fuel concentrations and flow rates studied.

Table 8.4 Flow rates and operating conditions for methanol hydrothermal flames used in stagnation temperature study.

Mass % Methanol	Fuel Mixture			O_2	CW	T_{fuel}	T_{O2}
	Methanol	Water	Total				
(%)	(g/s)	(g/s)	(g/s)	(g/s)	(g/s)	(°C)	(°C)
15	0.188	1.06	1.25	0.42	50	495	390
15	0.225	1.23	1.50	0.50	50	500	395
20	0.25	1.00	1.25	0.56	50	500	395

Once the flame was stabilized at the desired operating conditions, the Macor block was moved to a stand-off distance of 15 mm, and data collection began. The stand-off distance between the

Macor block face and the jet nozzle exit could be varied during the course of the experiment in increments as small as 0.01 mm using the movable probe assembly. The stagnation temperature of the impinging jet flame was measured in 1 to 2 mm intervals along the centerline axis of the jet. Close to the jet nozzle exit, where temperatures increased rapidly as the stand-off distance decreased, the spacing between measurements was decreased to 0.25 to 0.50 mm intervals. At each stand-off distance, temperatures were recorded at a rate of once per second over a 1-minute period. For the 15 mass% methanol fuel mixture flames, the Macor block was lowered to within 1.5 mm of the jet nozzle exit. For the 20 mass% case, a stand-off distance of 3.75 mm was used due to the higher flame temperatures to avoid damaging the Macor block and thermocouple.

The average stagnation temperature with a 95% confidence interval (CI) for the hydrothermal flames produced under the operating conditions listed in Table 8.4 are shown in Figure 8.11. The data show that the flame jet is rapidly quenched as it entrains the surrounding cooling water, as had been inferred from the thermocouple positioned above the combustion chamber exit in the earlier study. For each of the flame jets, there are two distinct regions, separated by the critical temperature of water. In the far-field region, when the stagnation temperature is below the critical temperature of water, the rate of stagnation temperature decay as a function of stand-off distance is relatively low. In the near-field region close to the jet nozzle exit, when the stagnation temperature is above the critical temperature of water, the stagnation temperature decay is much more rapid. Close to the jet exit, the stagnation temperature appears to level off to a constant value for the 15 mass% methanol cases, indicating that the center of the Macor block is likely in the core region of the jet, where entrainment of the surrounding fluid is minimal. The flame temperature of the 20 mass% methanol fuel was too high to attempt to use the Macor block in the core region.

The experimental results show that hydrothermal flames can generate sufficient temperatures to induce spallation in rock. Even for flames made with weak fuel mixtures, flame temperatures are well in excess of the 500 $^\circ$C, the level where rock spallation was observed to occur in earlier experiments conducted within our group at ambient condions (Rauenzahn and Tester, 1989; Wilkinson, 1989). However, the flame jets are quickly quenched by the surrounding cooling
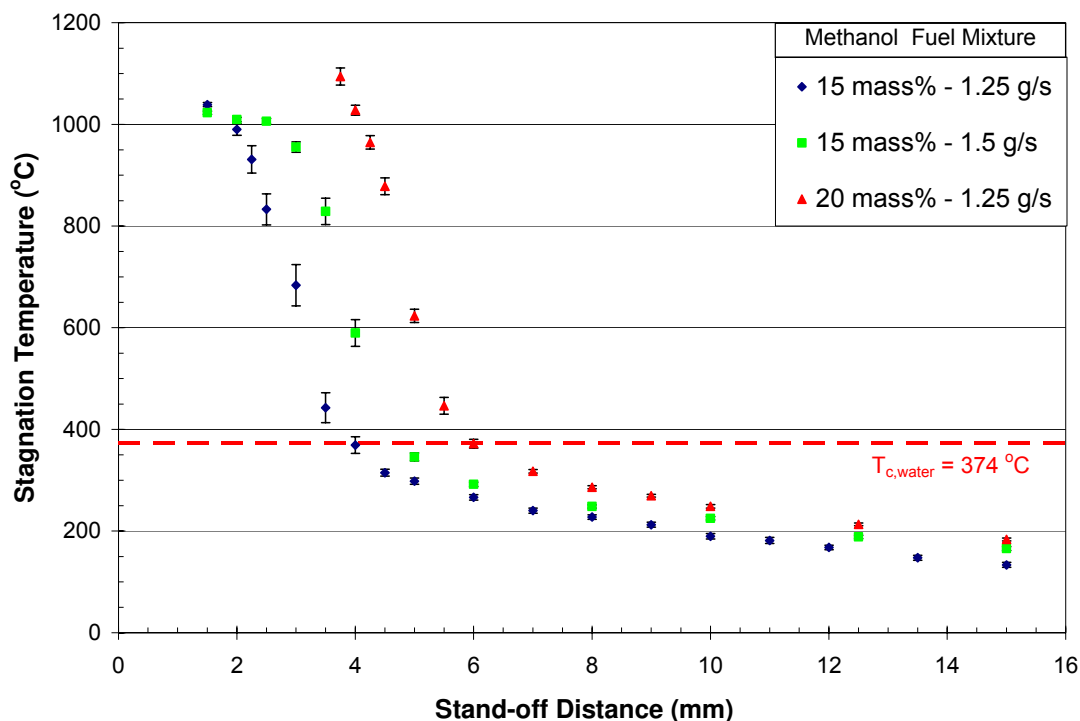
Figure 8.11 Average stagnation temperature (95% CI) as a function of stand-off distance for methanol hydrothermal flames.

water, so the rock surface must be placed extremely close to the jet nozzle exit to take advantage of the high flame jet temperatures.

Stagnation temperature measurements using hydrogen as a fuel were attempted, but the flame extinguished during the switchover from methanol to hydrogen, and could not be reignited.

8.7.3. Rock Spallation Feasibility Results

For the rock spallation experiment, a cylindrical sample (17.6 mm OD x 25 mm length) of Sioux quartzite was attached to a nut using epoxy and mounted on the end of the rock carrier and installed in the WCHB reactor. Sioux quartzite was chosen because previous studies had shown it to spall readily at low surface temperature (~350 ^{o}C) over a wide range of heat fluxes (Wilkinson and Tester, 1993). A hydrothermal flame was ignited using methanol as fuel. As in the stagnation temperature experiments, several attempts were needed to achieve ignition. Once ignited, the operating conditions were adjusted to same conditions used for the 1.5 g/s flow rate of 15 mass% methanol fuel mixture case in Table 8.4. Once the operating conditions had

stabilized, the rock was lowered into the flame jet. Based on stagnation temperature measurement, the rock surface was positioned at a stand-off distance of 1.5 mm, which should result in a jet with a stagnation temperature of ~1025 ^{o}C impinging on the rock surface. The rock was left at this position for 5 minutes before it was withdrawn from the flame jet. The flame was extinguished, the WCHB system shut down, and the Sioux Quartzite rock sample was removed for inspection.

Based on examination of the Sioux quartzite rock surface, it appears that spallation did occur initially, but quickly stopped, resulting in a very shallow hole, about 10 mm in diameter and 1 to 2 mm deep (Figure 8.12). Because of the relatively small rock sample sizes used, too large a portion of the surface of the rock is heated up and expanded, such that sufficient confining stress could not build up to maintain spallation. This is supported by the presence of several cracks that emanated radially from the center of the rock sample and over its entire length.

Figure 8.12 Sioux quartzite successfully spalled using 15 mass% methanol fuel flame jet.

An attempt was made to spall a sample of Westerly granite. Once again, difficulties were encountered while trying to ignite the hydrothermal flame. In one experiment, the flow rate of water was reduced to increase the methanol fuel mixture concentration entering the reactor. At some point, the fuel ignited. An intense white flame was observed through the sapphire view ports. Temperatures of 1510 ^{o}C and 1260 ^{o}C were recorded by the fuel mixture and oxygen inlet thermocouples, respectively. The intense flame burned for only several seconds. The flame was shortly followed by a large leak from the reactor head. The experiment was halted and the

WCHB system immediately shut down. The reactor was disassembled and inspected for damage. The fuel nozzle was severely damaged – only its base remained; the tubing had either burned away, which would explain the intense white flame, or had been melted. The fuel mixture and oxygen thermocouples were also damaged. The cooling water flow was sufficient to protect the reactor walls and oxygen nozzle from damage as it had been designed. This incident, along with the general difficulties encountered in igniting flames reinforce a concern that the WCHB reactor is too small to accommodate sufficiently large rock samples to permit continuous, steady-state spallation.

8.8. Conclusions and Path Forward

Experiments performed in the WCHB system demonstrated that hydrothermal flames can be produced in a downhole environment using both methanol and hydrogen as fuels. The ignition temperatures observed for methanol flames using the nozzle configuration shown in Figure 8.2 were higher than those seen in previous studies, but were low enough that flames could be ignited consistently with the WCHB system. Only a few extinction temperatures observed, but they were consistent with results from studies by ETH. When hydrogen fuel mixtures were used, autoignition of hydrothermal flames by preheating the inlets could not be reliably achieved, even for fuel-water mixture inlet temperatures as high as 585 ^{o}C. However, a method was developed for producing hydrogen flames by initially igniting a flame using a methanol fuel mixture and then switching over to hydrogen. Hydrogen flames were stable once lit, indicating that autoignition of hydrogen fuel mixtures should be possible using higher inlet temperatures or an improved nozzle design. Extinction temperatures of 320-330 ^{o}C were observed for hydrogen fuel mixtures. These values are similar to those observed for methane, another gaseous fuel. It was proposed that extinction is likely due to phase-splitting of the hydrogen-water fuel mixture into two phases at temperatures below critical temperature of water (374 ^{o}C).

The movable probe assembly was used to successfully measure the stagnation temperature of 15 and 20 mass% methanol hydrothermal flames as a function of stand-off distance. The measured flame jet stagnation temperatures were quenched quickly by the surrounding cooling water. For short stand-off distances, stagnation temperatures in excess of 1000 ^{o}C were recorded. A flame

spallation test on Sioux quartzite showed that spallation occurred initially, but then stopped. From thermally induced cracks that ran the length of the sample, it was inferred that the entire surface had been heated, causing spallation to stop due to a lack of confining stresses. It was concluded that the maximum rock sample size that could be used in the WCHB was too small for continuous spallation to be maintained.

Igniting flames using the nozzle configuration shown in Figure 8.8 proved to be difficult. Ignition was not reliable, and the techniques used to achieve ignition led to dangerous operating conditions. Once again, ignition could probably be achieved more easily with an improved nozzle design. However, even with an improved nozzle, the rock samples that can fit into the WCHB reactor are still too small to spall rock continuously. The results of continued studies of hydrothermal flames alone would be dependent on the nozzle configuration used, and would not necessarily translate to a new reactor configuration. Due to limitations of the reactor size and configuration, considerable effort would be required to improve nozzle design, limiting the ability to study how downhole conditions affect thermal spallation drilling and with no guarantee of success. Taking all these factors into consideration, continued hydrothermal flame studies did not appear to be the best course of action. Instead, it was decided to study behavior in the WCHB reactor that could be related to the dimensions of the reactor configuration and scaled in a general sense.

One phenomenon from the hydrothermal flame studies that could be better understood is the behavior of supercritical jets in liquid water. The stagnation temperature profile as a function of stand-off distance consisted of two distinct regions – one below the critical temperature of water where temperature decreased relatively slowly with stand-off distance, and one above the critical temperature where quenching of the thermal jet was rapid. Supercritical jet behavior in liquid water was characterized in terms of the nozzle diameter, jet nozzle temperature, and jet momentum flux. Moreover, it does not require the production of hydrothermal flames as the behavior of supercritical water jets in subcritical liquid co-flow can be studied using high temperature water jets produced by the WCHB reaction system preheaters. This study is the subject of Chapter 9.

Another important aspect of deep borehole drilling is the heat flux from the flame jets to the rock surface. The hydrothermal flames studies above had no mechanism for measuring heat flux from the impinging flame jet. If continuous rock spallation had been possible, it would have been characterized by measuring stagnation temperature alone. A means of measuring heat flux in the deep borehole environment is needed. However, building a heat flux meter that can withstand hydrothermal flame temperature is very difficult and may not even be possible. Nonetheless, as supercritical water jets can be used to study jet behavior, we are hopeful that they can also be used to characterize heat flux. This study is the subject of Chapter 10.

8.9. References

Clark, S. P., Ed. (1966). <u>Handbook of Physical Constants</u>. Memoir // The Geological Society of America ;. New York, NY, Geological Society of America.

Corning Incorporated. (2009). "Macor Machinable Glass Ceramics."   Retrieved January 30, 2009, from http://www.corning.com/specialtymaterials/products_capabilites/macor.aspx.

La Roche, H. L. (1996). <u>Wandegkühlter Hydrothermal-Brenner (WHB) für die überkritische Nassoxidation</u>. Doctoral Thesis, Swiss Federal Institute of Technology (ETH).

Narayanan, C., C. Frouzakis, K. Boulouchos, K. Príkopský, B. Wellig and P. Rudolf von Rohr (2008). "Numerical Modelling of a Supercritical Water Oxidation Reactor Containing a Hydrothermal Flame." <u>Journal of Supercritical Fluids</u> **46**(2): 149-155.

Pohsner, G. M. and E. U. Franck (1994). "Spectra and Temperatures of Diffusion Flames at High-Pressures to 1000 Bar." <u>Berichte Der Bunsen-Gesellschaft-Physical Chemistry Chemical Physics</u> **98**(8): 1082-1090.

Rauenzahn, R. M. and J. W. Tester (1989). "Rock Failure Mechanisms of Flame-Jet Thermal Spallation Drilling - Theory and Experimental Testing." <u>International Journal of Rock Mechanics and Mining Sciences & Geomechanics Abstracts</u> **26**(5): 381-399.

Seward, T. M. and E. U. Franck (1981). "The System Hydrogen - Water up to 440 ^{o}C and 2500 bar Pressure." <u>Berichte Der Bunsen-Gesellschaft-Physical Chemistry Chemical Physics</u> **85**(1): 2-7.

Shmonov, V. M., R. J. Sadus and E. U. Franck (1993). "High-Pressure Phase-Equilibria and Supercritical PVT Data of the Binary Water Plus Methane Mixture to 723-K and 200-MPa." <u>Journal of Physical Chemistry</u> **97**(35): 9054-9059.

Steeper, R. R., S. F. Rice, M. S. Brown and S. C. Johnston (1992). "Methane and Methanol Diffusion Flames in Supercritical Water." <u>Journal of Supercritical Fluids</u> **5**(4): 262-268.

Weber, M. (1997). <u>Apparate einer SCWO-Anglage und deren Leistungsfähigkeit</u>. Doctoral Thesis, Swiss Federal Institute of Technology (ETH).

Wellig, B. (2003). <u>Transpiring Wall Reactor for Supercritical Water Oxidation</u>. Doctor of Technical Sciences Thesis, Swiss Federal Institute of Technology, Available online at Available from: www.e-collection.ethz.ch.

Wilkinson, M. A. (1989). <u>Computational Modeling of the Gas-Phase Transport Phenomena and Experimental Investigation of Surface Temperatures During Flame-Jet Thermal Spallation Drilling</u>. Doctoral Thesis, Massachusetts Institute of Technology.

Wilkinson, M. A. and J. W. Tester (1993). "Experimental-Measurement of Surface Temperatures during Flame-Jet Induced Thermal Spallation." <u>Rock Mechanics and Rock Engineering</u> **26**(1): 29-62.

Williams, R. E., R. M. Potter and S. Miska (1996). "Experiments in Thermal Spallation of Various Rocks." <u>Journal of Energy Resources Technology - Transactions of the ASME</u> **118**(1): 2-8.

Chapter 9: Supercritical Free Jets in Subcritical Co-Flow

9.1. Objectives

In Chapter 8, it was observed that flame jets at supercritical temperatures were quickly quenched to sub-critical water temperatures within a few nozzle diameters of the nozzle exit by the surrounding, co-flowing cooling water in the reactor before impinging against a flat surface. According to current theory, discussed in Chapter 1, thermal spallation requires rapid heating of the rock surface to temperatures of approximately 500 ^{o}C and higher (Rauenzahn and Tester, 1989; Wilkinson and Tester, 1993) so that thermal expansion of the confined rock will induce stresses that lead to failure of the rock surface. The rapid quenching of the flame jet by the surrounding fluid needs to be better understood to effectively operate a thermal spallation drilling system in a deep borehole. However, it is not necessary to create flame jets to study this behavior – the WCHB reactor system is capable of producing jets of water at temperatures up to 525 ^{o}C, well above the critical temperature of water (374 ^{o}C). With proper scaling of the experimental variables, these supercritical jets should provide insight into the behavior of low density, supercritical temperature jets in a high density, subcritical temperature environment without having to overcome the documented difficulty in creating, maintaining, and studying flame jets in water at high pressures.

The objective of this study was to characterize the behavior of free turbulent jets at supercritical temperatures in subcritical temperature co-flow. Ideally, it would be possible to fully characterize the jets by measuring both the temperature and velocity profiles as a function of axial and radial position. However, the experimental setup of the WCHB reactor system only permitted the reliable measurement of the centerline axial temperature profile. Therefore, the centerline axial temperature behavior of jets of water at both supercritical and subcritical temperatures in co-flowing, ambient temperature (~25 ^{o}C) cooling water was studied.

9.2. Experimental Setup

9.2.1. Reactor Configuration

The reactor configuration and procedure for hot water jet experiments are similar to those used in the hydrothermal flame experiments described in Section 8.3, but the process and instrumentation scheme is greatly simplified. The hot water jet experiments require only two feed streams: a high temperature water jet and an ambient temperature, co-flowing cooling water stream. Since flames are not being produced for this study, the fuel and oxygen delivery lines in the WCHB reactor system shown in Figure 7.2 are not required. The oxygen delivery line was disconnected from the WCHB and a ¼" (0.64 cm) Hastelloy plug was used to seal the oxygen port (shown in Figure 8.1). The hydrogen delivery line was isolated from the reactor system using a needle valve, and the SD-1 pump normally used to deliver methanol was used to deliver water to the preheaters so that mass flow rates through the jet of up to 6 g/s of water could be achieved.

Figure 9.1 shows the reactor and nozzle configuration used for the hot water jet experiments. Two different nozzles, shown in Figure 9.2, were used during the experiment so that the use of the scaling parameters (discussed in Section 9.3.2) could be validated independent of the nozzle geometry. The first nozzle has an inner diameter of 2.3 mm and an outer diameter of 2.8 mm. The second has inner and outer diameters of 3.0 mm and 3.4 mm, respectively. The nozzles were constructed from SS316 tubing welded into an Inconel 625 base machined to fit inside the WCHB reactor head. In initial experiments a thick-walled insulating nozzle (2.3 mm ID x 9.5 mm OD) was used. It is believed that the large gap between the inner and outer diameter of the nozzle created a recirculation zone around the nozzle exit. Variations in the co-flowing cooling water flow rate interacted with the recirculation zone and affected the behavior of the jet, leading to variations in the observed axial temperature profile. For this reason, the nozzles were made with thin walls to prevent the formation of a recirculation zone at the nozzle exit.
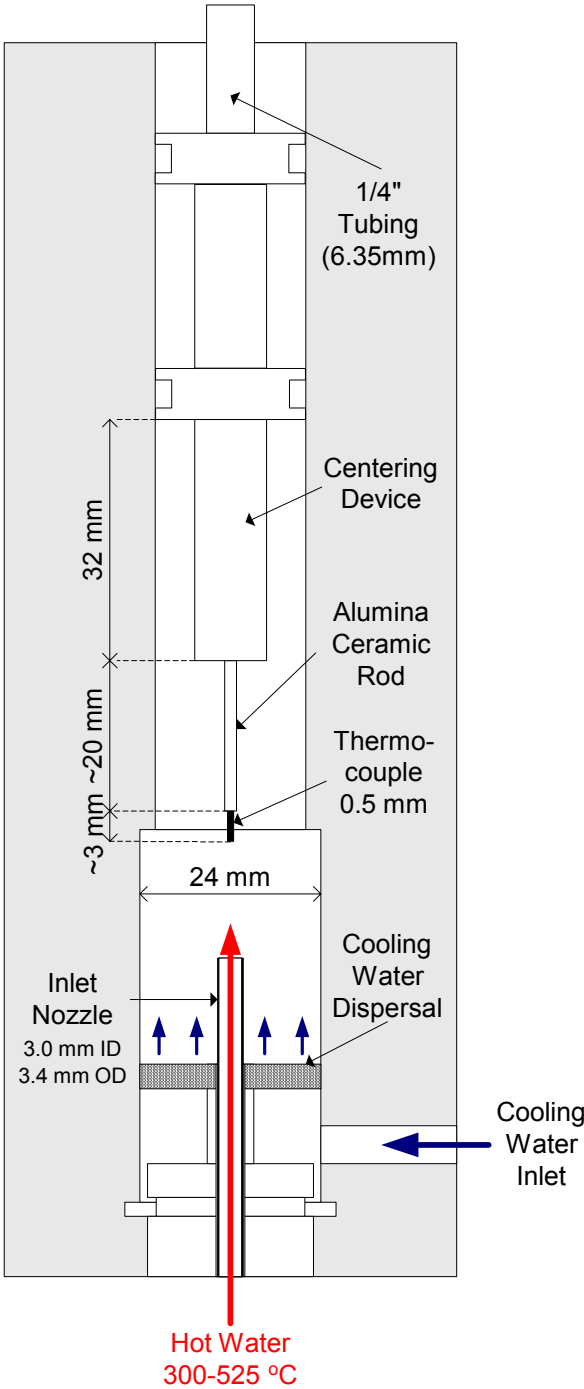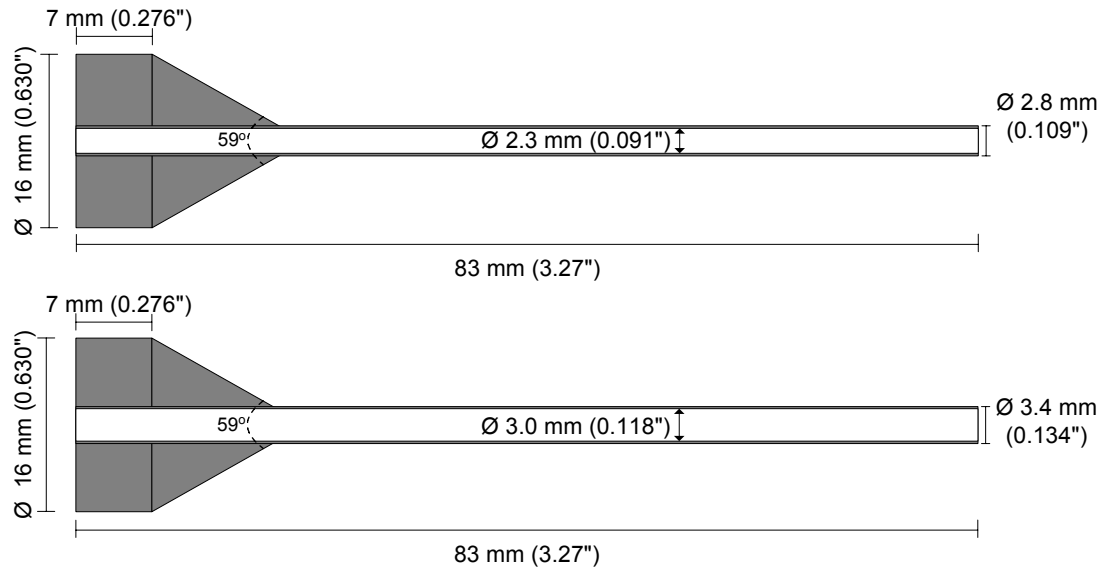
Figure 9.1 Reactor and nozzle configuration used in hot water jet experiments.

7 mm (0.276")

16 mm (0.630")

59°

Ø 2.3 mm (0.091")

Ø 2.8 mm (0.109")

83 mm (3.27")

7 mm (0.276")

16 mm (0.630")

59°

Ø 3.0 mm (0.118")

Ø 3.4 mm (0.134")

83 mm (3.27")

Figure 9.2 Detailed drawing of "thin-walled" nozzles used in hot water jet experiments.

Cooling water enters the WCHB reactor at a 90° angle to the direction it flows. To determine if there were any entrance effects from the cooling water on jet behavior, a cooling water distributor was installed. A detailed drawing of the cooling water distributor nozzle is shown in Figure 9.3. The distributor threads into the port where the oxygen nozzle would normally be located. The cooling water is dispersed by three #100 mesh wire screens sandwiched between two #24 wire mesh screens. The mesh eliminates any radial velocity components in the cooling water flow and ensures a constant velocity profile over the entire cooling water flow area. Preliminary experiments showed no discernible difference in jet behavior with and without the mesh dispersal system in place, indicating that entrance effects from the cooling water were negligible to begin with. Despite this, the experiments were carried out with the cooling water distributor in place because the distributor has the added benefit of creating an insulating gap between the cooling water and water jet nozzle over much of its length.
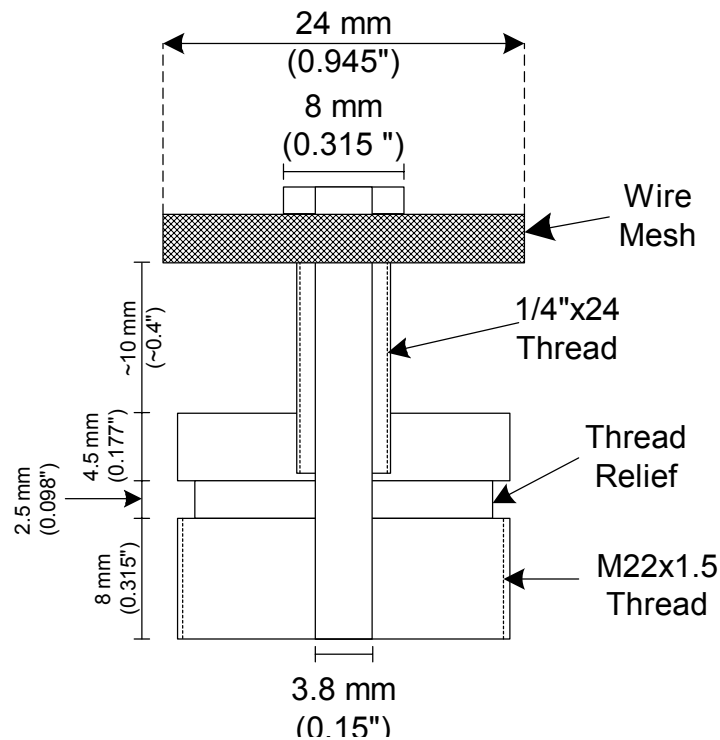
Figure 9.3 Detailed drawing of cooling water distributor nozzle. Wire mesh is made up of 3 layers of #100 Mesh sandwiched between #24 mesh layers.

9.2.2. Temperature Measurement

The axial temperature profile was measured using a Type K thermocouple inserted down the center of the movable probe rod and through the centering device (see Figure 9.1). The movable probe could then be moved along the centerline axis of the reactor. The axial position of the thermocouple probe tip was zeroed at the nozzle exit by visual inspection through the sapphire window view ports on the WCHB. The radial position was likewise verified as being centered along the central axis of the jet by visual inspection. The thermocouple could be inserted into the jet nozzle to obtain temperature measurements of the jet just prior to exiting the nozzle.

The temperature measured by the thermocouple is not necessarily the temperature of the jet at a given point along the axis due to heat losses from the thermocouple tip. Since the centerline temperature of the jet decreases as it moves away from the nozzle exit due to entrainment of the surrounding fluid, the temperature of the thermocouple coaxially immersed in the jet also decreases along its length. Heat is transferred from the water jet to the thermocouple tip, and is

conducted away from the tip along the length of the thermocouple. The temperature of the thermocouple can be determined by a steady state energy balance on the thermocouple tip. An analysis found that radiative heat transfer from the thermocouple to the surroundings is negligible. Therefore, the temperature of the thermocouple tip is determined by balancing the convective heat transfer from the jet to the thermocouple with the conductive heat transfer away from the tip down the length of the reactor. Both heat transfer processes depend on the area available for heat transfer – convective on the surface area of the thermocouple and conductive on the cross sectional area. As the thermocouple cross-sectional radius decreases, the area available for conductive heat transfer decreases more quickly than for convective heat transfer, so the temperature of the thermocouple should approach the temperature of the jet stream as the radius of the thermocouple approaches zero.

During preliminary experiments, thermocouples of increasingly smaller diameters were used to measure the axial temperature profile. Thermocouples of 1.6 mm, 0.8 mm, and 0.5 mm in diameter were tested. The 1.6 mm diameter thermocouple was sturdy enough to support itself against the force of the oncoming jet, but the smaller diameter thermocouples were not. Instead, they were supported by a stiff alumina ceramic rod with the tip of the thermocouple protruding 2 to 3 mm to measure the jet temperature. A trial in which the 1.6 mm diameter thermocouple was insulated by an alumina ceramic rod was also conducted to determine if its presence affects the measured temperature.

Axial temperature profiles were measured for nozzle exit temperatures ranging from 300 to 525 ^{o}C. Results for the case of a jet with a mass flow rate of 3 g/s and nozzle exit temperature of ~525 ^{o}C issuing into 25 g/s of co-flowing cooling water is shown in Figure 9.4. The measured temperature is scaled by the difference in temperature between the nozzle exit and the ambient co-flow to account for small differences in the actual nozzle temperature between runs. Away from the nozzle exit ($x \geq 6$ mm), the measurements made by the different diameter thermocouples are in good agreement. In this region, the temperature gradient is relatively low, so the driving force for thermal conduction away from the probe tip is also low and the jet temperature and probe temperature should be in good agreement. Close to the nozzle exit

($x < 6$ mm), where temperature changes quickly with axial position and the temperature gradient is very high, the temperature measurements differ as a function of thermocouple diameter. The 1.6 mm diameter thermocouples, both insulated with an alumina ceramic jacket and uninsulated, report significantly lower temperatures in this region than the 0.8 mm diameter thermocouple. The difference in measured temperature decreases quickly once the probe enters the nozzle (when x is negative) and the temperature gradient becomes negligible. These results indicate that the larger diameter thermocouples have large measurement errors in the region close to the nozzle exit due to conduction heat losses. The differences in measured temperature between the 0.8 mm and 0.5 mm diameter thermocouples are much smaller, indicating that the measured temperature is close to the actual jet temperature. Similar results were observed for all nozzle exit temperatures. The preliminary experiments show that the smallest feasible thermocouple diameter, 0.5 mm, should be used for measuring centerline temperature profiles, and that the measured temperatures accurately reflect the actual jet temperature.
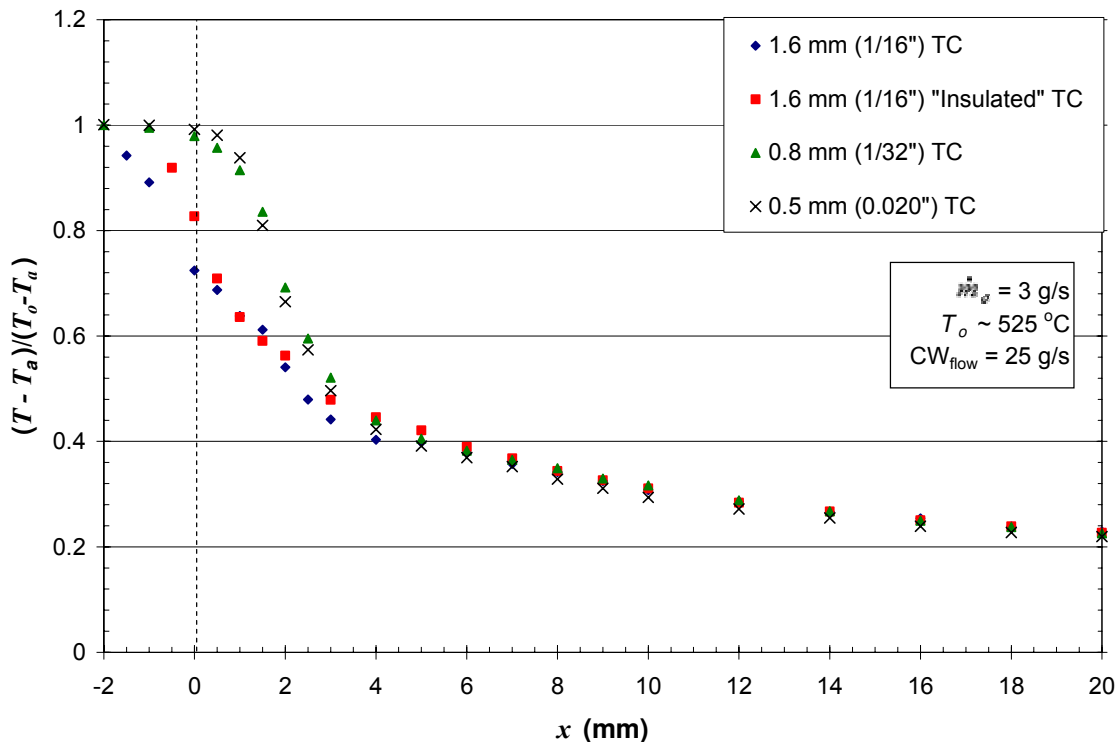

Figure 9.4 Scaled measured temperatures (T) of a supercritical water jet issuing into a subcritcal temperature co-flow (T_a=25 ^{o}C) as a function of axial position for thermocouples (TC) of differing diameters.

9.2.3. Procedure

The start-up, operating and shut down procedures for hot water jet experiments are similar to those for hydrothermal flame experiments discussed in Chapter 8, so an abridged version of the procedure highlighting the major differences is given here. After the system has been properly assembled and pressure tested, the operating procedure is as follows:

Start-Up

14.) Turn on all meters, temperature controllers, and sensors.
15.) Check that there are adequate process fluids for the entire experiment:
    a. De-ionized cooling water in the cooling water tank,
    b. Water in SD-1 pump feed carboys.
16.) Check initial valve positions (feeds to pumps open, bleed valves closed, etc.).
17.) Open necessary programs on DAQ PC:
    a. NI Labview,
    b. ER3000 controller software,
18.) Turn "Emergency Shutdown" switch to "On" position.
19.) Apply 100 psig (6.9 barg) compressed air to BPR and air-operated valves.
20.) Set initial flow rates:
    a. CW triplex plunger pump to ~20 g/s flowrate,
    b. SD-1 pumps to low flow rate (~25 mL/min).
21.) Increase system pressure to final operating pressure in ~15 bar increments.
22.) Turn on house water flow through heat exchanger located after the reactor.
23.) Increase water feed to reactor temperature using pre-heaters, taking care not to heat up the system to quickly.

Data Acquisition

5.) Begin data acquisition.
6.) Increase cooling water and fee water flow rates to desired starting experimental values.
7.) Adjust pre-heaters to obtain desired nozzle exit temperature.
8.) Using manual pressure generator to operate movable probe, position thermocouple tip and record centerline temperatures.
9.) Adjust flow rates, temperatures, and probe positions to acquire data as needed.

Shut Down

10.)   Slowly decrease temperature of feed water, taking care not to cool system too quickly.
11.)   Once fuel mixture inlet temperature is below 100 $^{\circ}$C, slowly decrease system pressure in ~15 bar increments.
12.)   Turn off SD-1 pumps, cooling water pump, and house cooling water flow.
13.)   Turn off computer software.

14.)   Turn off meters, temperature controllers, and sensors.

At the beginning of each experiment, the thermocouple was moved to a stand-off distance of $x =$ 20 mm, and data collection began. The region of the jet that could be studied was limited by the length of the 24 mm cross-sectional area of the reactor as well as by wall effects, as discussed below. The stand-off distance between the thermocouple and the jet nozzle exit could be varied during the course of the experiment in increments as small as 0.01 mm using the movable probe assembly. The centerline jet temperature of the hot water jet was measured in 1 to 2 mm intervals along the axis of the jet. Close to the jet nozzle exit, where temperatures increased rapidly as the stand-off distance decreased, the spacing between measurements was decreased to 0.25 to 0.50 mm intervals. Temperature measurements were taken inside the nozzle ($x < 0$ mm) to determine the nozzle exit temperature. At each stand-off distance, temperature data were collected at a rate of once per second over a 30 second period.

9.2.4. Operating Conditions

Jet temperatures and flow rates, as well as cooling water flow rates, were varied over a large range of values to study the behavior of high temperature, low density jets in a high density environment. Experiments with nozzle exit temperatures ranging from 300 to 525 $^{\circ}$C were carried out using two different nozzles (2.3 mm and 3.0 mm ID). For reasons described in the following section, the jet behavior depends heavily on the jet momentum flux, G_o, and the ratio of the momentum fluxes of the jet and co-annular cooling water flow, G_o/G_a. The nozzle temperatures, jet mass flow rates, jet momentum fluxes, and momentum flux ratios studied are shown in Table 9.1, Table 9.2 and Table 9.3. Two different nozzle momentum fluxes were studied with each nozzle. The momentum flux was kept constant for all nozzle exit temperatures considered during a series. The cooling water flow rate was varied by up to a factor of three to determine the effect of the momentum flux ratio on jet behavior. Because of limitations on the nozzle temperatures that could be achieved for a given flow rate, the jet momentum fluxes studied for each nozzle differ. To account for this, the cooling water flow rates were adjusted for the experiments listed in Table 9.2 and Table 9.3 so that the momentum flux ratios studied for the different nozzles were identical. The system pressure was maintained at $P = 250$ bar for all experiments.

Table 9.1 Nozzle temperatures, densities and jet and cooling water mass flow rates used for first series of experiments with 2.3 mm ID nozzle.

T_o (^oC)	ρ_o (kg/m^3)	$\dot{m}_o$ (g/s)	G_o (kg-m/s^2)	G_o/G_a 25.0 g/s	50.0 g/s	75.0 g/s
400	166.5	4.00	0.0231	16.6	4.16	1.85
400	166.5	2.00	0.0058	4.16	--	--
425	126.8	3.49	0.0231	16.6	4.16	1.85
450	109.0	3.23	0.0231	16.6	4.16	1.85
475	97.8	3.06	0.0231	16.6	4.16	1.85
500	89.7	2.94	0.0231	16.6	4.16	1.85
525	83.5	2.83	0.0231	16.6	4.16	1.85
300	743.0	2.88	0.0027	1.93	--	--
300	743.0	5.75	0.0107	7.72	1.93	--
350	625.5	5.28	0.0107	7.72	1.93	--
375	505.5	4.75	0.0107	7.72	1.93	--
400	166.5	2.72	0.0107	7.72	1.93	--
425	126.8	2.38	0.0107	7.72	1.93	--
450	109.0	2.20	0.0107	7.72	1.93	--
500	89.7	2.00	0.0107	7.72	1.93	--

Table 9.2 Nozzle temperatures, densities and jet and cooling water mass flow rates used for second series of experiments with 2.3 mm ID nozzle.

T_o (^oC)	ρ_o (kg/m^3)	$\dot{m}_o$ (g/s)	G_o (kg-m/s^2)	G_o/G_a 27.0 g/s	54.1g/s	81.1 g/s
400	166.5	4.00	0.0231	14.2	3.56	1.58
400	166.5	2.00	0.0058	3.56	--	--
425	126.8	3.49	0.0231	14.2	3.56	1.58
450	109.0	3.23	0.0231	14.2	3.56	1.58
475	97.8	3.06	0.0231	14.2	3.56	1.58
500	89.7	2.94	0.0231	14.2	3.56	1.58
525	83.5	2.83	0.0231	14.2	3.56	1.58
300	743.0	2.88	0.0027	1.65	--	--
300	743.0	5.75	0.0107	6.59	1.65	--
350	625.5	5.28	0.0107	6.59	1.65	--
375	505.5	4.75	0.0107	6.59	1.65	--
400	166.5	2.72	0.0107	6.59	1.65	--
425	126.8	2.38	0.0107	6.59	1.65	--
450	109.0	2.20	0.0107	6.59	1.65	--
500	89.7	2.00	0.0107	6.59	1.65	--

Table 9.3 Nozzle temperatures, densities and jet and cooling water mass flow rates used for series of experiments with 3.0 mm ID nozzle.

T_o	ρ_o	$\dot{m}_o$	G_o	G_o/G_a		
(°C)	(kg/m³)	(g/s)	(kg-m/s²)	20.7 g/s	41.3 g/s	62.0 g/s
400	166.5	4.00	0.0136	14.2	3.56	1.58
400	166.5	2.00	0.0034	3.56	--	--
425	126.8	3.49	0.0136	14.2	3.56	1.58
450	109.0	3.23	0.0136	14.2	3.56	1.58
475	97.8	3.06	0.0136	14.2	3.56	1.58
500	89.7	2.94	0.0136	14.2	3.56	1.58
525	83.5	2.83	0.0136	14.2	3.56	1.58
300	743.0	2.88	0.0016	1.65	--	--
300	743.0	5.75	0.0063	6.59	1.65	--
350	625.5	5.28	0.0063	6.59	1.65	--
375	505.5	4.75	0.0063	6.59	1.65	--
400	166.5	2.72	0.0063	6.59	1.65	--
425	126.8	2.38	0.0063	6.59	1.65	--
450	109.0	2.20	0.0063	6.59	1.65	--
500	89.7	2.00	0.0063	6.59	1.65	--

A uniform velocity profile was assumed for the jet at the nozzle exit. Therefore, the flow for all jets in the study is turbulent based on the Reynolds number, Re_o:

$$\text{Re}_o = \frac{\rho_o D_o U_o}{\mu_o} \qquad\qquad \text{Eq. (9-1)}$$

where:
$$\rho_o = \text{density at nozzle exit}$$
$$D_o = \text{nozzle diameter}$$
$$U_o = \text{velocity at jet exit}$$
$$\mu_o = \text{viscosity at nozzle exit}$$

The range of Reynolds numbers and of other experimental conditions covered in the study is shown in Table 9.4. Nomenclature and definitions for the other parameters listed in the table are given in Section 9.3.

Table 9.4 Ranges of experimental conditions covered in study.

jet temperature at nozzle exit	T_o	300-525	^{o}C
ambient (co-flowing) temperature	T_a	25	^{o}C
jet density at nozzle exit	ρ_o	83-745	kg/m^3
ambient density	ρ_a	1008	kg/m^3
initial density ratio	$(\rho_o/\rho_a)^{-1}$	1.35-12.1	
jet velocity at nozzle exit	U_o	0.55-8.2	m/s
ambient co-flowing velocity	U_a	0.05-0.18	m/s
initial velocity ratio	U_a/U_a	0.01-0.08	
jet nozzle diameter	D_o	2.3, 3.0	mm
Reynolds number at nozzle exit	Re$_o$	13,300-76,200	
Froude number at nozzle exit	Fr_o	29-430	
Thring-Newby parameter	C_{TN}	0.27-0.88	
Craya-Curtet parameter	Ct_{ni}	0.28-0.93	
momentum radius of jet	r_θ	82-964	mm
axial position	x	0-20	mm
system pressure	P	250	bar

9.3. Theory

9.3.1. Flow Characterization

At first glance, the flow under study, depicted in Figure 9.1, is a confined, vertical, buoyant, axisymmetric turbulent jet with co-flow. Determining the effect of supercritical exit temperatures on the jet behavior in such a complicated system would be difficult, especially when only the axial temperature profile can be measured. However, analysis of the flow can be greatly simplified by identifying the dominant forces acting on the jet in the region being studied and making simplifying assumptions accordingly.

First, it was assumed that the surrounding reactor walls have no effect on the development of the jet or entrainment of the cooling water in the region being studied. At some point within the confined space of the reactor, the spreading jet will either entrain all the surrounding, co-flowing fluid or encounter the reactor walls, and this will affect the jet behavior. A first-order analysis of the behavior of co-flowing jets in a duct or confined space was put forth by Thring and Newby (1953). The jet behavior is determined by the Thring-Newby parameter:

$$C_{TN} = \frac{\dot{m}_a + \dot{m}_o}{\dot{m}_o}\left(\frac{\rho_o}{\rho_a}\right)^{1/2}\frac{D_o}{D_R}$$

Eq. (9-2)

where:
C_{TN} = Thring-Newby parameter
$\dot{m}_a$ = mass flow rate of ambient (co-flowing) fluid
$\dot{m}_o$ = mass flow rate of jet
ρ_a = density of ambient fluid
ρ_o = density of jet at nozzle exit
D_o = nozzle inner diameter
D_R = reactor (chamber) diameter

According to their analysis, there is insufficient co-flowing fluid for the jet to entrain when $C_{TN} <$ 0.9 and a recirculation zone forms. The distance, X_o, within which the jet entrains all the available fluid is:

$$X_o = 2.5 \cdot D_R \theta_{TN}$$

Eq. (9-3)

For the flows in this study, the Thring-Newby parameter varies from 0.27 to 0.88, so recirculation zones likely exist in the reactor. However, according to Eq. (9-3), the recirculation zone should occur farther downstream than the region being studied for most cases, with the exception of the lowest cooling water flow conditions. Here, the Thring-Newby model predicts the recirculation zone begins at the end of the region being studied. According to experimental results presented by Thring and Newby, the jet behaves like a free jet in most of the region before the recirculation zone. Therefore, the assumption that the reactor walls will not affect jet behavior should be valid for most cases, and for low cooling water flow cases, only the end of the region studied should be affected. A much more in-depth analysis of confined jet flow was developed by Craya and Curtet (Curtet, 1958), elaborated by Becker et al. (1962), and modified to account for variable density jets by Steward and Guruz (1977). In this analysis, the behavior of the confined jet is determined by a similarity parameter commonly referred to as the Craya-Curtet parameter, Ct. Experiments with isothermal confined jets showed that recirculation is little to no recirculation when $Ct < 0.50$. Moreover, it was noted that confined jet behavior was identical to that of a free jet in a stagnant free stream when $Ct = 0.673$ (Becker et al., 1962). Using the formulation for variable density confined jets derived by Steward and Guruz (1977), the non-isothermal Craya-Curtet parameter, Ct_{ni}, for jets in this study vary from 0.28 to 0.93.

Once again, recirculation zones are predicted for flows with low co-flowing cooling water mass flow rates. The position of the start of the recirculation zone predicted by the two theories are in good agreement, with the Craya-Curtet theory prediction being slightly farther downstream (Curtet, 1958).

The influence of buoyancy on jet behavior caused by the large difference in density between the jet and ambient fluids can also be ignored in the region studied. A buoyant jet can be divided into three regions: the non-buoyant region, the intermediate region, and the buoyant region. In the non-buoyant region, close to the nozzle exit, inertial forces dominate and the jet behaves like a pure jet. In the buoyant region, located in the far-field, buoyant forces dominate and the jet behaves like a pure plume. The intermediate region, where both inertial and buoyant forces are important, links the two regions. The axial location of the start of this intermediate region depends primarily on the Froude number at the jet exit, Fr_o, which describes the ratio of inertial to buoyant forces:

$$Fr_o = \frac{U_o \rho_o}{g D_o (\rho_a - \rho_o)}$$

Eq. (9-4)

where:
U_o = velocity at jet exit
g = gravitational constant

The larger the value of the Froude number, the farther out the non-buoyant region extends. A review of experimental data for axisymmetric vertical buoyant jets (Chen and Rodi, 1980) found that in the non-buoyant region:

$$Fr_o^{-1/2} \left(\frac{\rho_o}{\rho_a} \right)^{-1/4} \frac{x}{D_o} < 0.5$$

Eq. (9-5)

and in the buoyant region:

$$Fr_o^{-1/2} \left(\frac{\rho_o}{\rho_a} \right)^{-1/4} \frac{x}{D_o} > 5$$

Eq. (9-6)

For the flows studied here, the Froude number ranges from 29 to 430. The maximum value of the expression in Eq. (9-5) and Eq. (9-6) for the flows studied here over the region studied ($0 \leq x$

$\leq$ 20 mm) vary from 0.45 to 2.4, increasing as the jet nozzle temperature increases. Based on this, it is possible that buoyancy forces affect jet behavior, especially near the end of the region studied. However, the transition from the non-buoyant to the intermediate is not abrupt. In their review of the subject, Chen and Rodi (1980) group the results from the non-buoyant and intermediate region together, arguing that the buoyant forces are still relatively small. For this study, the range of possible Froude numbers was limited by the power of the pre-heaters in the experimental system and the size of the nozzle diameters. The calculated Froude numbers must be high enough that inertial forces dominate over most of the region studied, so that the flow can be treated as being that of a pure jet.

Finally, the initial jet velocity is much larger than the velocity of the co-flowing stream, so the affect of the co-flowing cooling water can be ignored. If top-hat velocity profiles are assumed at the jet nozzle exit and in the surrounding cooling water, then the jet nozzle exit velocity, U_o, for the cases studied vary from 0.55 to 8.2 m/s, while the velocity of the co-flowing cooling water, U_a, varies from 0.05 to 0.18 m/s. Moreover, the ratio of the outer-to-inner initial velocities, U_a/U_o, is never greater than 0.08. A more rigorous criterion for determining the effects of co-flow on jet behavior used by Pitts (1991) utilizes the "momentum radius," r_θ, defined as:

$$r_\theta = \left(\frac{\rho_o \left(D/2 \right)^2 \left(U_o/U_a - 1 \right) \left(U_o/U_a \right)}{\rho_a U_a^2} \right)^{1/2}$$

Eq. (9-7)

The flow behaves as a free jet as $r_\theta \to \infty$. Pitts noted in his study of variable density, non-homogeneous jets that for the maximum downstream distances where measurements were taken, x/r_θ ranged from 1.7 to 2.9, only small variations from free jet behavior were to be expected. For this study, maximum values of x/r_θ only range from 0.02 to 0.24, so effects from the co-flow on jet behavior can safely assumed to be negligible.

For the reasons stated above, the jet can be considered a non-isothermal, axisymmetric, turbulent, free jet over the region being studied to a first order approximation. The goal of the study is to determine how the supercritical nature of jet affects its behavior. However the results

must take into consideration the possible effects from the reactor walls and buoyant forces to determine when the stated assumptions are not valid.

9.3.2. Scaling and Similarity Laws

Since the experimental set up allows the measurement of the centerline temperature as a function of axial position, analysis of experimental data requires identifying the proper scaling laws for length and temperature. Axisymmetric turbulent free jets are a simple flow and have been studied in detailed, so the relevant scaling laws and flow models are well characterized. For isothermal homogeneous jets, length is scaled by the diameter of the nozzle from which the jet exits. For the case of a non-isothermal jet, in which the density of the jet differs from the surrounding ambient fluid, the scaling law for length was first proposed by Thring and Newby (1953). Since buoyant forces are negligible in the region after the nozzle exit, the jet is characterized by the momentum flux at the nozzle, G_o. Assuming a uniform velocity profile U_o at the nozzle exit, the momentum flux at the nozzle exit is defined as:

$$G_o = 2\pi \int_0^{Do/2} \rho_o U^2 r\, dr = \frac{\pi D_0^2}{4} \rho_o U_o^2 = \frac{4\dot{m}^2}{\pi \rho_o D_o^2} \qquad \text{Eq. (9-8)}$$

For a non-isothermal jet, in which the jet has initial density ρ_o and the ambient fluid has density ρ_a, Thring and Newby used the effective nozzle diameter, D_{eff}, which is the nozzle diameter of a jet with the same mass flow rate, $\dot{m}$, and momentum flux as the experimental jet, but the density of the ambient fluid:

$$G_o = \frac{4\dot{m}^2}{\pi \rho_o D_o^2} = \frac{4\dot{m}^2}{\pi \rho_a D_{eff}^2} \qquad \text{Eq. (9-9)}$$

$$D_{eff} = D_o \left(\frac{\rho_o}{\rho_a} \right)^{1/2} \qquad \text{Eq. (9-10)}$$

so that the non-dimensionalized axial position, X_{eff}, is:

$$X_{eff} = \frac{x}{D_{eff}} = \frac{x}{D_o} \left(\frac{\rho_o}{\rho_a} \right)^{-1/2} \qquad \text{Eq. (9-11)}$$

The excess centerline axial temperature, T, relative to the ambient temperature, T_a, is scaled by the excess jet temperature at nozzle exit, T_o, so that the non-dimensionalized centerline temperature, θ, is:

$$\theta = \frac{T - T_a}{T_o - T_a}$$

Eq. (9-12)

Thring and Newby used these scaling parameters to describe flow in the region just downstream of the nozzle exit, where non-buoyant jets tend to become self-similar. Flow is considered self-similar when one length scale, one velocity, and one temperature (or concentration) are sufficient to describe the time-averaged, dimensionless quantities as functions of one geometrical variable only. In this region, the radial velocity and temperature profiles are identical regardless of axial position when scaled by the proper length. A good treatment of the scaling and similarity laws that apply to vertical turbulent jets is given by Chen and Rodi (1980). They show how dimensional reasoning based on the conservation of mass, momentum, and energy can be used to arrive at more general scaling laws that apply in all regions of the jet, and how, when combined with similarity analysis, they result in the centerline velocity and temperature decay laws for jets observed experimentally. For a non-buoyant axisymmetric turbulent jet, the centerline temperature decay in the self-similar region is found to decay inversely with axial position:

$$\theta^{-1} = c_1 \frac{(x - x_o)}{D_{eff}} = c_1 X'_{eff}$$

Eq. (9-13)

where: x_o = jet virtual origin
X'_{eff} = non-dimensional scaled axial position, corrected for virtual origin
c_1 = constant

Strictly speaking, self-similarity only applies when the density difference between the jet and the surrounding fluid is small. When there are large density differences, it can be shown that exact self-similarity is not possible, so Eq. (9-13) is not expected to apply in the initial jet region for variable density jets. However, the density difference between the jet and ambient will decay with increasing values of x, so that at some point downstream $\rho/\rho_a \sim 1$ and the similarity solution will apply. The validity of this hypothesis was specifically tested and confirmed by Richards and Pitts (1993) in their study of variable density, non-homogenous free jets. However, their study,

as well as all other variable jet studies found in the literature, was conducted with jets in which the density varies linearly with temperature or composition. Figure 9.5 shows that for jets in this study, the transition from supercritical to sub-critical temperatures will be accompanied by a rapid, highly non-linear change in density with temperature. Although the conservation equations on which the scaling laws and Eq. (9-13) are based are universal and should still apply, this study will further test the limits of the applicability of similarity analysis in describing jet flow.
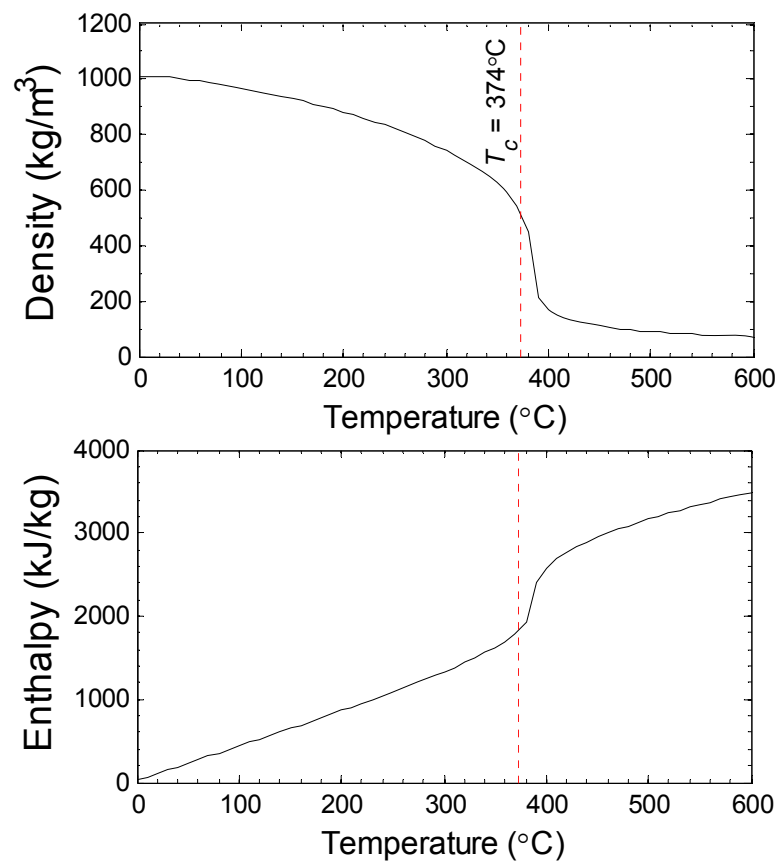
Figure 9.5 Density and enthalpy of water as a function of temperature at $P = 250$ bar (Wagner and Pruss, 2002).

For this study, Figure 9.5 shows that density differences between the hot water jets and surrounding fluid in this study should be small enough for the similarity solution to apply when the centerline jet temperature decays to $T < {\sim}300$ °C. The energy equation used to derive Eq. (9-13) also assumes a constant heat capacity so that temperature can be used directly as the independent variable. The plot of enthalpy vs. temperature in Figure 9.5 indicates that in the

region where the density differences are low enough, the similarity solution should apply; the heat capacity is nearly constant as well.

Based on a review of experimental data, Chen and Rodi (1980) recommended a value of $c_1 = 0.2$ for the constant in Eq. (9-13). They noted that even though the constant should have been obtained from the downstream similarity region only, deviations from similarity behavior are not large even in regions with considerable density variations. An average value of $c_1 = 0.204$ was found in the experimental data reviewed by Becker et al. (1967). Sforza and Mons (1978) reported a value of 0.215 from their study of hot air jets with $(\rho_o/\rho_a)^{-1} \sim 1.4$. Kataoka et al. (1982) also found that $c_1 = 0.2$ best fit their experimental measurements of the axial temperature decay of heated air jets for initial density ratios of $(\rho_o/\rho_a)^{-1}$ ranging from 2.73 to 5.26. A more recent and very extensive literature review of experimental values of c_1 included by Pitts (1991) in his study of the effect of global density ratio on centerline mixing behavior of axisymmetric turbulent jets showed an average value of $c_1 = 0.21 \pm 10\%$ for all the studies considered.

9.4. Results

During the analysis of experimental results, the nominal values of the nozzle exit temperature, T_o, and ensuing calculated and inferred parameters (such as ρ_o, G_o, etc.) are used in the figures and text. The measured experimental values of the nozzle exit temperature varied unavoidably from these nominal values, usually by less than ± 2 ^{o}C, but in some instances by up to ± 5 ^{o}C. The graphed data and scaling parameters account for these variations and represent the measured experimental data.

The measured axial temperature as a function of axial position for a subset of the water jet experimental conditions listed in Table 9.2 is shown in Figure 9.6. The experiments include both sub- and supercritical temperature jets, with nozzle exit temperatures ranging from 300 to 500 ^{o}C. The temperature and length variables have not yet been scaled. The data show that the sub- and supercritical jets appear to behave differently, with the subcritical jets possessing a much longer temperature core region, while the centerline temperature of the supercritical jets

decay quickly upon exiting the nozzle. Despite this, the temperature decay profiles appear to share a common shape, especially in the far-field region.
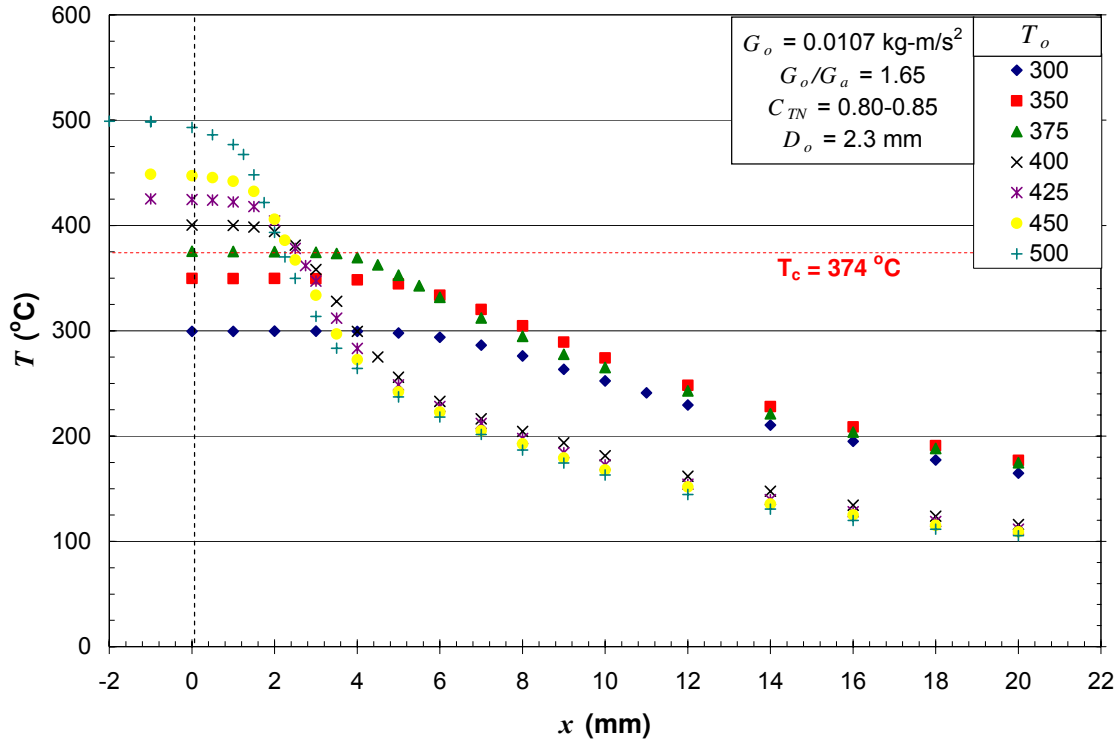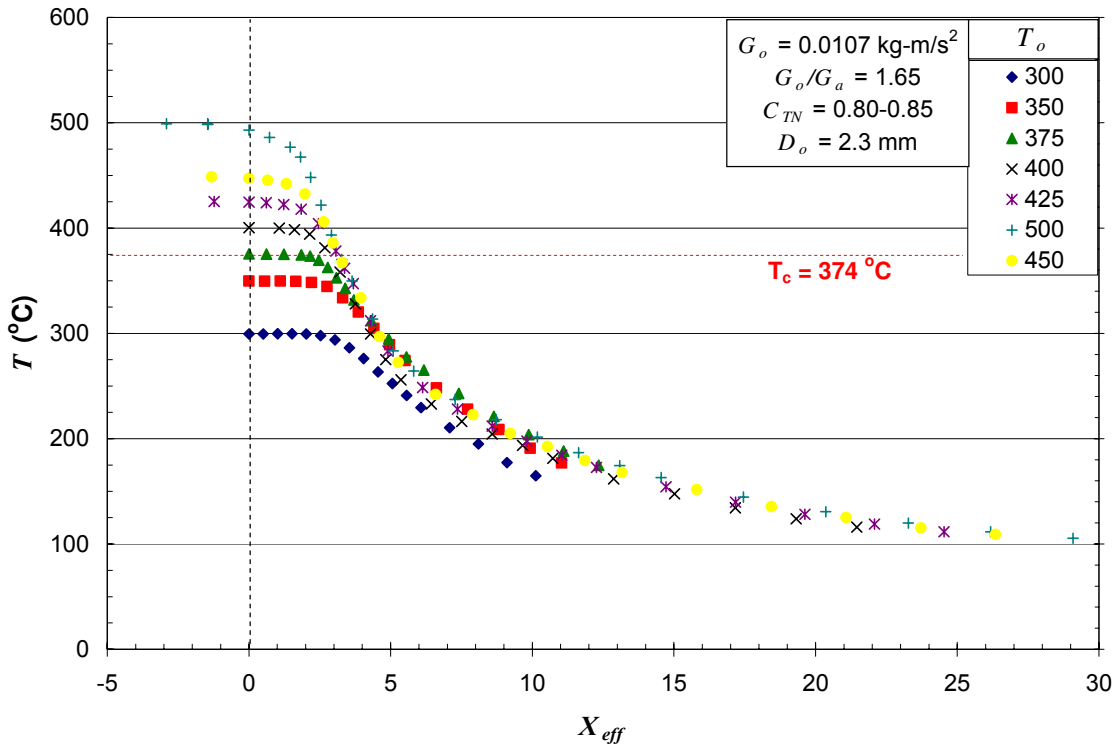

Figure 9.6 Measured centerline jet temperature as a function of axial position for water jets with nominal nozzle exit temperatures ranging from sub- to supercritical temperatures.

The same data in Figure 9.6 is also shown in Figure 9.7 with the axial position scaled and in Figure 9.8 with both the axial position and temperature scaled according to Eq. (9-11) and Eq. (9-12), respectively. From the figures, it is immediately obvious that the Thring-Newby length scaling is correct for this flow. In the far-field, where the centerline jet temperature is below the critical temperature of water and the density difference between the jet and the ambient is small, the temperature decay data collapses to a straight line as predicted by Eq. (9-13), with similar slopes for both sub- and supercritical temperature jets. In the jet-development region, immediately after the jet exit, the jet behavior varies as a function of nozzle exit temperature, with the jet core length decreasing as the nozzle exit temperature increases. The slope in this region also varies with nozzle exit temperature, which causes the separation in curves in the far-field. These two regions will be studied separately, starting with the far-field region.

Figure 9.7 Measured centerline temperature as a function of scaled axial position for water jets with nozzle exit temperatures ranging from sub- to supercritical temperatures.
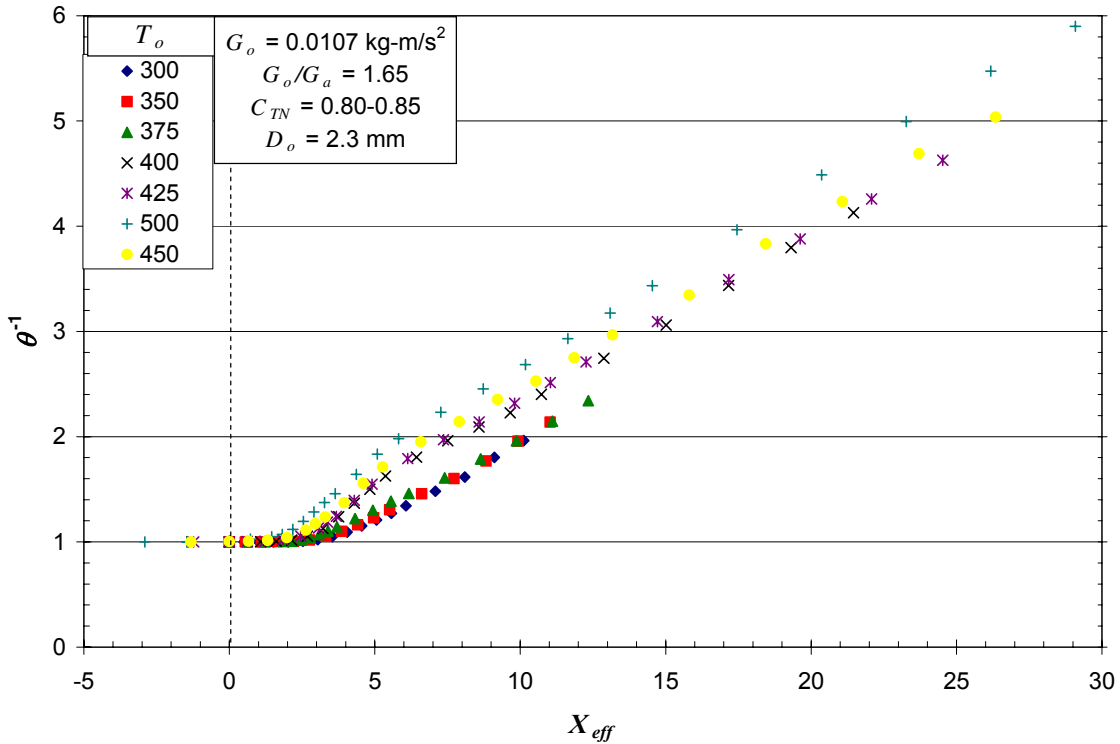

Figure 9.8 Scaled measured centerline temperature as a function of scaled axial position for water jets with nozzle exit temperatures ranging from sub- to supercritical temperatures.

9.4.1. Far-Field Jet Behavior

To begin, the validity of the assumptions made in Section 9.3.1 is verified. It was assumed that the jet behaves as a free non-buoyant turbulent jet, and that the reactor walls had no effect on the flow. If these assumptions are true, the scaled centerline temperature decay should scale inversely with axial position. If the assumptions are not valid, Figure 9.9 shows the behavior that can be expected of confined jets in which recirculation does play a role, as originally observed by Thring and Newby (1953). The centerline concentration (C_m) profile is shown for various Thring-Newby parameter values. Thring and Newby noted that it is well established that mass and energy are distributed by the same mechanism, so the observed trends will also apply for the case of temperature decay. The centerline decay of a confined jet is identical to that of a
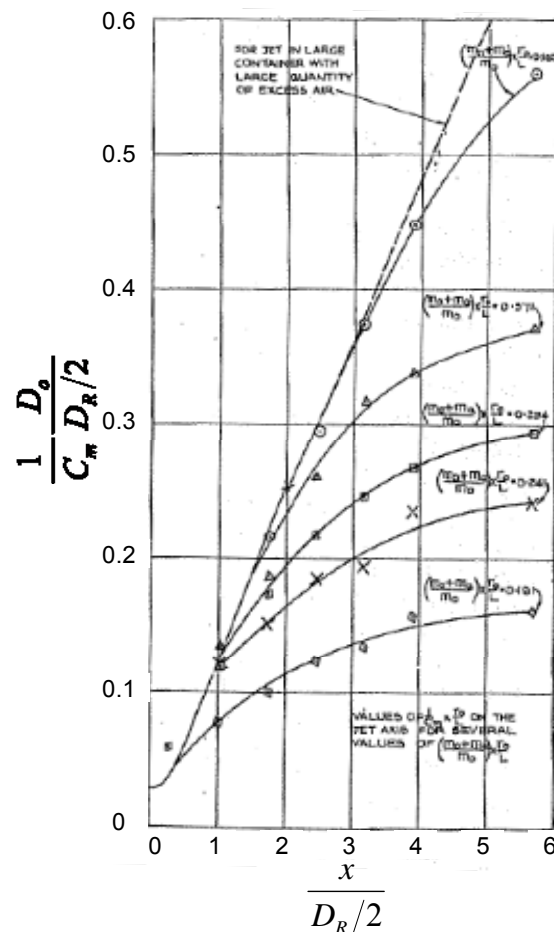
Figure 9.9 Centerline concentration decay as a function of axial position for enclosed isothermal constant density jets for different Thring-Newby parameters (adapted from Thring and Newby, 1953).

free jet until the recirculation zone is encountered. At this point, the jet begins re-entraining warm jet fluid so that the rate of centerline decay slows. As the Thring-Newby parameter decreases, the recirculation zone moves closer to the nozzle exit.

Since the Thring-Newby parameter, C_{TN}, varies from 0.27 to 0.88 for this study, Figure 9.9 suggests that recirculation could affect jet behavior in the region being studied, especially for experiments with low Thring-Newby parameters. Figure 9.10 shows the centerline temperature decay from all water jet experiments listed in Table 9.1, Table 9.2 and Table 9.3 with an exit nozzle temperature of $T_o = 500\ ^{\circ}\text{C}$.   The experiments are grouped by the value of C_{TN}, which is related to the momentum flux ratio of the center jet and co-annular flow, G_o/G_a. The figure shows that the jet behavior does vary as a function of the momentum flux ratios, and that this behavior is explained completely by the Thring-Newby parameter. For all jets, the inverse temperature scales linearly with axial position initially as predicted for non-buoyant free jets. As the jet moves downstream, flows with the lowest C_{TN} values encounter a recirculation zone first and the temperature decay deviates from linear behavior as observed by Thring and Newby. This pattern continues as the axial position increases for flows with successively higher values of C_{TN}. The jets with the highest values of C_{TN} appear unaffected by recirculation over the entire region studied. Confined jet behavior is observed for jets with low Thring-Newby parameter values at all nozzle exit temperatures studied.

Although the assumption that the reactor walls can be ignored is invalid for some flows studied, the assumption that buoyancy effects are negligible does hold. Table 9.1, Table 9.2 and Table 9.3 show that in experiments using water jets with a nozzle exit temperature of $T_o = 400\ ^{\circ}\text{C}$, the mass flow rates of both the jet and co-flowing cooling water were halved so that the momentum flux ratios of the jets remained constant, but the Froude number of the hot water jet was reduced by a factor of 4.   Despite this, Figure 9.11 shows that the temperature decay for these "half-flow" experiments is identical to the decay in the full-flow experiments. The Thring-Newby parameter remains the controlling factor.
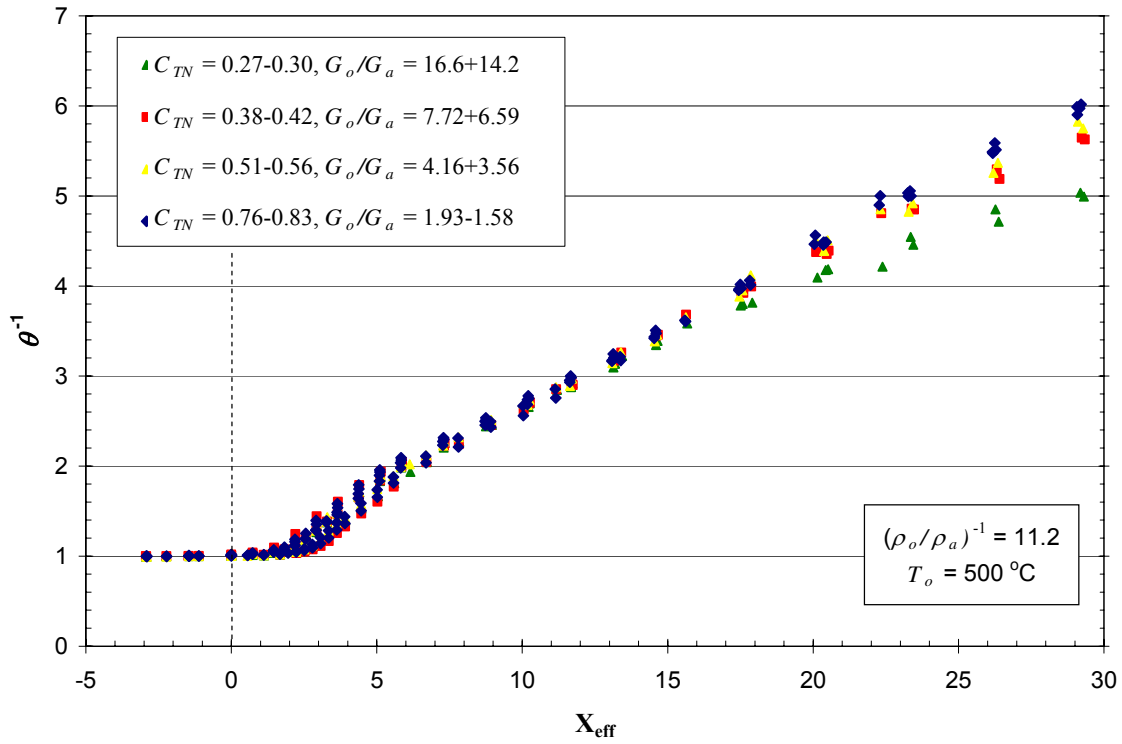
Figure 9.10 Centerline temperature as a function of axial position of jets with nozzle exit temperature of T_o = 500 °C for a range of Thring-Newby parameters.
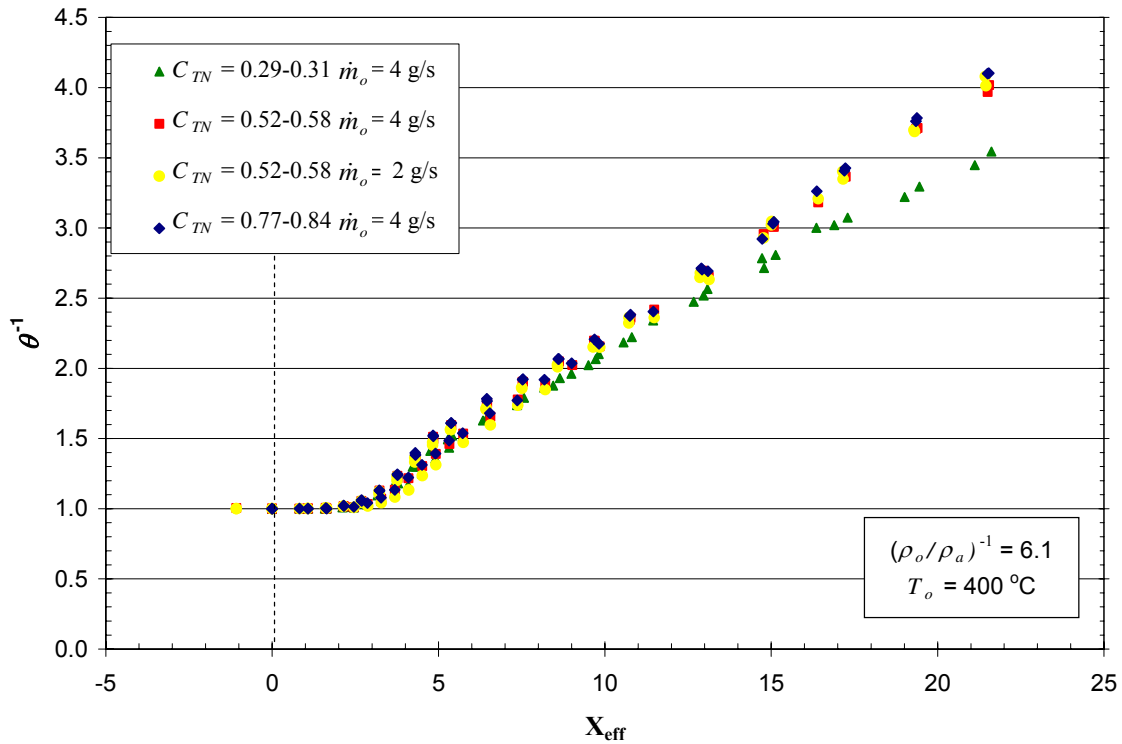

Figure 9.11 Centerline temperature as a function of axial position for jets with nozzle exit temperature of T_o = 400 °C for a range of Thring-Newby parameters.

The results in Figure 9.10 and Figure 9.11 show that the assumption of a free non-buoyant turbulent jet is only valid for hot water jet experiments with the highest C_{TN} values (the lowest momentum flux ratios). At lower values, recirculation causes temperature decay to deviate from the inverse linear dependence on the axial position typical of a free jet. The analysis shows that the Thring-Newby parameter determines jet behavior. Although there is only a slight effect for C_{TN} values over 0.5, the remainder of the analysis of free jet behavior in the far-field will only consider experiments with values of $C_{TN} > 0.75$. This limits the analysis to the jets in Table 9.1 through Table 9.3 with a momentum flux ratio of $G_o/G_a < 2$. The range of experimental conditions for the jets considered in this limited study are shown in Table 9.5.

Table 9.5 Ranges of experimental conditions covered in for analysis restricted to jets that exhibit free jet behavior over entire range studied.

momentum flux ratio	G_o/G_a	< 2	
jet temperature at nozzle exit	T_o	300-525	^{o}C
ambient (co-flowing) temperature	T_a	25	^{o}C
jet density at nozzle exit	ρ_o	83-745	kg/m^3
ambient density	ρ_a	1008	kg/m^3
initial density ratio	$(\rho_o/\rho_a)^{-1}$	1.35-12.1	
jet velocity at nozzle exit	U_o	0.55-8.2	m/s
co-flowing velocity	U_a	0.05-0.18	m/s
initial velocity ratio	U_a/U_a	0.02-0.08	
jet nozzle diameter	D_o	2.3, 3.0	mm
Reynolds number at nozzle exit	Re$_o$	13,300-76,200	
Froude number at nozzle exit	Fr$_o$	29-430	
Thring-Newby parameter	C_{TN}	0.74-0.88	
Craya-Curtet Parameter	Ct_{ni}	0.76-0.93	
momentum radius of jet	r_θ	82-315	mm
axial position	x	0-20	mm
system pressure	P	250	bar

The results also show that for a given exit nozzle temperature, the data is well correlated using the chosen scaling parameters over a range of nozzle momentum fluxes and diameters. To compare the results across different nozzle exit temperatures, the virtual origin must be subtracted from the axial position as indicated in Eq. (9-13). As Figure 9.8 demonstrates, the behavior of the jet in the development region causes the virtual origin to vary as a function of the nozzle exit temperature (or more precisely, the initial density ratio), especially for supercritical

jets. The virtual origin for each experiment was determined by calculating the slope and y-intercept of θ^{-1} vs. X_{eff} using linear regression and solving for the point where the resulting curve crosses the x-axis. The regression was limited to data in the developed region of the jet, which generally begins at a point 10-15 diameters from the nozzle exit, although the presence of turbulence in the jet core can drastically reduce this distance (Chen and Rodi, 1980). Based on visual inspection of the plotted data, the developed region was assumed to begin 9-10 effective diameters from the nozzle exit. The use of the effective diameter in place of the actual jet diameter was also justified by visual inspection of the plotted data. Kataoka et al. (1982) also used the effective nozzle diameter in their correlation of jet core lengths for non-isothermal jets. Due to the combination of a low initial density ratio and the limited region of jet studied, the subcritical temperature jets do not extend far into the far-field region. This can be seen in Figure 9.8 for experiments using a 2.3 mm diameter nozzle and in Figure 9.12 for experiments with a 3.0 mm diameter nozzle. In each figure, the subcritical temperature jets appear to be trending towards the same far-field behavior as the supercritical jets. For the case of the 2.3 mm nozzle, it is debatable whether or not the jets are fully developed. The subcritical temperature jets made with the 3.0 mm nozzle do not extend beyond $X_{eff} > 10$ and can be seen to still be developing, so it is doubtful that they will exhibit far-field behavior. For the sake of completeness, a slope and virtual origin were calculated for the subcritical jets using the four data points farthest from the nozzle exit, regardless of the value of X_{eff}.

The results of the correlation of centerline temperature decay with axial position using Eq. (9-13) for the data presented in Figure 9.8 and Figure 9.12 is shown in Figure 9.13 and Figure 9.14, respectively. The centerline decays are well correlated with the scaled axial position for both sub- and supercritical jets for the case of the 2.3 mm nozzle. As expected, the same is not true for the 3.0 mm nozzle. However, the supercritical temperature jets remain well correlated.
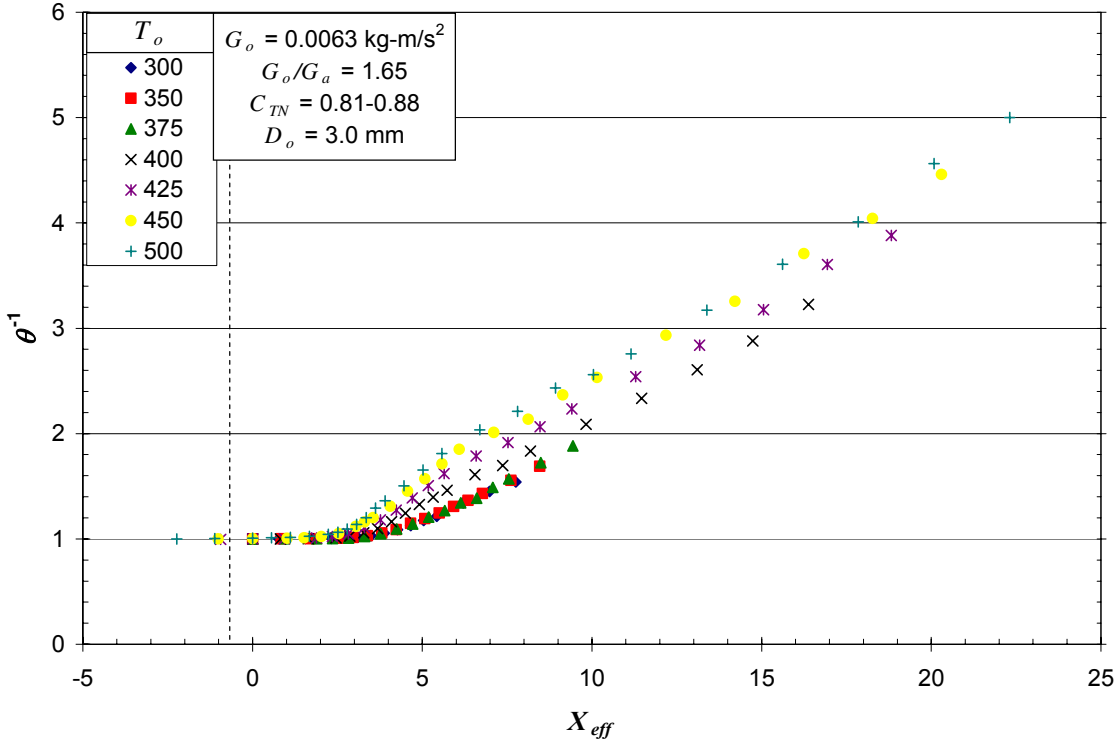
Figure 9.12 Centerline temperature as a function of axial position for water jets with nozzle diameter of $D_o =$ 3.0 mm.
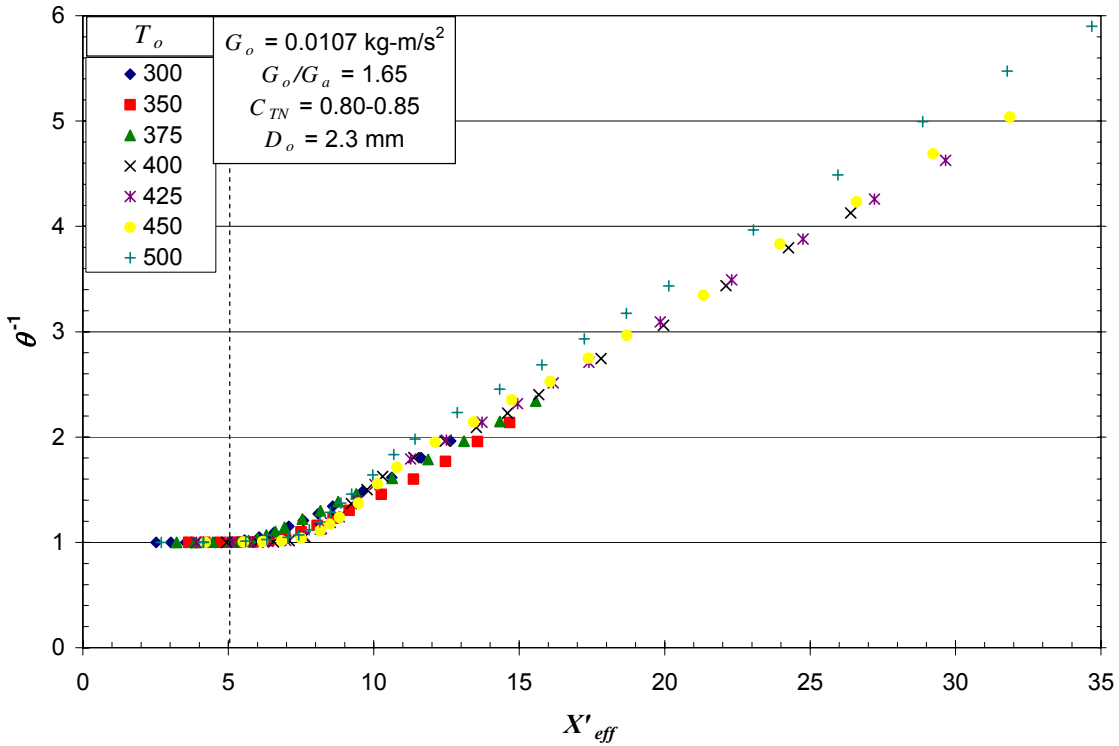

Figure 9.13 Centerline temperature decay of hot water jets with a range of nozzle exit temperatures, accounting for virtual origin ($D_o =$ 2.3 mm).
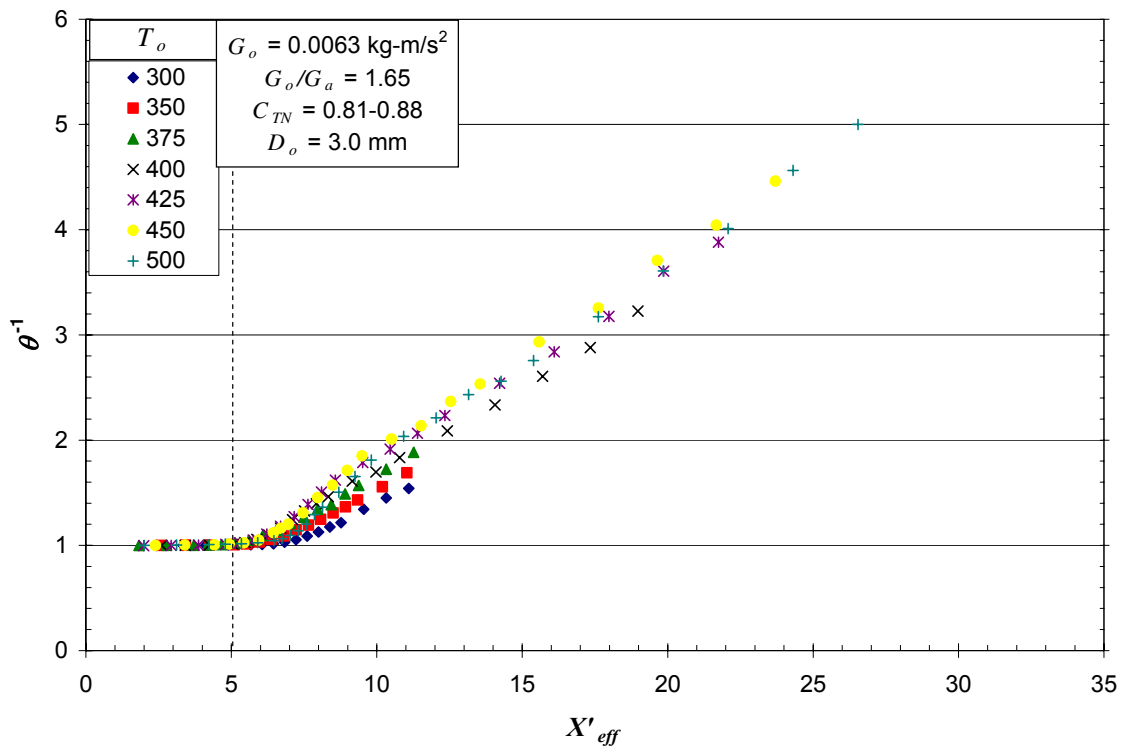
Figure 9.14 Centerline temperature decay of hot water jets with a range of nozzle exit temperatures, accounting for virtual origin s (D_o = 3.0 mm).

In both Figure 9.13 and Figure 9.14, a slight dependence of slope on nozzle exit temperature can be seen. Though slight, this behavior was noted in all experiments, regardless of nozzle diameter or jet momentum flux, as can be seen in Figure 9.15. The trend is more apparent in Figure 9.16, which shows the value of the parameter c_1 in Eq. (9-13) calculated using linear regression for all experiments. The values of the calculated slopes are lower than the literature accepted value of $c_1 = 0.2$. Both Pitts (1991) and Schefer and Dibble (1986) noted a similar dependence of the constant on density. Pitts, with Richards, later performed a more careful experiment which found the constant to be independent of the initial density ratio, and attributed his earlier results to probably buoyancy and co-flow effects (Richards and Pitts, 1993). Given the limitations of the experimental set-up in this study, these contaminating effects can not be ruled out. Figure 9.15 still demonstrates that the use of the Thring-Newby scaling law and similarity analysis in the far-field do an excellent job of correlating jet behavior over a wide range of initial density ratios, nozzle diameters, and Reynolds numbers. Further, the results show that these laws still apply even with the rapid, highly non-linear transition of the jet from the supercritical to subcritical region.
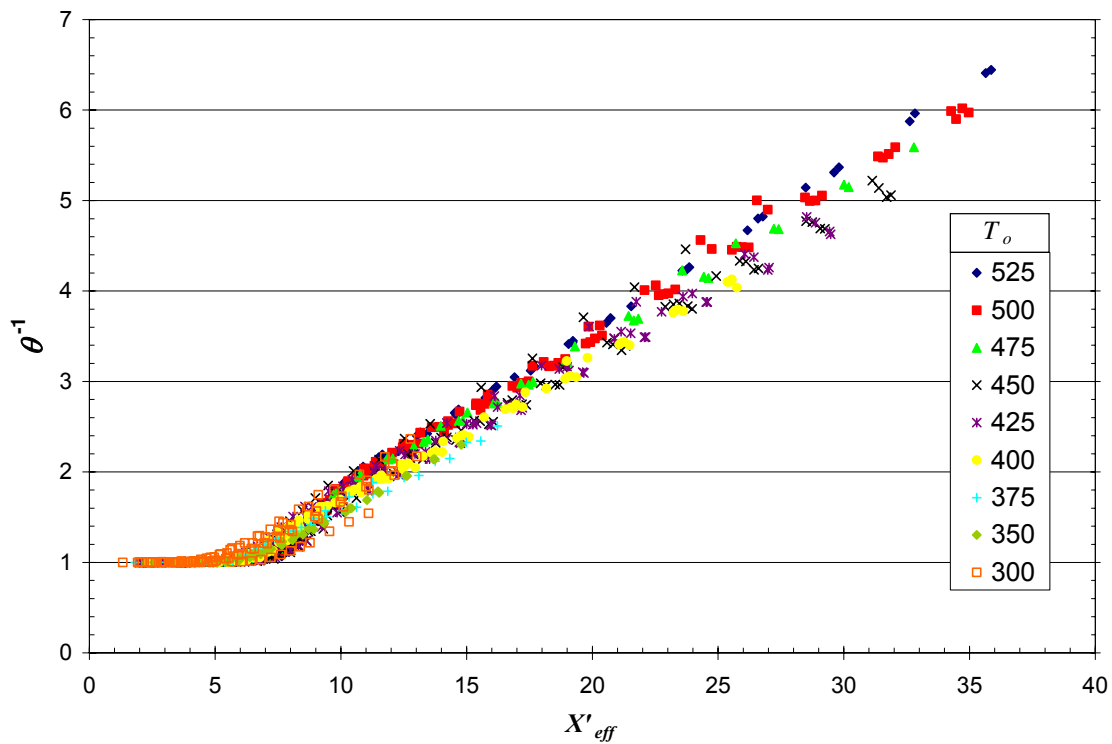
Figure 9.15 Correlation of centerline temperature as a function of axial position for all experiments with $G_o/G_a < 2.$
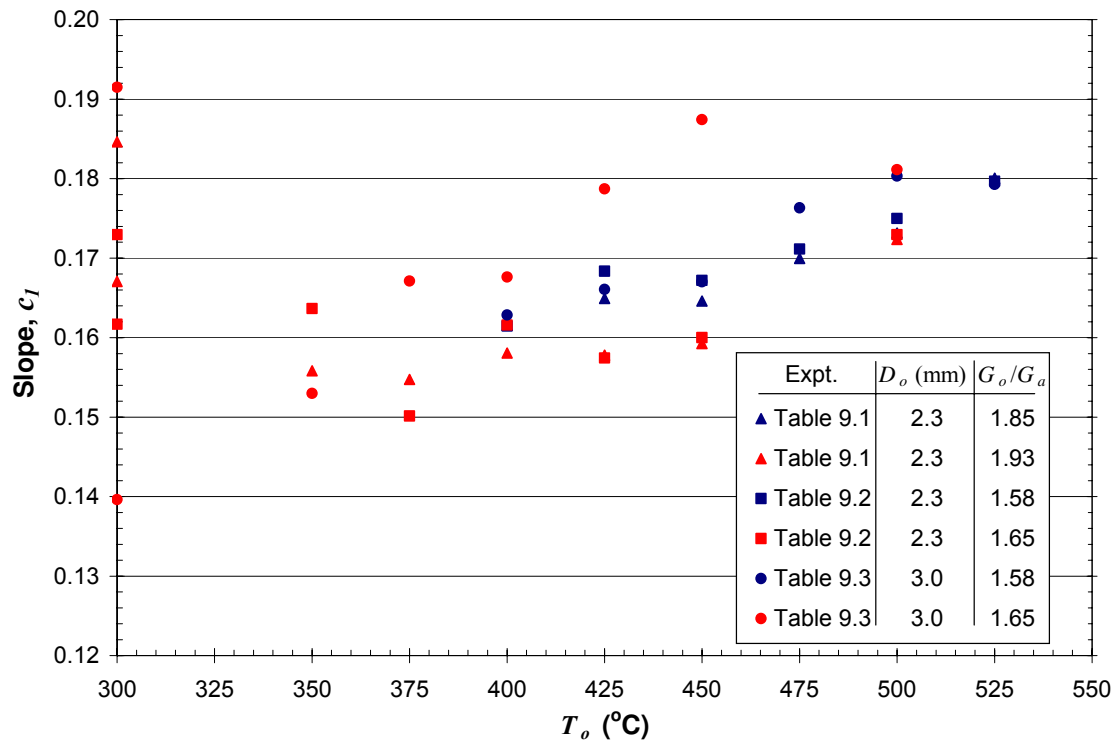

Figure 9.16 Calculated values of slope, c_1, from correlation in Eq. (9-13) of temperature decay with axial position for all hot water jet experiments with $G_o/G_a < 2.$

9.4.2. Jet Development Region

Although the similarity analysis described above is useful for describing and understanding the jet temperature behavior in the far-field region, the results are only applicable in regions where the temperature has dropped well below the critical temperature of water. Previous experiments from our laboratory indicate that thermal spallation requires rock surface temperatures on the order of ~500 ^{o}C. Therefore, any attempts to achieve thermal spallation using a reactor configuration similar to the one used in this study will require relatively short stand-off distances between the nozzle exit and rock surface that are within the jet development region, where the jet temperature is above the supercritical temperature of water.

In the jet development region, Figure 9.6 shows that the jet is rapidly quenched by the high density, low enthalpy ambient fluid. For jets with nozzle exit temperatures above the critical temperature of water, the temperature decay is more rapid on the absolute axial length scale, with the jets being quenched below the critical temperature of water within a little over one diameter of the nozzle exit. When the axial position was scaled using the Thring-Newby scaling law, as in Figure 9.7, it was observed that the supercritical temperature jets appeared to decay at a rate such that the centerline temperature of each jet intersected the critical temperature at nearly the same value of effective axial position (X_{eff}). This behavior was observed for all experiments. Figure 9.17 shows the jet temperature as a function of scaled axial position for all supercritical jets grouped by nozzle configuration and flow conditions as stated in Table 9.1, Table 9.2 and Table 9.3. This includes temperature decay data from experiments with low cooling water flow rates that were previously excluded due to recirculation effects. In the development region, the jet has not expanded to the point where it interacts with the wall. The figure shows that the nozzle configuration does have a noticeable effect on the effective axial position at which the flow becomes subcritical. This could be due to differences in the initial zeroing of the movable probe. For the experiments in Table 9.1, the true position of the nozzle exit is known to be inaccurate, since the nozzle exit could not be seen with a direct line of sight during zeroing. This problem was rectified with a longer nozzle design for the experiments in Table 9.2 and Table 9.3. The effective axial position at which the jet temperature equals the critical

temperature varies from 2.4 to 3.9. However, the spread for a given nozzle configuration is much smaller.

A physical explanation for the behavior observed for the supercritical jets can by found by examining the thermodynamic properties of the fluid around the critical temperature. The transition from supercritical to subcritical temperatures involves a large change in the specific enthalpy of the jet over a small change in temperature.   Although supercritical fluids by definition do not undergo phase changes, the rapid change in enthalpy over such a small temperature range, along with the accompanying large change in density, has the characteristics of a phase change from vapor to liquid. Figure 9.5 shows that at the system pressure of $P = 250$ bar, this large decrease in enthalpy is centered about 385 ^{o}C and extends about 5-10 ^{o}C to each side so that when the jet reaches the critical temperature ($T_c = 374$ ^{o}C) the rapid changes in thermodynamic properties have ceased and the fluid behavior increasingly assumes that of a supercooled fluid. Therefore, the behavior of the supercritical temperature jets in the development region can be likened to the behavior of a steam jet submerged in liquid water.
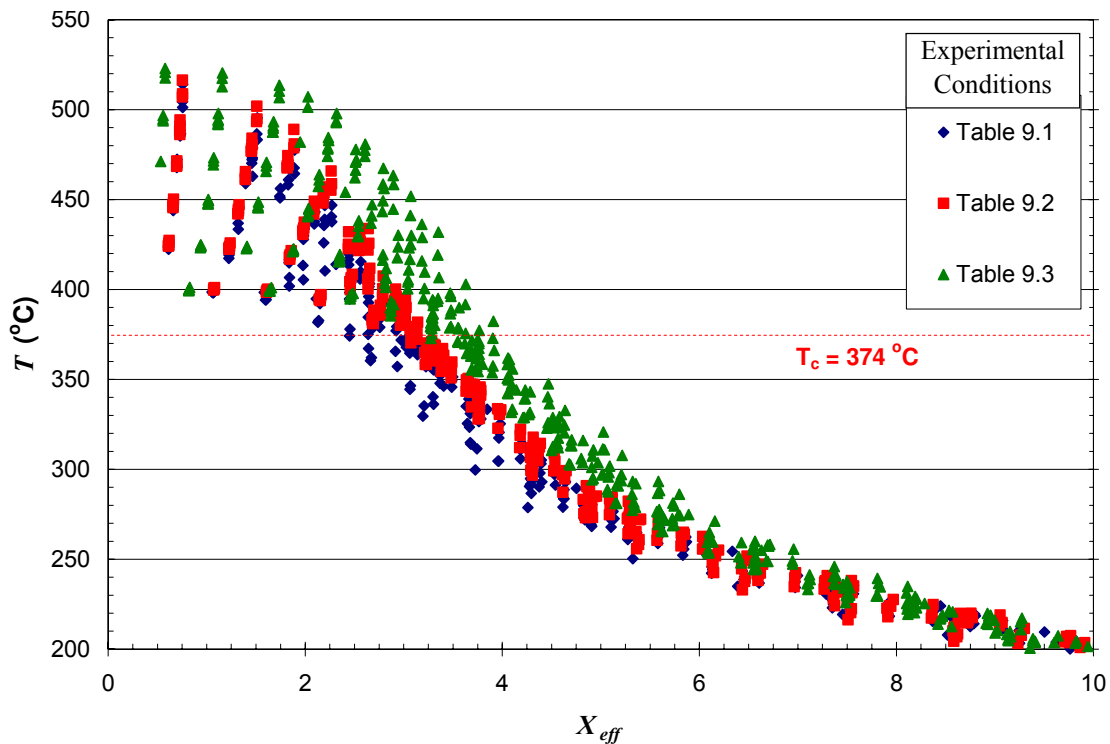

Figure 9.17 Centerline jet temperatuer as a function of effective axial position for all supercritical temperature jets in study.

As the jet entrains the surrounding fluid, it is cooled to the point where it begins to condense. The jet will persist into the liquid until it has entrained enough fluid to be completely condensed. Based on these arguments, the point at which the centerline temperature of the supercritical temperature jet reaches $T = 374 \,^{\circ}\text{C}$ is analogous to the point to which a submerged vapor jet penetrates a supercooled liquid of the same material. The penetration distance of vapor jet into a liquid depends on the specific enthalpy of the jet at the nozzle exit, the specific enthalpy of the ambient fluid and the rate at which the jet entrains the ambient fluid. The specific enthalpy of the ambient fluid is constant for all experiments in this study. The specific enthalpy of the jet increases with increasing nozzle exit temperatures. However, the rate of entrainment also changes with nozzle temperature due to density variations.

A simple model for determining the penetration distance of submerged vapor jets in subcooled liquids (Weimer et al., 1973; Kerney et al., 1972) was applied to the case of a supercritical temperature water jet injected into subcritical water. Top hat profiles were assumed for the mean axial velocity, density, and specific enthalpy:

$$u(x,r) = \begin{cases} u(x) & 0 \leq r \geq a(x) \\ 0 & a(x) < r \end{cases} \qquad u(0) = U_o$$

$$\rho(x,r) = \begin{cases} \rho(x) & 0 \leq r \geq \lambda a(x) \\ \rho_a & \lambda a(x) < r \end{cases} \qquad \rho(0) = \rho_o \qquad \text{Eq. (9-14)}$$

$$h(x,r) = \begin{cases} h(x) & 0 \leq r \geq \lambda' a(x) \\ h_a & \lambda' a(x) < r \end{cases} \qquad h(0) = h_o$$

where:
u = axial velocity
h = specific enthalpy
a = local radial length scale, $a(0) = D_o$
λ, λ' = constant scaling factors for density and enthalpy radial profiles

Since the flow in the jet development region is not well developed, the use of top hat profiles should approximate the actual radial profiles well. The expression used for the rate of entrainment of mass by the jet was:

$$\frac{dm}{dx} = E_o a u \rho_a \left(\frac{\rho}{\rho_a} \right)^{1/2} \qquad \text{Eq. (9-15)}$$

where:
E_o = jet entrainment coefficient

The form of Eq. (9-15) was suggested by Morton (1965) and makes use of the experimental measurements of the entrainment rates for round jets by Ricou and Spalding (1961). Ricou and Spalding found a constant value of 0.08 for the entrainment coefficient E_o over a over a wide range of initial density ratios. When these expressions are inserted into the equations of conservation of mass, momentum and energy and integrated over the jet cross-section, the specific enthalpy is found to be given by:

$$\frac{h_o - h_a}{h - h_a} = 1 + 4E_o \left(\frac{\rho_o}{\rho_a} \right)^{-\frac{1}{2}} \frac{x}{D_o} \qquad \text{Eq.(9-16)}$$

The Thring-Newby scaling can again be used, this time to give the scaled penetration distance of the jet, denoted $X_{eff,c}$. The penetration distance for the jet has been defined as the point at which the centerline jet temperature equals the critical temperature of water, so that:

$$\frac{h_o - h_a}{h_c - h_a} = 1 + 4E_o X_{eff,c} \qquad \text{Eq. (9-17)}$$

where: $\qquad\qquad\qquad h_c$ = specific enthalpy at $T = T_c = 374\ ^\circ\text{C}$

If Eq.(9-16) is divided by Eq. (9-17):

$$\frac{h_c - h_a}{h - h_a} = \frac{1 + 4E_o X_{eff}}{1 + 4E_o X_{eff,c}} \qquad \text{Eq. (9-18)}$$

The term on the left-hand side is similar to the temperature scaling in Eq. (9-12) used in the similarity analysis of the far-field region, with specific enthalpies used in place of temperatures and the specific enthalpy at the end of the jet penetration region, h_c, used as the reference enthalpy instead of the specific enthalpy at the nozzle exit. This term can be plotted against the effective axial position to determine the value of $X_{eff,c}$ graphically. When the left-hand term in Eq. (9-18) equals 1, $X_{eff} = X_{eff,c}$. For the supercritical temperature jets in Figure 9.18, Eq. (9-17) has values ranging from 1.41 for a 400 $^\circ$C jet to 1.82 for a 525°C jet. According to Eq. (9-17), this means that the jet with a nozzle exit temperature of 525 $^\circ$C should have twice the effective penetration depth as the 400 $^\circ$C depth. Although the trend of increasing effective penetration depth with increasing nozzle temperature is qualitatively correct, the relative values do not correspond to the model predictions.

Experimental values for $X_{eff,c}$ were calculated by linear interpolation between data points are a plotted against the value of Eq. (9-17) in Figure 9.19 for the experimental conditions described in Table 9.2 and Table 9.3. The figure clearly shows that as the specific enthalpy at the nozzle exit increases, the effective penetration depth of the jet increases as predicted by the model. The figure shows that for a series of experiments with a given nozzle configuration and cooling water flow rate, a clear correlation exists. However, the range of penetration depths is much smaller than predicted by the model. Also, the penetration depth model fails to capture the effects of factors such as momentum flux ratio and nozzle configuration that appear to be affecting jet behavior in the jet development region.

Values of the jet entrainment coefficient based on the penetration depth model results were calculated using the values of the penetration depth obtained from the experiments and are shown in Figure 9.20. Ricou and Spalding (1961) reported a value of 0.08 for E_o irrespective of the density ratio of the jet. The value of E_o from the penetration model results range from 0.03 to 0.07. The model the results show a strong dependence on both initial density ratio at the jet nozzle exit and the nozzle configuration for the experiment. Although these results are in good agreement with the literature value, especially for high nozzle inlet temperatures, it is unclear that these results signify that the model accuracy increases with increasing jet temperatures, or that another factor that scales with the initial density ratio is controlling the jet behavior in this region.
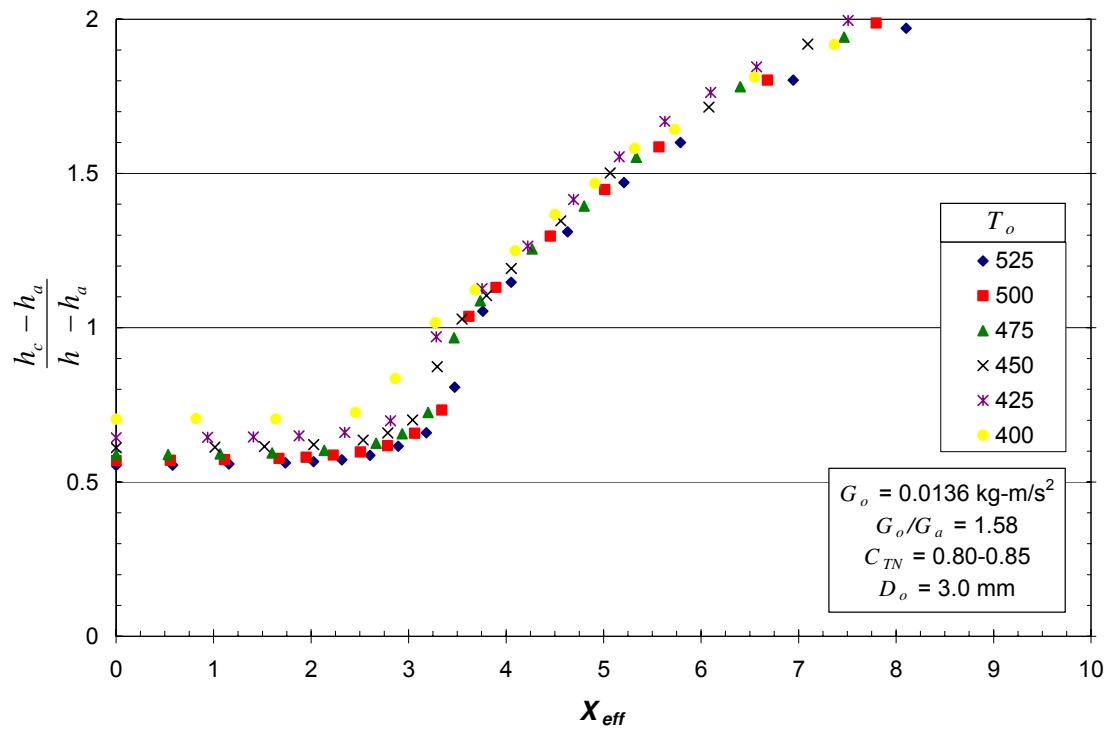
Figure 9.18 Centerline specific enthalpy of jet scaled by reference enthalpy at critical temperature of water as a function of effective axial position. Unity value on y-axis indicates penetration depth of jet.
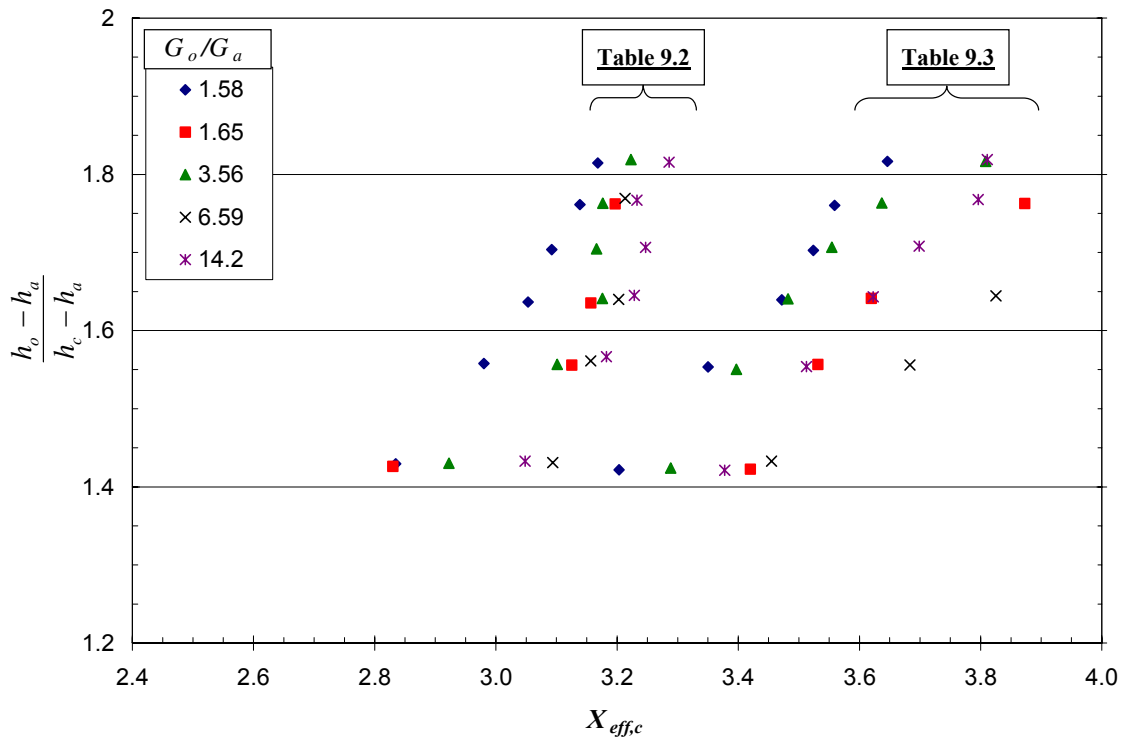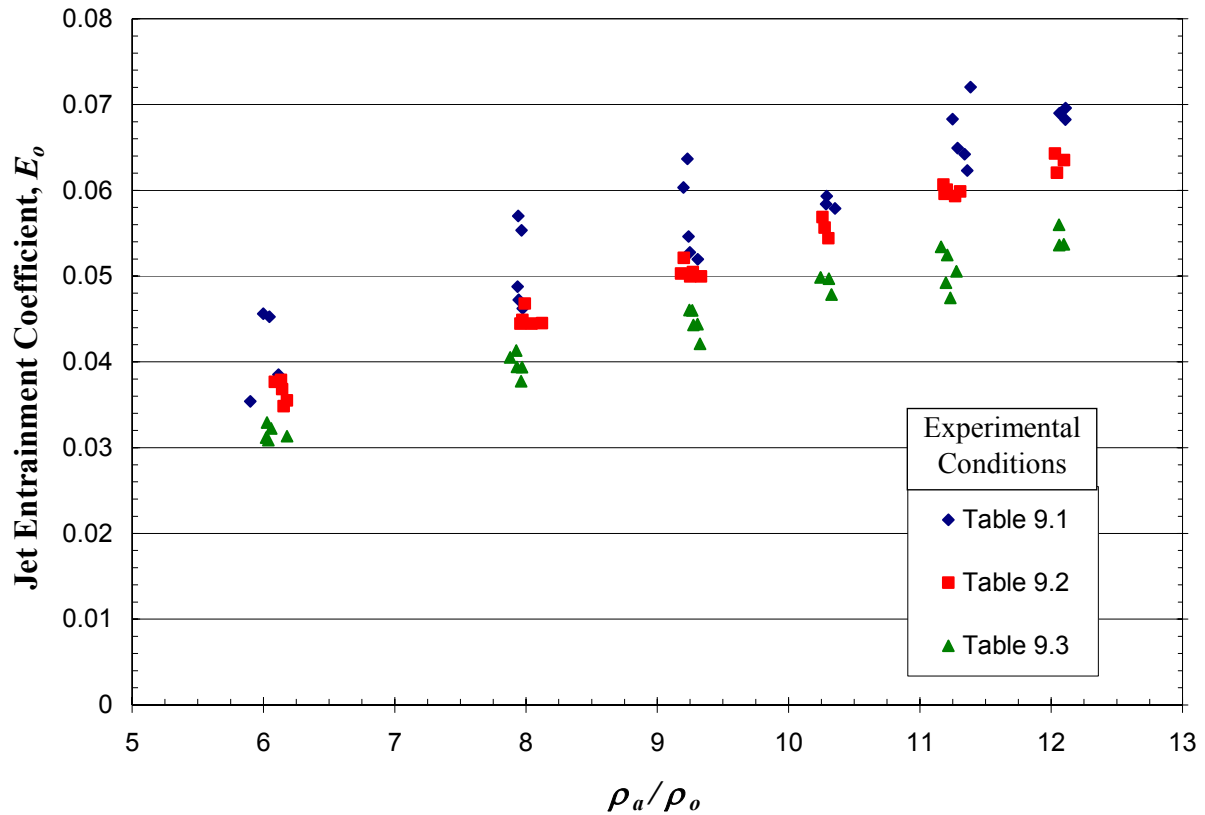

Figure 9.19 Effect of nozzle exit temperature on penetration depth model results for supercritical temperature jets.

Figure 9.20 Jet entrainment coefficient in jet development region as a function of initial density gradient for all superecritical jets in study.

The application of the penetration depth model for vapor jets submerged in supercooled liquids to supercritical jets in subcritical water was only a partial success. The model was able to qualitatively predict that increasing the jet nozzle temperature would increase the effective penetration depth of the jet, but the model overpredicted the relative effect on penetration distance. For an individual experimental series, the model again qualitatively predicted behavior in the jet development region, but other factors such as cooling water co-flow rates and nozzle configuration were seen to have a larger impact on results. Jet entrainment coefficients were calculated from the model and were in agreement with literature values, especially at elevated nozzle exit temperatures. The entrainment coefficients were seen to depend strongly on the initial density ratio. This may be indicative of some other controlling behavior not captured by the model. It should be noted again that the jet development region in which the temperatures are supercritical exists entirely in a region only one to two diameters from the nozzle exit. The experimental data was gathered from a 4 mm region using a 0.5 mm diameter thermocouple. A

more careful study on a larger experimental set-up that allows better sampling of the supercritical development region should be performed to verify the findings from this study. In terms of using low-density supercritical jets in a high-density subcritical environment, the results from the jet development region do make it clear that the jet is quenched rapidly and that short stand-off distances will be required to achieve high temperatures at the rock surface.

9.5. Conclusions

The behavior of high temperature, low-density hot water jets in a high-density liquid environment was studied. An experimental system capable of accurately measuring the centerline jet temperature as a function of axial position was used to determine the behavior of sub- and supercritical jets in a subcritical co-flow. A wide range of jet temperatures, flows, and nozzle configurations were studied. The jet was divided into two regions: the far-field region and the jet development region. In the far-field, the flow in the jet was characterized as a free turbulent jet, with negligible effects from buoyancy or the co-flowing cooling water. Conditions under which recirculation zones affected jet behavior were identified and removed from experimental consideration. A similarity analysis was applied to the flow. In the far-field, where the density gradient between the jet and ambient fluid was small, the jet behavior was self-similar, so that the axial temperature decay follows conventional jet scaling laws. The Thring-Newby scaling law accurately accounted for the large initial density ratio between the nozzle exit and ambient fluid. However, the slope of the axial decay of the jets varied slightly as a function of the initial density ratio. The variation is most likely attributable to experimental conditions rather than being a characteristic of the axial temperature decay of supercritical jets.

In the jet development region, supercritical jets were observed to be quickly quenched to below the critical temperature of water within one or two diameters of the nozzle exist by the ambient fluid. When the Thring-Newby scaling law was applied to the axial length scale, the effective axial distance at which the centerline temperature transitioned from supercritical to subcritical values was roughly the same for all supercritical jet temperatures studied. A model of steam jets injected into a supercooled liquid was used to describe the relationship between the nozzle exit temperature and the depth to which the supercritical temperature penetrated. Although the model

predictions were qualitatively correct, the degree to which nozzle exit temperature affected the observed penetration distance of the supercritical jet was much less than that predicted by the model. Jet entrainment coefficients were calculated based on the model results. Values of $0.3 < E_o < 0.7$ were observed. The entrainment coefficient varied strongly with the initial density ratio. The entrainment coefficient results indicate that another factor unaccounted for by the proposed model is likely controlling observed jet behavior in the jet development region. The variations in the slope of the temperature decay laws with initial density ratios in the far-field region supports this observation.

Overall, the WCHB system was not found to be ideal for studying the behavior of supercritical jets. In the far-field region, the experiments would benefit from the use of a smaller nozzle diameter to increase the Froude number, decrease wall effects, and extend the effective axial distance over which the free jet is studied. The opposite is true for experiments in the jet-development region. There, a larger nozzle diameter is needed so that the region where jet temperatures are supercritical can be better explored.

9.6. References

Becker, H. A., H. C. Hottel and G. C. Williams (1962). "Mixing and Flow in Ducted Turbulent Jets." Ninth Symposium (International) on Combustion, August 27-September 1, 1962, Academic Press, 7-20.

Becker, H. A., H. C. Hottel and G. C. Williams (1967). "The nozzle-fluid concentration field of the round, turbulent, free jet." Journal of Fluid Mechanics **30**(2): 285-303.

Chen, C. J. and W. Rodi (1980). Vertical turbulent buoyant jets : a review of experimental data. Oxford ; New York, Pergamon Press.

Curtet, R. (1958). "Confined Jets and Recirculation Phenomena with Cold Air." Combustion and Flame **2**(4): 383-411.

Kataoka, K., H. Shundoh and H. Matsuo (1982). "A Generalized-Model of the Development of Non-Isothermal, Axisymmetric Free Jets." Journal of Chemical Engineering of Japan **15**(1): 17-22.

Kerney, P. J., G. M. Faeth and D. R. Olson (1972). "Penetration Characteristics of a Submerged Steam Jet." AIChE Journal **18**(3): 548-553.

Morton, B. R. (1965). "Modeling Fire Plumes." Tenth Symposium (International) on Combustion, Pittsburgh, Pa., The Combustion Institute, 973-982.

Pitts, W. M. (1991). "Effects of Global Density Ratio on the Centerline Mixing Behavior of Axisymmetrical Turbulent Jets." Experiments in Fluids **11**(2-3): 125-134.

Rauenzahn, R. M. and J. W. Tester (1989). "Rock Failure Mechanisms of Flame-Jet Thermal Spallation Drilling - Theory and Experimental Testing." International Journal of Rock Mechanics and Mining Sciences & Geomechanics Abstracts **26**(5): 381-399.

Richards, C. D. and W. M. Pitts (1993). "Global Density Effects on the Self-Preservation Behavior of Turbulent Free Jets." Journal of Fluid Mechanics **254**: 417-435.

Ricou, F. P. and D. B. Spalding (1961). "Measurement of Entrainment by Axisymmetrical Turbulent Jets." Journal of Fluid Mechanics **11**(1): 21-32.

Schefer, R. W. and R. W. Dibble (1986). "Rayleigh Scattering Measurements of Mixture Fraction in a Turbulent Nonreacting Propane Jet." AIAA 24th Aerospace Science Meeting, Reno, NV, January 6-9, AIAA-1986-278.

Sforza, P. M. and R. F. Mons (1978). "Mass, Momentum, and Energy-Transport in Turbulent Free Jets." International Journal of Heat and Mass Transfer **21**(4): 371-384.

Steward, F. R. and A. G. Guruz (1977). "Aerodynamics of a Confined Jet with Variable Density." Combustion Science and Technology **16**(1-2): 29-45.

Thring, M. W. and M. P. Newby (1953). "Combustion Length of Enclosed Turbulent Jet Flames." Fourth Symposium (International) on Combustion, Baltimore, Williams & Wilkins, 789-796.

Wagner, W. and A. Pruss (2002). "The IAPWS Formulation 1995 for the Thermodynamic Properties of Ordinary Water Substance for General and Scientific Use." Journal of Physical and Chemical Reference Data **31**(2): 387-535.

Weimer, J. C., G. M. Faeth and D. R. Olson (1973). "Penetration of Vapor Jets Submerged in Subcooled Liquids." Aiche Journal **19**(3): 552-558.

Wilkinson, M. A. and J. W. Tester (1993). "Experimental-Measurement of Surface Temperatures during Flame-Jet Induced Thermal Spallation." Rock Mechanics and Rock Engineering **26**(1): 29-62.

Chapter 10: Heat Flux from Impinging Jets to Flat Surface

In Chapter 9, the temperatures of supercritical water jets injected into subcritical water were measured as a function of stand-off distance to determine the behavior of high temperature, low-density jets in high density environment similar to that expected in a deep borehole. The study found that although the jets were rapidly quenched by the surrounding fluid, the high jet temperatures necessary to induce thermal spallation could be achieved at small (one to two nozzle diameters) stand-off distances for the nozzle exit. However, high temperatures alone are not sufficient to ensure thermal spallation. High rates of thermal heat transfer from the jets to the rock surface are also needed. In conventional open-air thermal spallation experiments, heat fluxes ranging from 3-10 MW/m^2 were required to induce thermal spallation in rocks (Rauenzahn and Tester, 1989; Wilkinson and Tester, 1993). The use of flame jets in a deep borehole environment was experimentally investigated using a hydrogen-oxygen flame jet in water at a pressure of 100 bar in a lab-scale apparatus that replicates conditions that would be found in a fluid filled borehole at a depth of about 1 km. The heat flux from the jet flame to a brass block was determined by measuring the steady state temperature profile within the brass block. Estimated maximum heat fluxes on the order of 0.5 MW/m^2 were observed, which should be high enough to induce thermal rock spallation (Augustine et al., 2007). This study extends the investigation of heat transfer from impinging jets under deep borehole-like conditions to beyond the critical pressure of water using the WCHB system in our laboratory at MIT.

10.1. Objectives

The objectives of this study was to design a device that could measure the heat flux from an impinging jet in the deep borehole environment ($P = 250$ bar, high temperatures) and to use this device to measure the heat flux from supercritical water jets impinging against a flat surface. The measurements will determine whether sufficient heat fluxes can be generated under deep borehole conditions to induce thermal spallation and how the heat flux from the impinging jet varies as a function of stand-off distance.

10.2. Heat Flux Meter Design

A novel design for a heat flux meter (HFM) capable of functioning in the deep borehole environment simulated in the reaction system was developed. An in-depth search for an off-the-shelf heat flux meter did not yield any satisfactory results. The HFM was designed and constructed in collaboration with Potter Drilling LLC. Although hot water jets used in subsequent experiments with the HFM had a maximum temperature of only 525 $^{\circ}$C, the heat flux meter was designed for eventual use with hydrothermal flame jets at either Potter Drilling LLC or within our research group.

Theory

A rough schematic of the initial proposed geometry for the HFM is shown in Figure 10.1. The heat flux meter functions by conducting the incident heat flux on the surface of the HFM (the "sensor") through the central metal rod of the unit. A steady state energy balance gives the governing equation for heat transfer within the central rod:

$$0 = \frac{1}{r}\frac{\partial}{\partial r}\left(r\frac{\partial T}{\partial r}\right) + \frac{\partial^2 T}{\partial z^2}$$

Eq. (10-1)

with the boundary condition at the surface (sensor) defined as:

$$-k\frac{\partial T}{\partial z} = q(r) \quad @ \ z = 0$$

Eq. (10-2)

The heat flux from the jet to the flat surface, $q(r)$, is assumed to vary as a function of radial distance from the point of impingement. The surrounding insulation has a much lower thermal conductivity, so it is treated as a perfect insulator. Because of the high length-to-width aspect ratio of the central rod and the assumption of zero heat flux through the radial walls, any radial temperature profiles at the sensor surface should relax quickly so that the heat flux along the rod at a distance from the sensor surface can be assumed constant and the temperature profile one dimensional. In this region, Eq. (10-1) can be simplified and combined with the boundary condition in Eq. (10-2) to give:

$$q = \frac{\int_0^R q(r)\,dr}{\pi R^2} = -k_c \frac{dT}{dz} = -k_c \frac{T_1 - T_2}{x_1 - x_2} \qquad \text{Eq. (10-3)}$$

where:

q = area-averaged heat flux (W/m^2)
k_c = thermal conductivity (W/m-K)
R = radius of sensor surface (mm)
T_1, T_2 = temperature in metal rod at points 1 and 2 (K or $^{\circ}$C)
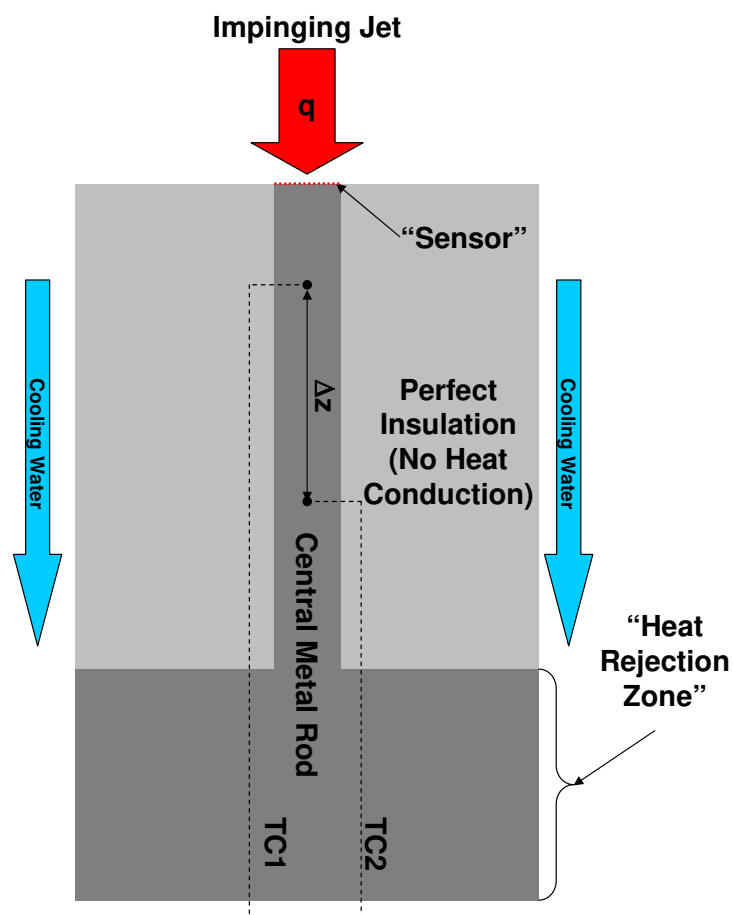x_1, x_2 = axial position of points 1 and 2 in metal rod (mm)

Figure 10.1 Conceptual schematic of novel heat flux meter design.

According to Eq. (10-3), the steady-state area-averaged convective heat flux from the impinging jet to the HFM sensor surface can be determined by measuring the difference in temperature between two points (T_1 and T_2) over a known distance within the central metal rod of the HFM. The heat flux between the impinging jet and HFM surface can also be calculated using a heat transfer coefficient, defined as:

$$q = h\left(T_{stag} - T_{surf}\right)$$ Eq. (10-4)

where:

h = heat transfer coefficient (W/m^2-K)
T_{stag} = impinging jet stagnation temperature (K or ^{o}C)
T_{surf} = solid surface temperature (K or ^{o}C)

If the heat flux, q, in Eq. (10-4) is assumed to be the area-averaged heat flux over the HFM sensor, then Eq. (10-4) can be equated with Eq. (10-3) to give:

$$q = h\left(T_{stag} - T_{surf}\right) = -k_c \frac{T_1 - T_2}{x_1 - x_2}$$ Eq. (10-5)

Temperature measurements from the HFM can be used to measure the average incident heat flux from the impinging jet over the sensor surface area. If the impinging jet stagnation temperature and sensor surface temperature of the HFM are also known, a heat transfer coefficient can be estimated.

Design and Material Selection

The design of the heat flux meter was a materials selection challenge. The design of the HFM went through several iterations of proposed design, materials selection, modeling, and evaluation. A design that called for an air-gap insulation made by welding two metal tubes together was quickly dismissed. Although the air-gap provided superior insulation, 2-D heat conduction models of the HFM design showed a large radial heat flux through the weld itself near the sensor, which resulted in a large portion of the heat flux incident on the sensor escaping through the weld. It was also believed that making a weld that could withstand the high temperature gradients, temperature cycling, and thermal stresses would be difficult. Instead, a simpler design in which the central metal rod would be surrounded by a high-temperature, low thermal conductivity ceramic was chosen.

Since the meter was designed to ultimately measure heat fluxes from flame jets, the insulation had to have a low thermal conductivity while still withstanding the high temperatures, pressures, and aqueous media encountered in hydrothermal flames. A zirconia syntactic closed-cell microstructure ceramic shell manufactured by Powdermet Inc. was chosen for insulation. The

syntactic ceramic has a thermal conductivity of ~0.15 W/m-K, can withstand pressures up to 275 bar (4000 psi), and temperatures up to 1700 $^{\circ}$C.

The metal for the central rod had to have a high enough thermal conductivity to remove heat from the sensor surface quickly enough to prevent the surface from overheating. A relatively low surface temperature would also better simulate heat flux conditions encountered during spallation drilling, since typical surface temperatures during thermal spallation are ~500 $^{\circ}$C. A maximum design surface temperature of 400 $^{\circ}$C was chosen. The temperature of the mixed jet and cooling water, T_{out}, to which the HFM rejects heat would vary from about 50 to 100 $^{\circ}$C. Assuming the HFM at the point of heat rejection would be close to T_{out}, the design temperatures would result in a temperature drop of ~300 $^{\circ}$C within the rod. Based on the expected temperature drop, two metals were chosen for two different heat flux ranges: Naval brass (Alloy 485, k_c = 116 W/m-K) for heat fluxes up to ~1.5 MW/m^2 and tellurium copper (Alloy 145, k_c = 385 W/m-K) for heat fluxes up to ~5 MW/m^2. Tellurium copper was chosen over pure copper for its superior machinability and increased corrosion resistance.

Modeling

The dimensions used for modeling heat transfer in the HFM are shown in Figure 10.2. The overall diameter of the HFM was constrained by the inner diameter of the WCHB reactor. A length of 20 mm (0.787") was chosen for the central rod. The two thermocouples were positioned 10 mm apart, 5 mm from the sensor surface and base, respectively. According to Eq. (10-3), this separation distance should result in a 130 $^{\circ}$C temperature difference, or HFM signal, for the heat fluxes and brass and copper alloys described above. The length of the heat rejection region, where heat that flows in through the sensor surface can be rejected to the passing mixture of jet and cooling water, was determined using a heat transfer correlation for concentric tube flow (Gnielinski, 1998) to ensure that there would be adequate cooling of the HFM. The temperature of the mixed jet and cooling water streams was assumed to be 100 $^{\circ}$C.
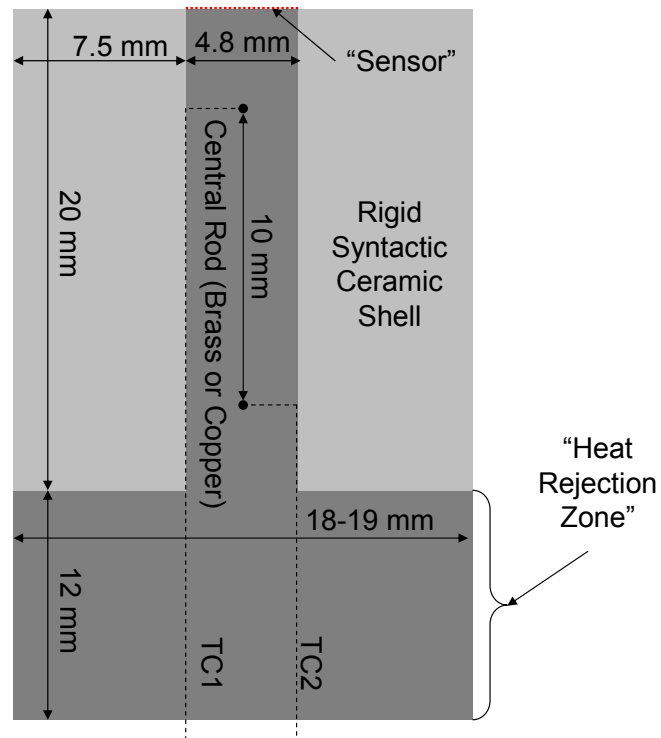
Figure 10.2 Schematic of rough dimensions used in modeling heat transfer within HFM.

Simulations of heat transfer through the proposed heat flux meter design were conducted using a 2-D steady state conduction heat transfer model in FEMLAB. The purpose of the simulations was to verify that the heat flux and temperature profile assumptions made during the HFM design apply for the chosen materials and HFM dimensions. The functioning of the HFM relies on the validity of the assumptions of a 1-D temperature profile in the axial rod and negligible heat transfer between the rod and the surrounding insulation.

Modeling of the HFM performance was complicated by the fact that it was unknown what the magnitude or profile of the heat flux at the sensor surface would be. Therefore, a range of incident heat flux profiles were used in the simulation. Eq. (10-4) was used for the incident heat flux, with the jet stagnation temperature varying as a function of the radius according to the correlation put forth by Kataoka (1985) for non-isothermal, variable-density jets:

$$T_{stag}(r) = T_{stag,r=0}\left[1 + 0.414(r/r_o)^2\right]^{-2}$$

Eq. (10-6)

where:

$$T_{stag,\,r=0} = \text{jet stagnation temperature at } r = 0$$
$$r_o = \text{jet half-radius}$$

This correlation for T_{stag}, along with the HFM sensor temperature (T_{sens}) from the simulation, was used with Eq. (10-4) to calculate the local heat flux from the impinging jet to the HFM. The heat transfer coefficient was assumed constant. Since its value was not known, a range of values was used. A complete list of the parameters and dimensions used in the model of steady-state heat transfer in the HFM is given in Table 10.1.

Table 10.1 Parameters and HFM dimensions used in HFM steady-state heat transfer model.

HFM dimensions	rod diameter	D_{rod}	4.8	mm
	rod length	L_{rod}	20	mm
	HFM overall diameter	D_{HFM}	20	mm
	HFM overall length	L_{HFM}	32	mm
thermal conductivities	Naval brass tellurium copper	k_c	115 385	W/m-K
	insulation	k_c	0.15	W/m-K
convective heat transfer: HFM surface	heat transfer coefficient	h	Table 10.3	
	stagnation temperature	T_{stag}	Eq. (10-6)	
convective heat transfer: insulation sides and heat rejection zone	heat transfer coefficient	h_{rej}	3000[a]	W/m^2-K
	mixed jet and cooling water temperature	T_{out}	100	^{o}C

[a] from (Gnielinski, 1998)

A wide range of jet stagnation temperatures, heat transfer coefficients, and jet half-radii were used to simulate heat transfer in the HFM. The parameters used and the simulation results for the Naval brass HFM design are shown in Table 10.2. Large values of r_o correspond to nearly constant jet temperatures over the heat flux sensor area, while smaller values represent rapidly changing jet temperatures as a function of radius, and hence changing heat flux. The maximum heat flux, q_{max}, is the maximum rate of heat transfer from the jet to HFM sensor surface and always occurred at $r = 0$, while q_{avg} is the area-averaged heat flux over the entire sensor surface. The range of r_o used covers nearly-constant incident heat flux profiles ($q_{max} \approx q_{avg}$) to localized heating of part of the sensor surface ($q_{max} >> q_{avg}$). The table shows that for the wide range of parameters tested, the heat flux measured by the HFM, q_{HFM}, should agree with the average incident heat flux to the HFM sensor to better than 10% accuracy. The only exception is when the jet half-radius is small compared to the radius of the sensor area, so there are large radial temperature gradients in the stagnation temperature profile. For a jet half-radius of $r_o = 1$ mm,

the jet temperature at the edge of the sensor would only measure 9% of its centerline value, which is not a realistic scenario for these experimental conditions.

Table 10.2 Heat flux profile parameters used and simulation results for heat transfer in HFM. Simulation assumes Naval brass used for central rod.

$T_{stag,\,r=0}$	h	r_o	q_{max}	q_{avg}	$T_{sens,\,r=0}$	T_1	T_2	q_{HFM}	% error
(°C)	(W/m²-K)	(mm)	(MW/m²)	(MW/m²)	(°C)	(°C)	(°C)	(MW/m²)	(%)
500	5000	10	1.01	0.97	297.0	252.8	165.5	1.01	4.1%
500	15000	10	1.64	1.49	390.6	324.3	196.1	1.49	-0.4%
500	30000	10	2.01	1.73	432.9	356.1	209.7	1.70	-1.8%
500	5000	5	1.11	0.91	278.5	237.2	158.8	0.91	0.4%
500	15000	5	1.98	1.40	367.6	303.9	187.3	1.35	-3.1%
500	30000	5	2.71	1.62	409.4	333.6	200.0	1.55	-4.4%
500	5000	3	1.26	0.76	246.5	210.7	147.4	0.73	-3.9%
500	15000	3	2.62	1.18	325.1	266.8	171.4	1.11	-6.5%
500	30000	3	4.03	1.38	365.1	291.8	182.1	1.27	-7.9%
500	15000	1	4.92	0.27	167.7	135.2	115.1	0.23	-14.1%
300	5000	10	0.51	0.48	197.7	175.8	132.5	0.50	4.0%
300	15000	10	0.83	0.74	244.4	211.4	147.7	0.74	-0.7%
300	30000	10	1.03	0.86	265.6	227.2	154.5	0.84	-2.1%
300	60000	10	1.24	0.94	279.4	237.2	158.8	0.91	-2.9%
300	5000	5	0.57	0.44	186.7	166.5	128.5	0.44	-0.7%
300	15000	5	1.04	0.69	230.7	199.1	142.5	0.66	-4.2%
300	30000	5	1.45	0.80	251.5	213.7	148.7	0.75	-5.2%
300	60000	5	2.01	0.87	266.5	222.9	152.6	0.82	-6.2%
300	5000	3	0.66	0.36	167.8	150.9	121.8	0.34	-5.6%
300	15000	3	1.42	0.56	205.3	177.1	133.0	0.51	-7.9%
300	30000	3	2.24	0.65	225.0	188.8	138.0	0.59	-9.2%
300	60000	3	3.48	0.72	241.8	196.2	141.2	0.64	-11.0%
300	15000	1	2.56	0.094	126.8	112.3	105.3	0.081	-14.1%

The simulation results also show that the assumptions of a 1-D temperature profile in the axial rod and negligible heat transfer between the rod and the surrounding insulation are justified. Figure 10.3 shows the temperature profile and radial heat flux contours for a typical run. Although there are some radial temperature profiles near the sensor surface, these are quickly damped out as heat is conducted down the central rod. All simulation results showed negligible radial temperature variation at r = 5 and 15 mm, where the thermocouples will be located.
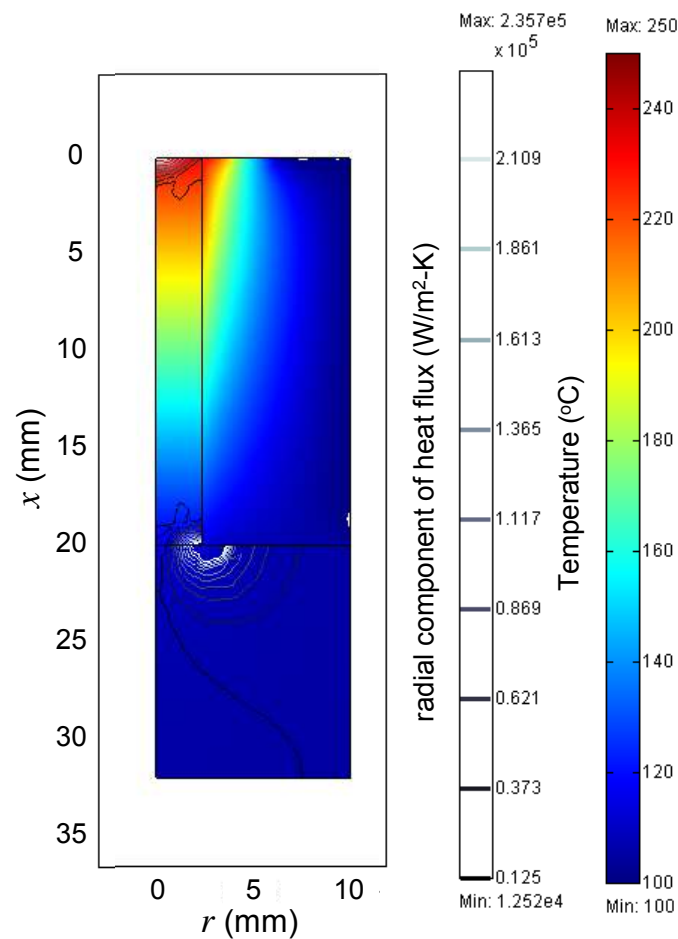
Figure 10.3 Temperature profile (color) and radial heat flux (contours) for simulation of heat transfer through HFM. (Naval brass HFM $T_{stag, r=0}$ = 300 ^{o}C, r_o = 5 mm, h = 15000 W/m^2-K).

Figure 10.4 shows the axial component of the heat flux along the axis of the central rod in the HFM. Near the surface, the axial heat flux can vary as a function of radius due to radial temperature gradients. However, as the heat is conducted through the rod, these temperature variations are quickly damped, so that the heat flux from the impinging jet over the entire surface area is channeled down the central metal rod. The heat flux through the HFM is measured by the temperature difference between the two thermocouples in the central rod. The simulation results for the centerline temperature profile, shown in Figure 10.5, confirm that the temperature profile in the rod is linear. The results also indicate that the linear temperature profile extends all the way to the HFM sensor surface to a good approximation.
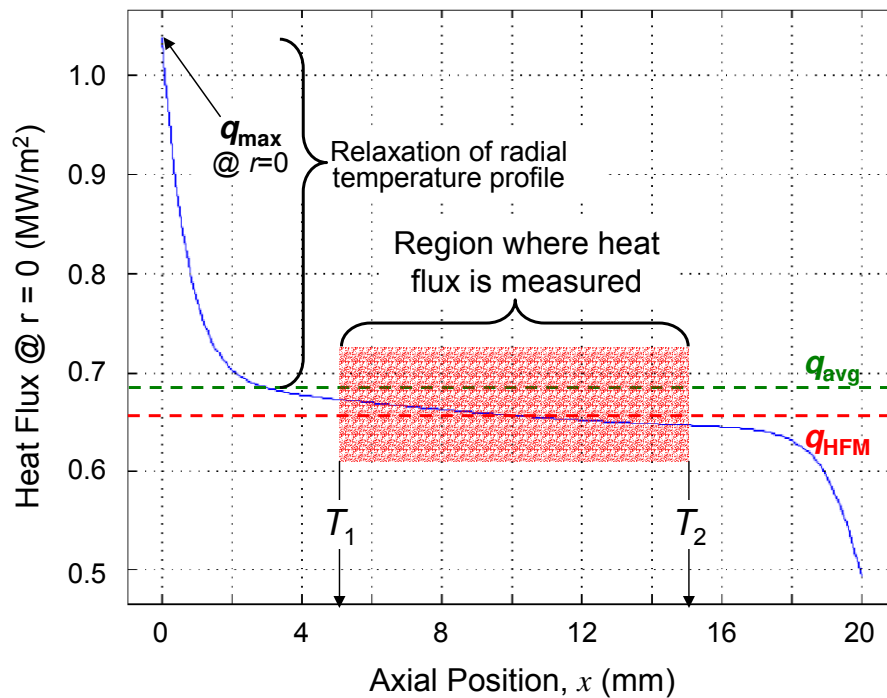
Figure 10.4 Simulation results for heat flux in axial direction at $r = 0$ as a function of axial position in HFM central rod. Actual average (q_{avg}) and measured (q_{HFM}) heat fluxes indicated by dashed lines. (Naval brass HFM $T_{stag, r=0}$ = 300 °C, r_o = 5 mm, h = 15000 W/m²-K).
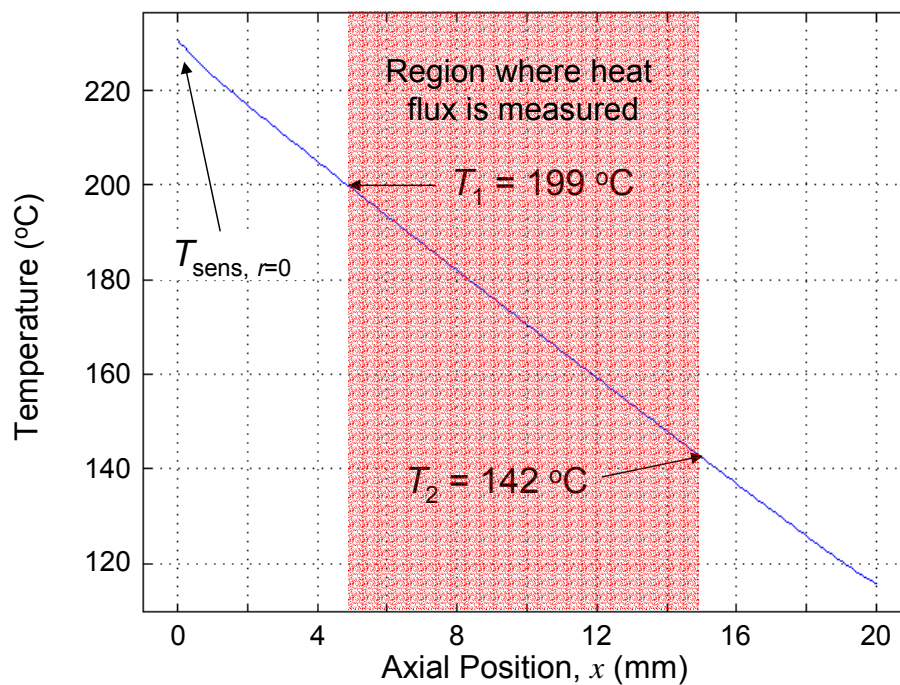

Figure 10.5 Simulation results for centerline temperature profile (at $r = 0$) in HFM central rod.   (Naval brass HFM $T_{stag, r=0}$ = 300 °C, r_o = 5 mm, h = 15000 W/m²-K).

Figure 10.4 shows that heat losses through the insulation in the region between the thermocouples are small. These losses account for part of the measurement error in Table 10.2 predicted by the simulations. Error is also introduced by the heat transfer between the central metal rod and the surrounding insulation near the surface. This flux can be either into or out of the central rod, depending on the stagnation temperature profile (which influences the temperature profile of the sensor and insulation surface). Unless there is some initial knowledge of the heat flux profile, a correction cannot be made. The modeling has shown that the heat flux measured by the HFM will give a good estimate of the average incident heat flux, regardless of the heat flux profile, so no attempt to correct for these errors was made. Since the only parameter that changes when tellurium copper is used as the HFM material of construction is the thermal conductivity, the results for those simulations were similar in nature.

Construction

Based on encouraging results from the FEMLAB modeling, construction of two heat flux meters commenced based on the detailed drawing design of the HFM is shown in Figure 10.6. The majority of the HFM construction was carried out at Potter Drilling LLC. The HFM consists of three parts: the central metal rod and body, the syntactic ceramic jacket, and the SS316 adapter. One central metal rod of the HFM was constructed of Naval brass for low heat flux (≤ 1.5 MW/m^2) measurements, and the other out of tellurium copper for high heat flux (≤ 5.0 MW/m^2) measurements. Channels and holes were drilled for 0.020" (0.5 mm) Type-K thermocouples using Electrical Discharge Machining (EDM). The thermocouples were then inserted, silver-soldered into place, and the central rod turned on a lathe to give a smooth finish. The SS316 adapter has an internal O-ring to seal the connection between the HFM body and adapter against the system pressure in the reactor. The adapter is then mounted on the tip of the rod of the movable probe assembly using a standard High Pressure (HIP) low-pressure ¼" (0.64cm) connection. The thermocouples travel out the bottom of the central rod and body, through the center of the adapter, into the rod of the movable probe assembly, and emerge out the end of the rod, where the thermocouple signals can be measured and recorded. The syntactic ceramic insulation jacket (OD = 18 mm) is slid over the central rod of the HFM and is held in place using high temperature epoxy applied to its base.
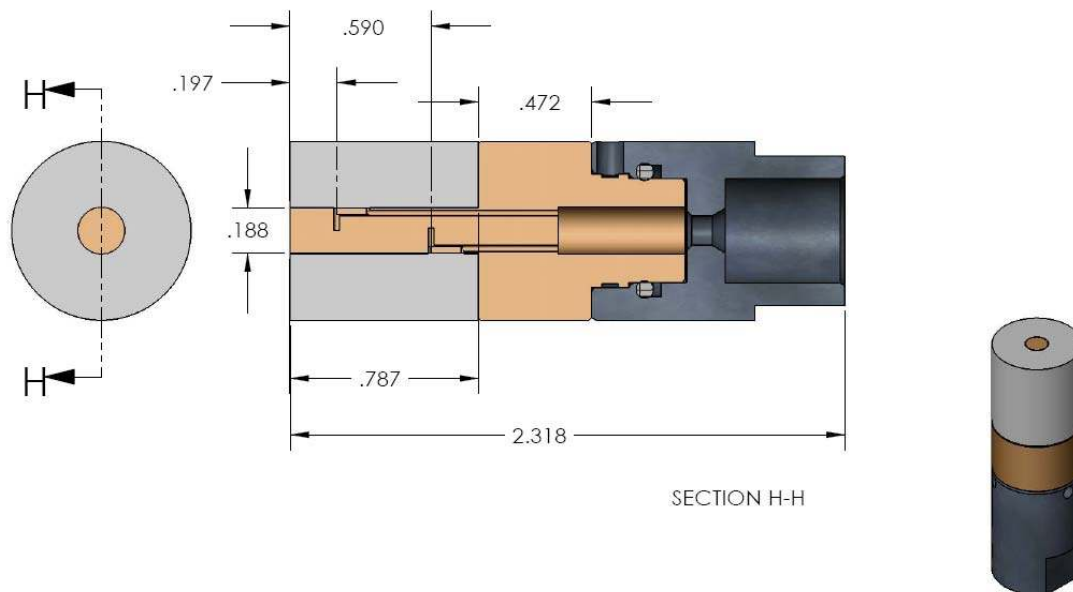
Figure 10.6 Detailed diagram for heat flux meter (HFM) constructed by Potter Drilling LLC. Body is constructed of either naval brass (k_c = 115 W/m-K) or tellurium copper (k = 385 W/m-K), insulation of syntactic ceramic (k_c = 0.15 W/m-K). Dimensions are given in inches.

10.3. Experimental Setup and Procedure

A major limitation in the heat flux measurement experiments was that with the HFM mounted on the movable probe, there was no means of directly measuring the jet temperature during the experiment. Therefore, each experiment was performed twice: once with the movable probe instrumented to measure the jet stagnation temperature as it impinged against a flat surface, and a second time with the HFM mounted on the HFM to measure the heat flux. Identical operating conditions were used for each experiment, so it was assumed that the stagnation temperature of the jet during the heat flux measurement experiments was the same as the stagnation temperature profile observed in the first experiment.

Stagnation temperatures were measured in a manner similar to that described in Section 8.7.2 using the experimental set-up shown in Figure 10.7. The nozzle configuration used is the same as that described in Section 9.2.1 and shown in Figure 9.1. A thin-walled nozzle with an inner diameter of 3.0 mm (0.12") and an outer diameter of 3.4 mm (0.13") (Figure 9.2) was used to make jets of hot water with both sub- and supercritical nozzle exit temperatures issuing into co-flowing subcritical water. The co-flowing subcritical, or cooling, water passed through a fine

mesh screen to mitigate entrance effects and ensure even distribution. A Macor ceramic block was mounted onto a threaded brass block using stand-offs and small machine screws. The brass block was then mounted on the end of the centering device ("rock carrier") of the movable probe. A type-K thermocouple (0.020" or 0.5 mm diameter) was passed through the probe and through a hole in the center of the ceramic block so that it was exposed ~1 mm above the surface of the block to measure the jet stagnation temperature at the point of impingement. The experimental setup for the heat flux measurements was the same as that shown in Figure 10.7, except the HFM was mounted at the end of the movable probe in place of the Macor block and brass nut. A modified centering device that slid over the ¼" (0.64 cm) tubing of the movable probe and was held in place using set screws was used to center the HFM.

The experimental procedure for making the hot water jets and gathering stagnation temperature data is similar to the one described in Chapter 9 for measuring the axial temperature profile of free jets. The WCHB pilot plant was started and pressurized using only deionized (DI) water as the process fluid. The temperature of the preheaters was increased slowly in 15 to 25 °C increments to prevent differential heating of the fittings from causing leaks in the system. Once the pilot plant had reached the desired operating conditions, the Macor block was moved to a stand-off distance of 20 mm (0.79") using the movable probe assembly and data collection began. The stagnation temperatures of the impinging hot water jets were measured in 1 to 2 mm intervals. Close to the jet nozzle exit, where temperatures increased rapidly as the stand-off distance increased, the spacing between measurements was decreased to 0.5 to 1 mm intervals. At each stand-off distance, data were collected once per second over a 30-second period. The average temperature and standard deviation were recorded. The temperature of the jet at the nozzle exit was measured by the thermocouple in the center of the Macor block at a very small stand-off distance (1 to 2 mm). Once data collection was complete, the Macor block was moved away from the nozzle exit and the operating conditions of the pilot plant were changed for the next data run.
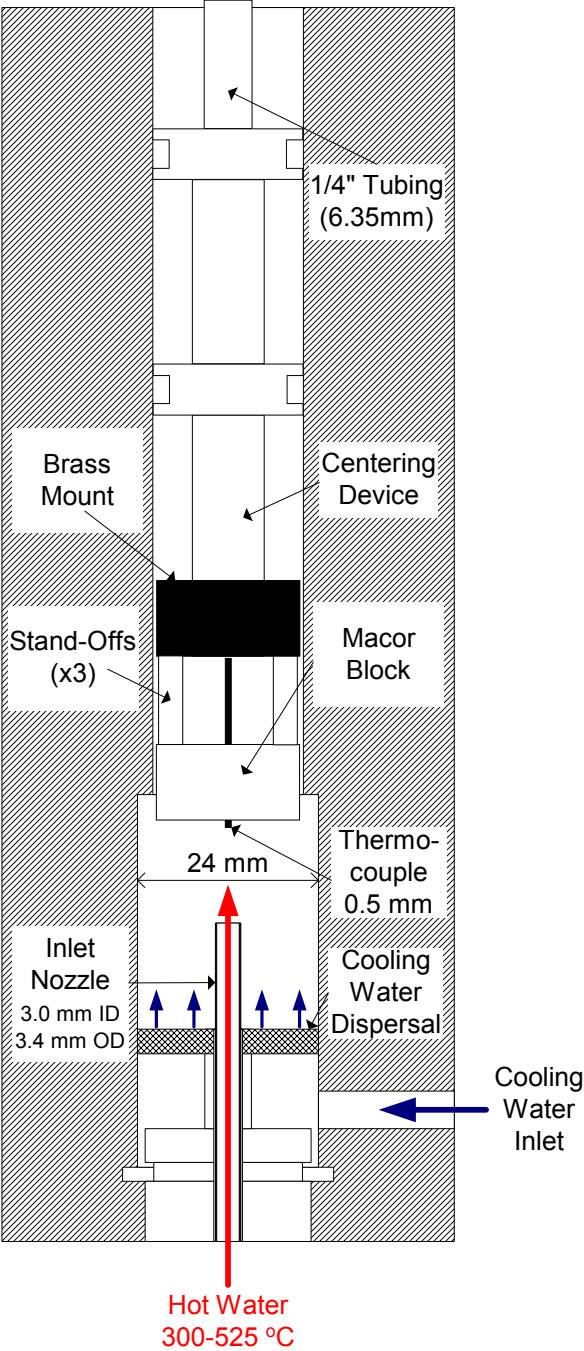
Figure 10.7 Experimental set-up for stagnation temperature measurements.

The experimental procedure for measuring the heat flux was identical to that for the stagnation temperature experiments. At each stand-off distance, data from the two thermocouples embedded in the HFM were collected once per second over a 30-second period. The average

temperatures and standard deviations were recorded. These average temperatures were used to calculate the heat flux from the impinging jet on the HFM surface using Eq. (10-3).

10.4. Results

Stagnation Temperature

Stagnation temperatures as a function of stand-off distance were measured for sub- and supercritical water jets. The stagnation temperature is defined as the temperature of the jet at the point where it impinges against a flat surface. At this point, the time-averaged radial and axial velocity of the jet is zero. The jet flow rates, jet nozzle exit temperatures, and co-flowing cooling water flow rates studied are shown in Table 10.3. The system pressure in all experiments was $P = 250$ bar. The experimental conditions were similar to those used in the study sub- and supercritical water jets issuing into co-flowing subcritical water in Chapter 9.

Table 10.3 Nozzle temperatures, densities and jet and cooling water mass flow rates used for stagnation temperature and heat flux experiments. Nozzle inner diameter, $D_o = 3.0$ mm.

T_o (^{o}C)	ρ_o (kg/m^3)	$\dot{m}_o$ (g/s)	G_o (kg-m/s^2)	G_o/G_a 20.7 g/s	41.3 g/s	62.0 g/s
400	166.5	2.00	0.0034	3.56	--	--
400	166.5	4.00	0.0136	--	3.56	--
425	126.8	3.49	0.0136	--	3.56	--
450	109.0	3.23	0.0136	--	3.56	--
475	97.8	3.06	0.0136	14.2	3.56	1.58
500	89.7	2.94	0.0136	--	3.56	--
525	83.5	2.83	0.0136	--	3.56	--
300	743.0	2.88	0.0016	1.65	--	--
300	743.0	5.75	0.0063	--	1.65	--
350	625.5	5.28	0.0063	--	1.65	--
375	505.5	4.75	0.0063	--	1.65	--
400	166.5	2.72	0.0063	--	1.65	--
425	126.8	2.38	0.0063	--	1.65	--
450	109.0	2.20	0.0063	--	1.65	--
500	89.7	2.00	0.0063	--	1.65	--

The scaling laws applied to free jets in Chapter 9 were also used to scale the stand-off distance and stagnation temperature of impinging jets. The stand-off distance, H, is defined as the distance from the nozzle exit to the flat surface. The stand-off distance is scaled using the

scaling law proposed by Thring and Newby (1953) for variable-density jets to give the effective stand-off distance, H_{eff}:

$$H_{eff} = \frac{H}{D_o}\left(\frac{\rho_o}{\rho_a}\right)^{-\frac{1}{2}}$$

Eq. (10-7)

where:
H = stand-off distance (mm)
D_o = nozzle diameter (mm)
ρ_o = density of jet at nozzle exit (kg/m^3)
ρ_a = density of ambient cooling water (kg/m^3)

The excess stagnation temperature (relative to the ambient temperature) is scaled by the excess jet temperature at nozzle exit to give the non-dimensionalized stagnation temperature, θ_s:

$$\theta_s = \frac{T_{stag} - T_a}{T_o - T_a}$$

Eq. (10-8)

where:
T_o = jet nozzle exit temperature (^{o}C)
T_a = ambient cooling water temperature (^{o}C)

Figure 10.8 shows that the decay of the stagnation temperature of the impinging subcritical and supercritical jets as a function of increasing stand-off distance is similar to that the temperature decay of free subcritical and supercritical jets discussed in Chapter 9. Once again, the behavior of jets with supercritical nozzle temperatures can be divided into two regions. Close to the nozzle exit, supercritical jets are rapidly quenched by the surrounding ambient temperature fluid. In the far-field, the non-dimensionalized stagnation temperature decays inversely with the effective stand-off distance ($\theta_s \propto H_{eff}^{-1}$). In fact, the behavior is so similar that as with the hot water free jets studied in Chapter 9, recirculation effects can be seen in the far-field for jets with insufficient co-flow. This is especially evident for the case of the jet in Table 10.3 with a nozzle exit temperature of 475 ^{o}C and a cooling water co-flow rate of 20.7 g/s. In Figure 10.8, the stagnation temperature decay of this jet can be seen to deviate from linear behavior, just as was observed for free jets with low cooling water flow rates.
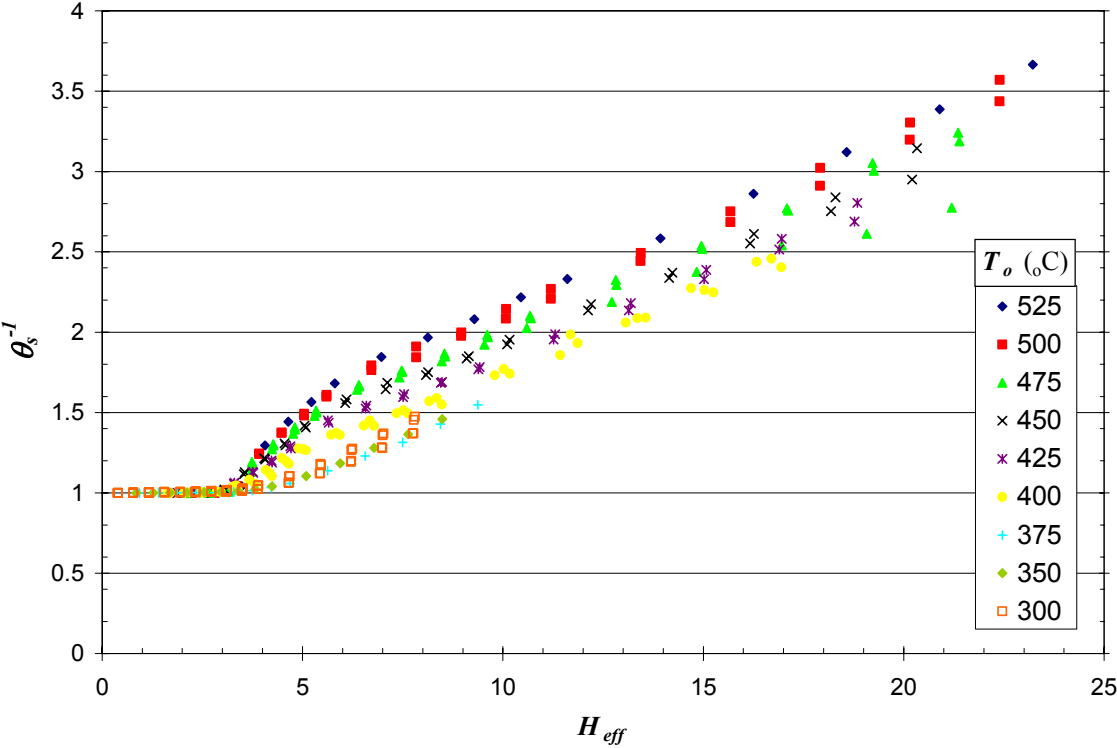
Figure 10.8 Stagnation temperature of hot water jets with sub- and supercritical nozzle exit temperatures as a f unction of stand-off distance.

It is not surprising that the behavior of the stagnation temperatures closely mimics free jet behavior, since the jet behaves as a free jet until it encounters the flat surface. Although the behavior is similar, it is not identical. The major difference between free jet and impinging jet temperature decay is that the rate of decay differs. The slope of the stagnation curves in Figure 10.8 range from 0.10 to 0.12 in the far-field; whereas for free jets they were observed to range from 0.16 to 0.18 (see Figure 9.16). The change in slope is caused by the change in jet behavior in the region near point of impingement. The same decrease in the rate of temperature decay was observed in the study of non-isothermal variable-density impinging jets by Kataoka et al. (1985). Their study looked at hot gas jets made by combusting methane, with initial density ratios $(\rho_o/\rho_s)^{-1}$ ranging from 3.10 to 5.99 impinging against a flat plate. Their experimental set-up permitted them to measure the centerline temperature of the impinging jet at all points between the nozzle exit and point of impingement. They observed that as the jet approached the flat plate, its temperature deviated from the centerline decay curve of free jets and remained nearly constant up to the point of impingement. Whereas a previous study had found that the centerline

temperature decay of free jets had slope of 0.20 (Kataoka et al., 1982), the decay in stagnation temperature of impinging jets had a fitted slope of 0.146. Kataoka et al. also observed that the Thring-Newby scaling did excellent job of correlating the data.

Measured Heat Flux

The heat transfer from impinging hot water jets to a flat surface was measured using the brass and copper heat flux meters (HFM's) described in Section 10.2 above. The hot water jets studied are described in Table 10.3. The HFM's operated as planned. A large temperature difference between the two thermocouples embedded in the HFM was measured, indicating heat flux through the probe. Results of the heat flux measurements using the Naval brass and tellurium copper HFM's are shown in Figure 10.9 and Figure 10.10, respectively. The results are limited to a single jet momentum flux to make the results readable. The maximum heat flux measured during the experiments was1.7 MW/m^2 for the brass HFM and 4.6 MW/m^2 for the copper HFM.

At first glance, the measured heat flux results run counter to the expected results. In the far-field, the heat flux from the low temperature jets is higher than that from the far-field jets. Also, the heat fluxes measured by the copper HFM are almost 3 times higher than those measured by the brass HFM for identical experimental conditions. As Eq. (10-4) shows, the heat flux is a function of the heat transfer coefficient, the stagnation temperature of the jet, and the temperature of the HFM sensor surface. The influence of all three of these parameters on the measured heat flux can be observed within the experiments and used to explain the observed results.

Much of the behavior of the observed heat flux among the different nozzle exit temperatures can be explained by analyzing the jet stagnation temperature. Figure 10.11 shows the measured jet stagnation temperature as a function of absolute stand-off distance for the heat flux measurements shown in Figure 10.9 and Figure 10.10. A comparison of the figures reveals that the measured heat flux agrees well with the jet stagnation temperature. As discussed in Chapter 9, the large density difference between the supercritical temperature jets and the ambient fluid causes the jet to be rapidly quenched near the nozzle exit, so that high temperatures do not penetrate far. The subcritical jets have a longer jet core, so their temperatures persist into the
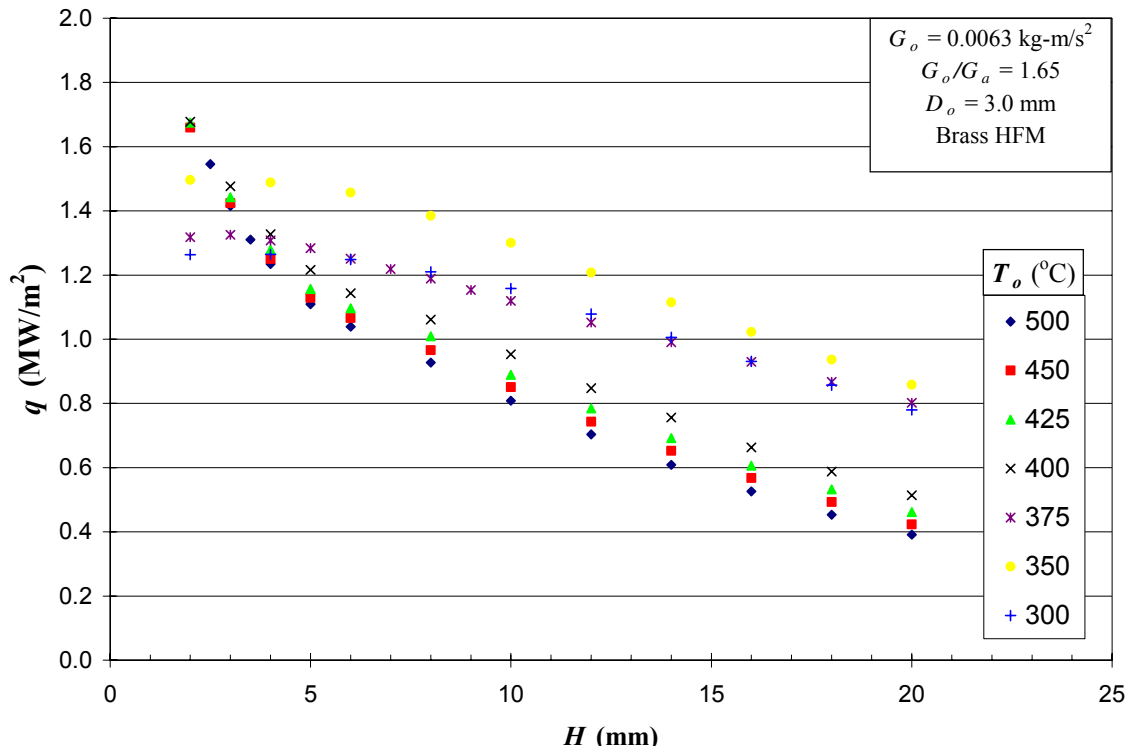
Figure 10.9 Heat flux from impinging jets to flat surface as a function of stand-off distance for a range of jet nozzle exit temperatures. Heat flux measured using Naval brass HFM.
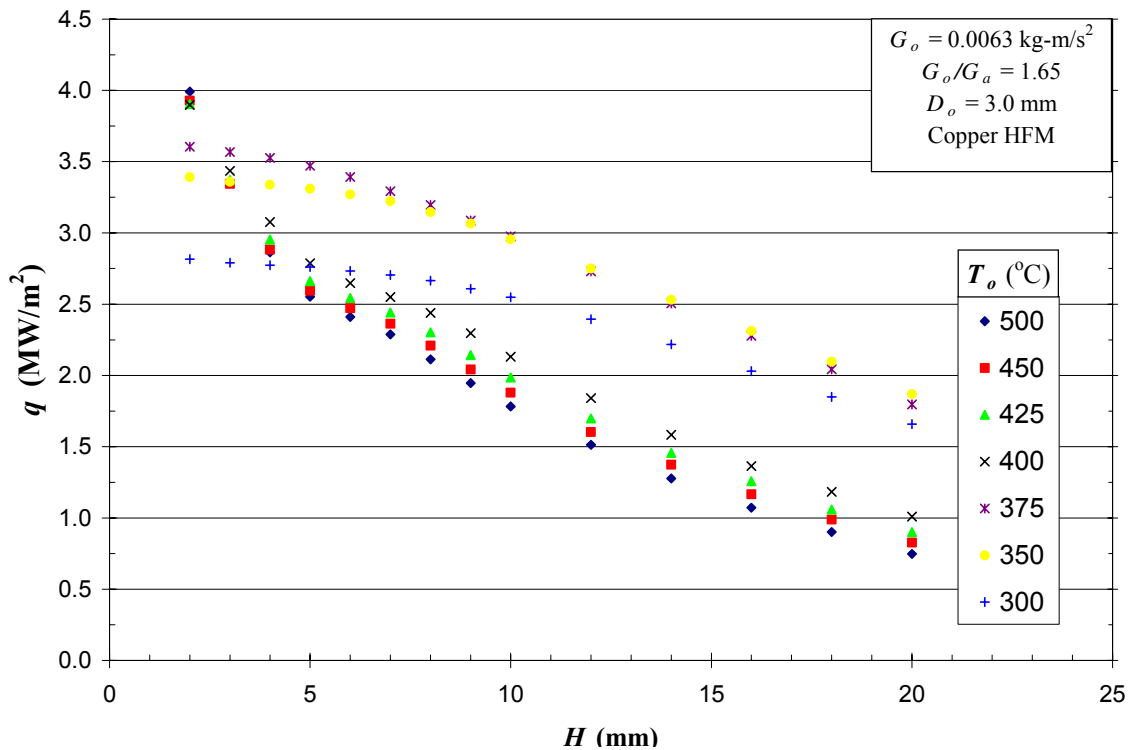

Figure 10.10 Heat flux from impinging jets to flat surface as a function of stand-off distance for a range of jet nozzle exit temperatures. Heat flux measured using tellurium copper HFM.

reactor for a greater absolute distance. The higher jet stagnation temperatures in the far-field result in higher rates of heat transfer from the subcritical jets to the HFM, despite having a lower initial temperature than the supercritical jets. Close to the nozzle exit, before the jets have had a chance to entrain a lot of ambient fluid, the supercritical jets have higher stagnation temperatures and correspondingly higher heat fluxes.
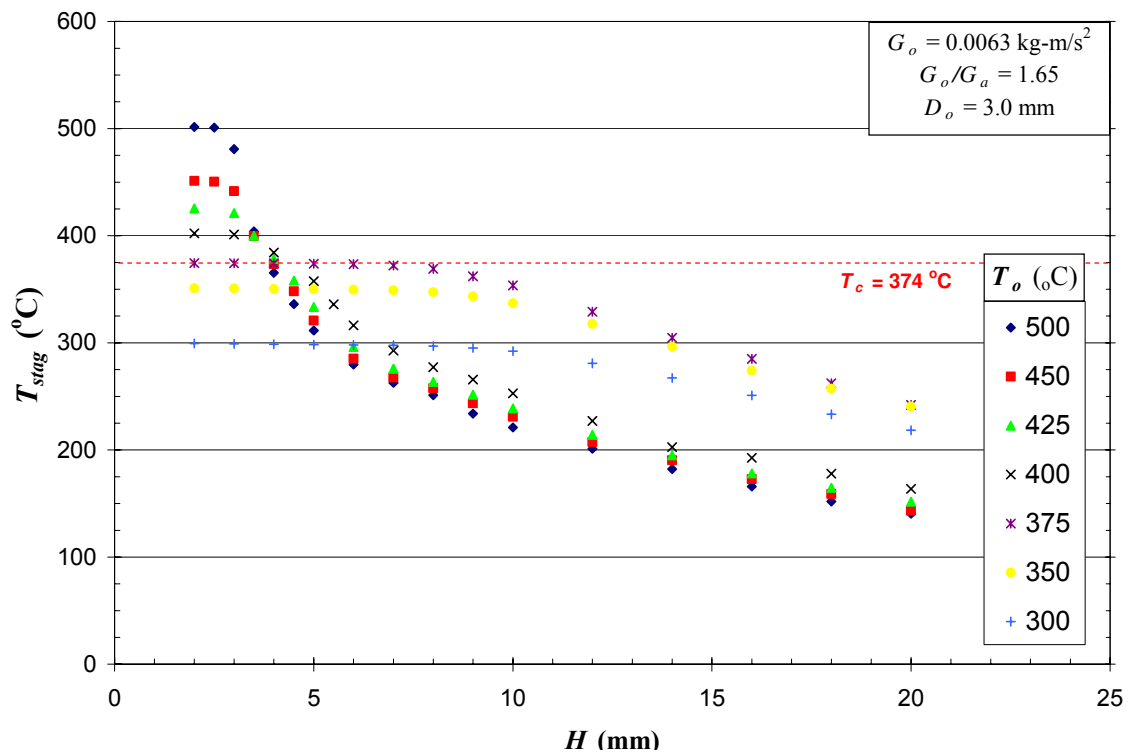

Figure 10.11 Jet stagnation temperature as a function of stand-off distance.

Unlike the stagnation temperature, which can be directly controlled, the HFM sensor surface temperature (T_{sens}) is controlled by the experimental conditions. Since the HFM is designed to measure the steady state heat flux, the amount of heat transferred convectively from the impinging jet equals the heat conducted through the block, as stated in Eq. (10-5). Assuming conduction through the insulation is negligible, heat conduction through the HFM is determined by the thermal conductivity of the metal in the HFM central rod and base and the temperature driving force between the sensor surface and the heat rejection zone. For a given set of impinging jet and cooling water conditions, the sensor surface temperature adjusts to accommodate the heat flux through the HFM so that the heat transferred from the impinging jet to the HFM, the heat conducted through the HFM, and the heat rejected to the passing cooling

water are balanced. The heat flow through the HFM can be changed by varying the stagnation

temperature, as seen above, or by changing the temperature in the heat rejection zone. A series

of experiments for a given jet with a range of different cooling water flow rates demonstrates this

point. The heat flux from an impinging jet with a nozzle exit temperature of 475 ^{o}C as a function

of stand-off distance was measured using three different cooling water flow rates, so that the

temperature of the combined jet and water flow (T_{out}) in heat rejection zone of the HFM varied

from 59 to 119 ^{o}C. The resulting heat fluxes through the HFM under the different experimental

conditions, shown in Figure 10.12, differ greatly, despite nearly identical conditions for the jet at

the HFM surface (a difference in stagnation temperatures in the far-field region can be seen in

Figure 10.8).
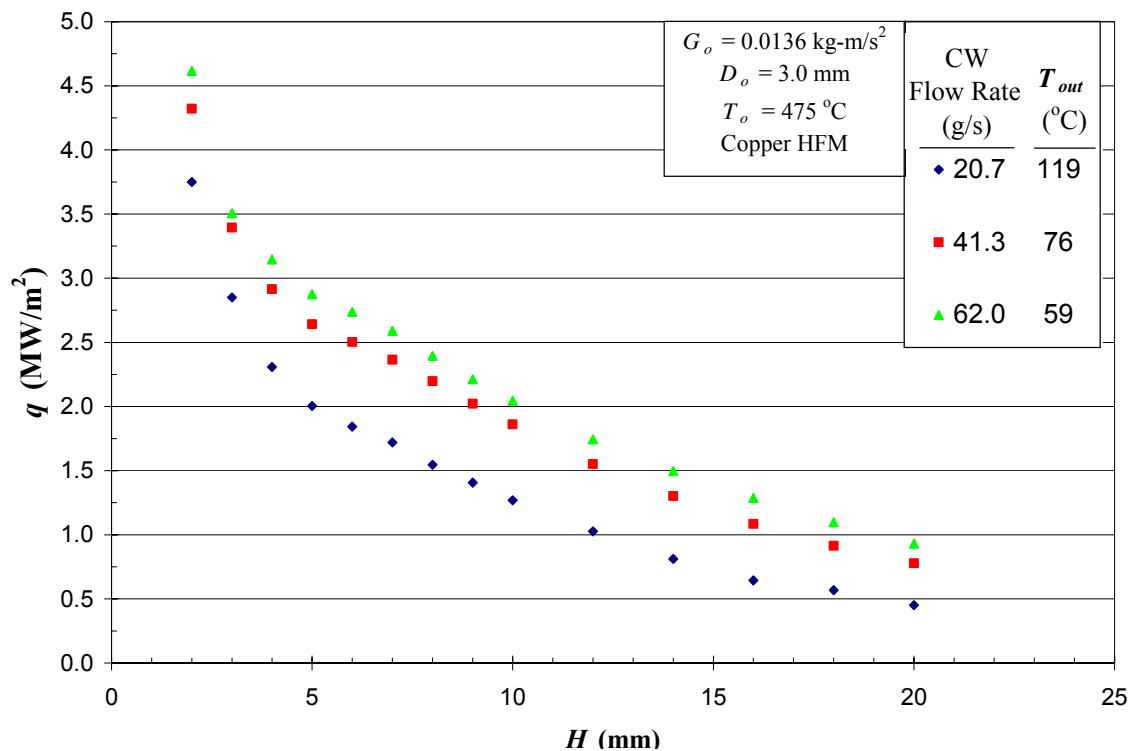
Figure 10.12 Effect of temperature in heat rejection region of HFM on measured heat flux.

The same principles also explain the large difference in measured heat flux for brass and copper

HFM's under otherwise identical operating conditions. Figure 10.5 shows that the temperature

at the sensor surface can be approximated by linear extrapolation of the temperature profile

measured by the thermocouples in the HFM, so that Eq. (10-5) can be re-written as:

$$h(T_{stag} - T_{sens}) \approx k_c \frac{(T_{sens} - T_2)}{(x_{sens} - x_2)} \qquad \text{Eq. (10-9)}$$

T_{sens} now appears on both sides of the equation. When the brass HFM is replaced by the copper HFM for a given experiment, k_c in Eq. (10-9) increases by over a factor of three, so that the right side is larger than the left. To balance the equation, T_{sens} must decrease, so that the total heat transferred from the jet to the HFM increases. A comparison of the extrapolated values of T_{sens} and the measured values of T_1 and T_2 from an experiment using both the brass and copper HFM's is shown in Figure 10.13.
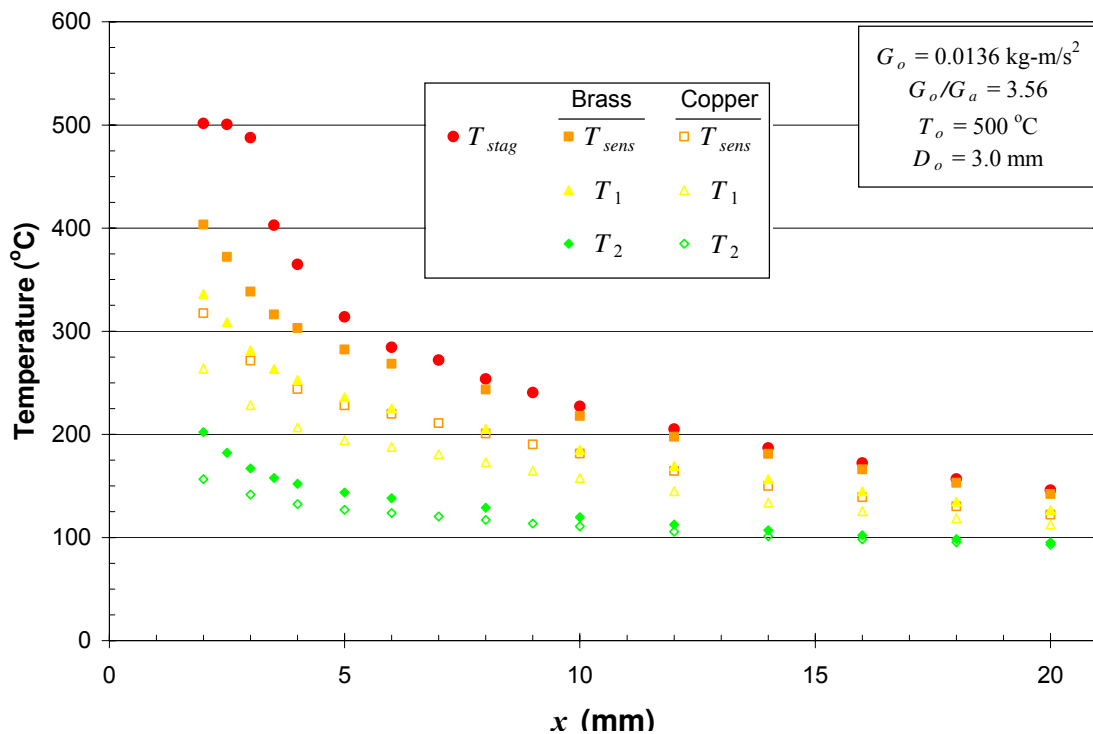

Figure 10.13 Effect of HFM type (brass or copper) on temperatures in HFM for all stand-off distances studied.

Heat Transfer Coefficient

The discussion above demonstrates that reporting the heat flux directly is of limited use since the measured heat flux depends heavily on the experimental conditions and set-up. A more useful parameter that could be derived from the experiments would be the heat transfer coefficient. The

heat transfer coefficient is defined in Eq. (10-4), which can be rearranged to give the heat transfer coefficient explicitly in terms of experimentally derived variables:

$$h = \frac{q_{HFM}}{\left(T_{stag} - T_{sens}\right)}$$

Eq. (10-10)

The quantities from which the heat transfer coefficient is calculated are themselves subject to measurement error. Since the calculation requires taking the inverse of a temperature difference, the error in the heat transfer calculation becomes large when the temperature difference between the jet stagnation temperature and HFM sensor surface becomes small. According to Figure 10.13, this is the case for measurements with the brass HFM, especially in the far-field region. Figure 10.14 shows how the difference in the jet stagnation and HFM sensor surface temperature varies between the brass and copper HFM's for a wide range of experimental conditions. For the brass HFM, many of the temperature differences are less than 10 ^{o}C when the stagnation temperature is below the critical temperature of water. Since the 95% confidence interval (CI) for the temperature difference is ±3 ^{o}C based on the limits of error of the thermocouples alone, there are large errors are associated with the heat transfer coefficient from experiments with the brass HFM. The copper HFM, on the other hand, maintains a reasonably large temperature difference between the jet and the sensor surface under all conditions, due to its high thermal conductivity. For this reason, only heat transfer coefficients calculated from experiments using the copper HFM will be discussed.
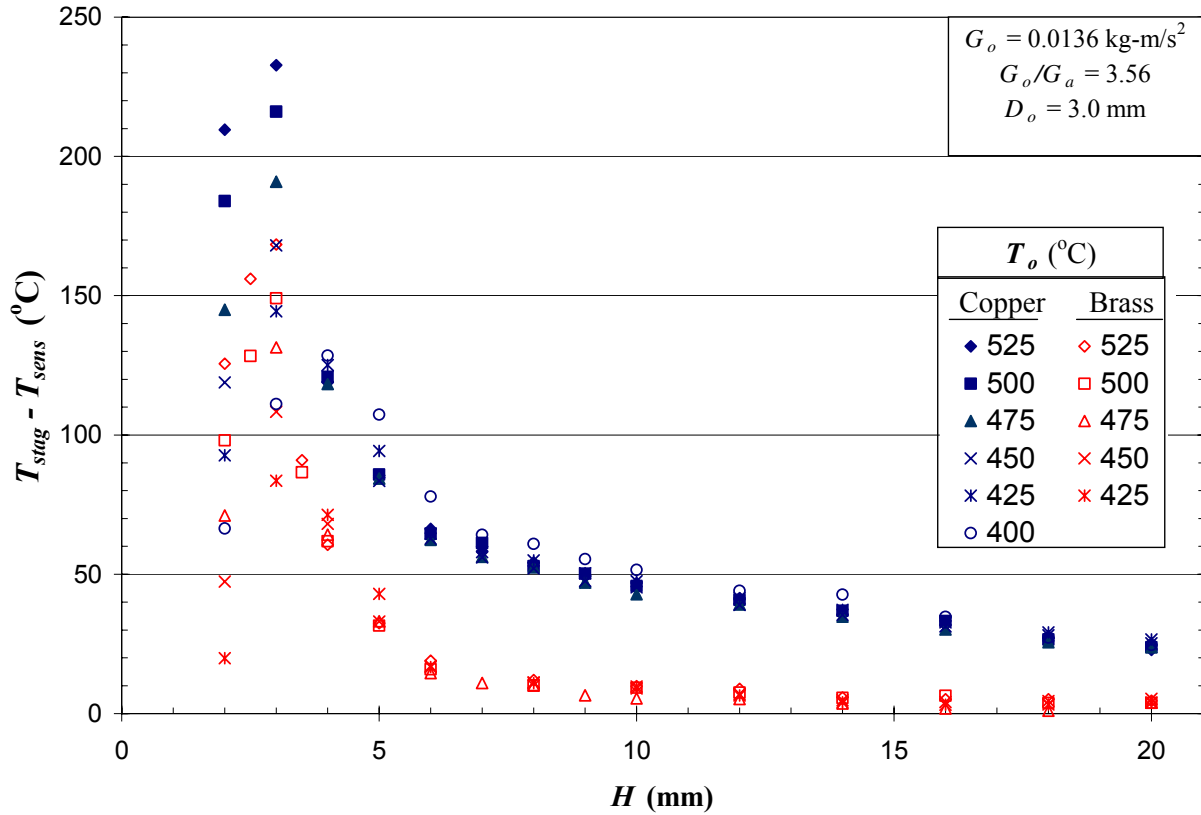
Figure 10.14 Temperature difference between jet stagnation temperature and calculated HFM sensor surface temperature as a function of stand-off distance for supercritical temperature jets. Results from experiments with both Naval brass and tellurium copper HFM's shown.

The error in the heat flux measurement q_{HFM}, was assessed using the 2-D heat transfer model discussed in Section 10.2. The jet stagnation temperature is not measured directly during the heat flux experiments, but instead is assumed to be the same as measurements in a previous experiment performed under the same operating conditions.   This assumption was supported by good agreement between the observed temperatures of the jet water as it exits the preheaters before proceeding to the nozzle. T_{sens} is calculated by linear extrapolation of the temperatures measured by the thermocouples in the HFM. Simulation results show that the actual value of T_{sens} can vary from the estimated value by anywhere from <1% to 5%, depending on the parameters assumed for the model.

The errors suggested by the model for the heat flux and HFM surface temperature measurements are systematic, and could be corrected with proper calibration, whereas the thermocouple measurements are subject to random errors. Without any means to check the calibration of the

HFM, the analysis will proceed by considering only the random errors associated with the measurements. Propagation of error analysis was used to calculate the 95% CI of the heat transfer coefficient. The 95% CI was calculated for T_{stag}, T_1 and T_2 based on the observed measurements. This value was compared to the manufacturer's reported standard limit of error for the thermocouple, and the larger of the two values was chosen. These values were then used to calculate the 95% CI for T_{sens}, q_{HFM}, and the heat transfer coefficient. The calculated heat transfer coefficient as a function of stand-off distance for experiments performed with the copper HFM are shown in Figure 10.15 and Figure 10.16. The 95% CI of the measurement error is inset in each figure. The propagation of error analysis found that the measurement errors are less than 10% at most condition. Heat transfer coefficients ranging from 30,000 to 40,000 W/m-K were observed for most of the jets, with the jets in Figure 10.16 tending to have higher heat transfer coefficients. The value of the heat transfer coefficient rises slightly for subcritical temperature jets in the jet development region. For supercritical temperature jets, the heat transfer coefficient is observed to drop significantly in the area of the jet development region where the stagnation temperature transitions from subcritical to supercritical temperatures. The increase in the stagnation temperature compensates for this decrease in the heat transfer coefficient so that the overall heat flux from the jet to the HFM continues to increase as the stand-off distance is decreased.

10.5. Conclusions

The heat flux from impinging supercritical temperature jets to a flat surface were successfully measured in the MIT WCHB system using specially designed heat flux meters (HFM's). The HFM's were designed to measure the heat flux from high temperature jets and flames in a high pressure aqueous environment. A two-dimensional model of heat conduction in the HFM was used to optimize its design. Two HFM's were constructed in collaboration with Potter Drilling, LLC: one using Naval brass for low heat flux measurements and the other using tellurium copper for high heat flux measurements. Maximum heat fluxes of 1.7 MW/m^2 and 4.6 MW/m^2 were measured using the brass and copper HFM's, respectively.

Figure 10.15 Measured heat flux for jets impinging against a flat surface as a function of stand-off distance for a range of nozzle exit temperatures and jet momentum flux of $G_o = 0.0063$ kg-m/s^2. (Inset: 95% CI of error measurement as a function of nozzle exit temperature and stand-off distance.)
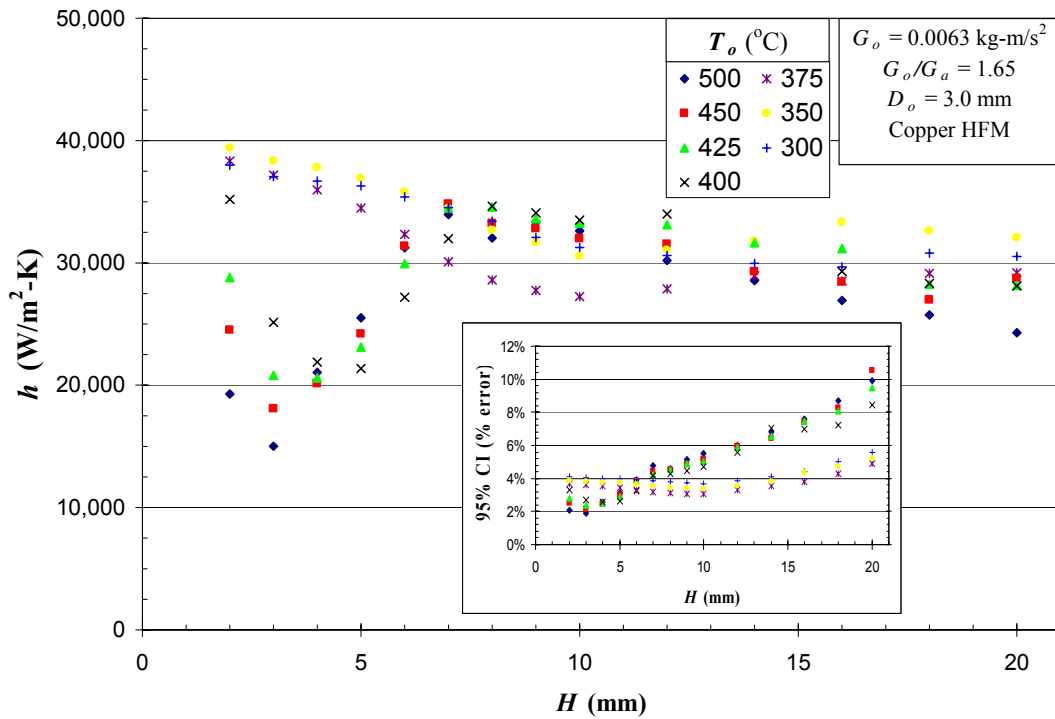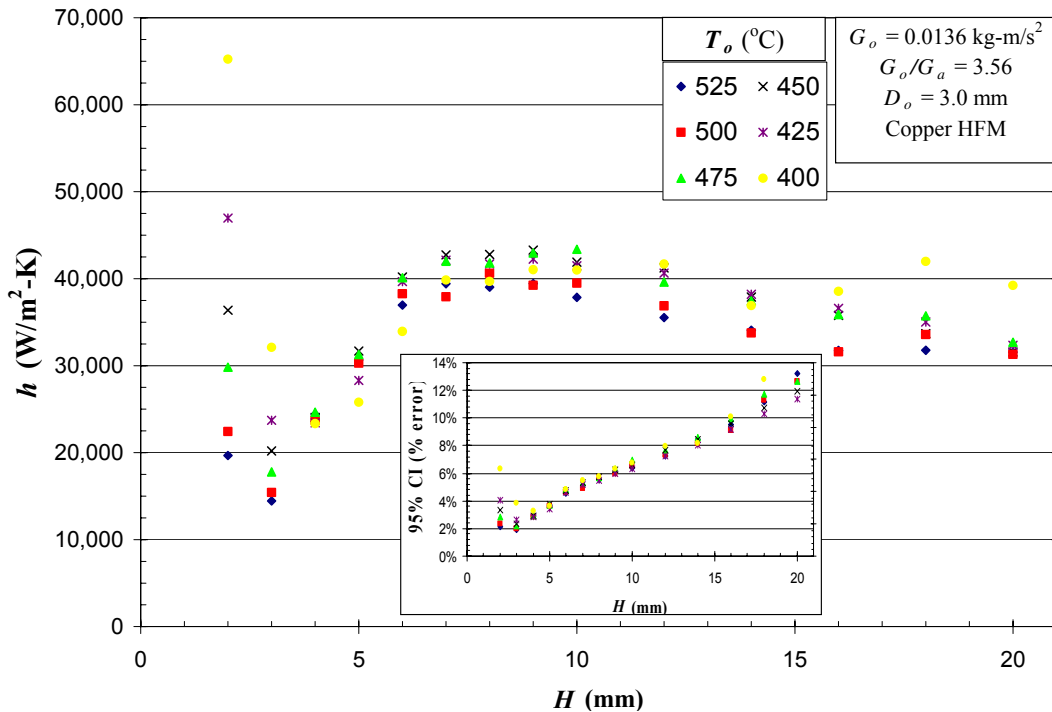

Figure 10.16 Measured heat flux for jets impinging against a flat surface as a function of stand-off distance for a range of nozzle exit temperatures and jet momentum flux of $G_o = 0.0136$ kg-m/s^2. (Inset: 95% CI of error measurement as a function of nozzle exit temperature and stand-off distance.)

The measured heat flux was not a static property of the jet and stand-off distance, but depended on the jet stagnation temperature, experimental conditions, and HFM used. Much of the behavior of the measured heat flux as a function of stand-off distance could be explained by the stagnation temperature of the impinging jet. Stagnation temperatures as a function of stand-off distance were measured for a range of sub- and supercritical temperature jets in a separate experiment. The axial decay profiles of the stagnation temperatures of the impinging jet behaved much like the free jets studied in Chapter 9: Supercritical jets were quenched quickly after the nozzle exit, and the stagnation temperature decay in the far-field scaled inversely with the stand-off distance. However, the slopes of the axial decays of the stagnation temperature differed from the slope observed for the axial decay of free jets. The measured stagnation temperature and heat flux profiles were well correlated, with higher stagnation temperatures resulting in higher heat fluxes.

The cooling water flow rate was also seen to impact the measured heat flux. Higher cooling water flow rates increased the ability of the HFM's to conduct by cooling them more, thus lowering the temperature at the sensor surface and increasing the measured heat flux. The copper HFM was able to measure much higher heat fluxes than the brass HFM due to its higher thermal conductivity. This allowed it to maintain a lower sensor surface temperature, which increased the temperature driving force for convective heat transfer. Because of the relatively lower thermal conductivity of brass, the brass HFM had a higher sensor surface temperature. In addition to lower measured heat fluxes, small temperature differences between the jet and HFM surface in the far-field region resulted in large errors in the calculated heat transfer coefficient for experiments using the brass HFM.

The copper HFM was able to maintain a large enough temperature difference between the jet and surface that the uncertainty errors of the calculated heat transfer coefficients have 95% confidence intervals of $\pm10\text{-}12\%$ or less. Heat transfer coefficients ranging from 30,000 to 40,000 W/m^2-K were measured at stand-off distances in the far-field region for jets with both sub- and supercritical nozzle exit temperatures. The subcritical temperature jets maintained these high heat transfer coefficients for stand-off distances in the temperature core region of the

jet. For supercritical jets, the heat transfer coefficient dropped significantly to values of less than 20,000 W/m^2-K in the area of the jet development region where the stagnation temperature transitions from subcritical to supercritical values. Rapidly increasing stagnation temperatures in this region compensate for the decrease in heat transfer coefficient so that the heat flux from the impinging supercritical temperature jets continually increases as the stand-off distance decreases.

Compared to previous spallation experiments, the heat fluxes measured using the brass and copper HFM's for the jets in this study should be more than adequate to induce thermal spallation in rocks, even for large stand-off distances. However, the free jet temperature measurements in Chapter 9 and the stagnation temperature measurements here show that very small stand-off distances are required to be able to heat the rock surface to a sufficiently high temperature to induce thermal spallation. Using a conservative value of $h = \sim 20,000$ W/m^2-K for the heat transfer coefficient of an impinging supercritical jet, a temperature difference of 50 $^\circ$C between the jet and rock surface would deliver a heat flux of 1 MW/m^2 to the rock surface. Based on these results and the observations of previous researchers in our group (Rauenzahn and Tester, 1989; Wilkinson and Tester, 1993), a jet with a nozzle exit temperature of 525 $^\circ$C should be able to induce thermal spallation in the rock surface at a stand-off distance of 1-2 nozzle diameters. The results of the studies in Chapters 9 and 10 indicate that thermal spallation is feasible in a high pressure, high density, aqueous environment similar to that which could be encountered in deep borehole conditions. They also support the conclusion that the reason spallation was not observed in the experiments on rock samples in Chapter 8 was due to insufficient rock sample size and not because of insufficient temperatures or heat fluxes. Future experiments should be performed on larger rock samples to ensure that heating of the rock sample is confined to a small portion of its surface.

References

Augustine, C., J. Potter, R. Potter and J. W. Tester (2007). "Feasibility of Spallation Drilling in a High Pressure, High Density, Aqueous Environment: Characterization of Heat Transfer from an H_2-O_2 Flame Jet." <u>Geothermal Resources Council Transactions</u> **31**: 241-245.

Gnielinski, V. (1998). "Forced Convection in Ducts." <u>Heat Exchanger Design Handbook, 1998</u>. G. F. Hewitt. New York, Begell House. **2:** 2.5.1-6.

Kataoka, K., H. Shundoh and H. Matsuo (1982). "A Generalized-Model of the Development of Non-Isothermal, Axisymmetric Free Jets." <u>Journal of Chemical Engineering of Japan</u> **15**(1): 17-22.

Kataoka, K., H. Shundoh, H. Matsuo and Y. Kawachi (1985). "Characteristics of Convective Heat-Transfer in Non-Isothermal, Variable-Density Impinging Jets." <u>Chemical Engineering Communications</u> **34**(1-6): 267-275.

Rauenzahn, R. M. and J. W. Tester (1989). "Rock Failure Mechanisms of Flame-Jet Thermal Spallation Drilling - Theory and Experimental Testing." <u>International Journal of Rock Mechanics and Mining Sciences & Geomechanics Abstracts</u> **26**(5): 381-399.

Thring, M. W. and M. P. Newby (1953). "Combustion Length of Enclosed Turbulent Jet Flames." Fourth Symposium (International) on Combustion, Baltimore, Williams & Wilkins, 789-796.

Wilkinson, M. A. and J. W. Tester (1993). "Experimental-Measurement of Surface Temperatures during Flame-Jet Induced Thermal Spallation." <u>Rock Mechanics and Rock Engineering</u> **26**(1): 29-62.

Chapter 11: Conclusions and Recommendations for Future Research

11.1. Conclusions

The purpose of this research was to study the various factors affecting the economic and technical feasibility of Engineered Geothermal Systems (EGS), with a special emphasis on advanced drilling technologies. The objectives of this thesis were twofold: to assess the feasibility of technical and economic aspects of EGS through modeling and analysis, and to gain a quantitative understanding of the behavior and use of high temperature jets in high pressure, high density, hydrothermal media for rock drilling. In the first part of the thesis, three studies devoted to modeling and analysis of the technologies used to develop EGS projects were performed. In the second part, laboratory experiments and analyses were carried out to determine the feasibility of deep borehole thermal spallation drilling and to characterize the processes that control heat transfer to the rock surface under deep borehole conditions.

Since the cost of completing wells is a major factor in determining the economic feasibility of EGS projects, historic well cost data were analyzed to identify trends, and a drilling cost index for updating historic geothermal well costs to present day costs was developed. From the analysis, it was concluded that both oil and gas well and geothermal well costs increase non-linearly with depth, but geothermal wells cost 2 to 5 times more than oil and gas wells drilled to comparable depths. The historic costs of oil and gas wells were found to be strongly linked to the price of crude oil due to fluctuations in demand for rotary drilling rigs for exploration and production of oil.

The effects of different advanced drilling technologies on drilling costs were estimated and incorporated into a techno-economic model to estimate their impact, as well as the impact of advanced reservoir stimulation technologies, on EGS levelized electricity costs (LEC). Cost curves were developed for three advanced drilling technologies: single diameter or monobore wells, increased rates of penetration, and reduced casing costs. The analysis showed that capital

costs and LECs for EGS power plants can be reduced significantly by advances in drilling technology that decrease drilling costs directly, or by advances in EGS reservoir technology that increase production well flow rates and decrease the number of wells needed.

A technical analysis of geothermal binary Rankine cycle surface power plants was also performed to determine the effect of novel working fluids on plant efficiency for both sub- and supercritical binary cycles. Models of sub- and supercritical binary Rankine power cycles utilizing a range of working fluids were developed and simulated using Aspen Plus 2006 software. The models were used to determine the optimum working fluid/operating conditions combination of binary cycles using geothermal resources ranging from 100-200 $^{\circ}$C. For the model design specifications considered, supercritical binary cycles were more efficient than subcritical cycles at all geothermal resource temperatures, producing 4-23% more net power. This was despite having parasitic pumping losses 2-3 times higher than the subcritical cases. For both the sub- and supercritical cases, refrigerants were often found to be the best working fluids, especially for lower temperature geothermal resources.

Although the high cost associated with drilling wells and their impact on EGS power plant economics were known before this project and were the motivation for research into advanced technologies that could decrease these costs, the studies and conclusions described above helped to better frame the context of the problem and to refine the quality and understanding of previous analyses. The conclusions clearly demonstrate that drilling costs for EGS projects are significant and greatly affect the economics of EGS projects, and demonstrate that advances in both drilling and reservoir stimulation technologies can greatly lower future EGS costs, increasing the range of resources that can be economically developed.

The objective of the second part of the thesis was the application of thermal spallation drilling to deep boreholes. Thermal spallation is the fragmentation of a brittle solid into small, disc-like flakes by rapidly heating a confined fraction of the rock. It was proposed that the necessary temperatures and heat fluxes needed to induce thermal spallation in the high pressure, high density deep borehole environment could be achieved using hydrothermal flame technologies.

An autoclave reaction system was designed and constructed to create flame jets in water at a pressure of 250 bar. Experiments using methanol and hydrogen as fuels demonstrated that hydrothermal flames can be produced in a downhole environment. Flame temperatures in excess of 1000 $^{\circ}$C were measured. Attempts were made to use the flames to spall small rock samples. A flame spallation test on Sioux quartzite showed that spallation occurred initially, but then stopped. It was inferred from thermally induced cracks that ran the length of the sample that the entire surface had been heated, causing spallation to stop due to a lack of confining stresses. It was concluded that the maximum rock sample size that could be used in the WCHB was too small for continuous spallation to be maintained.

The experimental system was modified to study the centerline temperature decay of non-isothermal turbulent free jets of water at supercritical temperatures injected into subcritical temperature water. Jet nozzle exit temperatures ranging from 300 to 525 $^{\circ}$C, corresponding to initial density ratios ranging from 1.35 to 12.1, were studied. The jet was divided into two regions: the far-field region and the jet development region. In the far-field, where the density gradient between the jet and ambient fluid was small, the axial temperature decay followed conventional jet scaling laws, indicating that the jet flow was self-similar. The Thring-Newby scaling law accurately accounted for the large initial density ratio between the nozzle exit and ambient fluid. However, the slope of the axial decay of the jets varied slightly as a function of the initial density ratio. The variation was attributed to experimental conditions rather than being a characteristic of the axial temperature decay of supercritical jets. In the jet development region, supercritical jets were observed to be quickly quenched to below the critical temperature of water within one or two diameters of the nozzle exit due to rapid entrainment of ambient fluid.

A device for measuring heat flux in the experimental system was designed, constructed, and used to determine the heat transfer coefficients of sub- and supercritical temperature jets impinging against a flat surface. A two-dimensional model of heat conduction in the heat flux meter (HFM) was used to optimize its design. Maximum heat fluxes of 1.7 MW/m^2 and 4.6 MW/m^2 were measured using HFM's constructed out of brass and copper, respectively. Heat transfer coefficients ranging from 30,000 to 40,000 W/m^2-K were calculated for stand-off distances in

the far-field region for jets with both sub- and supercritical nozzle exit temperatures. For supercritical temperature jets, the heat transfer coefficient dropped significantly to values of less than 20,000 W/m^2-K in the area of the jet development region where the stagnation temperature transitions from subcritical to supercritical values.

The studies of the axial temperature decay and heat flux from impinging supercritical temperature jets indicate that the necessary temperatures and heat fluxes required to induce thermal spallation in rocks can be achieved in a deep borehole. However, small stand-off distances of one or two nozzle diameters are required to be able to heat the rock surface to a sufficiently high temperature to induce thermal spallation under the experimental conditions studied.

11.2. Recommendations for Future Research

Research on the modeling and analysis of EGS power plants will continue as better and more complete data on Engineered Geothermal Systems becomes available with the construction of more and larger demonstration sites, and eventually commercial power plants. In particular, the drilling costs associated with EGS plants can continue to be updated as new drilling cost data becomes available. Since drilling costs vary greatly depending of the well design and location, a study of how drilling costs can be expected to decrease as knowledge of the drilling conditions in a particular EGS resource would be useful to EGS economic studies. Additional updates to the MIT EGS techno-economic model would also help to predict EGS costs as technology advances and improves. The study on the efficiency of subcritical and supercritical Rankine cycles could be enhanced by expanding the subcritical Rankine cycle scenario to include superheating of the working fluid before the preheater. Also, an economic analysis of the plant construction costs on a per-kW net power output basis is needed to determine if the efficiency gains from the supercritical cycle justify the increased capital costs.

There are many experimental studies remaining that could expand on the studies contained in this thesis and enhance the understanding of thermal spallation in deep boreholes. To begin, a new reactor design is needed that facilitates ignition of the hydrothermal flame and provides

more space for studying hydrothermal jets. The reactor should be large enough to accept 4" rock cores or larger, so that localized heating of the rock surface can occur while allowing the confining stresses that induce spallation to build up. This re-design could include the construction of pre-heaters (especially the oxygen pre-heater) with a smaller thermal mass, so that the response time of the pre-heaters to changes in the operating changes can be increased and heat-up and cool-down times can be decreased. Alternatives to auto-ignition via increasing the temperatures of the fuel and oxygen inlet streams should also be explored. One possible solution may be the use of catalysts to achieve ignition at lower temperatures.

The study of the behavior of axisymmetric free jets at supercritical temperatures issuing into subcritical ambient conditions and the heat flux experiments could be performed with different size diameter nozzles. Experiments with smaller diameter nozzles (~1 mm) would allow a larger portion of the far-field region to be studied using the current reactor system. Conversely, a much larger diameter nozzle is needed to better probe the jet development region. The smaller diameter results in larger values of the effective diameter, so the region far downstream of the nozzle exit can be explored. Conversely, larger diameters result in an increase in the absolute size of the jet development region. The temperature of the ambient fluid could be varied to validate the observed results for changing ambient conditions. Likewise, a different fluid with a lower critical temperature that would be easier to study experimentally, such as CO_2 ($T_c = 31$ ^{o}C) or Propane ($T_c = 97$ ^{o}C) could be used. The results from both the free-jet and the heat flux measurement experiments would benefit with a higher range of nozzle temperatures to confirm that the observed behavior extends to higher nozzle exit temperatures.

These studies were carried out for free jets and for jets impinging against a flat surface to gain an understanding of supercritical fluids in simple systems. An actual deep borehole drilling system will consist of a flow reversal after impingement, so that the jet is re-entraining its own fluid. This system will behave differently than the one studied here. Future experiments should focus on the fundamental behavior of these flow reversal systems. Future experimental systems should also be designed with this in mind so that they can be instrumented to study temperature profiles and heat flux within the borehole geometry.